From ultrastructure to near-atomic resolution: cryo-EM studies of the core molecular machineries of selective autophagy and protein biosynthesis

Inaugural dissertation

for the attainment of the title of doctor
in the Faculty of Mathematics and Natural Sciences
at the Heinrich Heine University Düsseldorf

presented by

Lisa Jungbluth
from Aachen

Düsseldorf, May 2024

from the institute of Biology
at the Heinrich Heine University in Düsseldorf
and the Ernst Ruska-Centre for Microscopy and Spectroscopy with Electrons:
Structural Biology (ER-C-3)
at the Forschungszentrum Jülich

Published with permission of the
Faculty of Mathematics and Natural Sciences at
Heinrich Heine University Düsseldorf

Supervisor: Prof. Dr. Carsten Sachse

Co-supervisor: Prof. Dr. Gunnar Schroeder

Date of the oral examination: 09.07.2024

Eidesstaatliche Versicherung

Ich versichere an Eides Statt, dass die Dissertation von mir selbständig und ohne unzulässige fremde Hilfe unter Beachtung der „Grundsätze zur Sicherung guter wissenschaftlicher Praxis an der Heinrich-Heine-Universität Düsseldorf“ erstellt worden ist.

Ort, Datum

Lisa Jungbluth

"Science and everyday life cannot and should
not be separated",

Rosalind Franklin

Summary

The different techniques in cryogenic electron microscopy can span resolution ranges from an ultrastructural scale to near-atomic resolution and are therefore suitable to investigate cellular processes including autophagy and protein biosynthesis. Autophagy directs the degradation of cargos with varying sizes from a single protein chain by chaperone-mediated autophagy up to whole organelles in (selective) macroautophagy. In this thesis, the selective degradation of ribosomes via NUFIP1 as well as the ultrastructural function of the selective autophagy receptor p62 were investigated with cryogenic electron microscopy. To understand the underlying molecular mechanism of NUFIP1-mediated ribophagy, NUFIP1 was studied in the context of different autophagy induced conditions by single-particle analysis of 80S human ribosomes. To study the interaction- between p62 and a phagophore membrane, cryogenic electron tomography was employed on samples of LC3 covered liposomes together with p62. Moreover, to investigate the higher-order structure of cellular p62 bodies and associated cargo, phase separation droplets of p62 filaments were formed by the addition of polyubiquitinated cargo and imaged using cryogenic electron tomography. To complete the available resolution range of cryogenic electron microscopy, the unique features of the Actinobacterium *Corynebacterium glutamicum* 70S ribosome were investigated by single-particle analysis. The contribution of bS22 to the ribosomal function in *C. glutamicum* was determined by solving the three-dimensional structures of the wildtype and ΔbS22 ribosome to near-atomic resolution. By exploiting the potential of single-particle analysis in the structural analysis of dynamic processes, 70S ribosomes were captured in four distinct translational states. In addition, the mode of action of Kasugamycin on the 70S ribosome was studied. The binding pocket of Kasugamycin within the 70S ribosomes could be identified and its modulation on the translational landscape for the wildtype and two resistant mutants resolved. The different results generated in this thesis demonstrate the capabilities of cryogenic electron microscopy to resolve high-resolution atomic-level detail in the case of a bacterial ribosome up to the ultrastructure of molecular assemblies for the selective autophagy receptor p62.

Table of contents

1 Introduction 1

1.1 Transmission electron microscopy 1

1.1.1 Basic set-up of a transmission electron microscope 2

1.1.2 Amplitude and phase contrast 8

1.1.3 The contrast transfer function in transmission electron microscopy 10

1.1.4 (Cryogenic) electron microscopy of biological specimen 12

1.2 Autophagy 23

1.2.1 Macroautophagy 25

1.2.2 Conjugation of ATG8 family proteins to phagophore membranes 29

1.2.3 Selective autophagy 31

1.2.4 Phase separation 41

1.3 Translation in *Corynebacterium glutamicum* 45

1.3.1 Bacterial translation 45

1.3.2 The Actinomycetota ribosome 47

1.3.3 The bS22 protein 48

1.3.4 The antibiotic Kasugamycin 50

2 Aims 53

3 Results and Discussion 55

3.1 The selective autophagy receptor NUFIP1 55

3.1.1 Cellular localization of NUFIP1 55

3.1.2 Purification of recombinantly expressed NUFIP1 61

3.1.3 Structural analysis of human 80S ribosomes in autophagy 65

3.2 The selective autophagy receptor p62 71

3.2.1 Protein expression and purification 71

3.2.2 Preparation of LC3B-Cys covered liposomes 75

3.2.3 Biochemical characterization of LC3B binding to p62 filaments 78

3.2.4 Cryogenic electron tomography of p62 filaments with LC3B covered liposomes 80

3.2.5 *In vitro* phase separation of p62 filaments by polyubiquitin 82

3.2.6 Cryogenic electron tomography of p62 filaments in *in vitro* phase separation 85

3.2.7 *In vitro* phase separation of p62 filaments by divalent cations 88

3.2.8 Discussion 90

3.3 Structure of the *Corynebacterium glutamicum* 70S ribosome 95

3.3.1 Single-particle analysis 95

3.3.2 The conformational landscape of *C. glutamicum* 70S ribosome 100

3.3.3 Structural characterization of Kasugamycin binding and its influence on the translational landscape of the *C. glutamicum* 70S ribosome 102
3.3.4 Influence of ΔbS22 on the structure, conformational landscape, and Kasugamycin resistance of *C. glutamicum* 70S ribosome 105
3.3.5 Influence of ΔKsgA on the structure, conformational landscape, and Kasugamycin resistance of *C. glutamicum* 70S ribosome 108
3.3.6 Discussion 110

4 Outlook 115

5 Material and Methods 119

5.1 Material 119
5.1.1 Plasmids 119
5.1.2 Cell lines, bacterial strains, media, and supplements 120
5.1.3 Protein purification and characterization buffers 122
5.1.4 Chromatography resins and columns 125
5.1.5 Software and online tools 126

5.2 Molecular biological methods 128
5.2.1 Plasmid isolation 128
5.2.2 Plasmid isolation for human cell culture 129
5.2.3 Polymerase chain reaction and Dpn1 digestion 129
5.2.4 Agarose gel electrophoresis and DNA clean-up 130
5.2.5 DNA assembly and transformation for selection 131
5.2.6 Sanger Sequencing 131

5.3 Human cell culture 131
5.3.1 Quantifying cell density in liquid cultures with cell counting 131
5.3.2 Maintenance of FreeStyle™ 293-F cell line 132
5.3.3 Transient protein expression in FreeStyle™ 293-F cells 133
5.3.4 Maintenance of HeLa 134
5.3.5 Immunofluorescence staining and imaging 134
5.3.6 Transient protein expression in HeLa and live cell imaging 136

5.4 Microbiological Methods 136
5.4.1 Quantifying cell density in liquid cultures with OD_{600} 136
5.4.2 Transformation and Pre-culture 137
5.4.3 Recombinant protein expression in *E. coli* BL21(DE3) 137

5.5 Purification and sample preparation 138
5.5.1 Fractionation of FreeStyle™ 293-F 138
5.5.2 Ribosome extraction from FreeStyle™ 293-F for SPA 140

5.5.3 Cell lysis of *E. coli* BL21(DE3) ... 141
5.5.4 Immobilized metal ion affinity chromatography ... 142
5.5.5 Maltose-binding protein affinity chromatography ... 142
5.5.6 Glutathione S-transferase affinity chromatography ... 143
5.5.7 Preparative size exclusion chromatography ... 143
5.5.8 Desalting chromatography ... 144
5.5.9 Membrane filtration ... 145

5.6 Biochemical, biophysical, and immunological Methods ... 145
5.6.1 Quantitation of nucleotide/protein concentration in solution with UV absorbance spectrophotometry ... 145
5.6.2 Quantification of lipids by fluorescence spectrophotometry ... 146
5.6.3 SDS-Polyacrylamide gel electrophoresis ... 146
5.6.4 Immunospecific staining of SDS-gels (Western Blot) ... 147
5.6.5 Pull-down assay ... 148
5.6.6 Liposome coating with LC3B-Cys ... 148
5.6.7 Light microscopy of phase separation ... 149

5.7 Electron microscopy ... 150
5.7.1 Negative stain electron microscopy ... 150
5.7.2 Single-particle analysis of human 80S ribosomes ... 150
5.7.3 Cryo-ET of p62 filaments and GST-4xUbiquitin ... 152
5.7.4 Cryo-ET of p62 filaments and LC3B-Cys coated liposomes ... 153
5.7.5 Single-particle analysis of *C. glutamicum* 70S ribosomes ... 154

6 References ... 157

7 Supplement ... 179

7.1 List of Figures ... 179
7.2 List of Tables ... 181

8 Acknowledgments ... 183

1 Introduction

1.1 Transmission electron microscopy

The first transmission electron microscope (TEM) was developed by Ernst Ruska and Max Knoll in the early 1930s (Knoll and Ruska 1932) and the first biological specimen were imaged around 1939 (Ruska et al. 1939). In 1986 Ernst Ruska was awarded the Nobel Prize in Physics for transmission electron microscopy, shared with Gerd Binning and Heinrich Rohrer for their development of the scanning tunneling microscope. Similar to transmission light microscopy, in transmission electron microscopy the image is formed by the interaction between the electron beam and the specimen. Transmission electron microscopy exceeds the resolution limit of light microscopy by several magnitudes. A light microscope is limited to about 200 nm in resolution compared to an electron microscope with a theoretical resolution limit of 40 pm for electrons accelerated to 200 kV (Kohl and Reimer 2008). Biological specimen are highly sensitive to radiation damage and historically needed to be stained with heavy metal stains to be able to image in a TEM (Brenner and Horne 1959). The first step towards modern transmission electron microscopy of unstained biological specimen was taken in 1975 when Henderson and Unwin solved sucrose-embedded but unstained bacteriorhodopsin to 7 Å resolution (Henderson and Unwin 1975). In the 1980s and 1990s, cryogenic transmission electron microscopy (cryo-EM) was developed in which the biological specimen are embedded in vitreous ice by plunge freezing into liquid ethane. The cryogenic temperatures allowed fixation of the samples on TEM grids without fixation agents or stain, which additionally kept the specimen in a near-native state. Further, the vitrification of the specimen allowed low-dose imaging to circumvent radiation damage degradation (Adrian et al. 1984). Finally, the invention and availability of direct electron detectors starting around 2012 led to the so called *resolution revolution*. Since then, a multitude of hardware and software improvements made cryo-EM become the structural biology method with an increase in published structures per year from 119 in 2013 to 4,582 in 2023 in the Protein Data Bank (RCSB PDB). The current resolution record in single-particle analysis is 1.22 Å (Nakane et al. 2020). Today, (cryo) transmission electron microscopy has become a major structure determination method in biological sciences, applied among others in cancer research, virology, and drug development (De Oliveira et al. 2021).

1.1.1 Basic set-up of a transmission electron microscope

Electron microscopes cover a family of instruments, including TEM, scanning transmission electron microscopes (STEM), scanning electron microscopes (SEM), and low-energy electron microscopes (LEEM). The basic set-up of a TEM is shown in Figure 1. From top to bottom, a modern TEM consists of an electron gun, condenser lens system, stage with specimen holder, objective lens system, objective aperture, projection lens system, and a detection unit. The different components will be discussed in the following paragraphs.

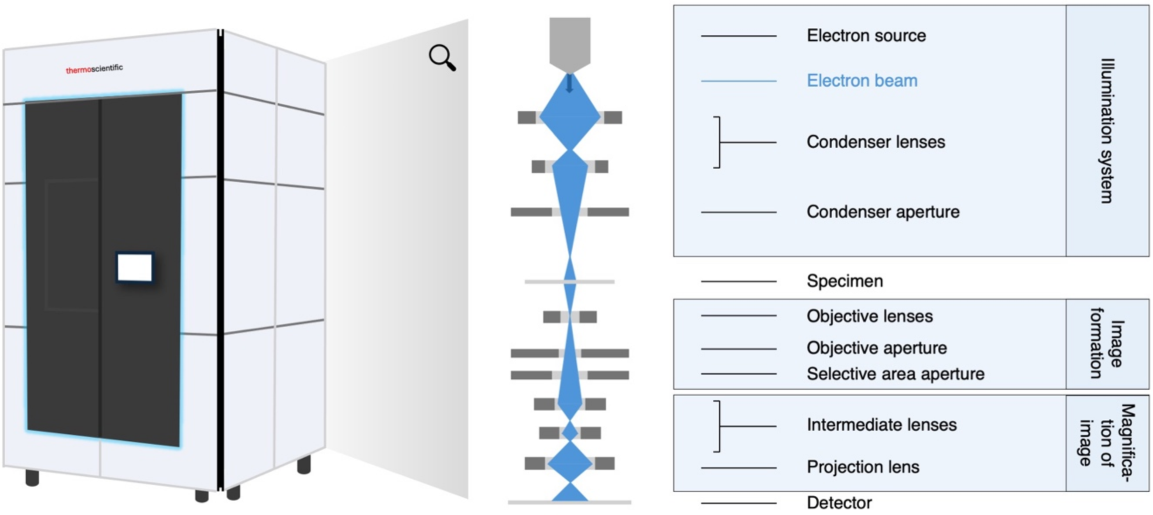

Figure 1: Basic set-up of a transmission electron microscope
Schematic depiction of a transmission electron microscope. The electron beam is produced by the electron source and focused in the condenser lens system. After passing the sample, the objective lenses focus the electron beam into the image plane. The projection lens system expands the electron beam onto the detector. Apertures in the microscope modify the electron beam by physically blocking electrons at high scattering angles or restriction to a limited size of the electron beam. (The Figure was conceptually inspired by Ortmann De Percin Northumberland and Sachse 2023).

The electron gun

At the top of the TEM sits the electron gun that ejects an electron beam through a combination of an electron source (cathode) and electrostatic lens elements (Rose 2008). The electron source can be built of a tungsten filament, a lanthanum hexaboride (LaB_6) single crystal, or a field emission gun (Egerton 2005). The tungsten filament and LaB_6 single crystal are thermionic sources. In both cases, a current is applied to the filament/crystal which results in an increase in temperature. At temperatures of approximately 2,400 – 2,600°C for a tungsten filament or 1,300 – 1,500°C for a LaB_6 crystal, the electrons gained sufficient thermal energy to escape the solid surface. Similar to light bulbs, the electron emission is randomly orientated. Since this is not desirable for an electron beam, an electric field is applied to focus the electron beam into the TEM, using, for example, a Wehnelt cylinder. The voltage between the anode and cathode accelerates the electrons to the desired kinetic energy and towards the column (Chao et al. 2013). A schematic depiction of a tungsten filament and LaB_6 single crystal is shown in Figure 2.

Field emission sources/field emission guns (FEGs) on the other hand utilize electrostatic emission. The electron emission is induced by a strong electrostatic field that is applied to a sharp tip of a tungsten wire. The emission area for a FEG lies within the nanometer range compared to the micrometer range for the thermionic electron sources (Rose 2008). Altogether, through the smaller diameter and more coherent and greater current density (up to three orders of magnitude), FEGs significantly improve the signal-to-noise ratio and resolution (Orloff 2009). In TEMs, FEGs can be built in two different ways, namely Schottky FEG and cold FEG (cFEG). In a Schottky FEG the tungsten tip is coated with zirconium oxide, adding additional thermal extraction to the electrostatic increasing its brightness (Bakker et al. 1996). The anode at the bottom of the electron gun accelerates the electrons to their defined kinetic energy, e.g. 300 kV, before the electrons enter the column of the microscope (Rose 2008). A FEG is schematically depicted in Figure 2.

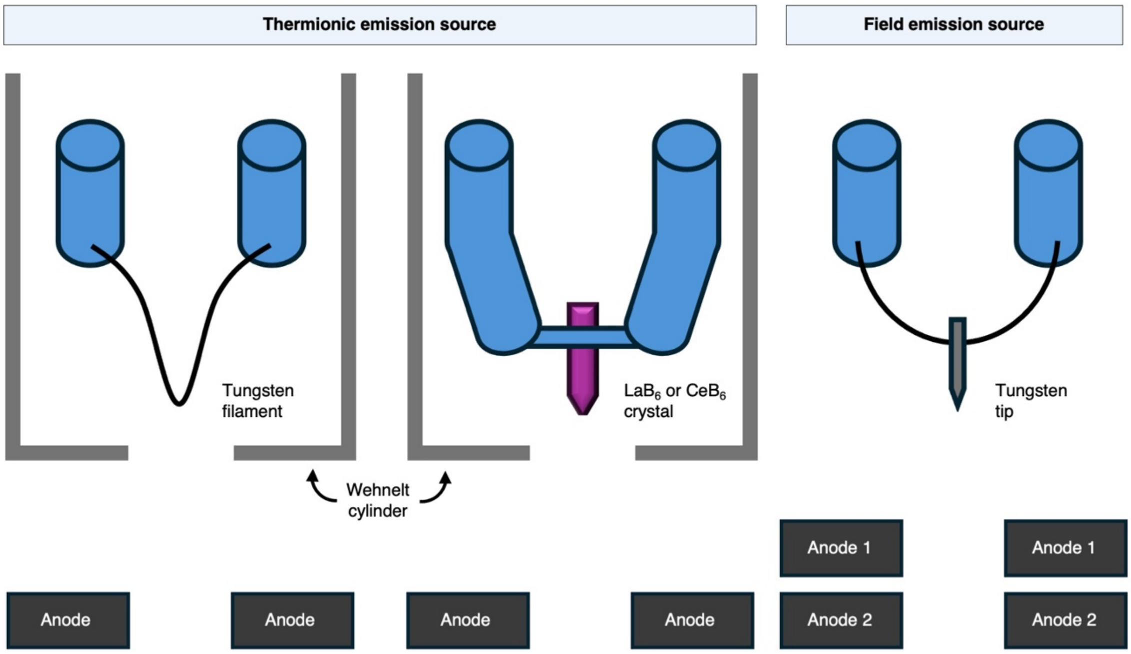

Figure 2: Electron sources in transmission electron microscopy
Schematic depiction of three different electron sources in a TEM. Thermionic emission sources heat up to decrease the barrier for electron extraction from the tungsten filament or LaB_6 crystal. In a field emission source, electrons are extracted by applying a strong electrostatic field to a tungsten tip. In both cases, electrons are accelerated towards the column by applying an electric field between the source and anode. (The Figure was conceptually inspired by Ilitchev 2019).

TEM optics

In the TEM, the lens systems are responsible for focusing the beam, image formation, and magnification. A typical TEM has three different lens systems: (i) the condenser lens system, (ii) the objective lens system, and (iii) the projection lens system. A lens in an electron microscope is usually a solenoid coil surrounded by ferromagnetic materials designed to concentrate the coil’s magnetic field into a precise, confined shape. The electron beam is deflected by the magnetic field created by the lenses in the column. The flexibility of the TEM’s operating modes, i.e. the ability of easily switching between various magnifications and TEM or STEM mode, comes from the magnetic lenses whose properties/focusing power can easily be manipulated by adjusting the current passing through the coils (unlike glass lenses used for light microscopy) (Orloff 2009).

Located below the electron gun is the condenser lens system which is involved in primary beam formation. In the condenser lenses, the preliminary beam from the electron gun is collimated into a parallel beam critical for obtaining high-resolution images (Rose 2008). In non-parallel illumination conditions two phenomena mainly contribute to deterioration of the image and thus loss in spatial resolution: (i) local defocus variations across the sample and (ii) local variation of magnification resulting from different focal planes within the objective lens (Christenson and Eades 1988; Eyidi et al. 2006). After passing through the specimen, the electron beam enters the objective lens system. The objective lens system focuses the transmitted electron beam into the image plane to form the real space image of the specimen. The magnification of the image depends on the distance between the specimen and the objective lens's imaging plane and can be adjusted by setting the focal strength of the objective lens (Williams and Carter 2009). The projection lens system below expands the electron beam onto the image detection device, e.g. fluorescent screen, film, charge-coupled device (CCD) camera, or direct electron detector (DED). The optical configurations within a TEM differ significantly depending on the implementation, manufacturer, or custom configurations e.g. spherical aberration correction (Rose 2008).

In addition to lenses, the TEM's optical system includes deflectors and stigmators which are usually made of small electromagnets. As their name indicates, deflectors deflect the electron beam and are used in independent positioning and shifting the electron beam onto the specimen and ensuring that the electron beam remains near the low-aberration centers of the lenses. Stigmators can compensate for slight imperfections and aberrations caused by astigmatism, the effect of a lens having a different focal strength in different directions (Bozzola and Russell 2006).

Apertures

Complementary to lenses, deflectors, and stigmators, apertures are an important tool in electron microscopy to mask part of the electron beam. Apertures have circular holes lined up on thin heavy metal strips. In general, two different classes of apertures are available. The first is fixed in size and position and is used to limit X-ray generation and improve vacuum performance. The second can be freely swapped among different sizes and their position needs to be adjusted. The flexible objective aperture sits below the specimen and allows the user to select the range of spatial positions or electron scattering angles to be used in image formation (Kohl and Reimer 2008).

Stage

The construction of the (cryo-)stage in a TEM is model specific and dependent on the application. In general, the specimen can be mounted in two ways into the TEM. Either via a side-entry holder or an autoloader system (Williams and Carter 2009; Thermo Fisher Scientific 2024). In a cryo-TEM, the specimen needs to be kept at low temperatures to preserve the vitrification state. Cryo-stages cool the specimen to -180°C (90 K) with liquid nitrogen or, less common, to -260°C (10 K) with liquid helium (Heide 1982). Cryo-TEM specific is a cryo-box that surrounds the stage to attract possible ice contaminations. During imaging, the stage is used to move the specimen to the region of interest as in high magnification the field of view is significantly smaller than the specimen support. For tomography imaging approaches, the stage needs to be tiltable at least in one direction.

Detection unit

The detection unit is located at the bottom of the TEM. In the most straightforward manner, TEM images can be observed on a fluorescent viewing screen. The detection via phosphorescence is based on the excitation of the ZnS or ZNS/CdS via cathodoluminescence (Kohl and Reimer 2008). Permanent images can be recorded on photographic film usually made of a gelatin and silver halide emulsion layer on plastic support (Zuo 2017). After chemical development, the image can be digitized for analysis with a film scanner (Zuo 2017). In today's state-of-the-art electron microscopes, film has been replaced widely by direct electronic read-out devices such as charge coupled device (CCD) cameras, scintillator and fiber optic coupled cameras based on complementary metal oxide semiconductor (CMOS), or direct electron detectors (DED). The CCD camera sensor can be damaged by a high-energy electron beam, therefore, CCD cameras are often used in combination with a scintillator like Yttrium aluminum garnet (YAG). A scintillator converts electrons into photons. After conversion, the photons are transferred to the sensor of the CCD camera via a fiber optic plate where the signal is finally detected. CCD cameras are typically cooled to approximately -30°C to reduce dark current and improve the signal-to-noise ratio (Kohl and Reimer 2008). CMOS cameras have been commercially available for TEMs since 2006 (Tietz 2008). The most prominent difference between CCD and CMOS sensors is their read-out strategy.

While CCD sensors read out one line at a time, CMOS sensors have a per pixel read-out (Fossum and Hondongwa 2014). The per pixel read-out gives the biggest advantage of CMOS over CCD sensors by reducing the likelihood for blooming significantly. Blooming occurs when the captured charge of over saturated pixels spreads to the nearby pixels causing a false signal and thereby decreasing image quality (Tietz 2008). Additionally, CMOS sensors can be read out faster compared to CCD sensors (Herres 2019). The detective quantum efficiency (DQE) is a measure of the amount of noise a detection device adds to the image given from zero to one. The closer the DQE to one, the fewer quanta needed to get an image of equal quality (Cheng et al. 2015; Zuo 2017). The conversion of electrons to photons in CCD and CMOS cameras reduces the detective quantum efficiency (DQE). Especially at high kinetic energies, electrons can be backscattered within the scintillator and provoke a signal elsewhere on the sensor (McMullan et al. 2009). A schematic drawing of a CCD camera is shown in Figure 3A.

In contrast to CCD and CMOS cameras, direct electron detectors (DEDs) are directly exposed to the electron beam. The hitting electrons are converted into an electric signal skipping the conversion step to photons. Therefore, DEDs have a higher DQE than scintillator-coupled devices (Cheng et al. 2015; Zuo 2017). DEDs have a 10 to 100 times higher sensitivity for electron detection than scintillator systems, making DEDs particularly suitable for low-dose imaging of biological specimen. The faster read-out times of the direct electron detector gives an additional advantage of collecting movies with multiple frames that can later be averaged into one micrograph *in silico* (Faruqi and McMullan 2018). A potential drawback of DEDs is an irreversible radiation damage of the sensor when the electron dose is too high. A direct electron detector is schematically depicted in Figure 3B. Between the projection lens system and the DED, an energy filter is often installed. Inelastically scattered electrons loose kinetic energy and are focused into a different plane than unscattered or elastically scattered electrons and, thus, contributing to noise within the image. An energy filter can be used to select electrons with a defined amount of kinetic energy or energy spread reducing noise in the acquired image (Carter et al. 2016).

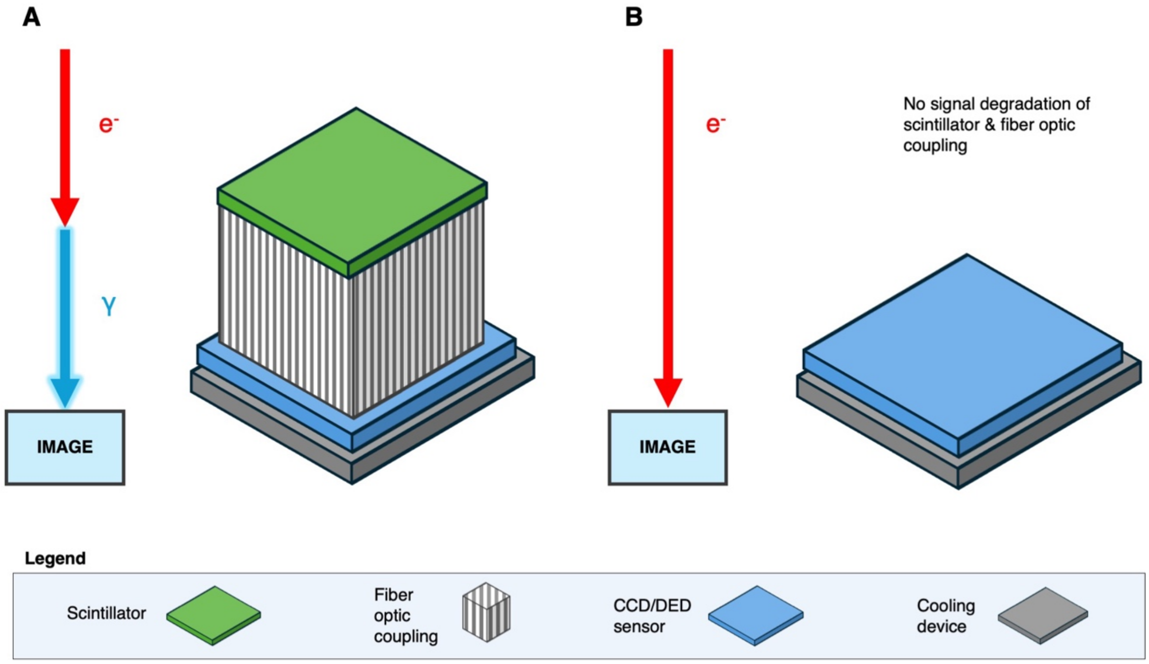

Figure 3: Electron detectors
Schematic depiction of a sensor of a CCD camera in **A** or direct electron detector in **B**. **A:** The CCD sensor is coupled to a scintillator via fiber optic coupling. Electrons that hit the scintillator are converted into a photon signal which is forward by the fiber optic to the CCD sensor. The photon signal is detected and converted into an image. **B:** The DED sensor detects the electrons without conversion into photons resulting in image formation by the electrons themselves. (The Figure was conceptually inspired by Levin 2021).

1.1.2 Amplitude and phase contrast

In transmission electron microscopy, the intensity of the electron wave reaching the detector is measured. The intensity is defined as the number of electrons per unit area of the detector per unit time (Kohl and Reimer 2008). When incident electrons pass through the specimen, they can either be transmitted unscattered, elastically scattered or inelastically scattered. Scattering of the electrons by the specimen leads to a modification of the amplitude and phase of the electron wave (Kirkland 1998). Most images contain both, amplitude and phase contrast, whereas in cryo-EM of biological specimen the phase contrast dominates the image (Cowley 1995; Orlova and Saibil 2011).

In the following description inelastically scattered electrons will be neglected since they do not contribute usefully to phase contrast. Unscattered electrons of the incident electron beam hit the objective lens in the optical axis and are focused into the zero-order or central beam spot in the back focal plane of the lens. Electrons, that are elastically scattered by the atoms of the specimen, maintain their amplitude but gain an angle compared to the direction of the incident beam (Kohl and Reimer

2008). The objective lens focuses elastically scattered electrons with the same scattering angle into one spot in the back focal plane. As a result, a diffraction pattern corresponding to the Fourier transform of the specimen is produced in the back focal plane. In the image plane of the objective lens, all electrons are focused into the same spot as they passed the specimen and, therefore, the image plane is the inverse Fourier transform of the diffraction pattern in the back focal plane (Kohl and Reimer 2008). As the elastically scattered electrons gained a phase shift, the interference in the image plane of the elastically scattered and unscattered electrons of one spot leads to phase contrast by the modification of the intensity of the incident electron beam. When the elastically scattered electrons have a phase shift of 90°, the resulting image intensity is lower compared to the incident electron beam leading to a positive phase contrast. For -90° the image intensity will be larger than the initial intensity producing negative phase contrast. Thin samples of light elements, e.g. frozen biological macromolecules, are weak-phase objects resulting in only a small phase shift (Frank 2006a; Kohl and Reimer 2008). The smaller the phase shift, the less significant the intensity of the incident electron beam changes resulting in low contrast. Phase contrast of biological specimen in focus is therefore weak and images are typically recorded in defocus to enhance it (Kirkland 1998). Details of the influence of defocus on the contrast are described in the Introduction section 1.1.3.

For ice-embedded biological specimen, amplitude contrast is very small (less than 10%) (Frank 2006a). Amplitude contrast of (high-density) materials is due to the loss of electrons before the image plane by scattering electrons to high angles or inelastic scattering. Electrons scattered to high angles cannot be captured and focused by the objective lens into the image plane. Therefore, they do not contribute to the signal on the detection unit leading to a reduction in intensity of the electron beam in this area. This effect can be enhanced by inserting an objective aperture to maximize the exclusion of high-angle scattered electrons from the image (Carter and Williams 2016). Inelastically scattered electrons transfer part of their energy into the specimen leaving them with a lower kinetic energy. Utilizing an energy filter, inelastically scattered electrons can be removed before the detection unit enhancing amplitude contrast further (Carter and Williams 2016).

Details of apertures and energy filters are described in more detail in the Introduction section 1.1.1.

Phase plates

Phase contrast in transmission electron microscopy can be enhanced by application of a phase plate. Phase plates are inserted into the TEM at the back focal plane (e.g. in the objective aperture stripe) of the objective lens (Kawasaki et al. 2009). A phase plate creates a relative change in phase between the transmitted and the by the specimen elastically scattered electrons. Weak phase objects, originally difficult to view, can be visualized as the additional induced phase shift enhances phase contrast in the image (Malac et al. 2012). As phase plates produce the relative phase change most effectively at small spatial frequencies (long distance in the image), phase plates can be effectively used in obtaining the necessary high contrast for biological specimen (Dries et al. 2014). In this thesis, micrographs were collected with Volta phase plate. In the following only the mechanism of Volta phase plates will be discussed neglecting Zernike phase plates. Volta phase plates (or hole-free phase plates) are made of an amorphous carbon film with a controlled thickness of 5-20 nm (Malac et al. 2021). A charged area is created on the thin film by the unscattered electron beam resulting in the desired relative phase shift (Hettler et al. 2018). The induced charge in the area of the unscattered electron beam can be positive or negative resulting in an advanced or retarded phase shift (Malac et al. 2021). The additional phase shift enhances phase contrast for weak phase objects due to the stronger modification of the unscattered wave in the image plane increasing signal intensity (Danev et al. 2014).

1.1.3 The contrast transfer function in transmission electron microscopy

The theory of contrast transfer in a TEM is based on the observation that not all spatial frequencies of an image are transferred with the same signal strength. How much of the phase signal is transferred into the real space image is described by the contrast transfer function (CTF). The CTF thereby accounts for contrast transfer as well as for aberrations in the microscope (Wade 1992). The quality of the real space image formation is determined by the shape of the CTF. Dependent on the phase shift of the spatial frequency, the contrast transfer oscillates between -1 (positive contrast) and 1 (negative contrast) crossing the X-axis multiple times resulting in the shape of a sine wave (Hawkes 1980). When the CTF crosses the X-axis the information for this spatial frequency is not transferred into the image and ultimately lost (Hawkes 1980). The spatial frequency with the first zero crossing in the CTF is called *point-resolution*, information afterwards are not interpretable and must be modeled computationally. Additionally, the higher the spatial frequency, the more the signal gets dampened by the CTF resulting in a lack of signal transfer for high-resolution features. The dampening is described by the envelope function that represents the effect of additional aberrations including chromatic aberrations, energy spread, focal spread, instabilities in the high voltage source, and instabilities in the objective lens current (Wade and Frank 1977; Wade 1992).

Image processing techniques rely heavily on low spatial frequencies, in focus the CTF shows almost no signal transfer for low spatial frequencies (Figure 4 the black curve). To enhance the signal of low frequencies, images are recorded in defocus which enhances the contrast transfer of low spatial frequencies (Figure 4 the blue and red curves) (Sigworth 2016). The benefit of imaging in defocus is that low spatial frequencies are much better transmitted, but the drawback is the shifting of the first zero point towards lower frequencies as well as the increase of x-axis crossings in a given interval (Scherzer 1949; Sigworth 2016). A physical drawback of defocus is the distortion of the image due to different focus points of the electron beam as scattered electrons are not focused into the same plane as the incident beam (Wade and Frank 1977). So, the optimal defocus point that achieves a balance between maximizing contrast and minimizing the detrimental effects of spherical aberration in TEM imaging is called Scherzer defocus (Scherzer 1949). At the Scherzer defocus the spherical aberration is minimized and image quality for high-resolution imaging optimized. It is important to note that the optimal defocus setting can vary depending on the specific imaging conditions and desired outcomes for a given TEM experiment.

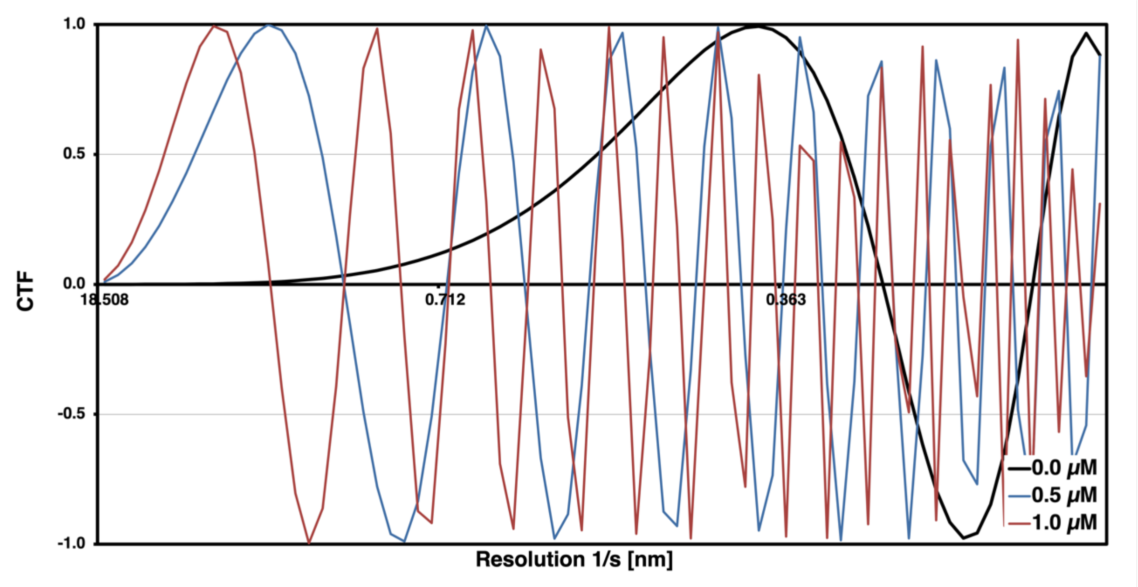

Figure 4: The contrast transfer function
The contrast transfer function (CTF) modulates the into the image transferred contrast information dependent on the spatial frequency. The CTF oscillates between -1 and 1 in the shape of a sine wave. The first zero point of the CTF is called *point-resolution* and corresponds to the directly interpretable resolution as beyond the contrast information are not continuously transferred and need to be computationally modeled. The CTF for a 300 kV instrument with a C_s = 2.7 mm in focus is plotted in black. The contrast transfer for low spatial frequencies is very little while the point-resolution is at a higher spatial frequency. To enhance contrast for low spatial frequencies, images can be acquired in defocus which modifies the CTF as shown in blue (for defocus of 0.5 µm) or red (for defocus of 1 µm). As drawbacks, the point-resolution moves to lower spatial frequencies, dampening of high spatial frequencies is increased, and the increased number of zero points results in increased loss of information. In defocus the contrast transfer of low spatial frequencies is improved allowing for computational image processing of micrographs. (The Figure was created utilizing the CTF simulation excel sheet from the Laboratory of Biological Electron Microscopy (LBEM) in Lausanne, Switzerland (LBEM)).

1.1.4 (Cryogenic) electron microscopy of biological specimen

Sample preparation

To image biological specimen in a TEM, two major techniques evolved, namely negative stain EM and cryo-EM. Dependent on the application, samples are fixed to an EM sample support grid by either heavy metal staining or vitrification. Fixation of the specimen to the support is a necessity as otherwise the aqueous solution would start to boil in the vacuum of the microscope. Further, either the heavy metal stain or the cryogenic temperatures protect the specimen from radiation damage (Bozzola and Russell 2006; Dobro et al. 2010).

To prepare negative stain grids, the sample is adsorbed onto a support substrate, typically amorphous carbon often in combination with a thin layer of polyvinyl (e.g. Formvar) or nitrocellulose (e.g. Collodion) polymer (Scarff et al. 2018). Excess liquid of the sample is blotted off and, after an optional washing step, the stain is applied. After a sample and stain dependent incubation time, the stain is blotted off and the grid is air dried. The whole process of staining usually takes a skilled user less than five minutes. Negative stain samples can be stored at room temperature and air exposed.

If not embedded in a suitable stain, biological macromolecules are imaged in cryogenic conditions embedded in a thin layer of vitreous ice. Cryo-EM allows to image the samples without dehydration or chemical fixation, which can disrupt or distort biological structures (Dubochet et al. 1988; Oikonomou et al. 2016). To prepare cryo-EM grids, the sample is applied to an EM grid, excess liquid blotted off, and the grid plunged into liquid ethane or liquid ethane mixed with propane. This procedure ensures that the aqueous buffer freezes fast enough to obtain vitreous ice. Slower freezing would lead to the formation of crystalline (hexagonal or cubic) ice which is not transparent to the electron beam (Dubochet et al. 1988). Dependent on the skillset, freezing a cryo-EM sample takes roughly 30 minutes if liquid ethane or ethane/propane has to be prepared. Additionally, cryo-EM grids need to be handled and stored in liquid nitrogen to prevent crystalline ice formation.

Negative stain electron microscopy

In negative stain electron microscopy, the sample of interest is embedded into an amorphous matrix of electron-dense stain on the surface of an EM grid. The embedment into the stain produces a relatively high contrast compared to cryo-EM by enhancing amplitude contrast which results from the difference in electron density between the stain and the less electron-dense biological specimen (Ohi et al. 2004). The specimen of interest scatters significantly fewer electrons than the stain, making it appear as a brighter area on a dark background. Details of the specimen can be observed as the stain will produce alternating contrast in crevice areas (Brenner and Horne 1959). Although cryo-electron microscopy can achieve much higher resolution compared to the limited ~18 Å in negative stain EM, negative stain EM remains a powerful technique and crucial for quick sample assessment (De Carlo and Harris 2011; Merk et al. 2016). Figure 5 shows schematically how contrast is formed for an electron translucent particle in negative stain EM.

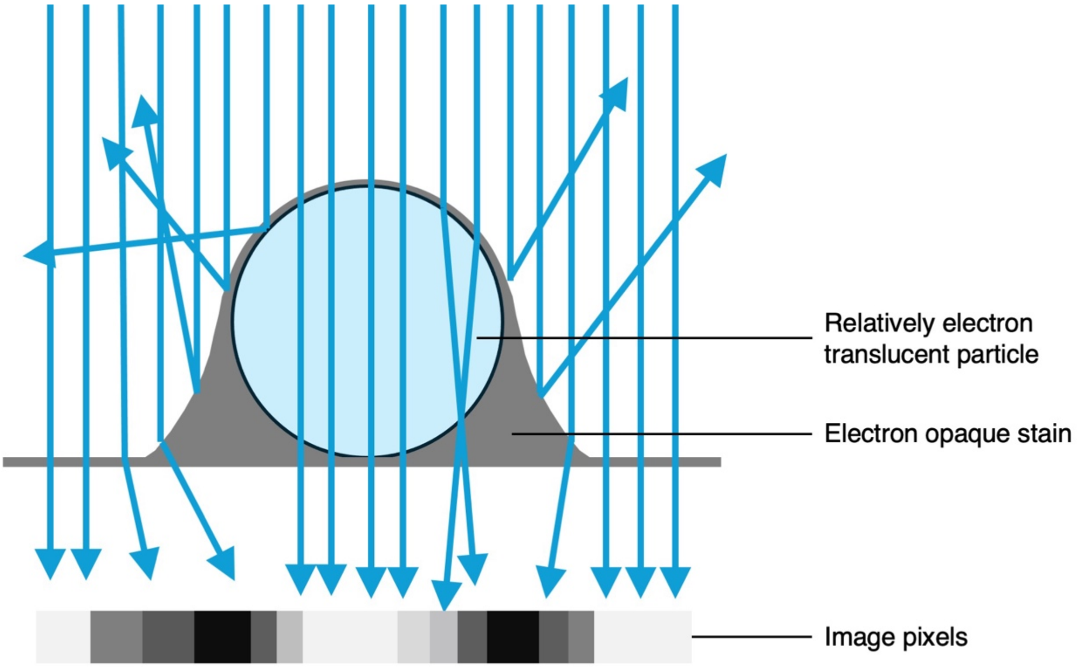

Figure 5: Negative stain electron microscopy
Schematic depiction of contrast formation in negative stain EM. The contrast in negative stain is formed due to the increased scattering of electrons by the electron opaque stain compared to the relatively electron translucent particle. Therefore, particles appear white in the image as more electrons can pass through while the outlines are darker from the stain as less electrons are passing through here. (The Figure was conceptually inspired by Center for celluar imaging: Electron Microscopy, University of Gothenburg 2021).

In some cases, although negative staining is desired, the sample is positively stained. A positive stain is characterized by a dark specimen of interest in front of a light background. In this case, the specimen attracted more stain than the support making it more electron dense and resulting in contrast inversion (Massover 1993).

Single-particle analysis

Cryo-EM structure determination of single particles, often called single-particle analysis (SPA), includes a series of computer-based image processing routines to retrieve high-resolution information from transmission electron microscopy images to yield high-resolution three-dimensional structures (Frank 2006a). Usually, the target sample contains purified and homogeneous biological macromolecules, most often proteins, protein complexes, or viruses present in solution in an isolated *single-particle* assembly state (Zhou 2008; Bartesaghi et al. 2015). SPA can be applied to images of cryo-EM as well as for negative stain electron microscopy. In both cases, the images have a low signal-to-noise ratio making interpretation rather difficult. Image processing can be performed by specialized software on multiprocessor computer clusters and dependent on the desired results, various two- or three-dimensional steps are included. Averaging multiple copies of the same particle enhances contrast and increases the interpretability of particle features. Further, a three-dimensional reconstruction of the particle can be built from multiple two-dimensional projection images. Due to hardware improvements in modern TEMs and software improvements in the data processing pipeline, SPA reconstructions with resolutions as good as 1.22 Å can be achieved (Nakane et al. 2020). A scheme of a simplified SPA workflow is shown in Figure 6A. Details of the depicted steps are described in the following paragraphs.

Pre-processing

As in modern cryo-TEMs images are usually recorded in movie frames, the first step in data processing is motion correction. During motion correction, the frames of the movie are averaged into a single micrograph correcting for the movement of the particles during the entire exposure (Bai et al. 2013). Particle movement can be caused by either stage drift or ice dooming due to the impact of the electron beam on the vitrified specimen. Today, advanced motion correction techniques are implemented that additionally take into account dose weighting, emphasizing early-mid frames with less radiation damage and reducing the influence of large specimen movements in early frames caused by beam induced motion (Grant and Grigorieff 2015; Rubinstein and Brubaker 2015). As described in the Introduction section 1.1.2 and 1.1.3 above, phase contrast in cryo-EM is enhanced by acquiring the images in defocus. If the sample is not entirely flat, the particles within the sample experience different defocuses and thus have an individual CTF to correct for. Therefore, CTF estimation is performed on a patch (directly after motion correction) or even per particle (after particle positions are known) basis to reconstruct the information for each particle best possible (Rohou and Grigorieff 2015; Zivanov et al. 2020). As an example for an CTF estimation algorithm, the CTFFIND4 algorithm first computes an amplitude spectrum from the input micrograph, and, after background subtraction, evaluates the similarity of the remaining oscillatory signal to theoretical two-dimensional CTF functions. In an iterative process, the parameters for the theoretical CTF functions are adapted until the similarity is maximized. As a result, an estimate for the microscope's defocus and astigmatism parameters are given (Rohou and Grigorieff 2015). Motion correction as well as CTF estimation are usually referred to as pre-processing steps.

Particle picking and two-dimensional classification

After pre-processing, particles are detected and excised. A few different methods have been developed to pick particles either manually or in an automated fashion, with a simple blob picker or template-based (Hoang et al. 2013; Punjani et al. 2017). Two-dimensional classification of extracted particles is performed as a first sorting step to remove incorrect picks and particles of poor structural integrity, i.e containing only parts of the particle and other irregularities. Also, particles of contaminants can be eliminated in two-dimensional classification if their shape and size is significantly different from the target. Selected particles after two-dimensional classification are used in ab-initio model reconstruction (CryoSPARC Guide 2023a).

Three-dimensional reconstruction and refinement

When recording a micrograph, the three-dimensional particles are projected onto the imaging device, resulting in two-dimensional images. Assuming that the particles are randomly oriented within the ice and a sufficient amount of particles was imaged, a 360° view of the particle is captured in the images from which the three-dimensional volume can be reconstructed (Frank 2006a). The basis for the three-dimensional reconstruction of the particle of interest from the two-dimensional images acquired in the TEM is the projection-slice theorem or Fourier slice theorem described by Bracewell (Bracewell 1956, 1990). Figure 6B is a schematic depiction of how the three-dimensional volume of the particle is formed into a two-dimensional projection by the TEM. Figure 6C shows how the projection-slice theorem is used to reconstruct the three-dimensional volume of the two-dimensional images. In brief, it states that the Fourier transformation of a two-dimensional projection is a slice within the three-dimensional Fourier transformation of the three-dimensional volume (Bracewell 1990). The two-dimensional Fourier transformations from projections at different angles will match within one line within the three-dimensional Fourier space. So, in volume reconstruction (and refinement), the Fourier transformations of the extracted particles are matched against each other to retrieve the relative projection angles towards each other. The resulting three-dimensional Fourier space is then subjected to an inverse Fourier transformation to retrieve the three-dimensional volume in real space. In modern ab-initio reconstruction algorithms the optimization of the unknown variable of three-dimensional rotation and two-dimensional translation for each single-particle is solved by Stochastic gradient descent (SGD). With SGD one or several low-resolution three-dimensional structure(s) that are consistent with the observed images can be identified. Once low resolution structures are determined a branch-and-bound algorithm can be applied to rapidly refine structures to high resolution (Punjani et al. 2017). In recent years and with increasing computational power, *in silico* purification of particles in heterogenic datasets became accessible. Three-dimensional classification jobs clustering particles of different compositional or conformational states are nowadays available often resulting in higher local resolution of flexible regions as different conformational states are not averaged anymore (Scheres 2016; Punjani and Fleet 2021, 2023).

A drawback of using two-dimensional projections to obtain the three-dimensional volume is that in two-dimensions the handedness of the particle gets lost, resulting in two possible reconstructions. An early approach to determine the absolute hand of a particle was imaging the particle at different tilt angles. In tilt angle reconstructions, the handedness of the particle is preserved and can later be used to determine the correct hand (Rosenthal and Henderson 2003). In high-resolution structures, the determination of the correct hand does not need to be performed by tilt angle acquisition anymore, as biological macromolecules exhibit preferred handedness. For example, the preferred handedness of a 4-helix bundle motif can be recognized at resolutions of approximately 10 Å, while the right-handed winding path of the backbone of an α-helix at around 5 Å (Beckers et al. 2021).

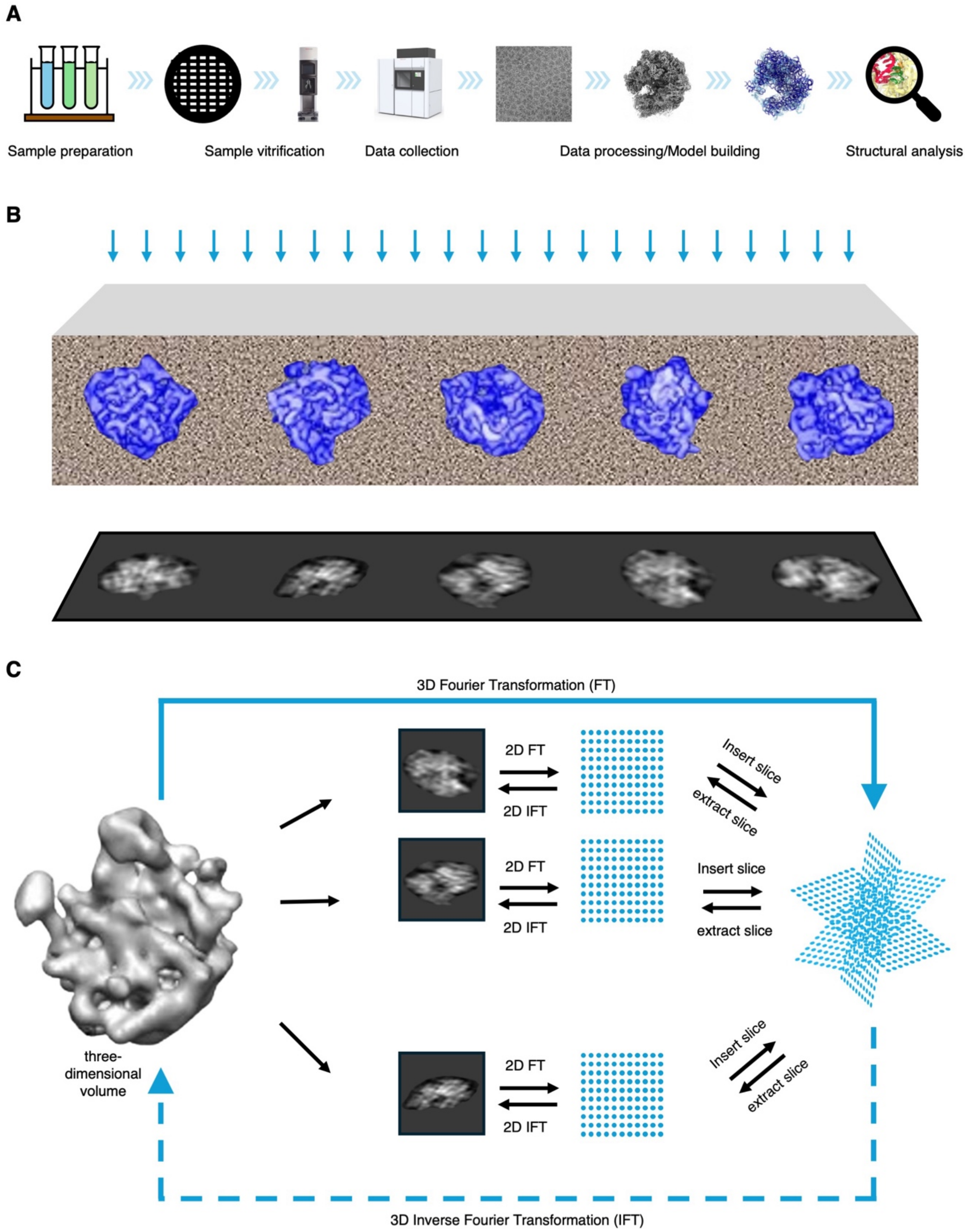

Figure 6: Single-particle analysis
A: Schematic depiction of a simplified single-particle analysis workflow starting with sample preparation and ending with structural analysis. **B:** In cryogenic electron microscopy the frozen particles orient randomly in the ice resulting in various views in their two-dimensional projection in the image. **C:** Illustration of the projection slice theorem highlighting the connection between real space and (invers) Fourier space by Fourier transformation. The Fourier transformation of the two-dimensional projection is a slice in the three-dimensional Fourier transformation of the three-dimensional real space volume. (Panel B was conceptually inspired by Joachim Frank and panel C was conceptually inspired by Wang et al. 2013).

Data interpretation

As the result of successful SPA data processing, a Coulomb potential map or EM-density map is obtained. The resolution of the final reconstruction is estimated by Fourier shell correlation (FSC). To do so, the data set is split in two random half-sets and for each half an individual and independent volume is reconstructed. The independently produced half-maps are correlated in three-dimensional Fourier space in a shell-like manner until the correlation between the half-maps drops below the threshold of 0.143. The spatial frequency at which the correlation drops below the threshold is termed the resolution of the map. However, the field is still in debate whether the threshold of the FSC should be at 0.143 and whether FSC is the correct measure to determine the resolution of the reconstruction (Harauz and Van Heel 1986; Rosenthal et al. 2003; Van Heel and Schatz 2005).

Dependent on the resolution of the final reconstruction, a molecular model can either be built de-novo or an existing, related model can be fitted and adjusted into the EM-density map. A large variety of different methods for homology modeling or de-novo model building was reviewed by Beckers et al. (Beckers et al. 2021). Briefly, reconstructions with a resolution better than 3.5 Å exhibit discernible sidechains and (with a known primary structure) can be used to build a complete atomic model de-novo. In the process of model building an iterative cycle between model building and map sharpening is often required to identify high-resolution features. Reconstructions with lower resolutions can often only by interpreted by homology modeling or rigid body fitting of related existing structures (Beckers et al. 2021). After initial modeling, the overall goal in model refinement is to generate a molecular model representing the experimental obtained EM-density map by maximizing the map-to-model correlation with a restraint on model features including bond lengths, bond angles, torsions, and ring geometries (Beckers et al. 2021). A simple way to refine a molecular model, is the cryo-EM specific real-space refinement in Phenix (Afonine et al. 2018). Figure 7 is an overview of model refinement parameters as described by Beckers et al. (Beckers et al. 2021).

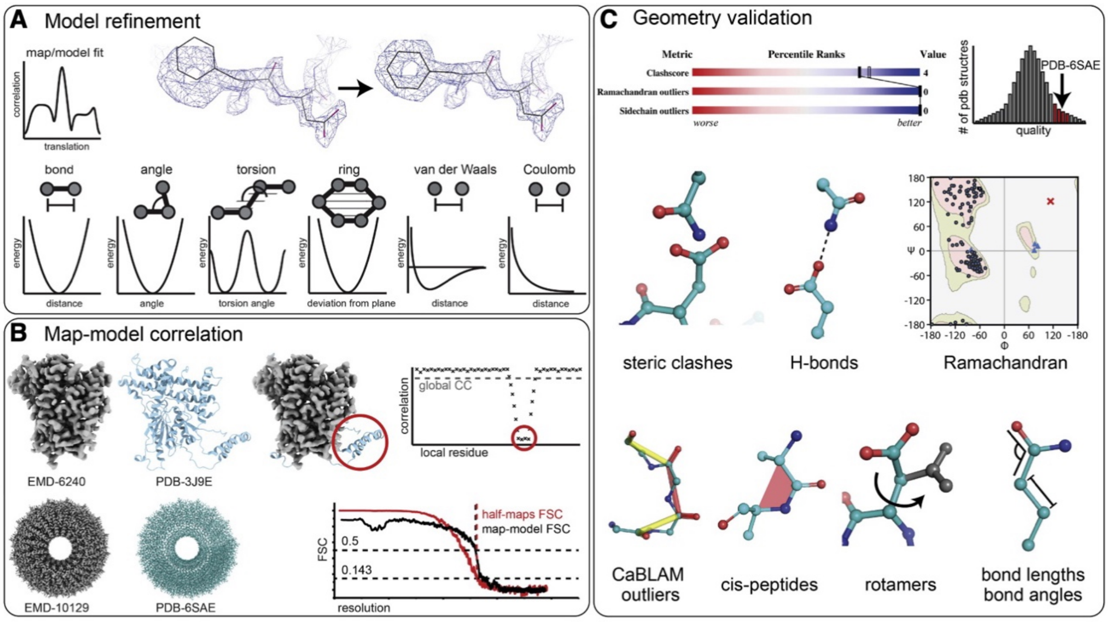

Figure 7: Atomic-model refinement and validation criteria
A: During model refinement the molecular model is placed into the cryo-EM density while being restrained to reference geometries including bond angles, torsion angle, ring deviations, in addition to van der Waals and Coulomb interactions. **B:** As an example for map-model correlation, the simulated map of the atomic model (PDB-ID: 3J9E) was correlated with the experimental EM-density map (EMD6240). The correlation of individual residues can be used to assess the local fit. To probe whether the molecular model represents the experimental reconstruction, map-to-model FSCs are used. **C:** The quality of the model can only be assessed by parameters that are not restrained in the previous refinement steps. Often used are the clash score and Ramachandran and side-chain rotamer values which are compared to expected PDB statistics. CaBLAM outliers and cis-peptides can be further used to identify outliers in the model. (The Figure was adapted from Beckers et al. 2021).

Cryogenic electron tomography

Cryogenic electron tomography (cryo-ET) is an imaging technique in which images of a single specimen are collected at different tilt angles to reconstruct a three-dimensional volume (Gan and Jensen 2012). Similar to SPA, the project-slice theorem is the basis for this technique but here the slices result from images collected at different tilt angles of the same site rather than from randomly oriented identical particles (Figure 8). In contrast to SPA, cryo-ET is applied but not limited to biological macromolecules and cells with unique structural features (Gan and Jensen 2012).

The number of projections that can be experimentally imaged by cryo-ET is limited by (i) rotation of the specimen and (ii) radiation damage. Rotating the specimen to more than approximately 60° is practically impossible as the sample thickness becomes too high to remain electron transparent. Additionally, only a limited amount of electron dose can be delivered to the acquisition area before detrimental radiation damage (Frank 2006b). The dose limit on tomography data leads to a significantly lower dose per image compared to SPA data acquisitions. Therefore, tomography data are often recorded utilizing a phase plate to enhance phase contrast in the image (phase plates are discussed in more detail in the Introduction section 1.1.2) (Danev et al. 2014). The limit in experimental obtained projections results in a *missing wedge* in the Fourier space alignment affecting structures orthogonal to the tilt axis and resulting in deformation of those in the reconstruction (compare Figure 6C). The second effect of the physical limitations of tilting is that the tilt increment is not infinitely small, so that at high spatial frequencies the Fourier space is not completely filled. The Crowther criterion describes the dependency between the resolution to which the information is complete to the number of tilt images and the particle diameter for a uniformly-distributed tilt-acquisition:

$$m = \frac{\pi \cdot D}{d} \tag{1}$$

with **m** number of tilt images, **D** particle diameter, and **d** resolution (Crowther et al. 1970). Nowadays, the method-of-choice during tilt series acquisition is the application of a dose-symmetric tilt scheme. The images are collected starting at 0° tilt and then alternating in + and – direction towards higher tilt angles. The benefit of this acquisition scheme is that high-resolution information (available mostly in small tilt angle images due to the small sample tickness) can be imaged before the sample accumulates radiation damage (Hagen et al. 2017). The left panel in Figure 8 schematically shows a tomography data acquisition.

Data processing of cryogenic electron tomography images

To reconstruct a tomogram, several key steps are undertaken. The first steps in data processing of cryo-ET images are analogous to pre-processing of SPA data sets, including motion correction and CTF estimation. Next, computational methods are employed to calculate a three-dimensional volume (or tomogram) from the set of aligned two-dimensional images. This process typically involves techniques including weighted back-projection (Radermacher 1992) or iterative reconstruction algorithms (Andersen 1984), that aim to reconstruct the three-dimensional volume of the sample from the experimental two-dimensional projections (Figure 8). In cryo-ET, a critical challenge is dealing with the inherent low signal-to-noise ratio in the acquired images due to the radiation-sensitive nature of biological specimen and the low dose used to minimize sample damage. Advanced image processing techniques, including noise reduction methods and advanced algorithms to reduce the missing wedge effect, are therefore employed to enhance the quality and fidelity of the final tomogram (Liu et al. 2022). After reconstruction, the tomogram provides detailed structural information about the specimen, revealing its intricate features and organization. Formerly a manual task, these features can be segmented by simple thresholding methods or deep-learning techniques to represent the final result (Stalling et al. 2005; Heebner et al. 2022). Analogous to SPA, structures present in multiple copies within tomograms can be extracted, aligned, and averaged to increase the resolution of their three-dimensional reconstruction (Wan and Briggs 2016). This reconstruction approach, termed *subtomogram averaging*, can be used to determine biological macromolecule structures achieving a resolution of e.g. 4.7 Å for the 20S proteasome of *Thermoplasma acidophilum* (Khavnekar et al. 2023). As subtomogram averaging is not relevant for the Results and Discussion section of this thesis, it will not be discussed here.

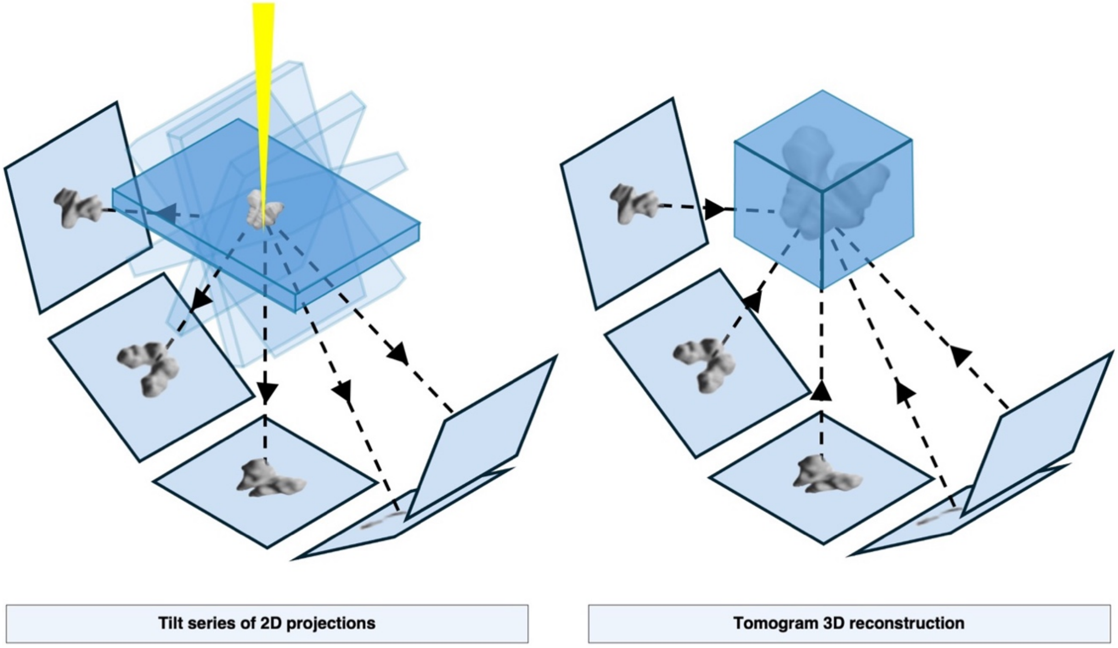

Figure 8: Cryogenic electron tomography
In cryogenic electron tomography the specimen is tilted to different angels to capture views from different sites of the specimen. In tomogram reconstruction, the different views are used to reconstruct the final three-dimensional volume. (The Figure was conceptually inspired by Knot 2023).

1.2 Autophagy

Autophagy is an evolutionary conserved degradation and recycling process that contributes to maintaining intracellular homeostasis in eucaryotic cells. to accomplish this, autophagy clears the cell of cytoplasmic material such as aggregated proteins, damaged or over-abundant organelles, and invading pathogens by promoting their removal. Finally, nutrients are recovered and made available again for anabolic metabolic pathways in the cell (Feng et al. 2014). In addition to low basal activity of autophagy to keep intracellular homeostasis, autophagic flux can be triggered by cellular stress factors including nutrient or growth factor deprivation, hypoxia, reactive oxygen species, DNA damage, protein aggregates, damaged organelles or intracellular pathogens (Kroemer et al. 2010).. Dysregulated autophagy is associated with various diseases such as cancer, neurodegeneration, and diseases of liver, heart, and kidney, emphasizing the importance of a strict regulation (Ichimiya et al. 2020). In disease, here described for cancer, autophagy can take on two opposing roles (White and DiPaola 2009). On the one hand, autophagy can serve as a tumor-suppressive mechanism by maintaining genomic stability, eradicating endogenous sources of reaction oxygen species, eliminating oncogenic proteins, and inducing an immune response (Galluzzi et al. 2015). On the other hand, once a tumor is developed the tumor cells are under severe survival pressure in their microenvironment in which autophagy assists by providing beneficial metabolites and thus promoting tumor survival and the metastatic cascade (Kocaturk et al. 2019). In the process of finding therapeutic treatments, understanding the role of autophagy in general and in the respective disease is therefore crucial.

Autophagy can be divided into three different pathways: macroautophagy, microautophagy, and chaperone-mediated autophagy. In macroautophagy, a double membrane organelle called autophagosome is formed within the cytoplasm enclosing all cellular material that is spatially present (Xie and Klionsky 2007). The recognition of cargo can proceed in a non-selective (enclosing the bulk) or selective manner (via selective autophagy receptors) (Feng et al. 2014). A detailed description of the macroautophagy pathway can be found in the Introduction section 1.2.1. In contrast to macroautophagy, in microautophagy the cargo is directly taken up by the lysosome through invagination of small intra-lysosomal vesicles. Similarly to macroautophagy, cargo can be non-selectively or selectively targeted for degradation. So far, two different types of microautophagy cargo uptake have been described: (i) fission-type microautophagy and (ii) fusion-type microautophagy. While fusion-type microautophagy relies on the core autophagy machinery also needed in macroautophagy together with soluble N-ethylmaleimide-sensitive factor attachment protein receptor (SNARE) complexes, fission-type microautophagy is mediated via endosomal sorting complexes required for transport (ESCRTs) (Wang et al. 2023). Chaperone-mediated autophagy (CMA) is a selective-only form of autophagy and appeared most probably later in evolution than macroautophagy and microautophagy. Cytoplasmic substrates of CMA carry a targeting pentapeptide motif KFERQ that is recognized by cytoplasmic chaperone heat shock-cognate protein of 70 kDa (Hsc70) (Kaushik and Cuervo 2012). Hsc70 recognizes the lysosomal surface via interaction with lysosome-associated membrane protein 2A (LAMP-2A). At the lysosomal surface the substrate protein unfolds and is translocated across the membrane by a LAMP-2A translocation complex. In the lumen of the lysosome the substrate protein is degraded (Kaushik and Cuervo 2012). The three forms of autophagy are illustrated in Figure 9.

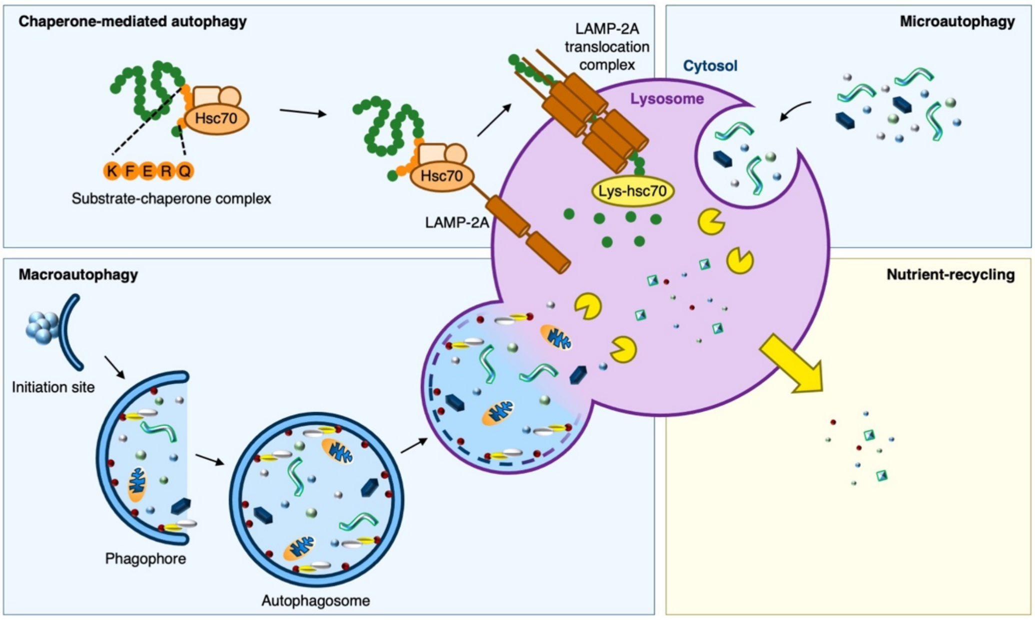

Figure 9: Autophagy pathways at a glance
The eucaryotic degradation process of autophagy can be divided into three distinct pathways. **Chaperone-mediated autophagy** is mediated via heat shock-cognate protein of 70 kDa (Hsc70) which recognizes substrate proteins and delivers them to the lysosomal membrane. At the lysosomal membrane the unfolded substrate proteins are translocated via lysosome-associated membrane protein 2A (LAMP-2A) translocation complex into the lumen of the lysosome, where the substrate protein is finally degraded. In **microautophagy**, cytoplasmic components are taken up by the lysosomes via invagination and are subsequently degraded. In **macroautophagy**, first, a double membrane organelle called autophagosome forms. The autophagosome encloses bulk material of the cytosol in a non-selective manner while cargo can also be specifically guided to the autophagosome by selective autophagy receptors. After closure of the double membrane bilayer, the autophagosome fuses with a lysosome and the cargo is degraded. The degradation products from all three pathways are released into the cell. (The Figure was conceptually inspired by Andrade-Tomaz et al. 2020).

1.2.1 Macroautophagy

In the following paragraph the process of macroautophagy in mammalian cells is described including only the mammalian nomenclature of the individual autophagy-related (ATG) proteins or protein complexes. Macroautophagy can be divided into five distinct steps: (i) initiation of autophagy (at omegasome), (ii) elongation of the isolation membrane/phagophore, (iii) maturation of the autophagosome, (iv) fusion of the autophagosome with a lysosome, and finally (v) the degradation of autophagic cargo within the autolysosome (Yin et al. 2016). The macroautophagy pathway is schematically depicted in Figure 10 with emphasis on early steps of macroautophagy, including initiation, membrane nucleation, and phagophore formation.

Autophagy initiation takes place at special regions of the endoplasmic reticulum (ER), which have a high content in the lipid phosphatidylinositol 3-phosphate (PI(3)P) (Hurley and Young 2017), and sometimes intricate membrane-contact sites with other intracellular organelles (Ktistakis 2020). These regions are called omegasomes and after autophagy initiation a complex array of proteins promptly co-localize there (Nguyen et al. 2023). The early events of autophagy initiation involve three main protein components: the most upstream being the UNC-51-like kinase 1 (ULK1) protein kinase complex consisting of the Ser/Thr kinase ULK1 and the adapter proteins ATG13, ATG101, and focal adhesion kinase-interacting protein 200 kDa (FIP200) (Zachari and Ganley 2017). In vertebrates, unlike yeast, the ULK1 complex is constitutively assembled, and its activation is controlled by distinct phosphorylation events (Kamada et al. 2000; Hosokawa et al. 2009). The regulation of the ULK1 complex activity is overseen by two energy-sensing kinases: (i) mechanistic target of rapamycin (mTOR) (Hosokawa et al. 2009) and (ii) AMP-activated protein kinase (AMPK) (Mack et al. 2012). In high nutrient conditions, the mTOR complex 1 (mTORC1), including the regulatory associated protein of mTOR (Raptor), associates with the ULK1 complex resulting in inactivation of it by mTOR dependent phosphorylation of ULK1 and ATG13 (Jung et al. 2009; Ganley et al. 2009). In nutrient depleted conditions, mTORC1 is inactivated and dissociates from the ULK1 complex. As a result, ULK1 performs autophosphorylation and transphosphorylation of ATG13 and FIP200. The different pattern of ULK1 phosphorylation is the signal for autophagy initiation (Jung et al. 2009; Alers et al. 2011). Aside from nutrient-depletion, the ULK1 complex can be activated by inhibiting mTOR with compounds like Rapamycin (Ravikumar et al. 2004) or Torin 1 (Liu et al. 2010). While mTOR senses amino acid levels in the cell (Laplante and Sabatini 2012), the second kinase to regulate ULK1 complex activity, AMPK, senses the ATP:AMP ratio within a cell. A low ATP:AMP ratio is a signal for a lack of energy that in turn activates AMPK. Activated AMPK activates ULK1 directly by phosphorylation (Mack et al. 2012) and indirectly by phosphorylating Raptor leading to the inactivation of mTORC1 activity (Gwinn et al. 2008). The activated ULK1 complex locates to a site of an omegasome and initiates autophagy by transduction of proautophagic signals through phosphorylation of downstream autophagic machinery proteins (Papinski and Kraft 2016). ULK1 is critical for initiation of both non-selective and selective macroautophagy. Proteotoxic stress induces phosphorylation of the selective cargo receptor p62/SQSTM1 by ULK1 increasing its binding affinity to ubiquitin and thus regulate selective autophagic clearance of polyubiquitinated protein aggregates (Lim et al. 2015). In Figure 10 the ULK1 complex is colored in green.

The second protein component involved in initiation of macroautophagy is the class III Phosphatidylinositol 3-kinase complex 1 (PI3KC3-C1) (Wesselborg and Stork 2015). PI3KC3-C1 is built of the catalytic subunit Vps34, the putative protein kinase Vps15, Beclin 1 (BECN1) and ATG14 (Rostislavleva et al. 2015). Within the PI3KC3-C1 complex ATG14 is the autophagy specific component and responsible for targeting the complex to sites of autophagy initiation (Itakura et al. 2008; Sun et al. 2008). After its activation, ULK1 phosphorylates Ser15 and other sites in BECN1 to activate the full PI3KC3-C1 complex and promote autophagy (Russell et al. 2013; Egan et al. 2015). Once activated, PI3KC3-C1 phosphorylates the lipid head group of phosphatidylinositol to generate phosphatidylinositol 3-phophate (PI(3)P) which accumulates at the omegasome site (Backer 2016). The formation of PI(3)P is critical for autophagy initiation (Kihara et al. 2001; Itakura et al. 2008) and PI3KC3-C1 facilitates the elongation of the growing isolation membrane which is formed from the omegasome (Uemura et al. 2014). Further, the accumulation of PI(3)P recruits downstream effectors including FYVE domain containing protein (DFCP) or WIPI1/2 to the omegasome (Axe et al. 2008; Proikas-Cezanne et al. 2015). In Figure 10, the PI3KC3-C1 complex is colored in yellow.

After successful initiation, DFCP1 is recruited to the omegasome. DFCP1 is an ATPase which is activated by membrane binding and dimerizes in an ATP-depended manner (Nähse et al. 2023). Depleting DFCP1 results in a significantly decreased autophagic flux of selective autophagy while non-selective bulk autophagy is not affected in both nutrient rich and nutrient depleted conditions. Nähse et al. showed that DFCP1 mediates ATPase-driven constriction of large omegasome to release autophagosomes for selective autophagy (Nähse et al. 2023). The isolation membrane is formed from the omegasome with lipid supply being mediated by ATG2 and ATG9. Both proteins co-localize at the growing edge of the isolation membrane. ATG2 functions as a lipid slide, delivering phospholipids from the ER to the growing isolation membrane. ATG9, a lipid scramblase, drives isolation membrane expansion by translocating the phospholipids between the outer and inner leaflet of the growing isolation membrane (Matoba et al. 2020). In Figure 10 ATG9 is colored in blue (ATG2 is not shown).

WIPI proteins bind to PI3P lipids at the growing isolation membrane (Proikas-Cezanne et al. 2004; Bakula et al. 2013). WIPI2B recruits the ATG12-5/ATG16 complex that conjugates LC3/ATG8 family proteins to phosphatidylethanolamine (PE) and, in doing so, possess an essential role for subsequent phagophore elongation (Dooley et al. 2014). Lipidated LC3 is involved in cargo recognition of selective autophagy as well as hemifusion of incoming membranes to promote isolation membrane elongation into phagophore formation (Weidberg and Elazar 2011; Proikas-Cezanne et al. 2015). In Figure 10 the ATG12 conjugation system is colored in orange and the LC3 conjugation system in red. The Introduction section 1.2.2 describes both conjugation systems in more detail.

The endosomal sorting complex required for transport (ESCRT) machinery is associated with cellular membrane scission processes including autophagosome closure (Henne et al. 2011; Vietri et al. 2020). Vps37A, an ESCRT-I subunit, with the ESCRT-I complex was identified to translocate to the isolation membrane and regulate autophagosome closure. Subsequently the ESCRT-III subunit CHMP2A is recruited (Takahashi et al. 2019). In 2018, Takahashi et al. demonstrated that the ESCRT-III subunit CHMP2A and the AAA-ATPase Vps4 are involved in autophagosome closure by membrane fission (Takahashi et al. 2018). Finally, the mature autophagosome fuses with a lysosome to form an autolysosome (Lőrincz and Juhász 2020).

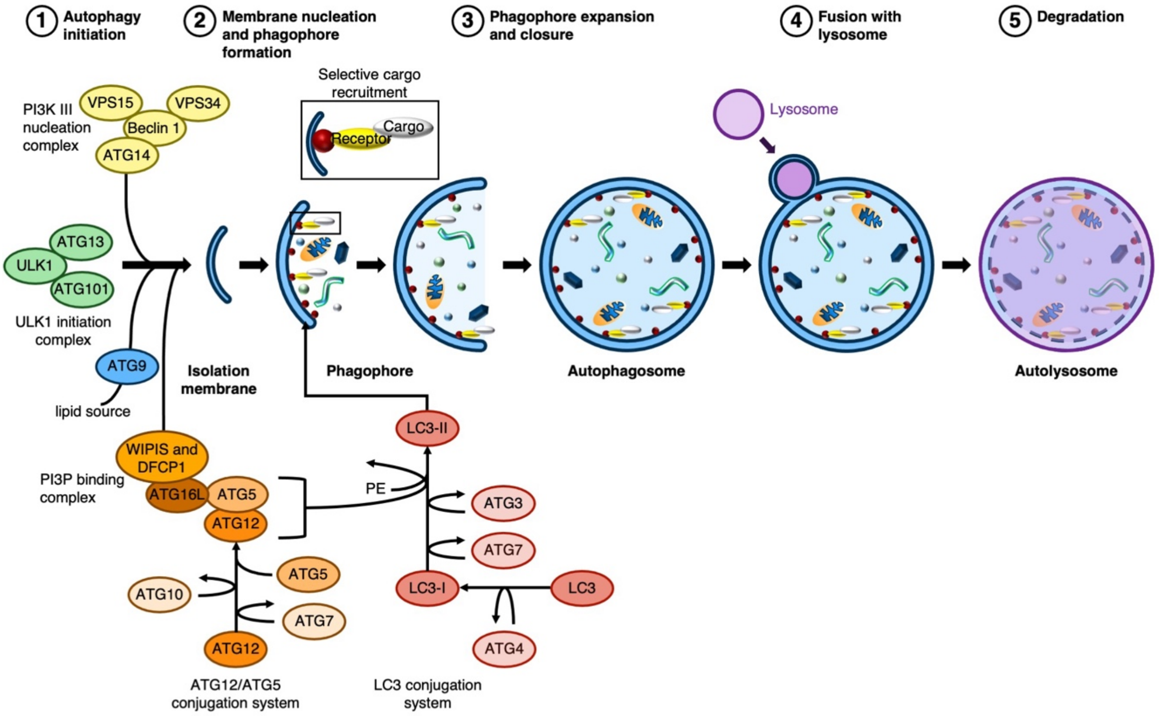

Figure 10: Schematic illustration of macroautophagy degradation of cellular components
Autophagy-related (ATG) proteins initiate autophagosome formation and promote elongation of the isolation membrane. ATG proteins of the core autophagic machinery can be classified into six functional groups: (i) the UNC-51-like kinase 1 (ULK1) protein kinase complex, (ii) the class III phosphatidylinositol 3-kinase (PtdIns3K) lipid kinase complex, (iii) the transmembrane protein ATG9, (iv) the WD repeat domain phosphoinositide-interacting protein (WIPI) complex, (v) the ATG5–ATG12 conjugation system, (vi) and the ATG8–phosphatidylethanolamine (PE) conjugation system. After autophagy initiation by the ULK1 initiation complex, the PI3K III nucleation complex joins to convert lipids which are supplied by ATG9 into phosphatidylethanolamine (PE). PE lipids recruit among others the WIPI2 complex which binds the E3-like complex of ATG16L, ATG5 and ATG12. ATG8 family proteins (only LC3 shown) are lipidated to PE which is integrated into the isolation membrane. The isolation membrane expands until the autophagosome closes with the help of ESCRT complexes (not shown). The mature autophagosome fuses with a lysosome. In the formed autolysosome the inner membrane of the autophagosome and the enclosed cargo is degraded. (The Figure was conceptually inspired by Hansen et al. 2018).

1.2.2 Conjugation of ATG8 family proteins to phagophore membranes

Selective autophagy is based on the interaction of cargo receptors with their cargo and ATG8 family proteins that decorate the membrane of the growing phagophore. ATG8 family proteins are ubiquitin-like and can be divided into two subfamilies: (i) microtubule associated protein 1 light chain 2 (LC3), and (ii) GABA type A receptor-associated protein (GABARAP) (Shpilka et al. 2011). For the lipidation of ATG8 family proteins, two autophagy-specific ubiquitin-like conjugation systems are essential, namely the ATG12 and the LC3 conjugation system (Nakatogawa et al. 2009).

The product of the ATG12 conjugation system is a covalently linked ATG12-ATG5 complex (Codogno et al. 2012; Proikas-Cezanne et al. 2015). To link ATG5 covalently to ATG12, first the E1-like enzyme ATG7 covalently binds to ATG12s C-terminal glycine by ATP-hydrolysis and formation of a thiolester bond (Mizushima et al. 1998a). Second, ATG12 is transferred to the E2-like enzyme ATG10 (Kaiser et al. 2012). Third, ATG12 is conjugated to ATG5 via an isopeptide bond (Mizushima et al. 1998b). The ATG12-ATG5 conjugate binds to dimerized ATG16L forming an E3-like complex (Mizushima et al. 2003; Fujioka et al. 2010). Important for the two ubiquitin-like conjugation system is to be spatiotemporally close to the autophagy initiation site. This is mediated via the interaction of ATG16L with the WIPI2 complex and is critical in the biogenesis of autophagosomes (Polson et al. 2010; Proikas-Cezanne et al. 2015). The ATG12-ATG5-ATG16L complex has E3-like function for the lipidation of LC3 or GABARAP (Otomo et al. 2013).

Because LC3B is in the focus of this thesis, the conjugation to PE is only described for LC3B. LC3B is synthesized in a pro-form that needs to be cleaved by ATG4 to expose a C-terminal glycine. The cleaved product is called LC3B-I (Kirisako et al. 2000). After activation of LC3B-I by ATG7 (Noda et al., 2011), LC3B-I is transferred to the E2-like enzyme ATG3 (Taherbhoy et al. 2011; Kaiser et al. 2012). Interaction of ATG3 with ATG12 enables the E3-like ATG12-ATG5-ATG16L complex to transfer LC3B-I from ATG3 to PE (Metlagel et al. 2013). Lipidated LC3B, called LC3-II, is anchored by its lipid tail into the growing isolation membrane (Dooley et al. 2014). When lipidation and thus integration into the isolation membrane of ATG8 family proteins is inhibited, by e.g. ATG3 or ATG5 knock-out, phagophore expansion and autophagosome closure is inhibited (Nakatogawa et al. 2007; Xie et al. 2008; Fujita et al. 2008).

It has been shown that ATG8 family proteins have fusogenic abilities by tethering pre-autophagosomal membranes to expanding phagophores (Nakatogawa et al. 2007; Weidberg et al. 2011). For the LC3 homolog in *Caenorhabditis elegans* an interaction with the HOPS tethering complex to promote fusion of mature autophagosomes with lysosomes was identified (Manil-Ségalen et al. 2014). Further, ATG8 family proteins that sit on the external membrane of the autophagosome are recycled by cleavage of ATG4 (Kirisako et al. 1999; Fernández and López-Otín 2015). It was suggested that in yeast ATG8 family proteins must be completely removed before successful fusion with the vacuole (Yu et al. 2012). In summary, ATG8 family proteins seem to have a dual role in autophagosome-lysosome fusion by recruiting tethering (and other) proteins and simultaneously preventing fusion until the outer membrane of the autophagosome was cleaned by ATG4 (Lőrincz and Juhász 2020).

1.2.3 Selective autophagy

The growing isolation membrane is decorated with ATG8 family proteins that form the binding platform for the core autophagy machinery as well as downstream targets of autophagy (Kraft et al. 2012; Lee and Lee 2016). The interaction to ATG8 family proteins is mediated via an approximately 13 amino acids long LC3-interacting region (LIR) motif. The core of the LIR motif contains a four amino acid long sequence starting with an aromatic amino acid (W, F, or Y), followed by two unsystematically positions, and ending with a hydrophobic amino acid (L, I, or V) (Birgisdottir et al. 2013; Rogov et al. 2014). Besides many ATG proteins, including ATG13 and ULK1, selective autophagy receptors carry the LIR motif connecting their cargo to the core autophagy machinery (Birgisdottir et al. 2013). Various selective autophagy pathways haven been described, and are listed in Table 1 (adapted from Johansen and Lamark 2020; Ichimiya et al. 2020). In addition to delivering cargo to the growing phagophore, several cargo receptors, including p62 and NDP52, have been described to actively promote the spatiotemporal formation of an autophagosome at the site of their cargo. Thus, selective autophagy receptors play an important role in regulating the degradation of their cargo (Ravenhill et al. 2019; Turco et al. 2019a).

The following paragraphs give a more detailed description of the selective autophagy of ribosomes, termed ribophagy, with the selective autophagy receptor NUFIP1, as well as the selective autophagy of protein aggregates, termed aggrephagy, with the selective autophagy receptor p62.

Table 1: Selective autophagy

Name	Target cargo	Identified cargo receptor
Aggrephagy	Protein aggregates	NBR1, OPTN, p62
ER-phagy	Endoplasmic reticulum	FAM134B, SEC62, RTN3, CCPG1, ATL3, TEX264
Ferritinophagy	Ferritin	NCO4A
Glycophagy	Glycogen	Stbd1
Lipophagy	Lipid droplets	
Lysophagy	Lysosome	NDP52, TRIM16
Midbody autophagy	Midbody rings	NBR1, p62, TRIM17
Mitophagy (Ubiquitin dependent)	Mitochondria	AMBRA1, NDP52, OPTN, p62, TAY1BP1
Mitophagy (Ubiquitin independent)	Mitochondria	AMBRA1, Bcl2L13, BNIP3, cardiolipin, ceramide, FKBP8, FUNDC1, NIX, NLRx1, PHB2
Nuclear lamina autophagy	Nuclear lamina	Lamin B1
Pexophagy	Peroxisomes	NBR1, p62
Ribophagy	Ribosomes	NUFIP1
Virophagy	Viral capsids	p62, TRIM5α
Xenophagy	Cellular pathogens	NDP52, OPTN, p62, TAX1BP1
Zymophagy	Secretory granule	p62

Ribophagy

The level of autophagic flux can be increased by different cellular stress factors, e.g. starvation. In starvation, autophagy provides a nutrient source, promoting survival of the cell by maintaining its homeostasis (Rabinowitz and White 2010). Many cellular components have a dual function by serving as nutrient storage in addition to their biological function, and autophagy plays a key role in providing access to such undedicated nutrients including amino acids and nucleotides (Rabinowitz and White 2010). In (fast-growing) cells, ribosomes constitute about 50% of the cell’s dry weight and are therefore a favorable nutrient source for amino acids in proteome remodeling during amino acid depletion (Rabinowitz and White 2010). In 2008, Kristensen et al. showed that in starvation-induced conditions ribosomes are degraded exhibiting a different kinetic compared to cytoplasmic and proteasomal proteins (Kristensen et al. 2008). This observation indicates that the degradation of ribosomes via autophagy is indeed progressing selectively in an ordered fashion, which is regulated differently compared to other components present in the cytoplasm (Kristensen et al. 2008). In yeast, the UBp3p/Bre5p ubiquitin protease was identified to be required for selective degradation of the 60S subunit (Kraft et al. 2008). Usually, ribosomes are protected against ribophagy by ubiquitination at lysine 74 in the large ribosomal subunit protein 25 (Rpl25). UBp3P/Bre5p deubiquitinates Rpl25 and marks the 60S subunit for degradation (Ossareh-Nazari et al. 2014). The human homolog to Rpl25 is L23a, but so far no protein homolog to UBp3P/Bre5p could be identified in mammalian cells making cross referencing unfeasible in this case (Kraft et al. 2008). In 2018 however, Wyant et al. proposed that the nuclear fragile X mental retardation-interacting protein 1 (NUFIP1) is a starvation induced selective autophagy receptor targeting ribosomes (Wyant et al. 2018). More details on NUFIP1 are described in the following paragraph. A mammalian pathway for ribophagy was recently described in human cells showing oncogene-induced senescence (OIS) by Lopez et al. During this persistent anti-proliferative response, the interactome of the ribosome is modified significantly. One important modification is the dissociation of the deubiquitinase USP10 from the small ribosomal subunit, enhancing ribosomal ubiquitination. Especially small subunit proteins, including RPS2 at lysine 275, are ubiquitinated and the selectively recruited to the autophagosome by p62 (López et al. 2023). The major role of ribophagy in promoting health and viability of cells is further supported by the confirmation of the contribution of mammalian ribophagy to DNA damage-induced neurodegeneration (Baltanás et al. 2011).

The selective autophagy receptor NUFIP1

Nuclear fragile X mental retardation-interacting protein 1 (NUFIP1) was first identified in 1999 as a nuclear protein interacting with the fragile X mental retardation (FMR1) protein, which in a silenced state is responsible for the mental retardation in fragile X patients (Bardoni et al. 1999). The FMRP complex, a multiprotein-mRNA complex containing FMR1, is involved in neuron development and a loss of FMR1 leads to mental retardation in the fragile x chromosome disease (Bardoni et al. 2001). The interaction between the FMRP complex and NUFIP1 is probably relevant for neuronal function *in vivo* and it is likely that NUFIP1 is involved in the neuronal maturation process (Levine and Kroemer 2008). NUFIP1 is able to cross the nuclear membrane in both directions, containing a nuclear localization signal (NLS) and nuclear export signal (NES), however, its abundance in the cytoplasm is quite low in non-stress induced conditions (Wyant et al. 2018). In context with its nuclear function, regions for binding small nuclear riboprotein 13 (snu13) (of FMRP complex) and the cofactor zinc finger HIT-type containing 3 (ZNHIT3) had been identified and characterized in its primary structure (Quinternet et al. 2016). Nevertheless, a large part of NUFIP1's primary structure remains uncharacterized, and no entire three-dimensional structure is available. More recent studies on the NUFIP1 and ZNHIT3 homologs in *Plasmodium falciparum* established the conservation of their interaction and underlined the difficulty to solve the three-dimensional structure of NUFIP1 as it is not soluble in a variety of purification conditions (Chagot et al. 2022). Figure 11A–C outlines the features identified in the primary structure of NUFIP1 as well as the three-dimensional structures of the binding regions of snu13 (FMRP complex) and ZNHIT3. Figure 11D shows the AlphaFold prediction of human NUFIP1 (AlphaFold-ID: AF-Q9UHK0-F1). AlphaFold can only predict the secondary structure in small regions of the protein with a high model confidence according to the per-residue confidence scores by the predicted local distance difference test (pLDDT). The majority of the protein is disordered in the prediction.

In their proteomics-based study, Wyant et al. showed that upon starvation-induced conditions the NUFIP1 population in autophagosomes increases significantly (Figure 11E). In a further fluorescence localization study, the translocation of

NUFIP1 from the nucleus to autophagosomes upon starvation was observed (Figure 11F). The previously identified binding partner FMRP, however, could not be detected in the autophagosomes, which indicated a different role of NUFIP1 in the context of starvation-induced autophagy (Wyant et al. 2018). Investigating further, Wyant et al. showed that NUFIP1 binds ribosomes *in vitro* and that ribosomes are almost solely present in autophagosomes of cells expressing a full functional NUFIP1 protein (Figure 11E). In addition, an interaction between NUFIP1 and the LC3 protein was described. Thus, Wyant et al. proposed that NUFIP1 is a selective autophagy receptor for ribosomes (Wyant et al. 2018). An additional localization study by Shim et al. described the translocaltion of NUFIP1 from the nucleus to the autophagosome in context of autophagy induced by cyclic mechanical stress. Similar to previous findings, NUFIP1 co-localized with LC3 on autophagosomes but in this case the level of ribosomal proteins in the cell did not decrease, indicating an additional role in autophagy than ribophagy. A new cargo, however, could not be identified (Shim et al. 2019).

In different cases, autophagy is described to have either a beneficial or a detrimental effect on survival of patients depending among others on the kind and state of disease (Levine et al. 2011). Defects in autophagy pathways in humans are linked to liver disease, neurodegeneration, Crohn’s disease, aging, cancer, and metabolic syndrome (Levine and Kroemer 2008). Based on the new interactions, Kim et al. investigated the levels of NUFIP1 and ribosomes in cancer cachexia and observed that muscle wasting in cancer involves suppression of ribosomal production and a four times increased expression of the ribophagy receptor NUFIP1. They concluded that in cancer cachexia, the anabolic capacity of skeletal muscle is diminished due to reduced ribosome production and likely increased ribosome degradation via ribophagy (Kim et al. 2020). However, the level of understanding the selective degradation of ribosomes via autophagy and the regulation of this pathway is currently not understood well enough to be targeted in medical applications since the actual role of NUFIP1 in ribophagy is still poorly defined. The mechanism behind NUFIP1’s translocation from the nucleus into the cytoplasm under the influence of stress and the change in its affinity towards ribosomes in starvation-induced conditions are hence a focal point of this thesis.

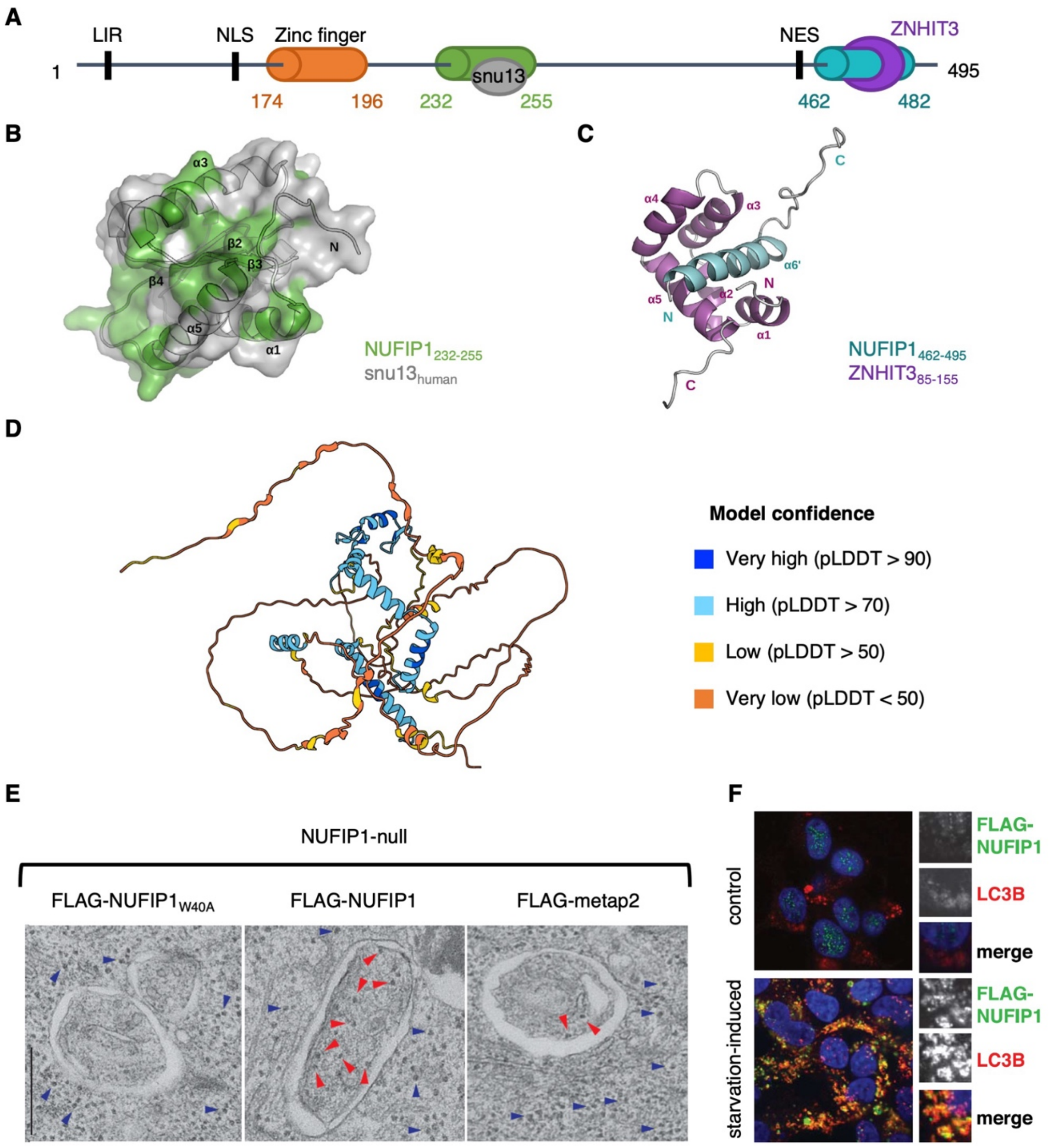

Figure 11: The NUFIP1 protein
A: Schematically depicting the localization of the biological active LC3B-binding region (LIR), the NLS, a zinc-finger motif, the snu13 binding site, the NES and the ZNHIT3 binding site in the primary structure of NUFIP1 (adapted from Quinternet et al. 2016; Wyant et al. 2018). **B:** Three-dimensional structure of snu13. Residues affected by NUFIP1$_{232-255}$ binding are colored in green on the snu13 surface (PDB-ID: 3SIU) (adapted from Quinternet et al. 2016). **C:** Solution NMR structure of NUFIP1$_{462–495}$:ZNHIT3$_{85–155}$ (adapted from Quinternet et al. 2016). **D:** AlphaFold prediction of human NUFIP1 (AlphaFold-ID: AF-Q9UHK0-F1) with model confidence according to the per-residue confidence scores by the predicted local distance difference test (pLDDT). **E:** Autophagosomes from HEK-293T cells lacking NUFIP1 or expressing the LC3B-binding deficient W40A mutant contain fewer ribosomes than those from control cells transfected with functional FLAG-NUFIP1. The analysis was carried out under starvation-induced conditions with electron microscopy. Red arrowheads indicate ribosomes inside an autophagosome. Blue arrowheads indicate ribosomes present in the cytoplasm. Scale bar: 500 nm (adapted from Wyant et al. 2018). **F:** A shift of NUFIP1 from the nucleus to LC3B-positive puncta can be observed in starvation-induced HEK-293T cells. The nucleus is stained blue, FLAG-NUFIP1's fluorescence appears green and LC3B's red (adapted from Wyant et al. 2018).

Aggrephagy

Aggrephagy is the selective degradation of protein aggregates by macroautophagy (Øverbye et al. 2007). (The degradation of protein aggregates by the proteasome or CMA requires the solubilization of single peptide chains from the aggregate and will not further be discussed here (Meacham et al. 2001; Kettern et al. 2010).) The formation of aggregates can be triggered by misfolded proteins that expose hydrophobic patches on their surface, which in turn stably interact with other (misfolded) proteins in a non-native way and without contributing to their biological function. Reasons for protein misfolding can originated from mutations, incomplete translation, misfolding after translation, aberrant protein modifications, oxidative damage, and from failed assembly of protein complexes (Dobson 2003). The degradation of protein aggregates via macroautophagy is mainly regulated via posttranslational modifications of autophagy receptors and substrates including ubiquitination, phosphorylation, and acetylation (McEwan and Dikic 2011). In case of the selective autophagy receptor p62, ubiquitination of the misfolded proteins seems to be the key driver for aggrephagy. The proposed role for p62 in aggrephagy is to bridge the ubiquitinated substrate to the macroautophagy machinery by recognizing ubiquitinated cargo and mediated contact to the ATG8 family protein LC3B via its own LIR motif (Lamark and Johansen 2012). More details on p62 and its interaction with cargo and LC3B are described in the following paragraph.

The selective autophagy receptor p62/SQSTM1

p62/SQSTM1 (from here p62) was first described in 1996 as a novel interaction partner to the SH2 domain of tyrosine-protein kinase Lck (Joung et al. 1996). In this context, p62 is involved in the activation of the NF-κB pathway by promoting the interaction of atypical protein kinase C (PKC) with RIP1 (Sanz 1999). Up until today, a multitude of interaction partners has been discovered, making p62 an interaction hub for multiple signaling pathways including the Wnt pathway, the Nrf2 pathway, the mTORC pathway, and the NF-κB-pathway (Puissant et al. 2012). Through the involvement in the above mentioned pathways, that are centrally positioned within the cellular metabolism, p62 is a key player in the maintenance of cellular homoeostasis and response to various extracellular signals. Within the cell, p62 is located in the cytoplasm and nucleus and can translocate to autophagy substrates such as protein aggregates, damaged mitochondria, or intracellular bacteria during stress response. The levels of p62 in the cell are regulated among others by autophagy. If autophagy is blocked, p62 accumulates in the cytoplasm and forms protein aggregates positive for p62 and ubiquitin (Komatsu and Ichimura 2010; Knævelsrud and Simonsen 2010; Rogov et al. 2014).

In context of autophagy, p62 is involved in mTORC1 activation on lysosomes, in the Keap1-Nrf2 pathway, and as a selective autophagy receptor (Moscat and Diaz-Meco 2011; Rogov et al. 2014; Filomeni et al. 2015). As described in the Introduction section 1.2.1, mTORC1 is involved in nutrient level sensing and is activated upon amino acid depletion. During high levels of amino acids, mTORC1 is located to the lysosomal surface via its interaction with Raptor bound to p62 which is recruited by LC3B (Puissant et al. 2012). On the lysosomal surface, mTORC1 is activated and therefore not degraded since autophagy is downregulated in this case. Here, p62 acts as an adaptor protein connecting regulatory units to possible initiation sites of autophagy (Puissant et al. 2012). During amino acid depletion, mTORC1 signaling stops and the ULK1 complex can initiate autophagy (Saxton and Sabatini 2017). In healthy conditions the Keap1-interacting region (KIR) motif of p62 is bound by the ubiquitinated KEAP1/Nrf2 complex (Katsuragi et al. 2016), which is a key player in the oxidative and electrophilic stress response (Kansanen et al. 2013). Binding to p62 triggers the degradation of the KEAP1/Nrf2 complex via autophagy. If oxidative stress occurs, the KEAP1/Nrf2 complex is deubiquitinated, dissociates from p62 and is not degraded anymore. KEAP1/Nrf2 can now perform its downstream activity to counteract oxidative stress (Katsuragi et al. 2016). A more general function of p62 in autophagy, is its role as selective autophagy receptor in e.g. aggrephagy (Lamark and Johansen 2012). Other selective autophagy pathways in which p62 is involved are listed above in Table 1. In selective autophagy, p62 recognizes polyubiquitinated cargo and delivers it to the autophagosome via LC3B binding.

p62 is a multidomain protein consisting of three structurally folded domains and one intrinsically discorded region (IDR). p62’s domain architecture, secondary structure, and tertiary structure of p62’s three folded domains are shown in

Figure 12. The Phox1 and Bem1p (PB1) domain of p62 (1-102) is its polymerization point. The PB1 domain of p62 can self-oligomerize into long flexible filaments or form hetero-oligomers with PB1 domains of other proteins, e.g. NBR1 (Jakobi et al. 2020). Additionally, the PB1 domain harbors the interaction sites for atypical PKC, Caspase-8 and ERK1 (Katsuragi et al. 2015). The zinc finger (ZZ)-domain of p62 (122-167) is a multiprotein and RNA interaction hub and is followed by a Tumor necrosis factor receptor-associated factor 6 (TRAF6) binding (TRAF6B) domain in the IDR. Together, the ZZ- and TRAF6B-domain are associated with RIP and TRAF6 binding, approximately between 117-266. Raptor, the link to mTORC1 signaling, also binds between the ZZ- and TRAF6B-domain (Katsuragi et al. 2015). Alongside the TRAF6B-domain, the IDR (168-388) contains multiple interaction motifs including the LIR and KIR motif, and nuclear localization and exit sites (Bjørkøy et al. 2005; Komatsu et al. 2010; Turco et al. 2019b). The structurally folded ubiquitin binding associated (UBA) domain (389-434) at p62's C-terminus captures ubiquitinated cargo for selective autophagy (Ciani et al. 2003). The domain structure of p62 is presented in Figure 12.

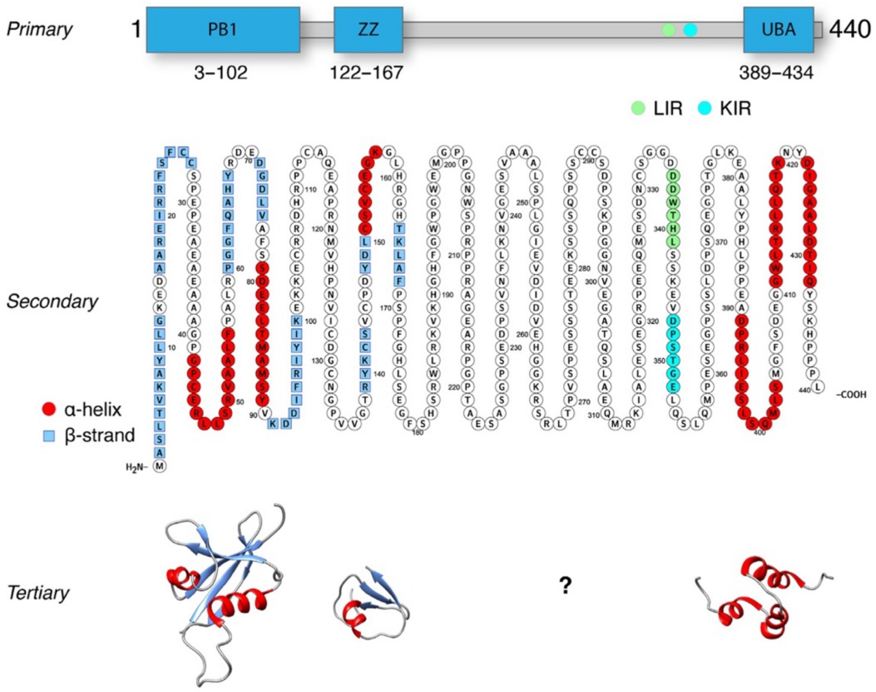

Figure 12: The p62 protein
Primary: Schematically depicting the localization of the PB1-domian, ZZ-domain, biological active LIR and KIR motif in the primary structure of p62. **Secondary:** Amino acid sequence of p62 labeled according to secondary structure elements. **Tertiary:** Three-dimensional structure of the PB1-domain (PDB-ID: 6TGY, Saio et al. 2009), ZZ-domain (PDB-ID: 5YP7, Kwon et al. 2018), and UBA-domain (PDB-ID: 2KNV, Ciani et al. 2003). (The Figure was adapted from Berkamp et al. 2021).

Until recently, no structural information for a longer truncation than a single domain of p62 was available. The PB1 domain of p62 has an acidic and basic surface patch allowing the polymerization into long, filamentous structures (Lamark et al. 2003; Ciuffa et al. 2015). Filaments of the PB1 domain can adopt several polymorphs which were solved by cryo-EM and classified as serpent-like (S) and ladder-like (L) type (Jakobi et al. 2020). The filament structure of full-length p62 was solved by Siavash Mostafavi at a global resolution of FDR-FSC = 0.143 of 4.8 Å. In full-length p62 filaments, the PB1 domains are arranged as two anti-parallel strands with D1 symmetry with a 135 Å pitch and symmetry parameters converged to 10.044 Å rise and -26.3387° twist (Mostafavi 2022). In the full-length structure, the ZZ-domain has an approximate resolution of 7-8 Å and the IDR and UBA domain are not well-resolved (Mostafavi 2022). A possible structure of how the PB1-domain of p62 can polymerize into a helical filament is shown in Figure 13A.

In the literature, it has been shown that p62 filaments can be capped at either end by other proteins containing PB1 domains, including PKCs, MEKKs, or NBR1 (Jakobi et al. 2020). Capping by NBR1 results in shorter filaments, as NBR1's PB1 domain has only acidic patches and polymerization cannot be continued (Jakobi et al. 2020). Crosslinking of filaments can be achieved by adding a multivalency crosslinker to the filaments. p62 filaments were shown to be crosslinked by polyubiquitin resulting in biological condensate formation (Zaffagnini et al. 2018). Another possible way, how proteins can interact with p62 filaments is decoration (Jakobi et al. 2020). The different types of how p62 filaments can interact with binding partners are schematically shown in Figure 13B. The polymerization ability of p62 is critical for its functionality in autophagy, as mutations, that prevent polymerization, lead to an exclusion of p62 from the autophagosome formation site (Itakura and Mizushima 2011).

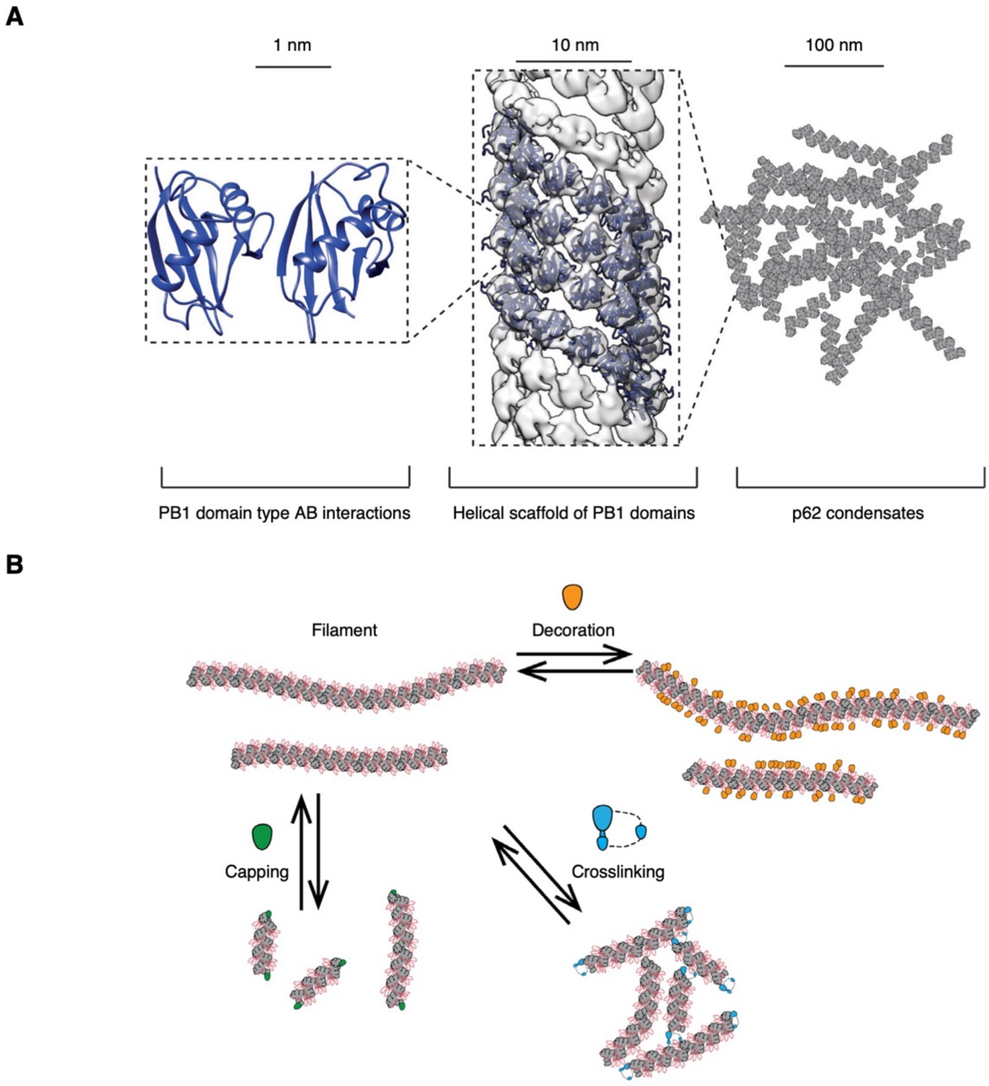

Figure 13: Three-dimensional structure of a helical filament formed by the PB1-domain of p62 and possible ways of interaction with binding partners
A: Macromolecular assembly of p62 into helical filaments. The PB1 domain of p62 contains acidic (A) and basic (B) patches to allow stacking into helical scaffolds. p62 filaments can arrange into biological condensates by crosslinking (adapted from Johansen and Sachse 2015). **B:** Different types of interactions of p62 filaments. p62 filaments can either be decorated, capped or crosslinked by interaction partners (adapted from .

1.2.4 Phase separation

With increasing complexity in cells, organelles evolved to provide spatiotemporal control over cellular materials, metabolic processes, and signaling pathways (Boeynaems et al. 2018). Organelles provide a separated environment suitable for chemical reactions to take place in and can either be organized by a surrounding lipid-bilayer (membrane bound) or in a membrane less form (Hyman et al. 2014). While in classical organelles the interior and exterior is physically separated by a membrane and organelle composition can be regulated through specialized membrane transport machinery, membrane-less organelles have no physical barrier to keep their components contained (Banani et al. 2017). Membrane-less organelles, more generally known as biomolecular condensates, can be found within the nucleus, cytoplasm, and on membranes. Studies revealed similarities in their shape, dynamics, and manner of assembly, despite differences in composition, location, and function (Banani et al. 2017). A well-studied representative of membrane-less organelles are P-granules that are RNA and protein-containing bodies in embryos of *Caenorhabditis elegans*. P-granules were first described in 1982 but the physical nature of the assemblies remained a mystery for quite some time (Strome and Wood 1982). In 2009 it was shown that P-granules have liquid-like properties and form by liquid-liquid phase separation (LLPS) (Brangwynne et al. 2009).

Per definition, phase separation is a physical process that occurs when a well-mixed solution spontaneously separates into two phases resulting in a high-concentration and a dilute phase (Boeynaems et al. 2018). Cells make use of phase separation by locally increasing the concentration of components locally and thereby modulating interaction kinetics (Brangwynne et al. 2009). Proteomic and genetic studies on protein components of several membrane-less organelles suggest that a common feature of proteins involved in phase separation is multivalency of adhesive domains and/or linear motifs (Andersen et al. 2005; Fong et al. 2013; Jain et al. 2016; Boke et al. 2016). Boeynaems et al. described three possible ways for multivalency: (i) oligomerization of folded proteins with well-defined interaction surfaces, (ii) folded domains linked by flexible regions to generate linear multivalent proteins, and (iii) intrinsically disordered regions (IDRs) as scaffolds for multiple, distinctive short linear motifs (Boeynaems et al. 2018). To drive phase transition, the interactions between these domains have to be stronger than their interaction with the solvent. High-valency usually decreases the barrier for phase transition because the entropic cost is less than for proteins with fewer interaction domains (Brangwynne et al. 2009).

Material states in phase separation

Although phase separation is often equated with liquid-liquid phase separation, biological macromolecules can form condensates with different material states that are either well-mixed or spatially organized (Handwerger et al. 2005; Patel et al. 2015; Molliex et al. 2015). Proteins and RNA can be described as associative polymers resulting in a large variety of material properties that the condensates can adopt. The physical crosslink between the polymers is the determinant for the material's properties by influencing the directional preferences for spatial ordering (Wang et al. 2014; Fei et al. 2017). The three most prominent material states a condensate can adopt are liquid, gel, or solid. Assuming that gelation is the transitioning from liquid to solid, gels display a system-spanning network of intermolecular interactions. The more short-lived the crosslinks are and/or the lower the level of crosslinking is, the more the material properties will shift into the direction of a liquid. In contrast, the more long-lived the crosslinks are and/or the higher the density of crosslinking is, the more the material properties will shift towards solid (Boeynaems et al. 2018). A schematic depiction of the material states a polymer can adopt in a condensate are shown in Figure 14.

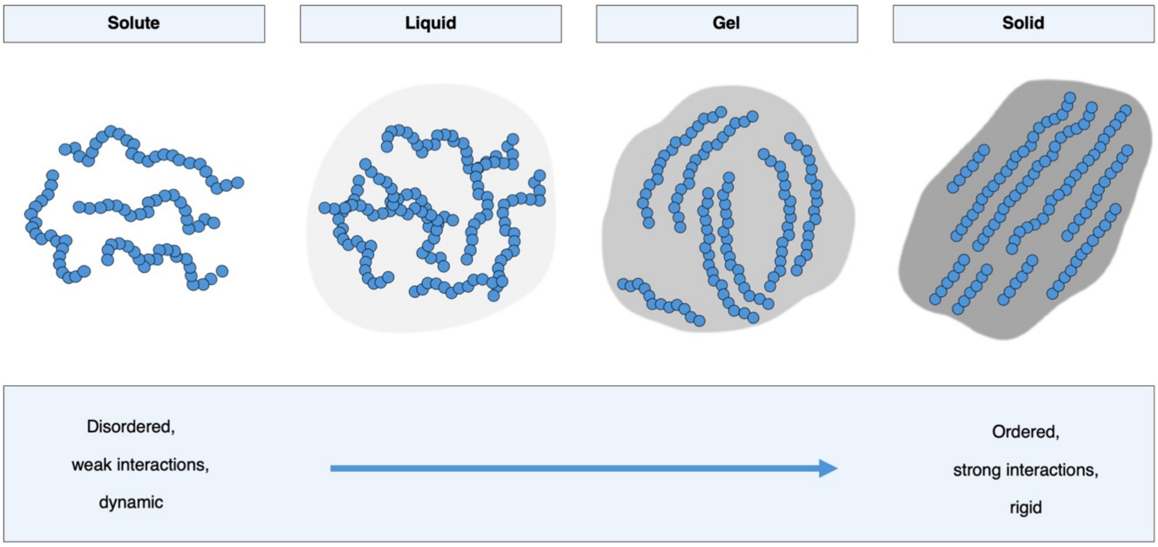

Figure 14: Material states of biological condensates in phase separation
In solution the interactions between the polymers are disordered and weak, causing well mixing with the solute. If phase separation occurs, the polymer can adopt states from liquid to solid characterized by an increase in order and interaction strength. Note: dependent on the material state of the phase separation, the form of the biological condensate changes. (The Figure was conceptually inspired by Boeynaems et al. 2018).

Phase separation in autophagy

In context of autophagy, LLPS could also be observed. In *Caenorhabditis elegans*, the LLPS of the autophagy receptor SEPA-1 and the scaffold protein EPG-2 was described to be modulated by post-translational modifications in PGL-1 (Zhang et al. 2018). The selective autophagy receptor p62 shows LLPS *in vivo* (p62 bodies) and *in vitro*. *In vitro*, the reconstitution of p62 with polyubiquitin is sufficient to induce phase separation that is mediated via the interaction of polyubiquitin with multiple polymerized p62 entities (Zaffagnini et al. 2018). The IDR of p62 harbors multiple sites for post-translational modifications (PTMs) and binding sites to a bunch of interacting proteins. The state of p62 in phase separation influences the properties of the formed condensate severely (Berkamp et al. 2021). For example, the ubiquitination of Lys7 in p62 by TRIM21 disrupts the helical scaffold and has been shown to reduce the number and size of p62 bodies formed inside cells (Pan et al. 2016). The affinity to polyubiquitinated cargo can be increased by acetylation in the UBA domain of p62 by TIP60 and results in the formation of more and larger p62 bodies (You et al. 2019). The quaternary structure of p62 as an oligomeric assembly seems to be a possible regulation point for cellular p62 phase separation and will be investigated further in this thesis.

1.3 Translation in *Corynebacterium glutamicum*

Corynebacterium glutamicum is a gram-positive, non-endotoxic, non-sporulating, and generally recognized as safe Actinobacterium. First identified in search for a natural glutamate producer in 1957, *C. glutamicum* is nowadays widely used as a host for industrial production of L-glutamate and L-lysine (Kinoshita et al. 1957; Lee et al. 2016). In 2003, the complete genome sequence of *C. glutamicum* ATCC 13032 was published, helping *C. glutamicum* become the key organism in the field of industrial microbiology and biotechnology (Kalinowski et al. 2003). In addition to its importance in large scale amino acid production, *C. glutamicum* is being used in value-added chemical, fuel, and polymer production and an increasing number of studies establish *C. glutamicum* as a platform microbe for heterologous protein expression (Lee et al. 2016). *C. glutamicum's* low level extracellular protease activity combined with two native protein secretion mechanisms underline its great potential for this application. So far, various examples of successful heterologous protein expression have been published (Date et al. 2006; Yim et al. 2014, 2016; Matsuda et al. 2014).

1.3.1 Bacterial translation

In general, translation is the process of protein biosynthesis by ribosomes which translate an mRNA sequence into a protein sequence (Ramakrishnan 2002). Bacterial protein biosynthesis has been extensively studied and is described in the following in a simplified manner, neglecting initiation and termination of translation, as well as essential elongation factors. After translation is initiated by canonical or leaderless initiation, the decoding of the mRNA and elongation of the peptidyl chain by the ribosome starts (Ramakrishnan 2002). At the beginning of translation, the fMet-tRNA binds the start codon in the P-site of the ribosome, inducing conformational changes to open the A-site for a new aminoacyl-tRNA to bind. By conformational proofreading the ribosome recognizes the next fitting and charged tRNA that subsequently binds to the A-site (Savir and Tlusty 2013). The resulting configuration of two charged tRNAs, one in the P-site and one in the A-site, is called pretranslocational state (Frank et al. 2007). In the peptidyl transfer center, the fMet- residue of the initiation tRNA is transferred to the amino acid of the A-site tRNA by catalysis of the ribozyme 23S rRNA forming a peptide bond between both amino acids (Tirumalai et al. 2021). The A-site tRNA, now a dipeptidyl-tRNA, translocates into the P-site position and the P-site tRNA, now deacylated, into the E-site. After the process of peptidyl-transfer and tRNA translocation is completed, the ribosome adopts the posttranslocational state (Frank et al. 2007) and the deacylated E-site tRNA is released from the ribosome (Dinos 2005). The translocation of the tRNAs through the ribosome is accompanied by a simultaneous move along of the mRNA. After translocation the next codon is presented in the A-site returning the ribosome to the initial state of the elongation cycle. The process of tRNA binding, amino acid transfer and translocation goes on until the ribosome encounters a stop codon. At the stop codon elongation is terminated (Griffiths 2008). A simplified elongation cycle is shown in Figure 15.

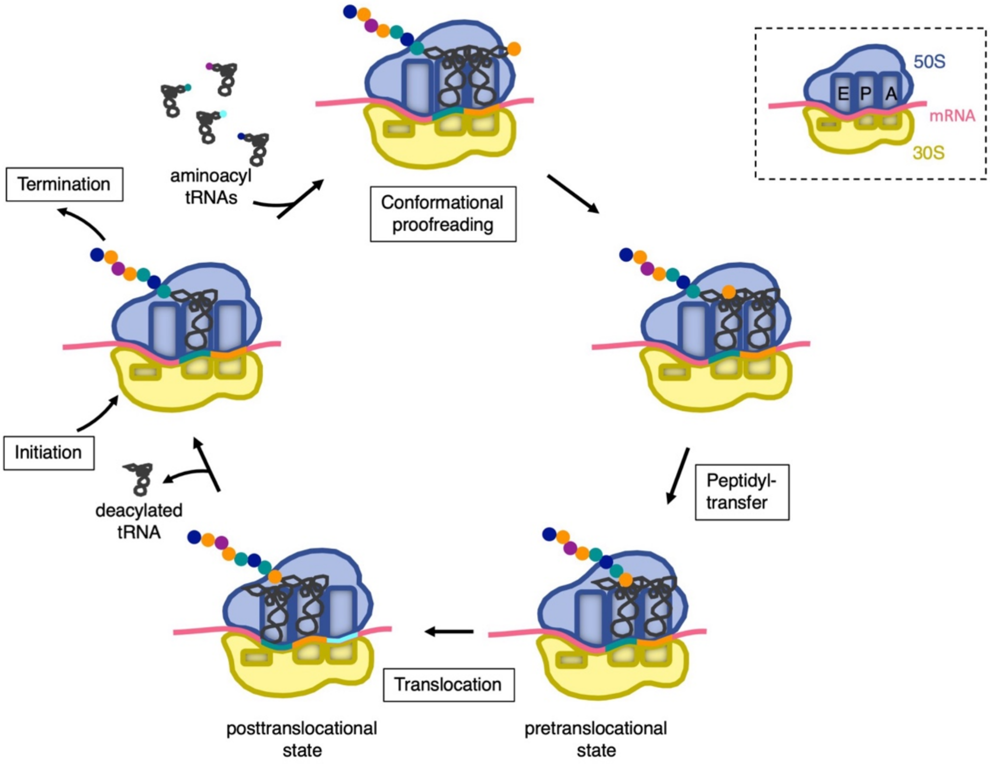

Figure 15: Bacterial translation - a simplified elongation cycle
Schematic depiction of the elongation cycle in bacterial translation. Initiation and termination as well as critical elongation factors are not displayed. If an aminoacyl tRNA is in P-position of the ribosome and the next codon is not a stop codon, the ribosome starts conformational proofreading of aminoacyl-tRNAs until a tRNA with a matching anticodon bound in the A-site. The peptidyl chain bound to the P-site tRNA is transferred to the tRNA in the A-site via the formation of a peptide bond. After transfer, the tRNAs are shifted in the ribosome to the next positions. This process is termed translocation. After translocation the deacylated tRNA can dissociate from the E-site bringing the ribosome back into the initial state.

1.3.2 The Actinomycetota ribosome

The translational machinery of *Escherichia coli*, a model organism for proteobacteria, has been intensively studied in its function and structure (Kaczanowska and Rydén-Aulin 2007; Keiler 2015; Fromm et al. 2023). The ribosome of Actinomycetota was investigated much less, impeding its structure-function analysis, and limiting drug optimization for this translational system. Additionally, as a key component in heterologous protein production, understanding the functionality of the ribosome is of outmost importance when controlling expression on translational level. So far, the structure of the more closely related 70S ribosomes of *Mycobacterium tuberculosis* (PDB-ID: 5V93, Yang et al. 2017), *Mycobacterium smegmatis* (a non-pathogenic model for tuberculosis) (PDB-ID: 5O61 and 8WHX, Hentschel et al. 2017; Kumar et al. 2024), and *Cutibacterium acnes* (PDB-ID: 8CRX, Lomakin et al. 2023) were studied by cryo-EM motivated by the epidemiological significance of tuberculosis and pathogenic acne. Although the structures of bacterial ribosomes are mostly conserved, a few significant differences between *E. coli* and Actinomycetota ribosomes could be identified in the rRNA and ribosomal protein content. The 23S rRNA of Actinomycetota has an extensive insertion of around 110 nucleotides after helix 54 (H54), which is thought to be involved in subunit interaction and polysome formation and is termed helix 54a (H54a) or *handle* (Shasmal and Sengupta 2012). In addition to H54a on the solvent side of the large subunit, Actinomycetota possess three more nucleotide insertions after helices 14, 16, and 31, termed H15, H16a, and H31a (Shasmal and Sengupta 2012). These insertions are less protruding compared to H54a but still make up a different surface of the ribosome compared to *E. coli*. Figure 16A presents the rRNA insertions on the surface of the Actinomycetota ribosome. Two new ribosomal proteins were identified in the Actinomycetota 70S ribosome, namely bL37 in the large and bS22 in the small subunit (Hentschel et al. 2017). The absence of the bS21 protein in the small ribosomal subunit of Actinomycetota ribosome was also reported (Lomakin et al. 2023). The molecular structure and location within the 70S ribosome of bL37 and bS22 are shown in Figure 16B. Previously, structures of active Actinomycetota 70S ribosome were solemnly observed with at P-site tRNA (Hentschel et al. 2017; Yang et al. 2017; Lomakin et al. 2023), the E-site tRNA was only observed for hibernating ribosomes (Mishra et al. 2018). Recently, Kumar et al. reported a structure containing a single E-site tRNA and the hibernation promotion factor RafH bound for the *M. smegmatis* 70S ribosome. Hibernation of 70S ribosomes in *M. smegmatis* by RafH is hypoxia induced and inhibits protein biosynthesis. Interestingly, RafH induces hibernating 70S monosomes instead of 100S disomes as dimerization with another RafH bound 70S ribosome is due to a comparatively large C-terminal domain of RafH sterically impossible. The formation of a hibernating 100S is further blocked by H54a and bS1 (Kumar et al. 2024).

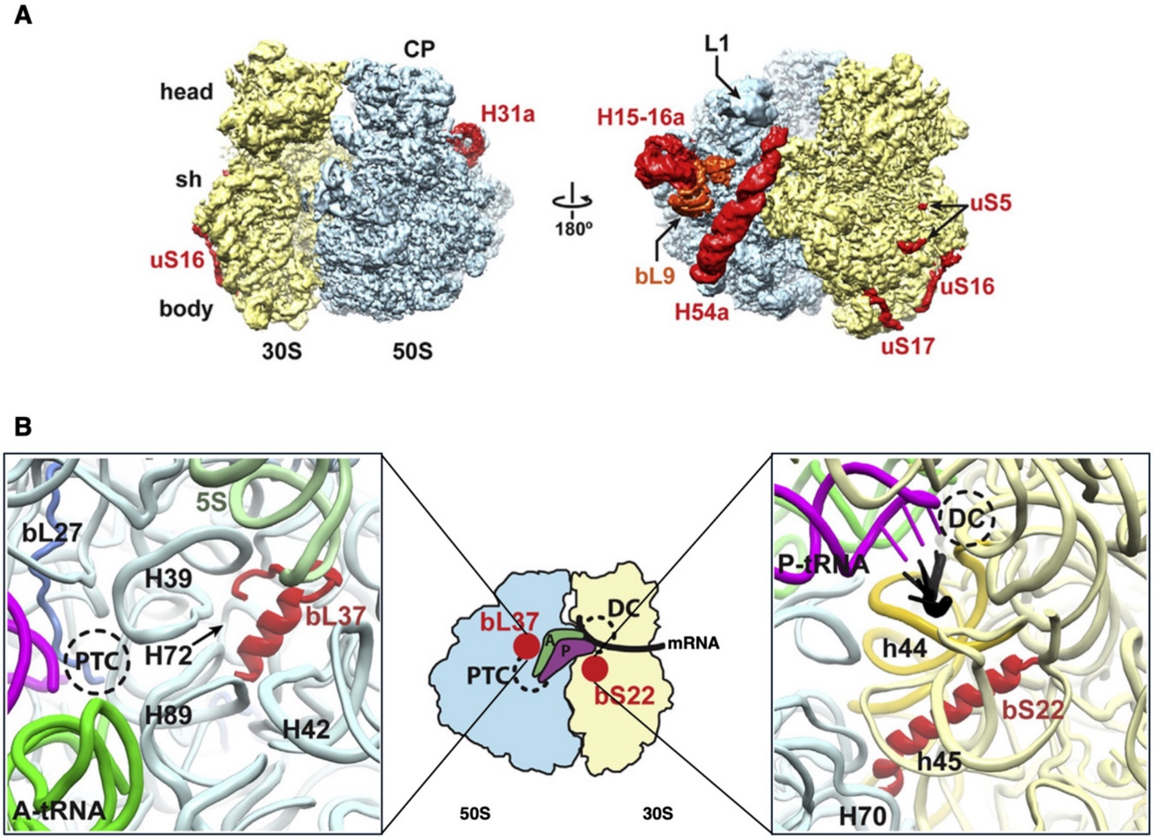

Figure 16: The Actinomycetota ribosome
A: EM-density map of the 70S ribosome from *M. smegmatis* depicting the 50S subunit in light blue and the 30S subunit in yellow. Highlighted in red are the Actinomycetota-specific rRNA insertions and protein modifications. **B:** Binding site of the bL37 protein near the peptidyl-transferase center (PTC) and the bS22 protein between helix 44 (gold) and helix 45 near the mRNA channel and the decoding center (DC). The contact between bS22 and 23S rRNA (light blue) helix 70 is shown. (The Figure was adapted from Hentschel et al. 2017).

1.3.3 The bS22 protein

The small ribosomal subunit protein bS22 has recently been described for the Actinomycetota *M. smegmatis* (Hentschel et al. 2017), *M.* tuberculosis (Yang et al.

2017), and *C. acnes* (Lomakin et al. 2023), as well as for bacteria of other kingdoms including the *Flavobacterium johnsoniae* (Bacteroidetes) (PDB-ID: 7JIL, Jha et al. 2021), but is absent in *E. coli*. The molecular structure of the bS22 protein of *F. johnsoniae* is shown in Figure 17A. bS22 is located at the H44 of the 16S rRNA, and is in direct contact with H70 of the 23S rRNA, therefore bridging the small and the large subunit of the 70S ribosome (Hentschel et al. 2017). The location of bS22 within the 30S subunit is depicted in Figure 17B. Due to the location of bS22 at the subunit interface and the proximity to the mRNA channel, Hentschel et al. proposed that bS22 may be involved in translation initiation, ribosome biogenesis, or dormancy, by promoting the binding of ribosome-associated proteins to the 30S subunit. Jha et al. recently argued against the role of bS22 in translation initiation as Shine Dalgarno sequences are quite prevalent in Actinomycetota, compared to Bacteroides, still bS22 is present in both (Jha et al. 2021). Lomakin et al. demonstrated a bacteriostatic effect of bS22 on *E. coli in vivo*. *In vitro* complementation of the *E. coli* 70S ribosome with bS22 resulted in a diminished activity of the *E. coli* ribosomes. As *E. coli* ribosomes contain the bS21 protein, which is absent in Actinomycetota, it was hypothesized whether a ribosome can only be functional with either bS21 or bS22. In Bacteroidetes, like *F. johnsoniae*, both proteins are present making the translation inhibition for *E. coli* ribosomes more difficult to explain (Jha et al. 2021). A structural and sequence comparison between bS22 of *F. johnsoniae* and bS22 of *M. smegmatis* is shown in Figure 17C–D.

As described below in the Introduction section 1.3.4 for Kasugamycin in more detail, the aminoglycoside antibiotic binding site is located at the upper part of H44 in the 16S rRNA (Carter et al. 2000; Stanley et al. 2010). Several contacts of the bS22 protein to H44 and H45 in *M. smegmatis* are expected to contribute to the maintenance of rRNA architecture of the binding site for aminoglycoside antibiotics. The contribution is promoted via the side chains of Lys16 and Lys19 of bS22 which interact with the phosphate group of U1406 in the 16S rRNA (Hentschel et al. 2017). In the literature it has been shown that the substitution of U1406 in H44 leads to Kanamycin resistance (Watanabe et al. 2012) strongly suggesting the need for investigation of bS22 as a drug target.

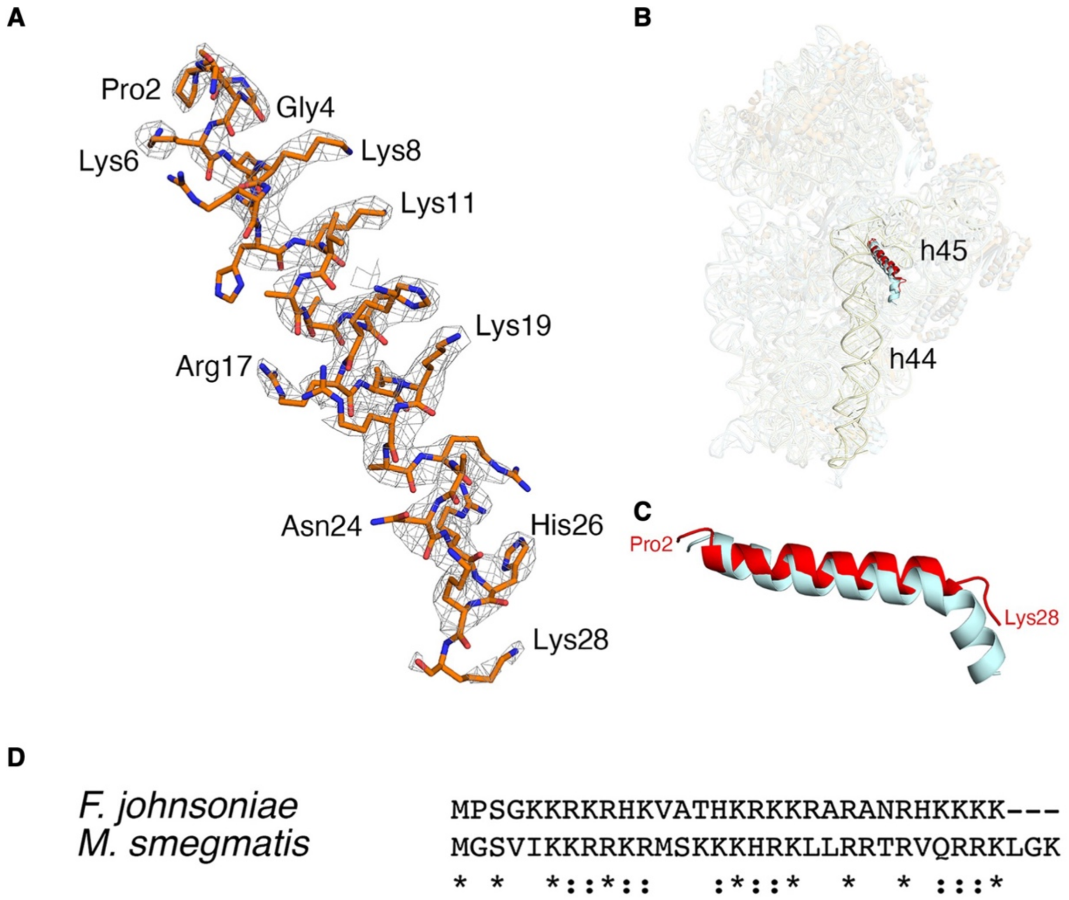

```
MPSGKKRKRHKVATHKRKKRARANRHKKKK---
MGSVIKKRRKRMSKKKHRKLLRRTRVQRRKLGK
* *  *::*::   :*::*  *  * :::*
```

Figure 17: The bS22 protein in *F. johnsoniae* and *M. smegmatis*
A: EM-density map and the derived molecular model of the bS22 protein in *F. johnsoniae*. **B:** Structural comparison of bS22 of *F. johnsoniae* (red) and bS22 in *M. smegmatis* (cyan) in the 30S subunit. **C:** Structural comparison between *F. johnsoniae* (red) and bS22 in *M. smegmatis* (cyan), highlighting the structural homology. **D:** Amino acid sequence alignment of bS22 from *F. johnsoniae* and bS22 from *M. smegmatis*. Sequence identity is marked with a * and sequence similarity with a :. (The Figure was adapted from Jha et al. 2021).

1.3.4 The antibiotic Kasugamycin

The antibiotic Kasugamycin belongs to the class of aminoglycosides with a unique structure of two sugars, a d-chiro-inositol moiety and a kasugamine moiety (2,4-diamino-2,3,4,6-tetradeosy-d-arabino-hexose), with a carboxy-imino-methyl group (Fukagawa et al. 1968). The molecular structure of Kasugamycin is shown in Figure 18A. Kasugamycin is naturally produced by *Streptomyces kasugaensis* which was isolated from soil at Kasuga Shrine in Nara, Japan in 1965 (Umezawa et al. 1965). Since its discovery, Kasugamycin is widely used in agriculture with a focus on rice blast caused by the fungus *Magnaporthe grisea* and to control bacterial rice grain and seedling rot caused by the proteobacterium *Burkholderia glumae* (Müller et al. 2011). Kasugamycin is a riboactive antibiotic, inhibiting protein synthesis in prokaryotes and *M. grisea*, but failing to induce translational misreading due to the lack of a deoxystreptamine moiety, which is common among other aminoglycosides (Ikekawa et al. 1966; Yoshii et al. 2012). Structural studies of Kasugamycin bound to ribosomes located its binding site in the bacterial ribosomal 30S subunit in close proximity to the mRNA-binding tunnel of the E-site and P-site. Thus, Kasugamycin indirectly inhibits tRNA binding at the P-site by perturbing the mRNA-tRNA codon-anticodon interaction during translation initiation (Okuyama and Tanaka 1972; Okuyama et al. 1974; Poldermans et al. 1979). A recent high-resolution cryo-EM study on several antibiotics resolved the Kasugamycin binding pocket in *E. coli* 70S ribosome at a resolution of 2.04 Å (Paternoga et al. 2023). The binding pocket of the *E. coli* 70S ribosome with the contacts of Kasugamycin to the bases A792, A794, G926, A1499, G1505, and U1506 (*E. coli* numbering) as described in the literature is presented in Figure 18B (Schuwirth et al. 2006; Paternoga et al. 2023).

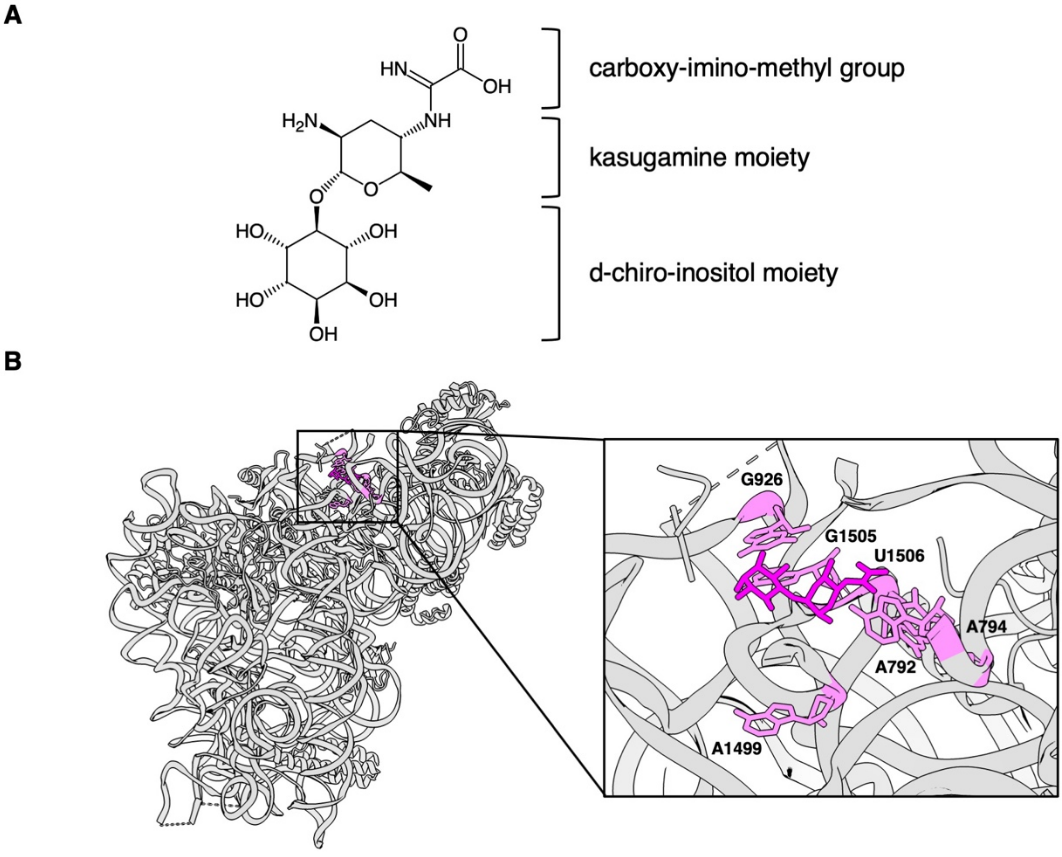

Figure 18: The antibiotic Kasugamycin and its binding to the 30S subunit of *E. coli*
A: Molecular structure of Kasugamycin. **B:** Molecular structure of the 30S subunit of an *E. coli* 70S ribosome in complex with Kasugamycin. Kasugamycin is colored in deep magenta, and binding contacts of Kasugamycin in light magenta. The labels of the binding contacts of Kasugamycin in the 16s rRNA are in *E. coli* numbering (PDB-ID: 8CEP, Paternoga et al. 2023).

Resistance to the antibiotic Kasugamycin

In general, bacterial resistance of bacteria to antibiotics can be induced by different mechanisms: (i) a modification of the binding site, thus, reducing affinity or abolishing binding completely (ii) decreasing uptake or increasing efflux of the antibiotic, or (iii) inactivation of the antibiotic by enzymatic modification (Munita and Arias 2016). In *E. coli*, the first detected resistance to Kasugamycin was mapped to the *ksgA* gene (Helser et al. 1971, 1972). KsgA is a methlytransferase that dimethylates two adjacent nucleotides, namely A1518 and A1519 (*E. coli* numbering), in H45 of the 16s rRNA (*E. coli* numbering) (Ochi et al. 2009). By deletion or inactivation of KsgA, *E. coli* shows an increased resistance to Kasugamycin. A1518 and A1519 are adjacent to the Kasugamycin binding site in the small subunit but are not involved in the formation of the binding pocket (Schuwirth et al. 2006). The mechanism for resistance for KsgA has not been understood yet. In contrast, the mutations A794G, G926A, and A1519C in the 16S rRNA induces a strong resistance to Kasugamycin by simply abolishing Kasugamycin binding (Vila-Sanjurjo et al. 1999). Mutations in three other genes (*ksgB*, *ksgC*, and *ksgD*) in *E. coli* cause resistance independently (Sparling et al. 1973; Yoshikawa et al. 1975; Fouts and Barbour 1981). While *ksgC* alters the amount of ribosomal protein S2 and therefore also targets the ribosome (Yoshikawa et al. 1975), resistance through *ksgB* is most likely induced by changing the membrane permeability to Kasugamycin (Dabbs 1978). *In vitro* translation experiments of ribosomes extracted from a Δ*ksgB* strain showed that ribosomes of Δ*ksgB* were still sensitive to Kasugamycin, while ribosomes of Δ*ksgA* and Δ*ksgC* mutants are not. These results suggest that while Δ*ksgA* and Δ*ksgC* mutations target the ribosome, Δ*ksgB* does not (Sparling et al. 1973). The detailed molecular mechanism of Kasugamycin resistance has not been elucidated yet for any of the mutations. In the efforts to combat antibiotic resistance investigating the mode of action of current antibiotics is crucial as well as for identifying new targets for the development of novel antibiotics or potentiators of existing drugs.

2 Aims

The goal of this thesis is to study and structurally characterize protein complexes of autophagy and protein biosynthesis using the entire range of structural characterization tools of cryogenic electron microscopy. In the context of autophagy, the overall aim is to gain an improved structural and functional understanding of the selective autophagy receptors NUFIP1 and p62. For NUFIP1, evidence describing its involvement in autophagy is still scarce. As no molecular structure of NUFIP1 is available, the goal for NUFIP1 was to recombinantly express the protein and prepare purified samples suitable for structure determination by single-particle analysis to reveal the molecular basis for the interaction between NUFIP1 and human 80S ribosomes. For p62, the specific aim was to set up suitable experiments, in which the interaction of p62 with a phagophore membrane and cargo can be investigated in a simplified system *in vitro*. Once LC3B is conjugated to liposomes, the LC3B covered liposomes can be mixed with p62 filaments and the resulting macromolecular assembly captured with cryogenic electron tomography. Further, in order to investigate the molecular assembly of p62 within phase separation induced by cargo binding, cryogenic electron tomography can be performed on p62 filaments mixed with model cargo. In context of protein biosynthesis, the molecular structure of the 70S ribosome of *Corynebacterium glutamicum* is not available. Therefore, the specific aim is to solve the molecular structure of the 70S and two mutant 70S ribosomes to high-resolution with single-particle analysis. With multiple rounds of three-dimensional classification, a better understanding of the ribosome's conformational space can be generated. Additionally, as *C. glutamicum* is susceptible to the antibiotic Kasugamycin, the molecular structure of the 70S ribosome and both mutant 70S ribosomes can be solved in complex with the antibiotic Kasugamycin. As both mutants show a higher resistance to Kasugamycin, the obtained structures will be compared to understand the mechanism of antibiotic resistance. In this thesis, the proposed applications from single-particle analysis of homogeneous highly pure samples to electron tomography of more complex protein mixtures will reveal the broad range of target structures that can be visualized at different levels of structural detail by cryogenic electron microscopy.

3 Results and Discussion

3.1 The selective autophagy receptor NUFIP1

3.1.1 Cellular localization of NUFIP1

In order to investigate the recently identified role of NUFIP1 as selective autophagy receptor, both, its cellular function as well as its molecular structure was investigated. As selective autophagy receptor, co-localization with the autophagy LC3 adaptor in the cytoplasm is a prerequisite for lysosomal degradation. Upon starvation NUFIP1 has been described to translocate from the nucleus to the cytoplasm (Wyant et al. 2018), therefore, the cellular localization of NUFIP1 was investigated by fluorescence microscopy assays. The cellular localization of NUFIP1 was analyzed in three different conditions of autophagy induction either by immunostaining of endogenous NUFIP1 or by live-cell fluorescence microscopy of HeLa cells transfected with fluorescently labeled NUFIP1.

In the immunofluorescence assay, autophagy was induced by incubation of HeLa cells with the mTOR inhibitor Torin 1 (250 nM for 2 h), in EBSS salt solution (4 h), or in DMEM medium without glucose (4 h). The cells were fixed and permeabilized with methanol and stained with an α-NUFIP1 antibody or an α-p62 antibody as control. Hoechst 33342 was added to stain the DNA within the nucleus to allow the identification of NUFIP1's location in the cell. Figure 19A shows HeLa cells stained with α-NUFIP1 antibody. In none of the above described conditions, a translocation of NUFIP1 from the nucleus to the cytoplasm could be observed. As expected, the p62 control forms punctae in the cytoplasm of the cells but is not present within the nucleus (Figure 19B) (Bjørkøy et al. 2005).

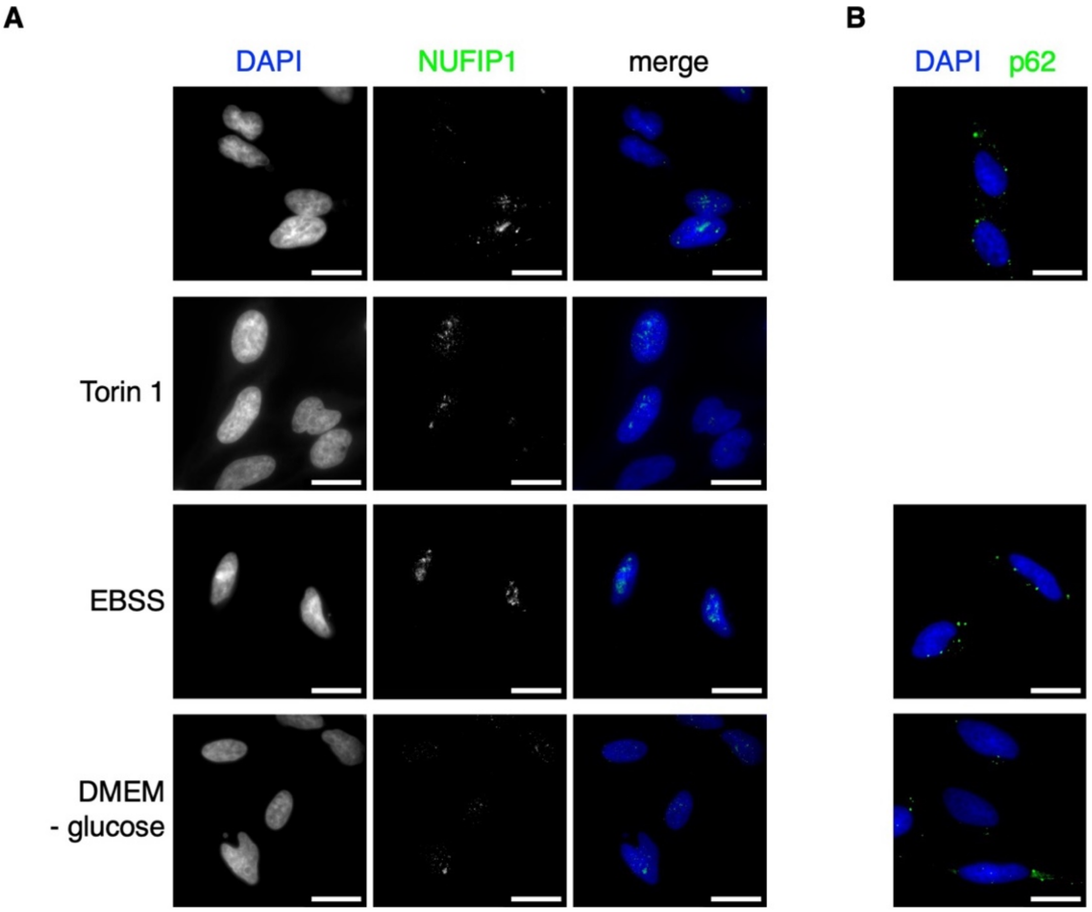

Figure 19: Immunofluorescence assay of endogenous NUFIP1
Representative images from immunofluorescence staining of NUFIP1 in **A** or p62 in **B** in HeLa cells. To induce autophagy either 250 nM of Torin 1 were added to the cells and incubated for 2 h or the full-medium was replaced by EBSS or DMEM medium without glucose and incubated for 4 h. Cells were fixed with methanol and subsequently stained with α-NUFIP1 or α-p62. The secondary antibody was coupled to Alexa488. 30 min before imaging, Hoechst 33342 was added to the cells to stain the DNA within the nucleus and allow localization of NUFIP1.

Since the immunofluorescence assay of endogenous NUFIP1 did not show the expected results, live-cell imaging by confocal fluorescence microscopy was performed to verify whether the antibody or fixation method had an influence on the results. HeLa cells were transfected with fluorescently labeled NUFIP1 constructs. The first construct was designed to investigate the co-localization of NUFIP1 with LC3B by simultaneously carrying the information for NUFIP1 coupled to the red fluorescent protein mCherry and LC3B coupled to a cyan fluorescent protein (CFP). Details of the employed fusion proteins are displayed in Figure 20A and Figure 20B. After transfection, cells were cultured for 24 h before imaging. To induce autophagy 250 nM Torin 1 were added to the cells for 2 h. Figure 20C shows the results of the live-cell imaging with the NUFIP1/LC3B construct. The majority of the mCherry signal, corresponding to NUFIP1, is located within the nucleus for both control and autophagy induced conditions. No translocation of NUFIP1 into the cytoplasm could be observed. The missing translocation of NUFIP1 consequently resulted in no observable overlap between NUFIP1 and cytoplasmic LC3B punctae. Although a few cells showed a fluorescence signal for NUFIP1-mCherry within the cytoplasm, the translocation was independent whether the cells were treated with Torin 1 or were of the control. Additionally, cells showing NUFIP1 signal in the cytoplasm appeared to be apoptotic. During apoptosis, the silent cell death, the nucleus disrupts into a few fragments (karyorrhexis) resulting in mixing of nuclear and cytoplasmic components (Bohm 2003) which could explain the fluorescence signal for NUFIP1-mCherry in the cytoplasm.

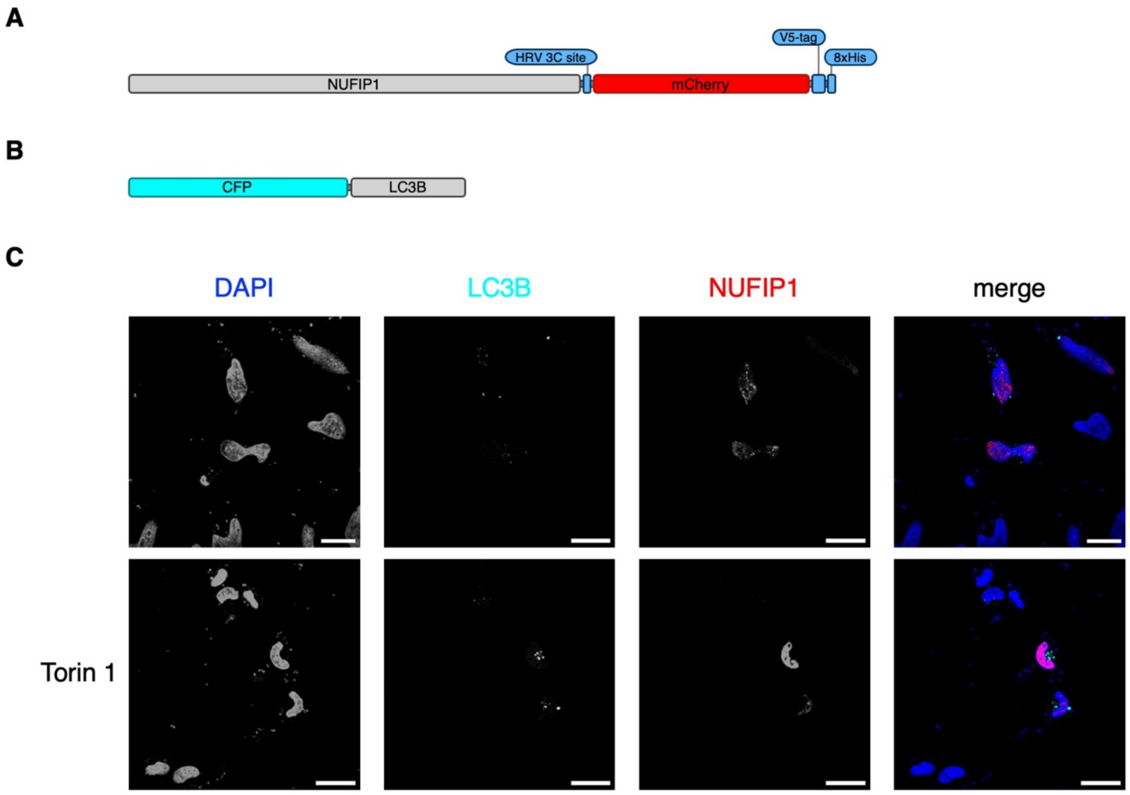

Figure 20: Live-cell imaging of fluorescently labeled NUFIP1
A: Domain architecture of recombinant NUFIP1 labeled with mCherry. **B:** Domain architecture of recombinant LC3B labeled with CFP. **C:** Representative images from live-cell imaging of HeLa cells transfected with fluorescently labeled NUFIP1 and LC3B. The DNA was stained with Hoechst 33342. NUFIP1-mCherry and CFP-LC3B were transfected into HeLa cells to observe localization in control and starvation-induced conditions (250 nM Torin 1, 2 h).

As a second live-cell imaging experiment, a NUFIP1 traffic light reporter was designed to assess the pH of the surrounding of NUFIP1. A tandem construct of NUFIP1 coupled to mCherry and a yellow fluorescent protein (YFP) can be used to probe the pH of the surrounding environment by looking at both emission signals independently (Rennick et al. 2022). The fluorescence signal of mCherry is stable even at low pH (as in lysosomes) while the fluorescence signal of YFP is bleached in these conditions (Li et al. 2024). The domain architecture of the NUFIP1 traffic light reporter is shown in Figure 21A. Fluorescence signal of mCherry and YFP was observed in the cytoplasm as well as the nucleus for both conditions tested (Torin 1 treated and control) (Figure 21B). As cytoplasmic localization could be observed in autophagy induced as well as control conditions, it remains elusive if in this case the induction of autophagy is the driving force for translocation.

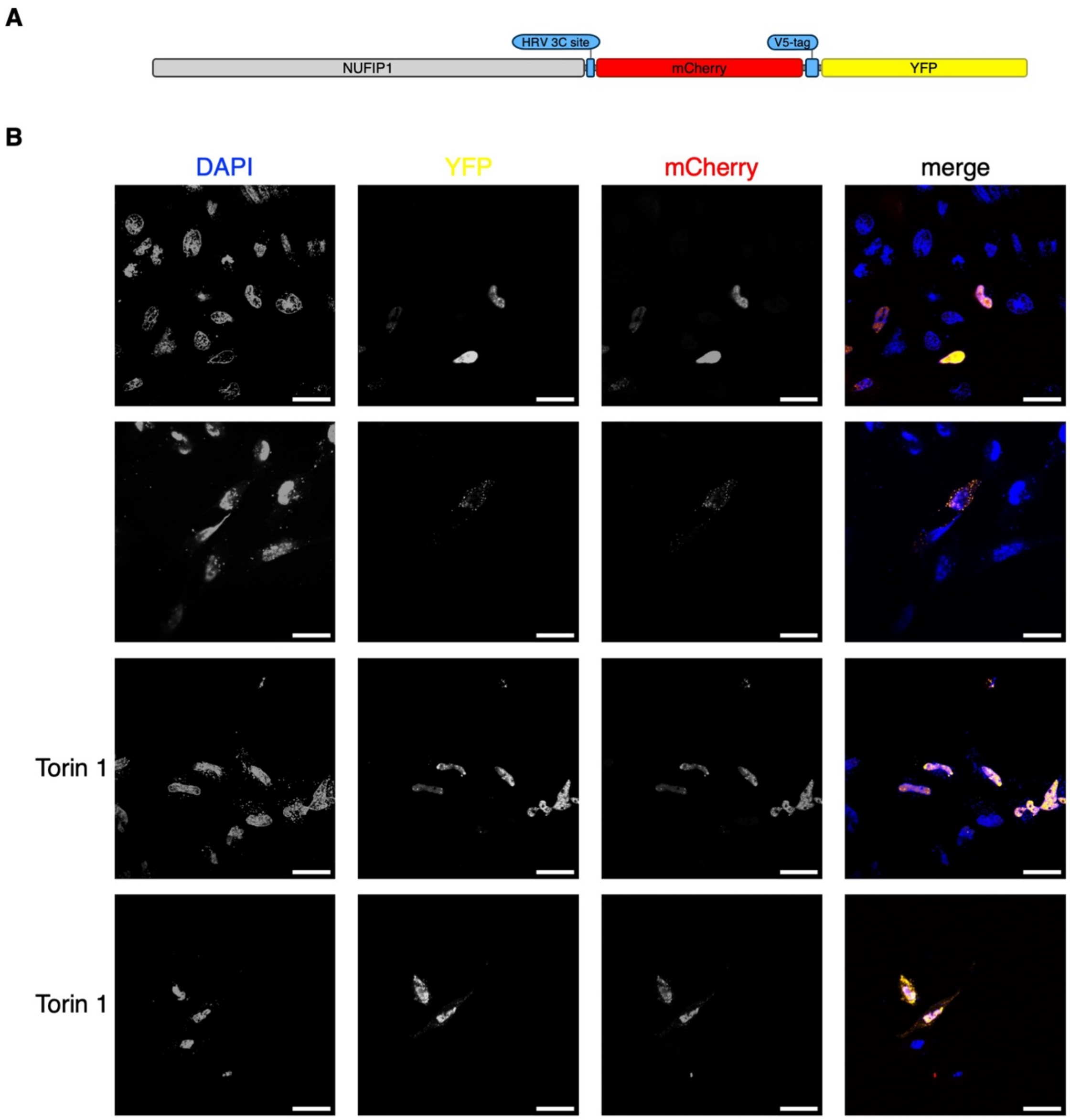

Figure 21: Live-cell imaging of NUFIP1 traffic light reporter
A: Domain architecture of recombinant NUFIP1 traffic light reporter. **B:** Representative images from live-cell imaging of HeLa cells transfected with fluorescently labeled NUFIP1 as shown in A and DNA stained with Hoechst 33342. The NUFIP1 traffic light reporter was transfected into HeLa cells to observe cellular localization in control and starvation-induced conditions (250 nM Torin 1, 2 h) as well as indication for local pH.

To further verify a possible lysosomal localization of the NUFIP1 traffic light reporter, a lysotracker dye was used to stain compartments with low pH including lysosomes. HeLa cells were transfected with the NUFIP1 traffic light reporter and stained with a lysotracker dye (Figure 22A). A co-localization of NUFIP1 traffic light reporter signal with the signal of the lysotracker dye would mean that NUFIP1 is degraded within the lysosomes. To probe co-localization, Figure 22B shows signal overlap for the indicated channels by displaying pixels as white if a signal in both channels was detected. The images for lysotracker dye with YFP or mCherry do not reveal co-localization. The control image of the traffic light reporter (mCherry with YFP) shows signal due to the inherent co-localization of the construct. As described for the NUFIP1/LC3B construct above, cells which displayed NUFIP1 fluorescence within the cytoplasm often had an apoptotic appearance impeding the interpretation of the results. The translocation of NUFIP1 to the cytoplasm and thereby a possible lysosomal co-localization could not be reproducibly controlled. To avoid a false positive interpretation of the results, the microenvironment of NUFIP1 traffic light reporter was not further analyzed regarding the pH.

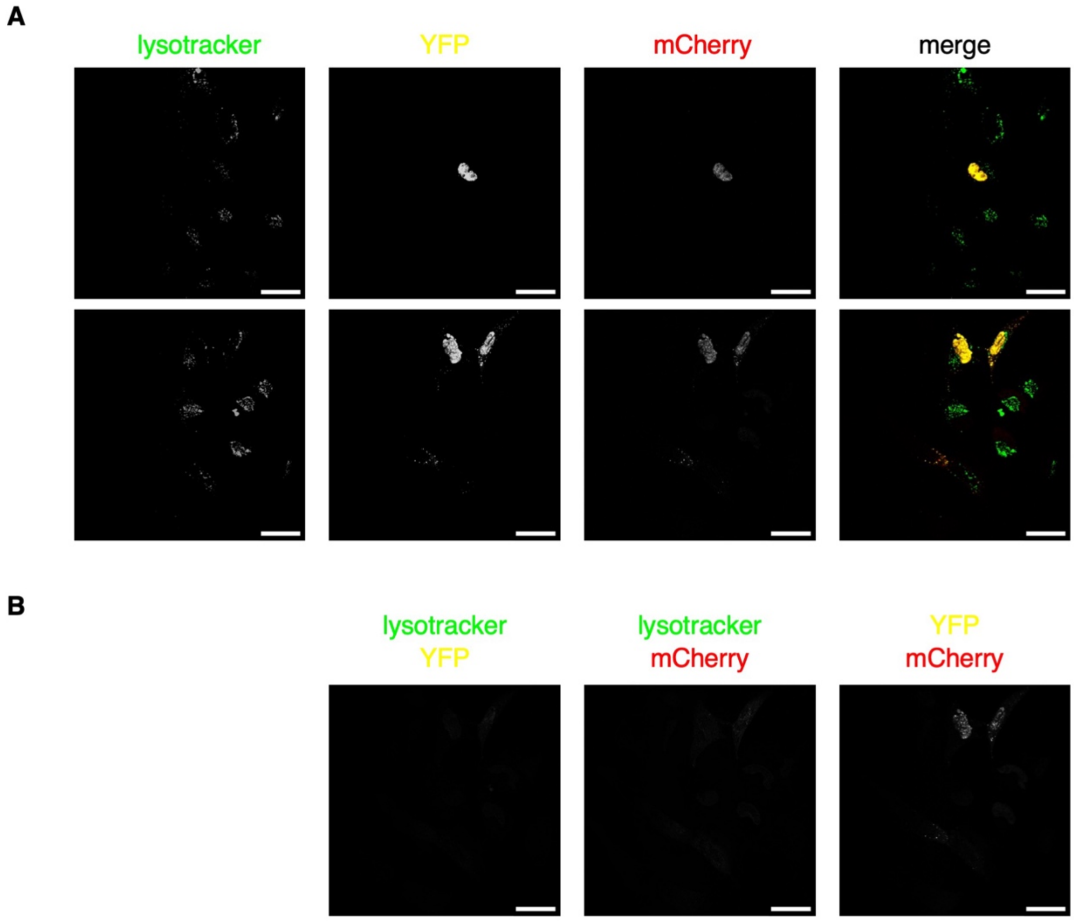

Figure 22: Live-cell imaging of NUFIP1 traffic light reporter with additional lysotracker dye
A: Representative images from live-cell imaging of HeLa cells transfected with fluorescently labeled NUFIP1 traffic light reporter. To investigate a possible co-localization, lysosomes were stained with a lysotracker dye. **B:** Co-localization of lysotracker dye with YFP or mCherry signal. Pixels with a positive signal in both indicated channels light up, while pixels with signal only in one channel remain black. YFP versus mCherry signal as control.

Translocation of NUFIP1 into the cytoplasm was described for starvation induced as well as cyclical mechanic stress conditions in the literature (Wyant et al. 2018;

Shim et al. 2019). In relation to autophagy, different conditions of nutrient depletion as well as the mTORC inhibitor Torin 1 were tested in this thesis to replicate the published results. Unfortunately, replication was not yet possible, neither in immunofluorescence assays nor for live-cell imaging. So far, no concluding remarks on the localization of NUFIP1 within the cell can be made from the fluoresecence imaging results. Although most of the fluorescently labeled NUFIP1 localized to the nucleus, small quantities of NUFIP1 could be observed within the cytoplasm in live-cell imaging. Unexpectedly, the translocation was independent of autophagy induction or control condition. Possible experimental reasons for this observation are that due to transfection stress, cells went into apoptosis resulting in disruption of the nucleus and releasing nuclear components into the cytoplasm. Or, due to excessive translation of the transfected plasmid DNA, thus an increased protein biosynthesis of NUFIP1 in the cytoplasm, inclusion bodies within the cytoplasm occurred resulting in fluorescent punctae. In their study, Wyant et al. used a transfection approach to express FLAG-tagged NUFIP1 in the cytoplasm which subsequently was detected with an α-FLAG antibody (Wyant et al. 2018). Under stress conditions this approach might lead to false positive results, as was most probably the case here since in the immunostaining of endogenous NUFIP1 no translocation could be observed in autophagy induced conditions.

3.1.2 Purification of recombinantly expressed NUFIP1

For structure determination by single-particle analysis, NUFIP1 needed to be overexpressed and purified. Recombinant MBP-NUFIP1 was overexpressed in FreeStyle^{TM} 293-F cells from a plasmid carrying an additional enhanced green fluorescent protein (eGFP) after an internal ribosomal entry site (IRES). In this case, NUFIP1 and eGFP were expressed as individual proteins. The details of the coding sequence are shown in Figure 23A. During cultivation, the protein expression was monitored with bright field (fluorescence) microscopy in which transfected and actively translating cells show a signal in the green fluorescent channel while non-transfected cells remain dark. In Figure 23B the difference between cell count and actively translating cells becomes visible as only a part of the cells light up with eGFP signal in the green fluorescent channel. Samples for SDS-PAGE and Western Blot analysis were taken during protein expression and analyzed with an α-NUFIP1 antibody. The Western Blot analysis confirmed that MBP-NUFIP1 was successfully expressed after transfection. The endogenous NUFIP1 concentration in the cells is much lower compared to transiently expressed MBP-NUFIP1, resulting in no signal in the Western Blot for endogenous NUFIP1 in the applied imaging conditions (Figure 23C).

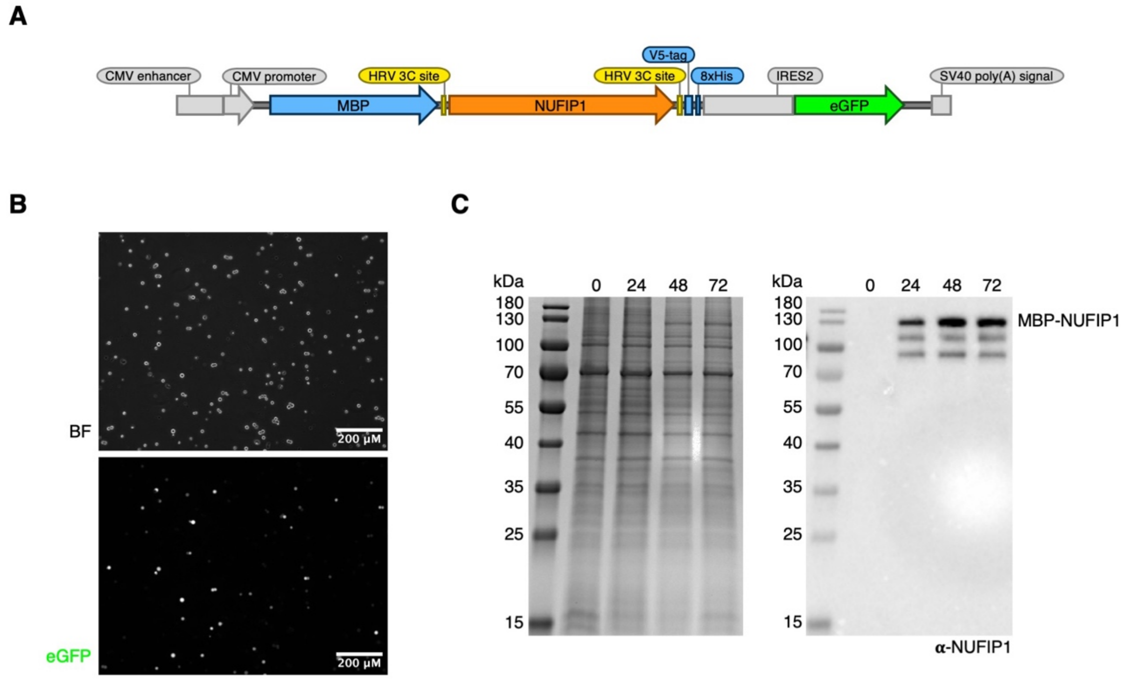

Figure 23: Transient protein expression of MBP-NUFIP1 in FreeStyle™ 293-F cells
MBP-NUFIP1 was transiently expressed in FreeStyle™ 293-F cells for 72 h. **A:** Expression construct of fusion protein MBP-NUFIP1 with internal ribosomal entry site and eGFP (DNA sequence level). **B:** Microscopy images of the cells 72 h after transfection in brightfield (BF) or green fluorescent channel (eGFP signal). **C:** Coomassie stained SDS-gel and immunospecific staining with α-NUFIP1 of expression culture samples before transfection and at 24, 48, 72 h post transfection.

As presented in the Results and Discussion section 3.1.1, NUFIP1 mainly localizes to the nucleus. Therefore, it was attempted to separate the nuclear from the cytoplasmic fraction in NUFIP1 purification. The idea was to identify the fraction with the highest purity and yield for NUFIP1. First, the nuclear fraction was separated from the cytoplasmic fraction by mild lysis in a glass Dounce homogenizer with a type A pestle. During this procedure the cell membrane is disrupted while the nuclei are kept intact. The intact nuclei were pelleted in a centrifugation step together with other cell debris while cytoplasmic proteins remained in the supernatant. The cytoplasmic fraction was further split into ribosomal fraction and soluble fraction by density gradient ultracentrifugation. Due to their high molecular weight, 80S ribosomes pellet through the high-density sucrose cushion while small soluble proteins remain in the supernatant. The nuclear fraction was subjected to a harsher lysis (glass Dounce homogenizer with a type B pestle) and cell debris removed by another centrifugation step to harvest soluble nuclear components. All three cellular fractions were individually used in MBP-affinity chromatography to enrich MBP-NUFIP1 or MBP-NUFIP1 bound ribosomes. Figure 24A is a schematic depiction of the purification workflow. The SDS-PAGE analysis of the elution fractions from the MBP-affinity chromatography clearly shows that MBP-NUFIP1 is present in all three cellular fractions with a different degree of purity (Figure 24B).

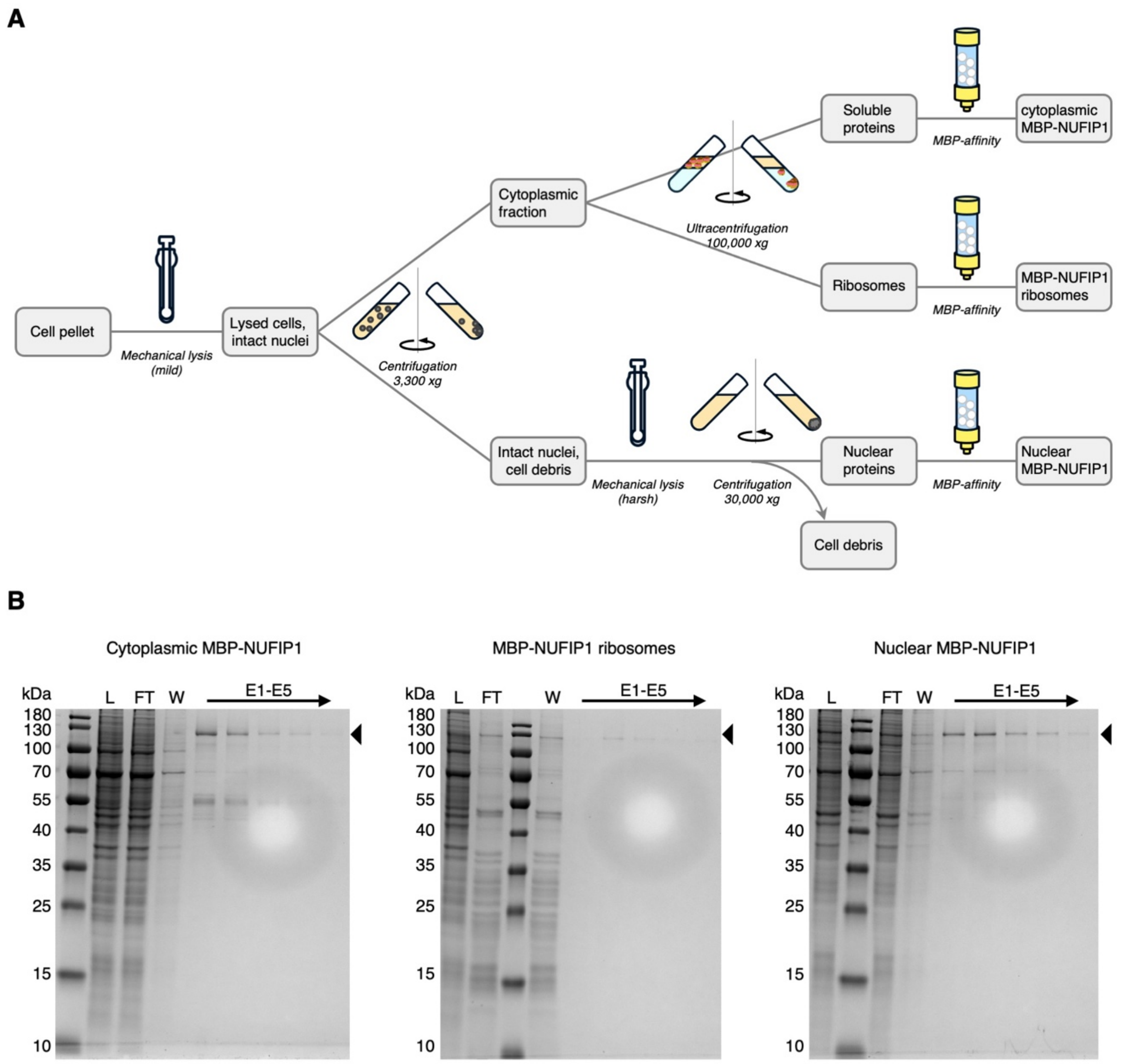

Figure 24: Purification of NUFIP1
A: Purification scheme for separation of nuclear, cytoplasmic and ribosomal MBP-NUFIP1 fractions. **B:** Coomassie stained SDS-gels of the MBP-affinity purification for all purification pathways with load (L), flow-through (FT), wash (W), and elution fractions (E).

The ribosomal fraction mainly contains ribosomes and has an RNA concentration of about 15.7 ng/µL in the peak fraction. The MBP-NUFIP1 concentration in the elution of the nuclear fraction is with 0.048 mg/mL in the peak fraction higher as for the cytoplasmic fraction with 0.034 mg/mL in the peak fraction. The protein or RNA concentration after MBP-affinity chromatography are listed in Table 2.

Table 2: NUFIP1 protein concentration after purification

Sample	A280	MBP-NUFIP1 [mg/mL]	A260	260/280	RNA [ng/µL]
Cytoplasmic MBP-NUFIP1					
E1	0.045	0.034		1.4	
E2	0.022	0.017		1.42	
E3	-0.002	-		-4.78	
E4	-0.021	-		-0.12	
E5	0.000	-		25.88	
MBP-NUFIP1 ribosomes					
E1			0.314	1.83	15.7
E2			0.084	1.34	4.2
E3			0.071	1.41	3.6
E4			0.086	1.45	4.3
E5			0.03	0.77	1.5
Nuclear MBP-NUFIP1					
E1	0.049	0.037		2.00	
E2	0.064	0.048		1.98	
E3	0.015	0.011		2.94	
E4	-0.001	-		-56.53	
E5	0.004	0.003		4.64	

Unfortunately, the here presented protein expression and purification approach did not yield a sample suitable for SPA because the protein concentration in the elution fractions of the MBP-affinity chromatography was too low. With an elution fraction volume of 3 mL and a protein concentration below 0.05 mg/mL or RNA concentration of 15.7 ng/µL, no grids could be prepared. Handling of full-length NUFIP1 in general turns out to be rather difficult as was described by Chagot et al.

as well (Chagot et al. 2022). A low amount of protein expression as well as protein instability with a strong tendency to aggregate *in vitro* make the purification of NUFIP1 a challenging task. The AlphaFold prediction of NUFIP1 shows a mainly disordered protein with only a few and short structured regions (Figure 11D). As NUFIP1 has no know sequence homolog with an experimentally solved structure within the PDB database, the low confidence regions within the AlphaFold model could be a result of missing training data. More probable is that NUFIP1 is indeed mainly disordered explaining the difficulties in handling. As NUFIP1 is part of different macromolecular complexes and capable of binding RNA and other proteins, NUFIP1 might need the presence of specific interactors to adopt a more structured fold. In summary, the current NUFIP1 preparations did not yield a suitable sample for structural studies due to its aggregation tendency, probably due to the inherent structural disorder. A more focused biochemical analysis on the solubility properties of NUFIP1 may yield conditions in which a suitable sample for SPA can be prepared.

3.1.3 Structural analysis of human 80S ribosomes in autophagy

As no pure samples of NUFIP1 could be prepared and the molecular structure of NUFIP1 and its interaction with 80S ribosomes remains elusive, 80S ribosomes were extracted from FreeStyle^{TM} 293-F cells from three different conditions for examination with SPA. The cells were either treated with 250 nM Torin 1 for 2 h, transfected with MBP-NUFIP1 72 h before harvest, or simply cultivated as per usual (control). After lysis, ribosomes were separated from cytoplasmic proteins by a density gradient ultracentrifugation. For MBP-NUFIP1 transfected cells, the ribosomal pellet was resuspended and applied to MBP-affinity chromatography to enrich ribosomes with MBP-NUFIP1 bound. The elution fractions of the MBP-affinity chromatography were concentrated by another ultracentrifugation step. For ribosomes from Torin 1 treated and control cells, MBP-affinity chromatography was replaced by a second density gradient ultracentrifugation with a higher sucrose concentration to pellet polysomes and obtain monosomes in the supernatant. The last ultracentrifugation was similar to MBP-NUFIP1 enriched ribosomes to concentrate the monosomes. The purification for MBP-NUFIP1 enriched ribosomes is schematically depicted in Figure 25A. The RNA concentration in the elution fractions of the MBP-affinity chromatography was followed by absorbance spectroscopy and the chromatogram is shown in Figure 25B. The presence of NUFIP1 in the elution of the MBP-affinity chromatography was confirmed with SDS-PAGE (Figure 25C). Negative stain electron microscopy of different samples was performed to ensure that ribosomes were still intact before vitrification (Figure 25D). The final concentrate of all samples was vitrified by plunge freezing at the Vitrobot Mark IV.

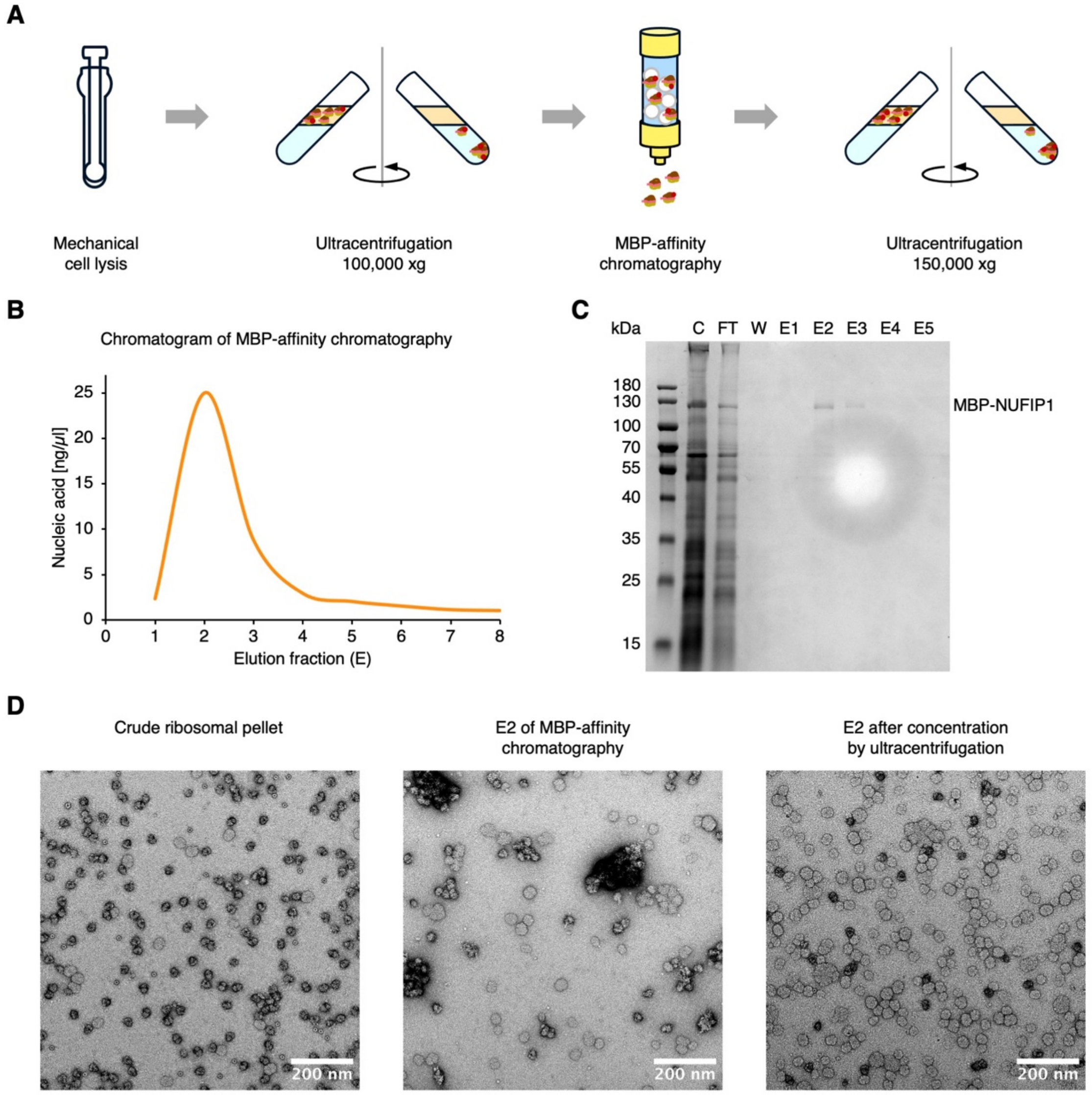

Figure 25: Purification of MBP-NUFIP1 enriched ribosomes for SPA
A: Purification scheme of the purification of MBP-NUFIP1 enriched ribosomes for SPA. **B:** Chromatogram of MBP-affinity chromatography of crude ribosome extract of MBP-NUFIP1 transfected FreeStyle™ 293-F cells. **C:** Coomassie stained SDS-gel of MBP-affinity chromatography with crude (C), flow-through (FT), wash (W), and elution fractions (E). **D:** Representative micrographs of negative stain EM of different ribosomal fractions collected during purification.

SPA datasets were collected at a Talos Arctica 200 kV instrument at 100,000x magnification with a varying defocus between -0.5 to -3.0 µm. With the standard single-particle image processing workflow implemented in CryoSPARC, a total of 213,379 (control), 159,189 (Torin 1), or 77,260 (MBP-NUFIP1 enriched) particles were included in a final three-dimensional reconstruction resulting in a global resolution of 3.1 Å (control), 3.1 Å (Torin 1), or 2.9 Å (MBP-NUFIP1 enriched) at FSC = 0.143 cutoff. Details of the data collection and data processing are listed in Table 3.

Table 3: SPA data collection of human 80S ribosomes

	Control	**Torin 1**	**MBP-NUFIP1**
Movies	3,693	2,688	6,419
Magnification	100,000x		
Voltage	200 kV		
Total dose ($e^-/Å^2$)	37	37	31
Defocus range	-0.5 to -3 µM		
Physical pixel size (Å)	0.8389		
Detector	K3 direct electron detector with BioQuantum energy filter		
Final no. of particles	213,379	159,189	77,260
Global map resolution (FSC = 0.143)	3.1 Å	3.1 Å	2.9 Å
Local map resolution range (FSC = 0.500)	3.1-4.7 Å	3.3-5.2 Å	2.9-5.1 Å

A representative micrograph of the MBP-NUFIP1 enriched dataset is shown in Figure 26A and the selected classes after two-dimensional classification are shown in Figure 26B. The FSC curves for all three samples are shown in Figure 26C. The high-resolution cryo-EM structure of the human 80S ribosome (PDB-ID: 6qzp, Natchiar et al. 2017) was docked into the EM-density maps. The model fits nicely into the EM-density maps of all three samples, following almost all the rRNA helices and protein backbones. Representative for all, the EM-density map of the control is shown in Figure 26D with the docked model. In yeast, Rpl25 was established to be involved in ribophagy (Kraft et al. 2008). The human homolog to the yeast protein Rpl25 is L23a. To elucidate whether a similar ubiquitination/deubiquitination mechanism for regulation of ribophagy as described for yeast is in place, the EM-density maps were investigated with a particular focus on L23a and compared to the human ribosome model (PDB-ID: 6qzp, Natchiar et al. 2017)). For the obtained maps no significant difference in the density of and around L23a could be observed (Figure 26E). Similarly, no additional density for NUFIP1 binding could be observed in the MBP-NUFIP1 enriched sample anywhere in the 80S.

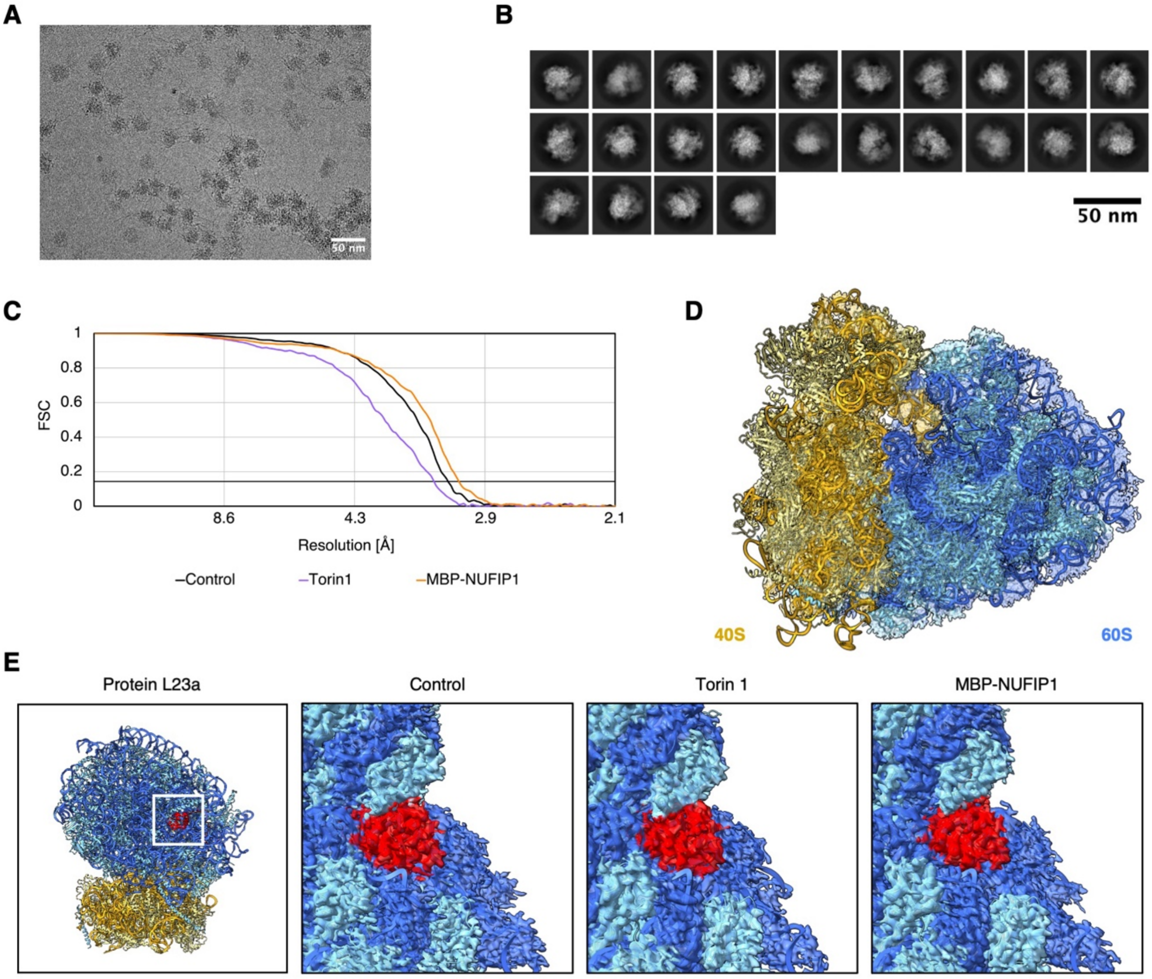

Figure 26: SPA of 80S human ribosomes
A: Representative micrograph of SPA data collection of MBP-NUFIP1 enriched ribosomes. **B:** Selected classes after two-dimensional classification of MBP-NUFIP1 enriched ribosomes. **C:** FSC of homogeneous refinement after ab-initio reconstruction of the control (black), Torin 1 treated (lilac) and MBP-NUFIP1 enriched ribosomes (orange). **D:** Fit of a human ribosomes model (PDB-ID: 6qzp, Natchiar et al. 2017) into the EM-density map of control 80S ribosomes after homogenous refinement. **E:** Zoom on the target protein L23a in the experimentally obtained EM-density maps.

The structure of 80S human ribosomes was investigated in the context of autophagy in regards to differences in starvation induced ribophagy. The focus on the L23a protein was based on the study of Kraft et al. for yeast 80S ribosomes, describing the pathway of ribophagy requiring the Ubp3p/Bre5p ubiquitin protease (Kraft et al. 2008). In yeast ribophagy, the Rpl25 protein is deubiquitinated to mark ribosomes for degradation via selective autophagy (Ossareh-Nazari et al. 2014). Although the ribosomes structures could be successfully visualized at 2.9 - 3.1 Å resolution, no difference between control and autophagy induced (by Torin 1) could be detected. Wyant et al. located the binding site of NUFIP1 as ribophagy receptor to the large subunit but could not specify it further (Wyant et al. 2018). Ribosomes of MBP-NUFIP1 transfected cells, which were enriched by an additional MBP-affinity step, did neither show any difference at L23a, nor anywhere else in the large subunit compared to control ribosomes. As overexpressed MBP-NUFIP1 is continuously translated within the cells and ribosomal subunits were not separated in purification, it is well possible, that the enrichment was due to active translation of MBP-NUFIP1 with a protein chain still attached rather than MBP-NUFIP1 bound. The here presented workflow, can be optimized by increasing the number of particles in data collection and performing a more thorough data processing. Recently described in the literature, was the ribophagy of polyubiquitinated ribosomes in oncogene-induced senescence by p62 (López et al. 2023). The data presented here, do not allow any conclusions on these matters, as the small subunit is rather badly resolved and the focus was set to L23a. Further, ribosomes were extracted from the FreeStyle™ 293-F cell line that does not go into senescence, and, therefore, should not display polyubiquitination as described by López et al. (López et al. 2023).

As NUFIP1's function in selective autophagy is still very vague due to missing experimental data, first, a more complex biochemical analysis of NUFIP1's binding to ribosomes and RNA in general needs to be performed. Based on the results, a more detailed description of NUFIP1's involvement in selective autophagy and ribophagy in particular can follow. If a binding site on the 80S ribosome can be identified, a more sophisticated cryo-EM workflow can be applied to focus the structure refinement towards this site of the ribosome. The workflow presented in this thesis only uses a limited amount of particles for structure determination. An increase in particle number can lead to the identification of different conformations, as the presence of less populated conformations need to exceed a certain threshold to become detectable. Additionally, a better understanding of NUFIP1's binding partners can result in the evidence needed to create more suitable conditions for protein expression and, especially, purification. With a stabilizing binding partner, NUFIP1 may be purified in a quantity suitable for cryo-EM structure determination. If no suitable binding partner can be identified, nanobodies could serve to enhance stability of NUFIP1 for cryo-EM. Last, with extended biochemical data, truncation versions of NUFIP1 might be designed to study the single domains of the protein individually first.

3.2 The selective autophagy receptor p62

3.2.1 Protein expression and purification

In order to study the structural mechanism of p62 selective autophagy, the p62, LC3B and GST-4xUbiquitin proteins were recombinantly overexpressed and purified. p62 was expressed as MBP-fusion protein in *E. coli* BL21(DE3) from pETM43 vector to enhance solubility and allow affinity chromatography purification. Details of the protein construct are shown in Figure 27A. After mechanical cell lysis, purification of MBP-p62 was performed by immobilized metal ion affinity chromatography (IMAC), a consecutive MBP-affinity chromatography, and a final desalting chromatography. All fractions were analyzed with SDS-PAGE and the results are shown in Figure 27B.

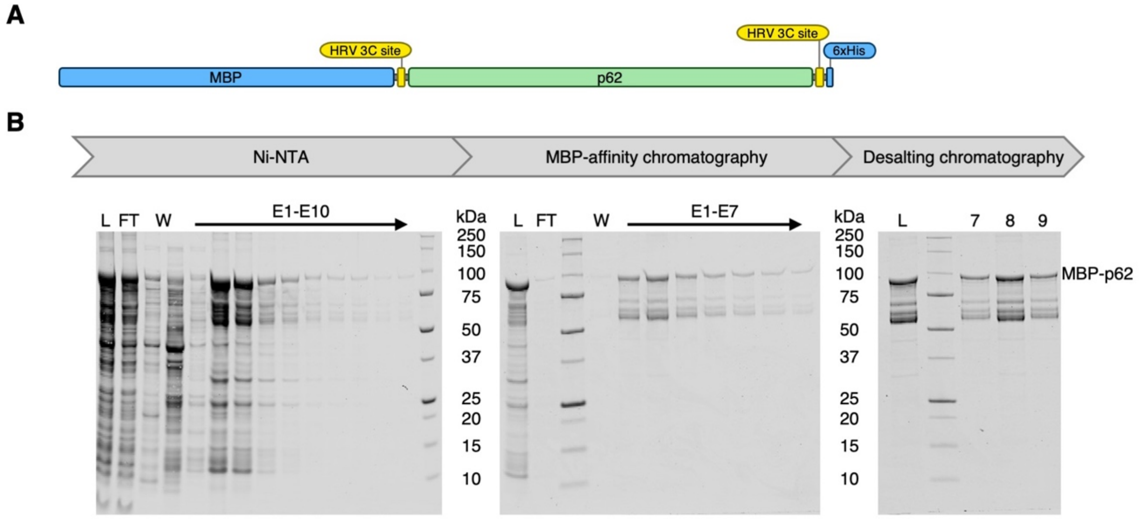

Figure 27: Purification of MBP-p62
A: Domain architecture of recombinant MBP-p62 fusion protein. **B:** Coomassie stained SDS-gels of MBP-p62 fusion protein purification with load (L), flow-through (FT), wash (W), and elution fractions (E).

A second expression construct including the fluorescent mCherry-tag was expressed in an identical manner to MBP-p62; details of the construct are shown in Figure 28A. In contrast to MBP-p62, after IMAC, MBP-mCherry-p62 was further purified by preparative size exclusion chromatography (SEC) (Figure 28B and Figure 28C).

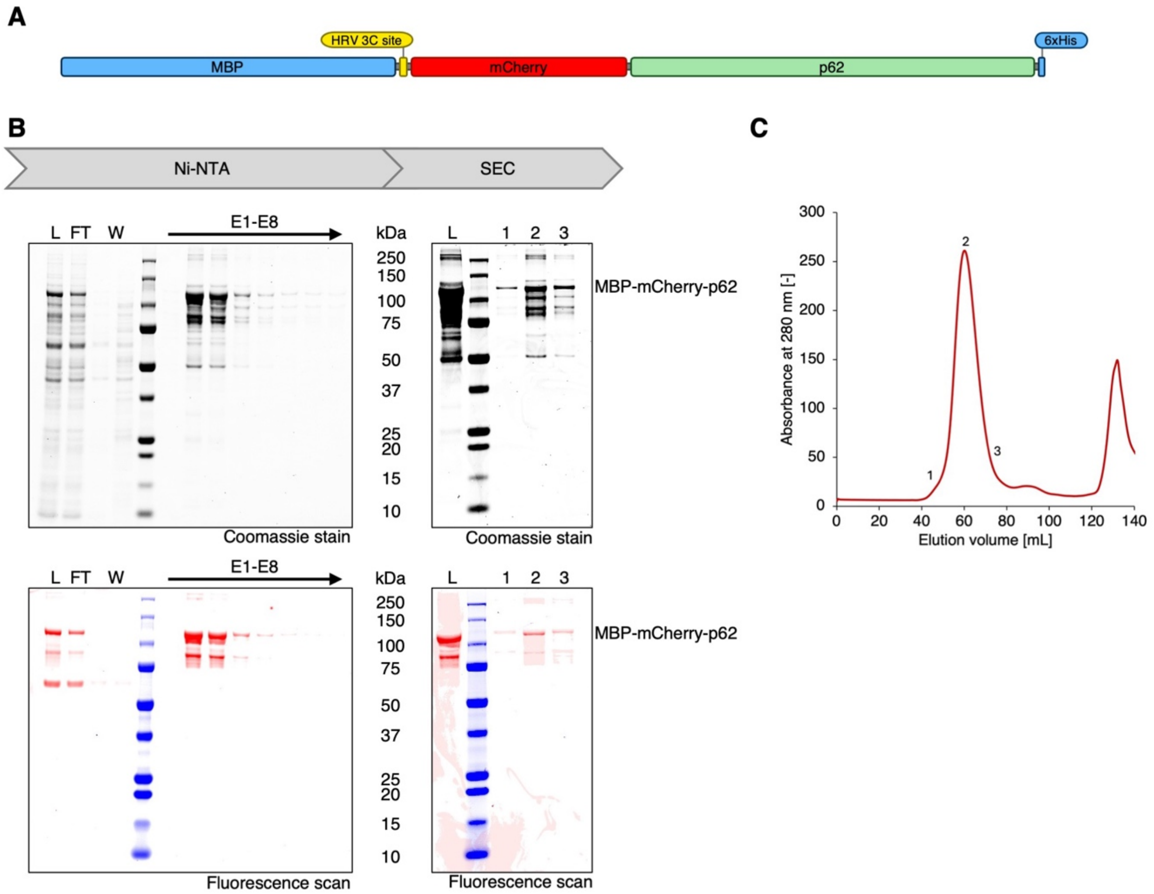

Figure 28: Purification of MBP-mCherry-p62
A: Domain architecture of recombinant MBP-mCherry-p62 fusion protein. **B:** Coomassie stain and fluorescence scans of the same SDS-gels of MBP-mCherry-p62 fusion protein purification with load (L), flow-through (FT), wash (W), and elution fractions (E). **C:** Chromatogram of size exclusion chromatography of MBP-mCherry-p62 fusion protein.

Purified MBP-p62 and MBP-mCherry-p62 were concentrated to about 1 mg/mL and the solubility MBP-tag removed by HRV3C protease digestion to induce polymerization. The success of the protease digestion was confirmed by SDS-PAGE (Figure 29A for MBP-p62 and Figure 29B for MBP-mCherry-p62). To remove the protease and cleaved MBP-tag, the digestion reactions were centrifuged at 20,800 xg and the supernatant decanted. The pellets containing p62 or mCherry-p62 were resuspended and negatively stained. Negative stain electron microscopy was performed to access the quality of the expected p62 filaments. While helical filament formation worked well for p62 (Figure 29C), mCherry-p62 shows only very short assemblies (Figure 29D).

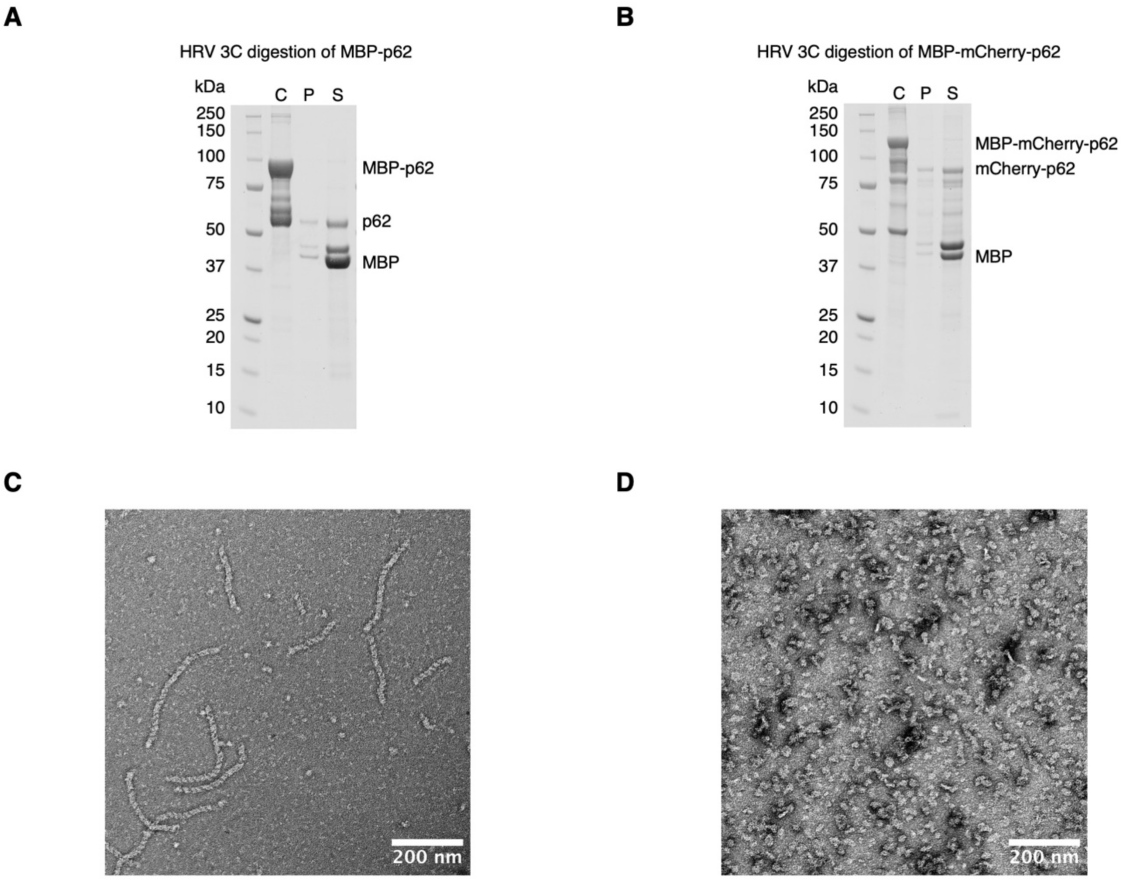

Figure 29: HRV3C digestion of MBP-p62 and MBP-mCherry-p62
A: Coomassie stained SDS-gel of the HRV3C digestion of MBP-p62 with concentrate (C), pellet (P), and supernatant (S). **B:** Coomassie stained SDS-gel of the HRV3C digestion of MBP-mCherry-p62 with concentrate (C), pellet (P), and supernatant (S). **C:** Representative micrograph of negative stain EM of the pellet of p62. **D:** Representative micrograph of negative stain EM of the pellet of mCherry-p62.

In addition to p62 and mCherry-p62, the p62 interactors LC3B and Ubiquitin were expressed and purified. The different LC3B variants and linear 4xUbiquitin were recombinantly expressed as GST-fusion proteins in *E. coli* BL21(DE3) and successfully purified by GST-affinity chromatography with subsequent size exclusion chromatography. To remove the GST-tag from LC3B, the fusion protein was digested with GST-HRV3C. After digestion, the GST-tag and GST-HRV3C were removed by GST-affinity chromatography in which LC3B was collected from the flow through. Details of the three different LC3B variants used in this thesis are shown in Figure 30A. LC3B, thereby, corresponds to the human wildtype version before cleavage. LC3B-Cys corresponds to human wildtype LC3B-I with an additional cysteine at the C-terminus. An enhanced p62 binding variant obtained from Andreas Ernst, here called LC3Be, carries several mutations which increase the affinity to the LIR motif of p62 (Putyrski et al. 2020). An exemplary digestion reaction and subsequent clean-up for GST-LC3B is shown in Figure 30B.

For phase separation experiments, GST-4xUbiquitin was covalently labeled with Alexa488 via a maleimide modification of cysteine. After labeling, free dye was removed by a 2 mL Zeba™ Dye and Biotin Removal Spin Column. The protein was analyzed by SDS-PAGE before and after labeling and the SDS-gel is shown in Figure 30C as fluorescent scan and Coomassie stain. The SDS-gel confirms that labeling with Alexa488 was successful.

A

	1 … 50
LC3B	MPSEKTFKQRRTFEQRVEDVRLIREQHPTKIPVIIERYKGEKQLPVLDKT
LC3B-Cys	MPSEKTFKQRRTFEQRVEDVRLIREQHPTKIPVIIERYKGEKQLPVLDKT
LC3Be	MPSEKTFKQRRTFEQRVEDVRL**A**RE**LY**PTKIPVIIERYKGEKQLPVLDKT
	* * *
	51 … 100
LC3B	KFLVPDHVNMSELIKIIRRRLQLNANQAFFLLVNGHSMVSVSTPISEVYE
LC3B-Cys	KFLVPDHVNMSELIKIIRRRLQLNANQAFFLLVNGHSMVSVSTPISEVYE
LC3Be	KFLVPDHVNMSELIKIIRRRLQLNANQAFFLLVNGHSMVSVSTPISEVYE
	101 … 125
LC3B	SEKDEDGFLYMVYASQETFGMKLSV
LC3B-Cys	SEKDEDGFLYMVYASQETFG**C**
	*
LC3Be	SEKDEDGFLYMVYASQETFG

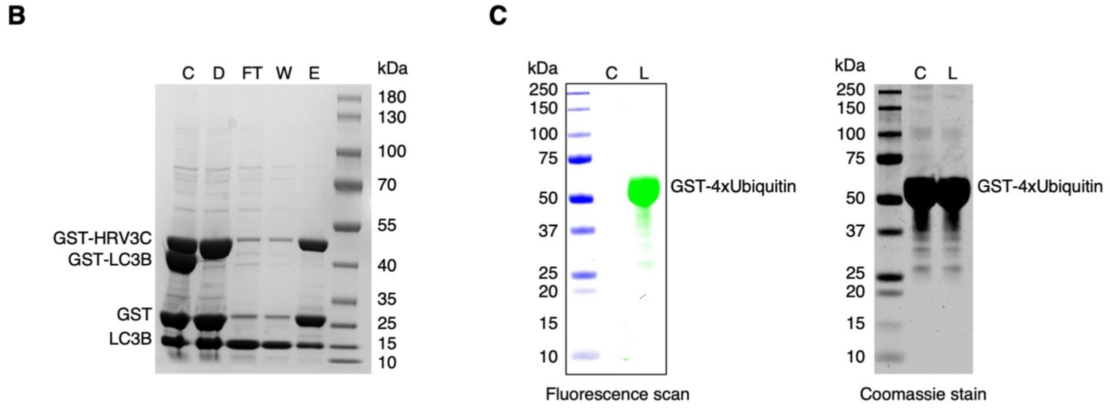

Figure 30: Preparation of LC3B variants and labeled GST-4xUbiquitin
A: Amino acid sequence of LC3B, LC3Be, and LC3B-Cys. Amino acid mutations are highlighted in red and marked with a *. **B:** Coomassie stained SDS-gel of GST-LC3B HRV3C digestion and subsequent purification of LC3B with digestion reaction at t = 0 (D) and after digestion (D), flow-through (FT), wash (W) and elution fractions (E) of GST-affinity chromatography. For further experiments the FT was picked. **C:** Fluorescence scan and Coomassie stain of the same SDS-gel with GST-4xUbiquitin before (C) and after labeling with Alexa488 (L).

The ratio between labeled and unlabeled GST-4xUbiquitin was determined by absorbance spectrophotometry. First, the protein concentration was determined by absorbance spectroscopy at 280 nm and second the concentration of the Alexa488 dye was measured by the absorbance at 488 nm utilizing a NanoDrop Microvolume Spectrophotometer. The respective concentrations in µM were calculated by applying the Lambert-Beer-Law as described in the Material and Methods section 5.6.1. The resulting concentration ratio of Alexa488 [µM] to protein [µM] was 0.26, indicating that 26% of the protein molecules were labeled assuming that one cysteine was labeled per GST-4xUbiquitin molecule (Table 4).

Table 4: Ratio of labeled GST-4xUbiquitin

Absorbance 280 nm	**GST-4xUbiquitin [µM]**	**Absorbance 488 nm**	**Alexa488 [µM]**	**Alexa488 : GST-4xUbiquitin**
2.671	53.09	0.983	13.8	
2.766	54.98	1.003	14.1	
2.678	53.41	0.998	14.1	
	53.82		**14.0**	**26%**

3.2.2 Preparation of LC3B-Cys covered liposomes

For structural characterization of p62 with phagophore membranes, liposomes containing 5% maleimide-DSPE were prepared exploiting the maleimide modification of cysteine to cover them with LC3B-Cys. Additionally, to determine the lipid concentration after the final purification step, 0.01% of Atto390-PE were added to the lipid mixture. Liposomes were extruded to a size of 50 nm and incubated with LC3B-Cys for 2 h at room temperature and, subsequently, overnight at 4°C (without mixing). To remove unbound protein, liposomes were loaded onto a Sephacryl S-500 size exclusion column. For easy identification of the elution fractions containing the covered liposomes or free protein, the absorbance in the elution was monitored at 280 nm (protein) and 390 nm (Atto390-PE). The modification and purification workflow is schematically depicted in Figure 31A with a focus on the thioether bond formation between the maleimide group and cysteine residue. The chromatogram of the size exclusion chromatography is shown in Figure 31B. In the chromatogram two peaks can be observed corresponding to the covered liposomes (P1) and free protein (P2). A near baseline separation between covered liposomes and free protein peak could be achieved. To confirm the presence of LC3B-Cys in the liposomal fraction, SDS-PAGE analysis of P1 was performed (Figure 31C).

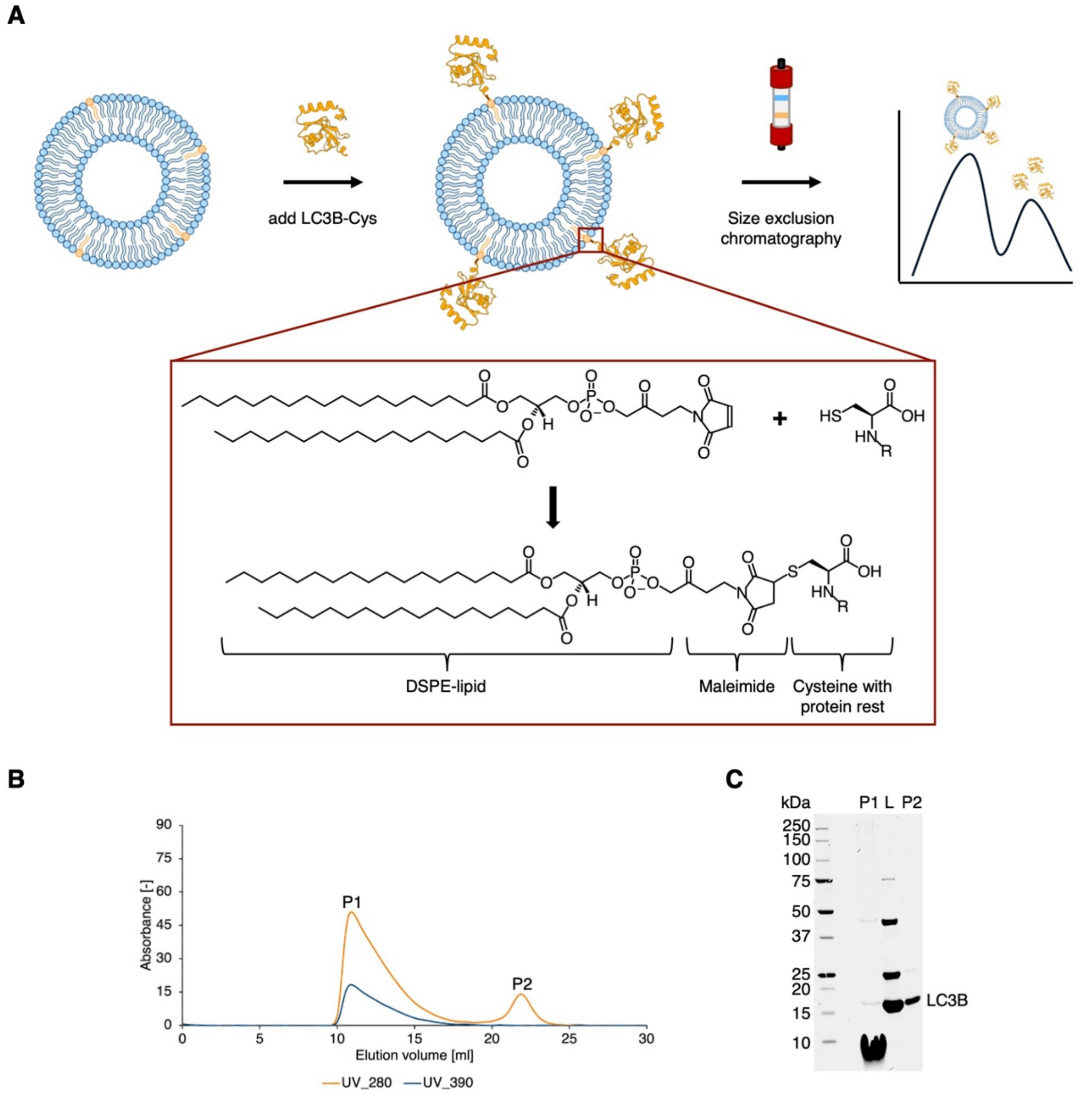

Figure 31: Preparation of LC3B-Cys covered liposomes
A: Schematic workflow of covering and purifying liposomes with LC3B-Cys. **B:** Chromatogram of size exclusion chromatography after cysteine modification of LC3B-Cys with maleimide-DSPE spiked liposomes. The absorbance in the elution was measured at 280 nm (protein specific) and 390 nm (Atto390-PE specific). **C:** Coomassie stained SDS-gel of size exclusion chromatography of LC3B-Cys covered liposomes with the first peak (P1), load (L), and second peak (P2).

To determine the lipid concentration after size exclusion chromatography and thereby the concentration of DSPE-maleimide and bound protein, the fluorescence signal of Atto390-PE was measured. A calibration curve was prepared by detecting the emission level of different dilutions with known concentrations beforehand. The dilutions were prepared from the liposome extrusion before modification. The emission was measured at 460 nm after excitation at 360 nm. The emission was plotted over the concentration and a linear fit was applied to obtain the calibration curve (Figure 32). The P1 peak fraction of the size exclusion chromatography was diluted, and the emission measured similarly as for the calibration curve. The emission signal of the P1 peak fraction was inserted into the linear fit of the calibration curve to retrieve the lipid concentration after size exclusion chromatography: 2.6 mg/mL total lipids with 118 µM maleimide-DSPE, respectively. The concentrations of the total lipids and maleimide-DSPE after size exclusion chromatography are listed in Table 5.

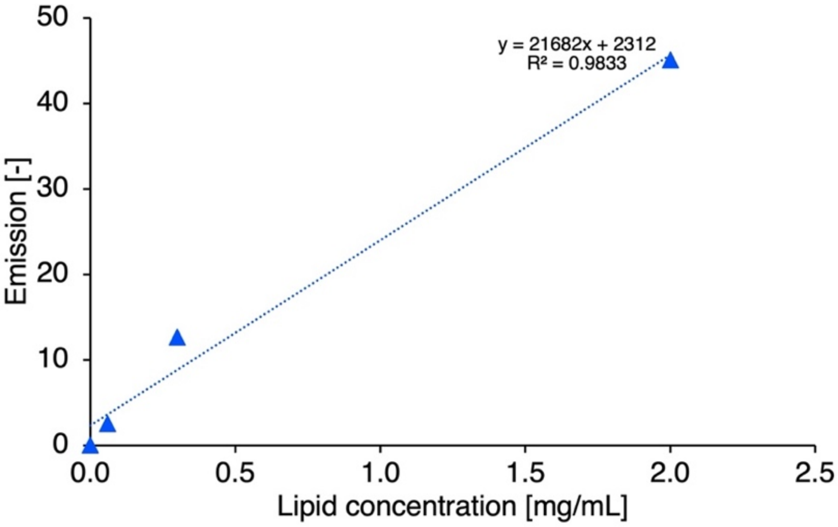

Figure 32: Calibration curve to determine the lipid concentration after size exclusion chromatography
From the initial resuspension of the lipid mixture after extrusion a calibration curve was prepared. The fluorescence emission after excitation at 390 nm was measured at 460 nm for Atto390-PE of different dilutions and plotted over the concentration. A linear fit was applied.

Table 5: Concentration of lipids after size exclusion chromatography

	Concentration total lipids	Concentration maleimide-DSPE
LC3B	2.6 mg/mL	118 µM

3.2.3 Biochemical characterization of LC3B binding to p62 filaments

Previous experiments indicated that LC3Be is able to shorten and, in high molar excess, dissolve p62 filaments (Mostafavi 2022). To extend the results to the biological more relevant LC3B, a binding assay with structural analysis by negative stain electron microscopy was performed. Beforehand, to ensure biological active proteins after purification, a pull-down experiment of MBP-p62 or MBP-mCherry-p62 by LC3B and LC3Be was performed. Similar experiments have been described in the literature (Wurzer et al. 2015; Zaffagnini et al. 2018). The GST-fusion proteins of LC3B or LC3Be were immobilized on GST-affinity material and incubated with MBP-p62 or MBP-mCherry-p62. Excess protein was washed off and bound proteins eluted. The elution fraction was analyzed by SDS-PAGE (Figure 33A and Figure 33B). The intensities of the full-length bands in the image for MBP-p62 or MBP-mCherry-p62 were analyzed as the intensity in the image is linearly related to the concentration in the sample (Figure 33C and Figure 33D). The band intensity and therefore the concentration of MBP-p2 or MBP-mCherry-p62 retained by GST-LC3B was set to 100%, and the other put in relation to it. (No absolute concentrations were analyzed.) For both, MBP-p62 and MBP-mCherry-p62, the highest retention was obtained by GST-LC3Be with approximately 11% for MBP-p62 and 15% for MBP-mCherry-p62 more retained protein compared to GST-LC3B. The controls for GST only and blank GST-affinity material show significantly less retention compared to GST-LC3B and GST-LC3Be.

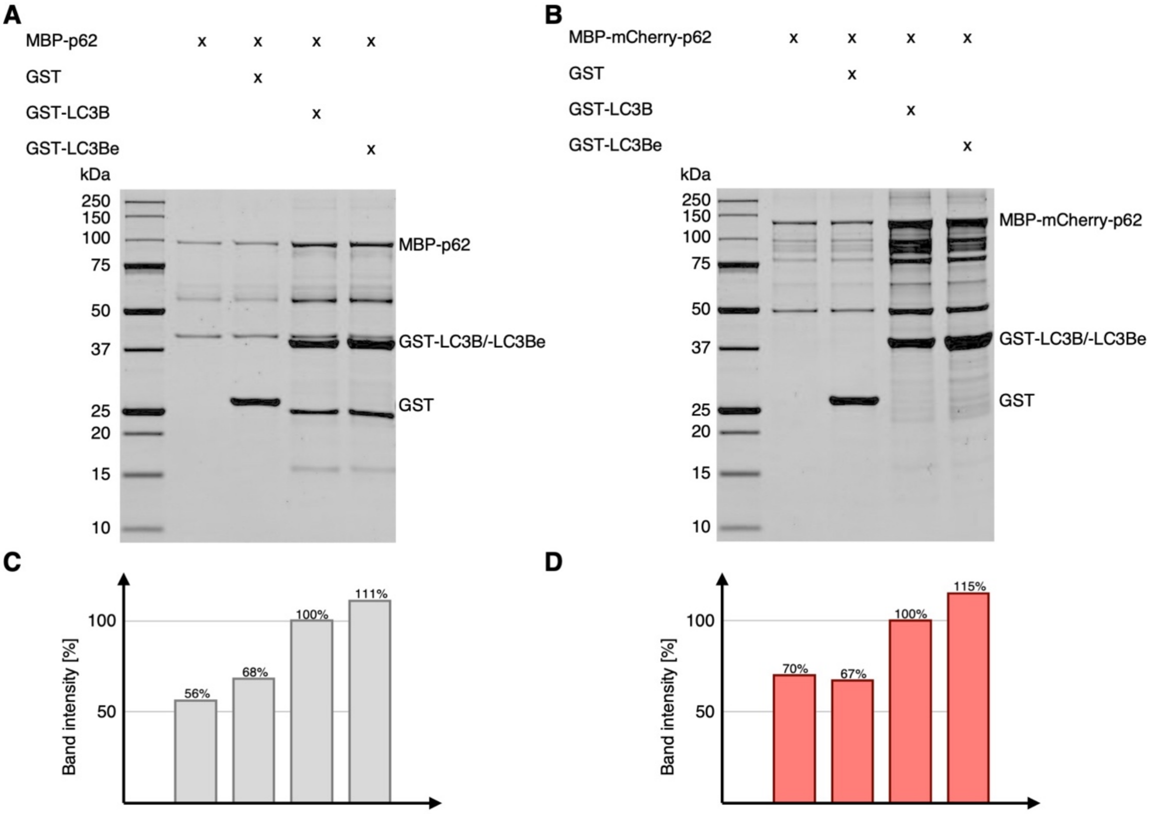

Figure 33: Pull-down of MBP-p62 or MBP-mCherry-p62 by LC3B and LC3Be
A: Coomassie stained SDS-gel of pull-down experiment of MBP-p62 with immobilized GST-LC3B or GST-LC3Be. **B:** Coomassie stained SDS-gel of pull-down experiment of MBP-mCherry-p62 with immobilized GST-LC3B or GST-LC3Be. **C:** Quantification of the band intensity for MBP-p62 in the image relative to the band intensity of MBP-p62 in the image retained by GST-LC3B. **D:** Quantification of the band intensity for MBP-mCherry-p62 in the image relative to the band intensity of MBP-mCherry-p62 in the image retained by GST-LC3B.

To compare the influence of LC3B and LC3Be on p62 filaments, p62 filaments were mixed with different LC3B or LC3Be concentrations ranging from 0.5 – 4x molar excess. As a control, the sample buffer of LC3B/LC3Be was added. The samples were incubated for 30 min at room temperature and subsequently stained. Negatively stained grids were imaged at a Talos L120C 120 kV instrument. Representative images for each sample are shown in Figure 34. The remaining sample after staining was analyzed by SDS-PAGE. The SDS-gels show the difference in LC3B or LC3Be concentration clearly (Figure 34). Filamentous p62 could be observed in all conditions tested, no disassembly of p62 filaments could be confirmed in this experimental set-up.

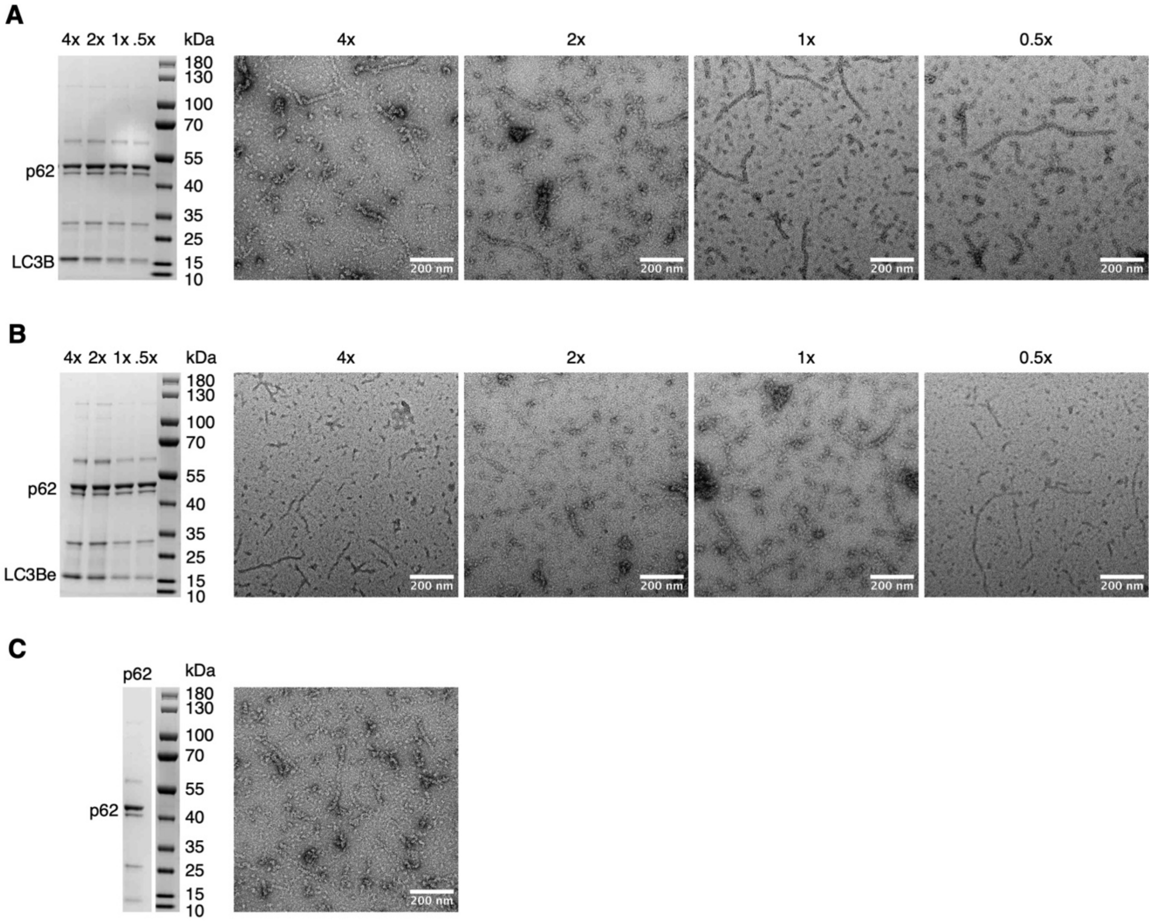

Figure 34: Binding of LC3B and LC3Be to p62 filaments
Coomassie stained SDS-gel and representative negative stain EM micrographs of p62 filaments with LC3B in **A**, p62 filaments with LC3Be in **B**, and p62 filaments with buffer in **C**. The molar excess of LC3B or LC3Be to p62 is indicated above the lanes in the SDS-gel and above the respective micrographs.

3.2.4 Cryogenic electron tomography of p62 filaments with LC3B covered liposomes

To investigate the possible interaction of p62 in autophagy with growing phagophore membranes a simplified *in vitro* system was designed consisting of purified p62 filaments and LC3B covered liposomes. As described in the Results and Discussion section 3.2.2, the liposomes were covered with LC3B-Cys via a chemical modification of cysteine by maleimide-DSPE. The modified liposomes (118 µM maleimide lipid) were mixed with p62 filaments (12 µM) to a final ratio of 4.5 µM p62 filaments to 73.8 µM maleimide lipid (approximately 1:16). The sample was incubated for 10 min at 4°C and plunge frozen with an EM GP2 Automatic Plunge Freezer. Tomograms were collected at a Titan Krios 300 kV instrument at 64,000x magnification with a defocus variation between -2.0 to -4.0 µm. The raw micrographs were motion corrected with WARP, and CTF estimation and image stack creation were also performed in WARP. The subsequent data processing was performed according to the scheme depicted in Figure 35.

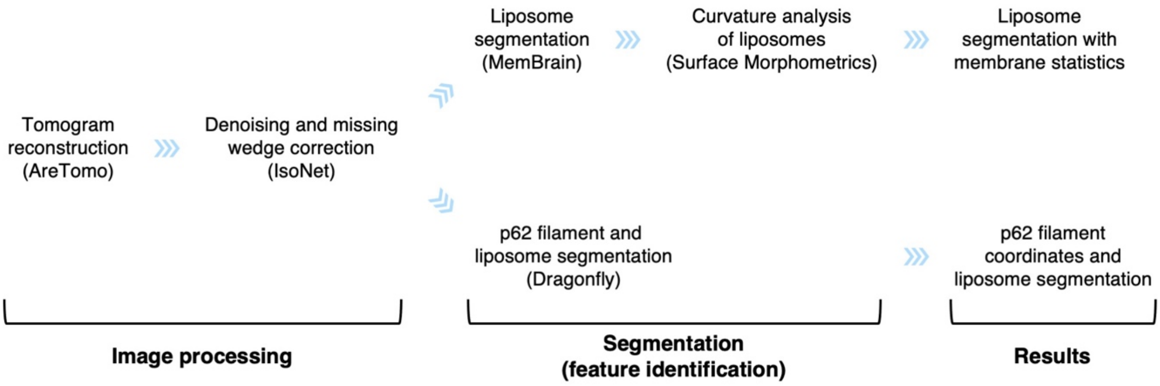

Figure 35: Data processing workflow of tomograms collected on p62 filaments with LC3B covered liposomes
Data processing workflow of micrographs collected on p62 filaments mixed with LC3B covered liposomes. Pre-processing was performed in WARP (not shown), tomograms were reconstructed with AreTomo. Denoising and missing wedge correction was performed with IsoNet. Segmentation of liposomal membranes was performed with MemBrain. The MemBrain segmentation was analyzed with Surface Morphometrics regarding membrane curvature. Segmentation of p62 filaments and liposomal membranes was performed in Dragonfly.

The three-dimensional reconstruction of the tomograms was performed in AreTomo and reconstructed tomograms denoised and missing wedge corrected with IsoNet. The results of a representative tomogram reconstruction and IsoNet denoising and missing wedge correction are shown in Figure 36, with Figure 36A being the reconstructed and Figure 36B being the corrected tomogram. An enhancement in contrast for both, p62 filaments and liposomal membranes, is clearly visible in the corrected tomogram, as well as a smoother background compared to the uncorrected tomogram (Figure 36B). To identify and segment p62 filaments and liposomal membranes, Dragonfly was used. The final segmentation is shown in Figure 36C with p62 filaments colored in yellow and liposomal membranes colored in blue. A slice through the segmentation is shown in Figure 36D highlighting how p62 filaments can wrap around liposomes and how one p62 filaments can interact with multiple liposomes at a time. For liposomal membrane segmentation only, MemBrain was used, and, subsequently, the segmentation results were analyzed with Surface Morphometrics regarding membrane curvature. The curvature analysis is shown in Figure 36D. No remarkable differences in curvature between liposomes surrounded by p62 filaments and stand-alone liposomes in the tomogram could be confirmed.

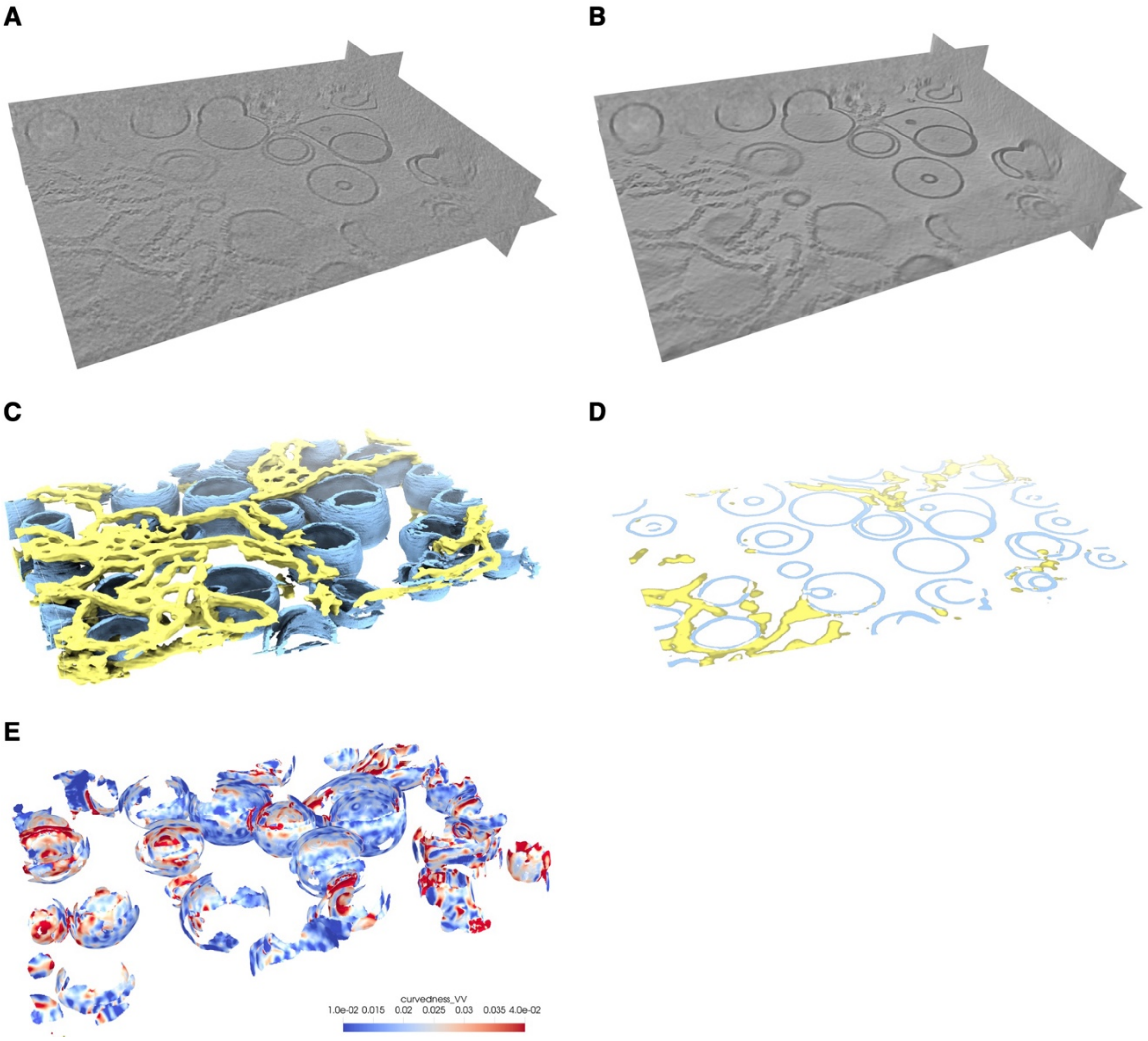

Figure 36: Cryogenic electron tomography of p62 filaments with LC3B covered liposomes
A: Representative tomogram of p62 filaments and LC3B covered liposomes. **B:** The same tomogram as shown in A after IsoNet denoising and missing wedge correction. **C:** Dragonfly segmentation of the tomogram with liposomes displayed in blue and p62 filaments displayed in yellow. **D:** Slice through the Dragonfly segmentation of the tomogram displayed in C. **E:** MemBrain segmentation displayed with Surface Morphometrics curvature analysis.

3.2.5 *In vitro* phase separation of p62 filaments by polyubiquitin

Phase separation of p62 by polyubiquitin (here GST-4xUbiquitin) has been described in the literature (Zaffagnini et al. 2018). In the literature the phase separation is usually observed by fluorescently labeling p62 with a fluorescent protein domain, e.g. GFP or mCherry. During protein purification the different biochemical behavior of mCherry-p62 to p62 was observed, especially in regards to filament formation. To investigate the phase separation properties of wildtype p62, p62 filaments were prepared and mixed with Alexa488 labeled GST-4xUbiquitin. Four different conditions were tested and in all containing p62 filaments fluorescent punctae emerged (Figure 37A). Dependent on the molar ratio between p62 filaments and Alexa488 labeled GST-4xUbiquitin, the punctae grew larger in size with increasing p62 filament concentration (Figure 37A). 1,6-Hexanediol was used to probe if the observed fluorescent punctae are indeed phase separation. In the literature 1,6-Hexanediol is described to dissolve phase separation due to its interference with weak hydrophobic interactions (Düster et al. 2021). p62 filaments and Alexa488 labeled GST-4xUbiquitin were mixed in a molar ratio of 1:15 µM in either 1% or 5% of 1,6-Hexanediol. In both conditions no fluorescent punctae were visible confirming that p62 filaments phase separate upon binding to Alexa488 labeled GST-4xUbiquitin (Figure 37B). To compare phase separation of mCherry-p62 oligomers and p62 filaments, 1 µM mCherry-p62 was mixed with 15 µm GST-4xUbiquitin in either buffer or 5% 1,6-Hexanediol. The emerging punctae seem to be smaller and more roundish compared to the punctae formed by p62 filaments. For mCherry-p62, the 1,6-Hexanediol test was positive as well confirming phase separation. The results of mCherry-p62 are shown in Figure 37C. Additionally, both samples were negatively stained to investigate the molecular arrangement at high magnification (57,000x). For p62 filaments, in phase separation the filaments seem to arrange in directional arrays which could be the cause for the 'misshapen' punctae observed in light microscopy. For mCherry-p62, the arrangements are smaller and seem to be more in line with the roundish shaped punctae observed in light microscopy. Figure 37D and Figure 37E show representative negative stain images of p62 filament and mCherry-p62 phase separation induced by GST-4xUbiquitin at different magnifications. To analyze the order of p62 filaments in *in vitro* phase separation by GST-4xUbiquitin in more detail the sample with a molar ratio of 1:15 µM was vitrified by plunge freezing at the Vitrobot Mark IV as describe in the Materials and Methods section 5.7.3. The results of the cryo-EM data analysis are presented in the Results and Discussion section 3.2.6.

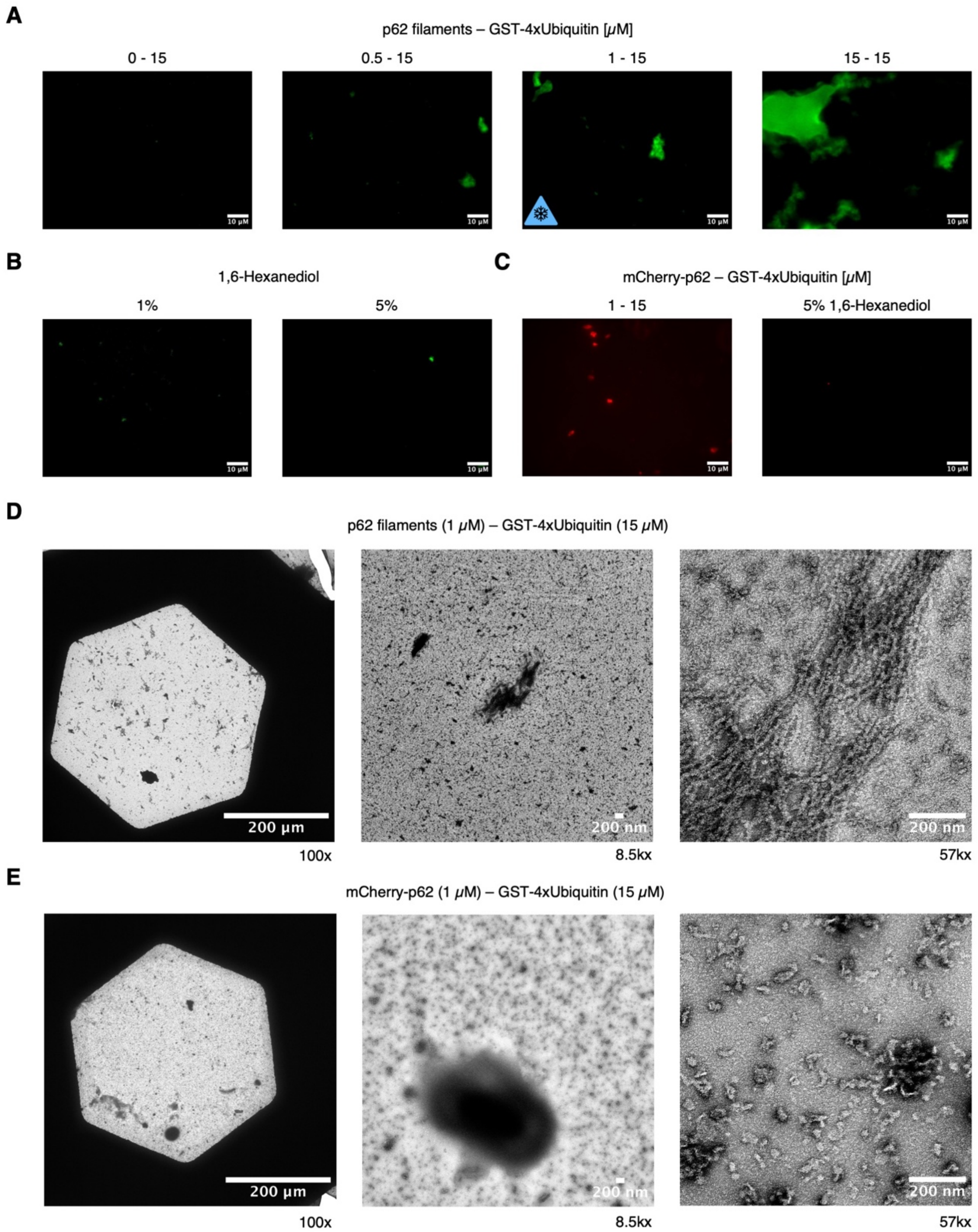

Figure 37: Phase separation of p62 and mCherry-p62 induced by GST-4xUbiquitin
A: Brightfield fluorescence microscopy of p62 filaments mixed with GST-4xUbiquitin labelled with Alexa488 at different molar ratios. The molar concentration of p62 filaments and GST-4xUbiquitin are indicated above the images in μM. **B:** Brightfield fluorescence microscopy of 1 μM p62 filaments mixed with 15 μM GST-4xUbiquitin labelled with Alexa488 in 1 or 5% of Hexanediol. **C:** Brightfield fluorescence microscopy of mCherry-p62 filaments mixed with 15 μM GST-4xUbiquitin labelled with Alexa488 (in 5% of Hexanediol). **D:** Representative micrographs of negative stain electron microscopy at different magnifications of 1 μM p62 filaments mixed with 15 μM GST-4xUbiquitin. **E:** Representative micrographs of negative stain electron microscopy at different magnifications of 1 μM mCherry-p62 filaments mixed with 15 μM GST-4xUbiquitin.

3.2.6 Cryogenic electron tomography of p62 filaments in *in vitro* phase separation

To exclude that the in the Results and Discussion section 3.2.5 described array of p62 filaments in phase separation is an artefact of staining the sample with a heavy metal stain, cryo-ET was performed on vitrified phase separation droplets of p62 filaments induced by GST-4xUbiquitin. As a control served tomograms recorded by Julio Ortiz on a sample of p62 filaments without GST-4xUbiquitin prepared by Siavash Mostafavi. For the control sample, p62 filaments were purified by Siavash Mostafavi similarly as described in the Material and Methods section in this thesis. The tomograms were recorded by Julio Ortiz on a Talos Arctica 200 kV at 63,000x magnification utilizing a phase plate to enhance the contrast of the p62 filaments. The control tomograms were motion corrected, CTF estimation and tilt series alignment were performed by Julio Ortiz in WARP. Three-dimensional reconstruction was performed in IMOD by Julio Ortiz. The reconstructed tomograms were taken and denoised and missing wedge corrected in IsoNet. Two representative tomograms are shown in Figure 38A and Figure 38B. It was observed that p62 filaments are randomly oriented, covering the whole grid. The filaments are located at roughly the center of the tomogram, in a one-layer fashion. A high degree of flexibility of the p62 filaments could be observed.

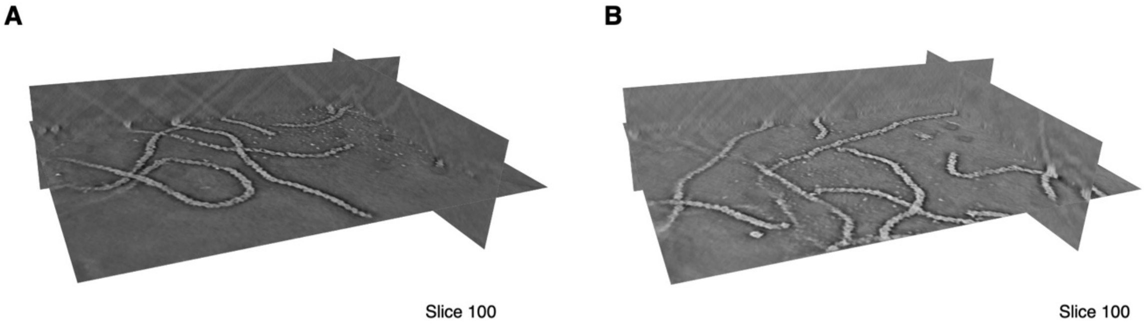

Figure 38: Cryogenic electron tomography of p62 filaments
Two representative tomograms of p62 filaments imaged at Talos Arctica 200 kV instrument at 63.000x magnification with a phase plate. The p62 filaments are central to the tomogram, flexible and show no specific arrangements.

The tomograms of the p62 filaments in phase separation induced by GST-4xUbiquitin were collected at a Titan Krios 300 kV instrument at 64,000x with a variation in defocus between -2.0 to -4.0 µm. The raw micrographs were motion corrected in WARP, CTF estimation and image stack creation were also performed in WARP. The three-dimensional reconstruction was performed with AreTomo, and denoising and missing wedge correction with IsoNet. Two representative tomograms are shown in Figure 39A and Figure 39B. The slices through the tomograms confirm that p62 is present in a filamentous form within the phase separation and that those filaments can be found in an oriented array. Here, p62 filaments are present through the whole depth of the tomogram resulting in a much denser packing compared to the control sample. Unfortunately, due to the entangled structure of the p62 filaments within the phase separation, no segmentation or filament tracing package/software gave interpretable results for segmentation.

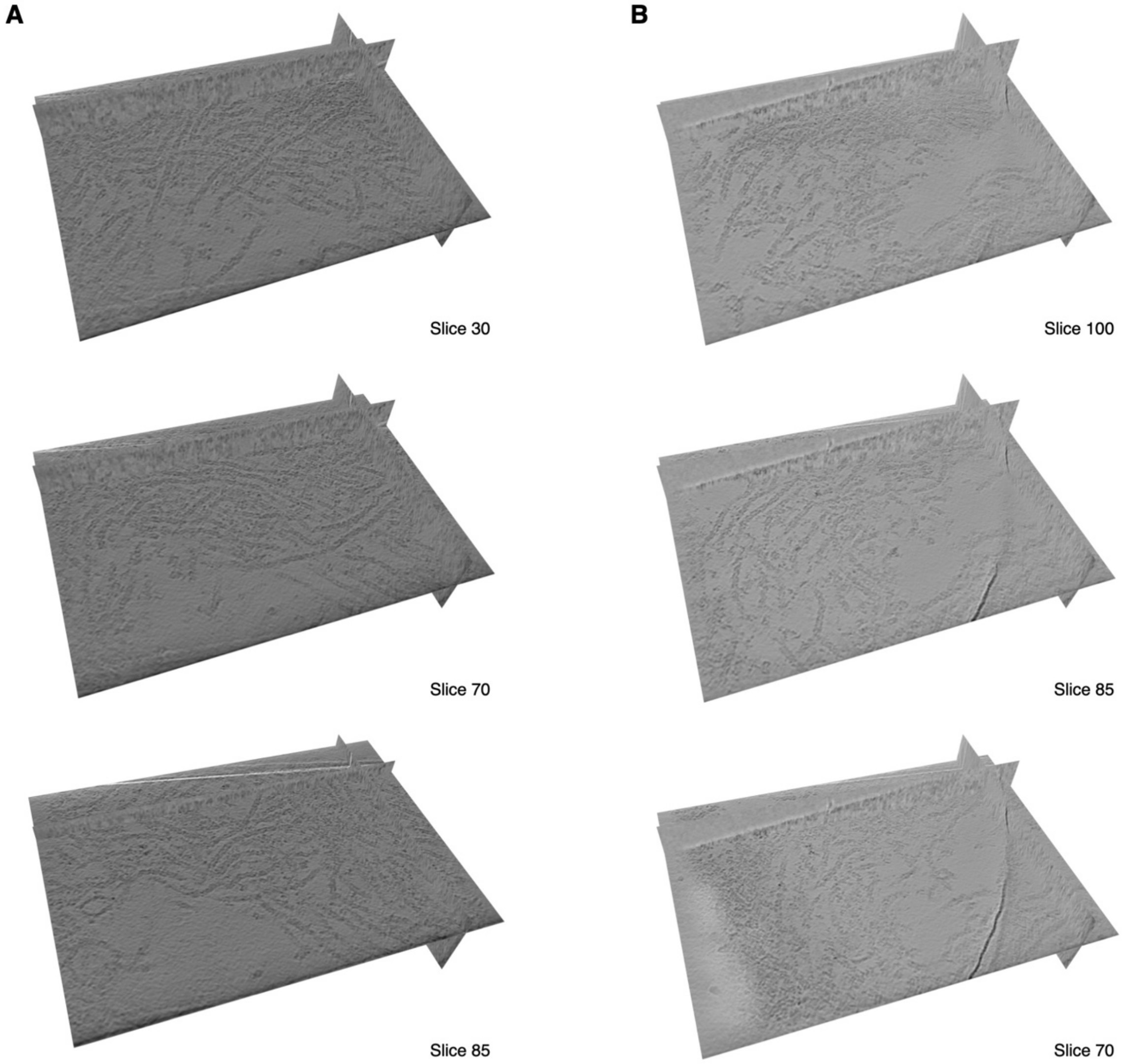

Figure 39: Cryogenic electron tomography of p62 filaments in phase separation
Two representative tomograms of p62 filaments with GST-4xUbiquitin imaged at Titan Krios 300 kV instrument at 64.000x magnification. The p62 filaments span the whole depth of the tomogram and are often aligned in the same direction.

During data acquisition set-up at the microscope, it was noted that different areas of the grid have a different degree of arrangement of the p62 filaments. In all cases, p62 filaments did not dissolve upon GST-4xUbiquitin addition, in line with the results presented above. In Figure 40A and Figure 40B two different sceneries as observed over the whole grid are shown. In Figure 40A, a similar array like arrangement of the p62 filaments could be observed comparable to the negative stain electron microscopy results presented in the Results and Discussion section 3.2.5 (Figure 37D). In this type of arrangement, the p62 filaments seem to align along one axis as to form a bundle. A more chaotic arrangement of p62 filaments in presence of the model cargo can be observed in Figure 40B where the p62 filaments do not seem to be aligned in one direction. Still, the relative density of the p62 filaments within the area exceeds the density compared to the control sample significantly.

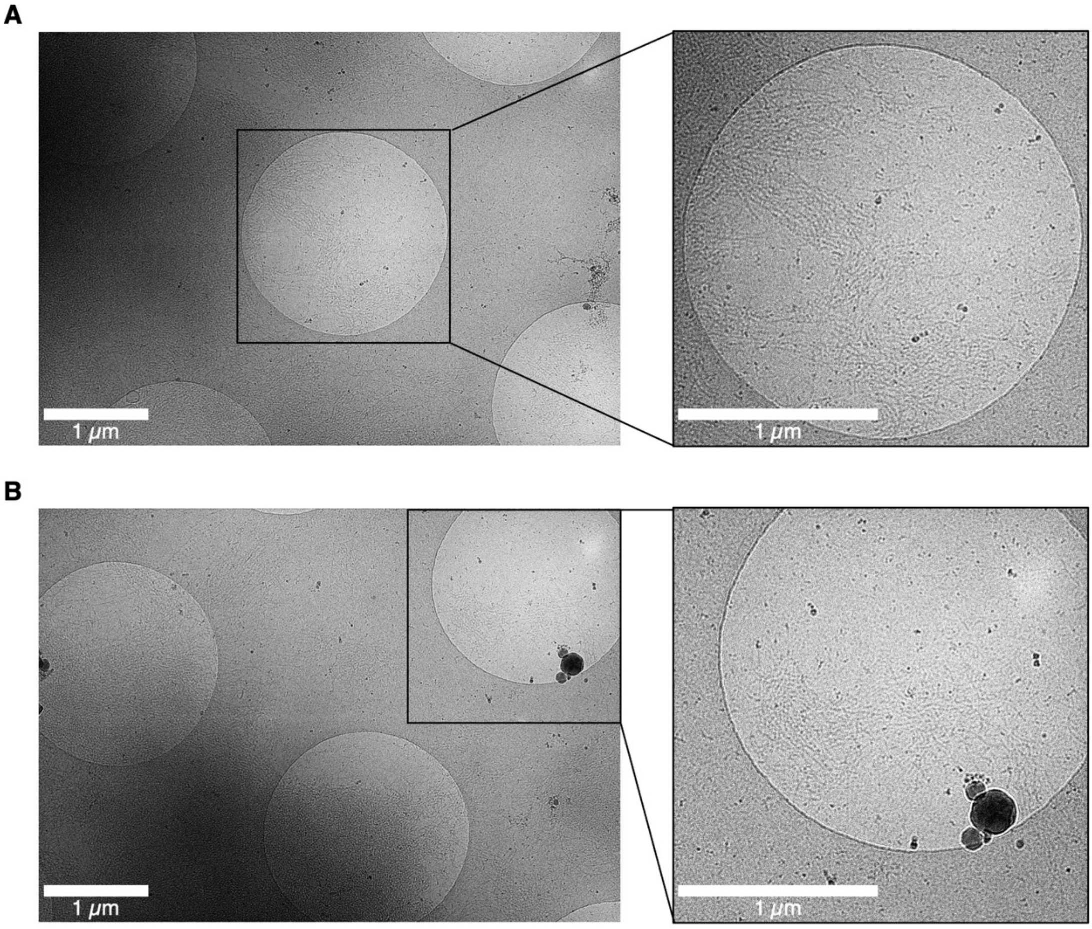

Figure 40: Cryogenic electron microscopy of p62 filaments in phase separation
Two search maps with a close-up of the acquisition area during data acquisition of phase separation tomograms. Here, the difference in organization of p62 filaments in phase separation is visible as the p62 filaments orient strongly in one direct in **A** or are more randomly oriented in **B**.

3.2.7 *In vitro* phase separation of p62 filaments by divalent cations

Preliminary results from Sabrina Berkamp (ER-C-3) (unpublished) using a correlative light and electron microscopy workflow to study the *in situ* structure of p62 in human retinal pigment epithelium (RPE-1) cells showed a co-localization of mCherry-p62 to lipid droplets. Surrounding the lipid droplets, a strange electron dense shell was observed that is thought to contain the protein of interest. The elemental composition of the dense shell was analyzed by energy-dispersive X-ray microscopy (EDX) and is enriched in calcium, magnesium and phosphorus. Calcium, in general, seem to be a possible initiator for autophagy at the ER by inducing FIB200 phase separation (Zheng et al. 2022a). To investigate the effect of different divalent cations on purified p62 filaments, p62 filaments were mixed with either $ZnCl_2$, $CaCl_2$ or $MgCl_2$ at 100 nM, 100 µM, or 100 mM concentration. For all tested cations, the counter ion was chloride, as it is known to have no effect on p62 filaments (up to 1 M concentrations are frequently used in purification buffers). After the addition of the different metals to the p62 filaments, the samples were incubated for 1 h at 4°C and subsequently negatively stained. Negatively stained grids were imaged at a Talos L120C 120 kV at 57,000x magnification. For $ZnCl_2$ at 100 µM as well as for $CaCl_2$ at 100 mM similar structures as for the phase separation induced by GST-4xUbiquitin could be observed. Here also, the p62 filaments cluster together in directionally arrays but do not disassemble. A higher $ZnCl_2$ concentration resulted in aggregation of p62 filaments accompanied by the loss of their ordered three-dimensional structure. Lower $ZnCl_2$ and $CaCl_2$ as well as all $MgCl_2$ conditions tested showed p62 filaments similar to the control. Representative micrographs of all samples are shown in Figure 41.

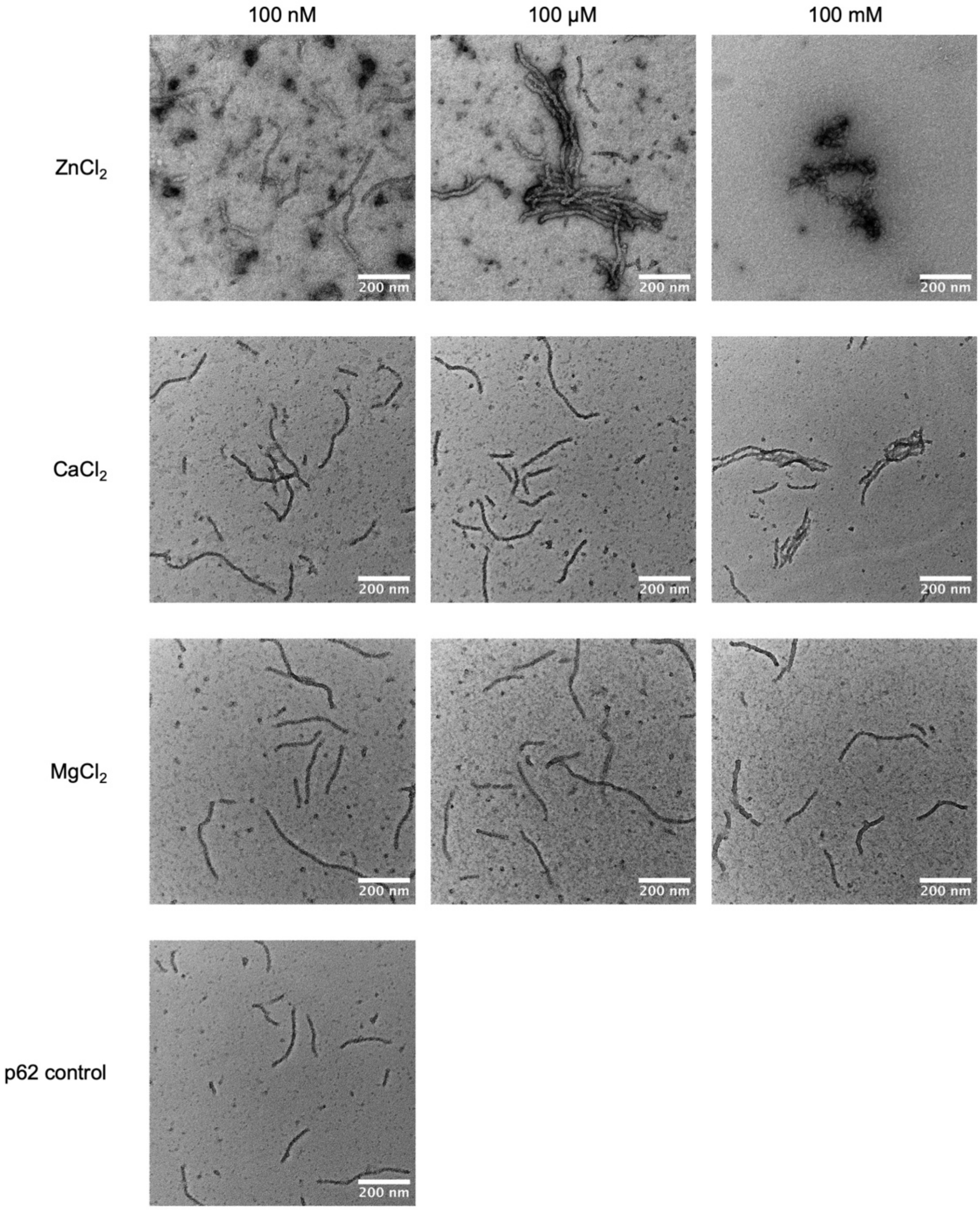

Figure 41: ***In vitro* phase separation of p62 filaments by divalent cations**
Representative micrographs of p62 filaments mixed with different divalent cations or buffer. The respective concentration is indicated above each column and the respective additive at the beginning of each row. The p62 filaments were incubated at the indicated concentrations for 1 h at 4°C before staining.

3.2.8 Discussion

The PB1 domain of p62 as well as the full length p62 protein have been shown to form helical filaments *in vitro* in purified samples (Ciuffa et al. 2015; Jakobi et al. 2020; Mostafavi 2022). As expected, filament formation of full-length p62 after protease cleavage of the MBP-p62 fusion protein, could be observed as well. In the purification of the PB1 domain of p62 or the full-length p62 protein, the MBP-tag is critical to solubilize the protein and prevent early filament formation. With MBP attached, only oligomeric structures can be observed which still allow a purification via chromatography columns. In the literature, a fusion protein of p62 with a fluorescence protein domain of the GFP family is often used to study p62 *in vivo* as well as *in vitro* (Zaffagnini et al. 2018; Turco et al. 2019a). As these fluorescent protein tags have a comparable size to the MBP-tag, the filament formation of mCherry-p62 was investigated further. Here, no helical filaments as described for p62 could be observed for mCherry-p62 in negative stain EM. Most probably, this is due to either a steric hinderance of the relatively large mCherry-tag preventing the formation of larger molecular assemblies or the mCherry-tag influences the solubility of a p62 monomer so that the equilibrium between filaments and soluble mCherry-p62 is tuned towards a higher solubility. As the molecular function of p62 is highly connected to its polymerization behavior (Itakura and Mizushima 2011), the observation in change of polymerization properties for mCherry-p62 is of interest for the interpretation of results generated by fluorescently labeled p62 in general. The influence of the fluorescent protein tags on the oligomeric state of p62 within the cell has to be further examined. On the contrary although described *in vitro* no p62 filaments have been observed *in situ* so far. Additionally, it has been described in the literature that upon the interaction with other proteins, e.g. NBR1, the length of p62 filaments decreases *in vitro* (Jakobi et al. 2020). As these binding partners are also present within living cells, the long filamentous assemblies observed for p62 *in vitro* may represent a particular species that is not so commonly observed in cells. To summarize, the in correlative light and electron microscopy (CLEM) needed fluorescent protein tags can influence the behavior of the protein-of-interest significantly. This influence must be taken into account when interpreting the collected data. For p62, experiments of unlabeled p62 need to be performed to exclude that the fluorescent protein tag changes the oligomeric state of the protein *in situ*.

The binding of the autophagy adaptor protein LC3B to the LIR motif of selective autophagy receptors including p62 is responsible for the recruitment to the growing phagophore membrane (Johansen and Lamark 2020b). In previous experiments, it was indicated that p62 filaments disassemble in the presence of excess LC3B *in vitro* (Mostafavi 2022). In this thesis, the described disassembly of p62 filaments could not be observed with the concentrations of LC3B and LC3Be tested. As the here applied conditions and concentrations differ significantly from the conditions described before, the results do not reflect the mechanism in other environmental conditions. Further unpublished experiments performed by Alexandros Katranidis (ER-C-3) underlined the indication for filament shortening in the presence of LC3B. To portray a more realistic but still simplified model of the p62 filament and LC3B interaction, liposomes were covered with LC3B and the interaction with p62 filaments was investigated. In the recorded tomograms, the p62 filaments seem to stay intact. One p62 filament can interact with multiple liposomes at the same time, connecting different sites and keeping them in close proximity. The ability of connecting multiple binding partners and spatially organizing them may represent a critical aspect of p62 for autophagosome biogenesis.

In its function as selective autophagy receptor, the UBA domain of p62 can bind to polyubiquitinated cargo and mediate the phase separation of ubiquitylated proteins into larger condensates, which are subsequently degraded by autophagy (Danieli and Martens 2018). *In vitro* phase separation experiments of p62 are usually performed with a fusion protein of p62 with a fluorescence protein domain of the GFP family (Zaffagnini et al. 2018). As discussed above, the presence of a large additional domain influences the solubility properties of p62, therefore, the phase separation experiment in this thesis were performed with GST-4xUbiquitin labeled with a small fluorescent dye. As Ubiquitin itself has no cysteine and the dye was attached via a maleimide modification of a cysteine, only the GST domain was fluorescently labeled, resulting in the least disturbance of the binding possible between p62 and Ubiquitin. The light microscopy results presented here, are similar to the results published, that in the presence of a multivalent model cargo, p62 undergoes phase separation and forms condensates (Zaffagnini et al. 2018). Interestingly, the shape and size of the observed phase separation condensates in light microscopy differ between p62 filaments and mCherry-p62, while the results for mCherry-p62 are in line with what has been observed in the literature. As observed during protein purification and filament formation, mCherry-p62 does not form macroscopic helical filaments, which means that the organization within the droplet is different for wildtype p62 than for mCherry-p62. As described in the Introduction section 1.2.4, the material state of the dense phase within the phase separation can differ from liquid to solid (Boeynaems et al. 2018). The difference in appearance between p62 filament and mCherry-p62 phase separation, most probably stems from the fact that the material state of p62 filaments within the condensate is significantly more solid than for mCherry-p62 resulting in a less round shape. The higher valency of p62 filaments compared to mCherry-p62 oligomers might also explain the larger assemblies observed for p62 filaments. Negative stain EM as well as cryo-ET confirmed that in phase separation, p62 filaments do not disassemble but can aligned in an oriented fashion to form a solid network. Different mutations of p62 have been described to modulate the phase separation behavior towards more liquid or solid like material states (Faruk et al. 2021). An investigation on mutations of disease can help shed light on the mechanism how a differing phase separation behavior can influence autophagy degradation of cargo. Additionally, in the regular cellular context, the modulation of p62's phase separation properties is regulated by posttranslational modifications (PTM) of p62 (Matsumoto et al. 2011; Lamark et al. 2017). An investigation of the PTMs of p62 regarding liquidity in phase separation may bring new insides into how cells regulate autophagy degradation via p62.

Zheng et al. recently described how calcium transients on the ER surface trigger liquid-liquid phase separation of FIP200 to specify autophagosome initiation sites (Zheng et al. 2022a). Further, unpublished results of Sabrina Berkamp (ER-C-3) report a co-localization of mCherry-p62 in RPE-I cells with a locally increased calcium concentration compared to the surrounding cytoplasm. In this thesis, it could be shown that for purified p62 filaments a similar phase separation behavior at 100 mM $CaCl_2$ could be observed as in the presence of GST-4xUbiquitin. For the tested $ZnCl_2$, the concentration was even decreased to 100 µM. p62 has been described to regulate autophagy by recruitment of autophagy initiation complex to the sequestration site of cargo (Lamark et al. 2017). In summary, the here presented results indicate that similar to FIP200, p62 could be triggered into phase separation by divalent cations like calcium as an additional mechanism to locally initiate autophagy.

Although the full-length p62 helical filament structure was solved in previous work, still a number of open questions remain including the relative orientation of p62's domains within the filament scaffold. As p62 functions as a multi protein interaction hub it is important to understand how the interactions with different binding partners modify the structure of p62. The interaction of LC3B with p62 is critical in selective autophagy, it remains to be understood how the binding of LC3B to p62 oligomers change the structure of those. In a cellular context the disassembly of p62 filaments in autophagy may not be desired, as p62 is the connection between cargo and autophagy machinery. Work on model phagophore membranes that are covered with LC3B needs to be examined further to understand the interaction of p62 with membrane bound LC3B. Further, the here presented work suggests, that p62 in presence of polyubiquitinated cargo, forms large, crosslinked condensates. The avidity of the p62 oligomers appear to play an important role in the material state of the condensates. Additional studies on how different mutations and PTMs in p62 modulate phase separation behavior and therefore influence autophagy initiation need to be performed. Additionally, the oligomeric state of p62 within living cells needs to be investigated more to understand how p62 can bring together proteins from various pathways into close proximity to facilitate their interaction. Studying slices of cells thinned by cryogenic focused ion beam milling followed by cryo-EM techniques can help reveal whether p62 exists in a filamentous form within cells.

3.3 Structure of the *Corynebacterium glutamicum* 70S ribosome

3.3.1 Single-particle analysis

In order to understand the structural basis for Kasugamycin resistance, single-particle analysis was employed to determine the structure of the *C. glutamicum* 70S ribosome (hereafter Cg70S) and two mutants with increased resistance, namely ΔbS22 and ΔKsgA. The Cg70S fraction was purified from *C. glutamicum* by two step density gradient ultracentrifugation showing a characteristic ribosomal peak pattern by Susana Matamouros (IBG-1) and subsequently plunge-frozen for cryo-EM structure determination. The dataset for the Cg70S was collected at a Titan Krios 300 kV instrument at 96,000x magnification. The defocus was varied between -0.5 to -3.0 µm. Using a standard single-particle image processing workflow implemented in CryoSPARC, a total of 562,059 particles were included in the final three-dimensional reconstruction resulting in a global resolution of 2.9 Å according to the FSC = 0.143 cutoff. A representative micrograph is shown in Figure 42A and selected 2D classes are shown in Figure 42B. As the obtained structural details of the map revealed the expected densities of rRNAs, polypeptide backbone and even medium-sized side chains, an atomic model of the Cg70S ribosome with a tRNA molecule in the P/P-state was built. Peripheral flexible parts of the ribosome were resolved at a poorer local resolution, and it was refrained from building a molecular model in the H54a region and H15-H16a. The final model contained the three rRNAs, 50 ribosomal proteins, an mRNA fragment, as well as the P/P-tRNA molecule. The presence of the Actinomycetota specific proteins bS22 and bL37 was confirmed in the map, as well as the absence of bS21. Details of the cryo-EM map and the molecular model are shown in Figure 42C.

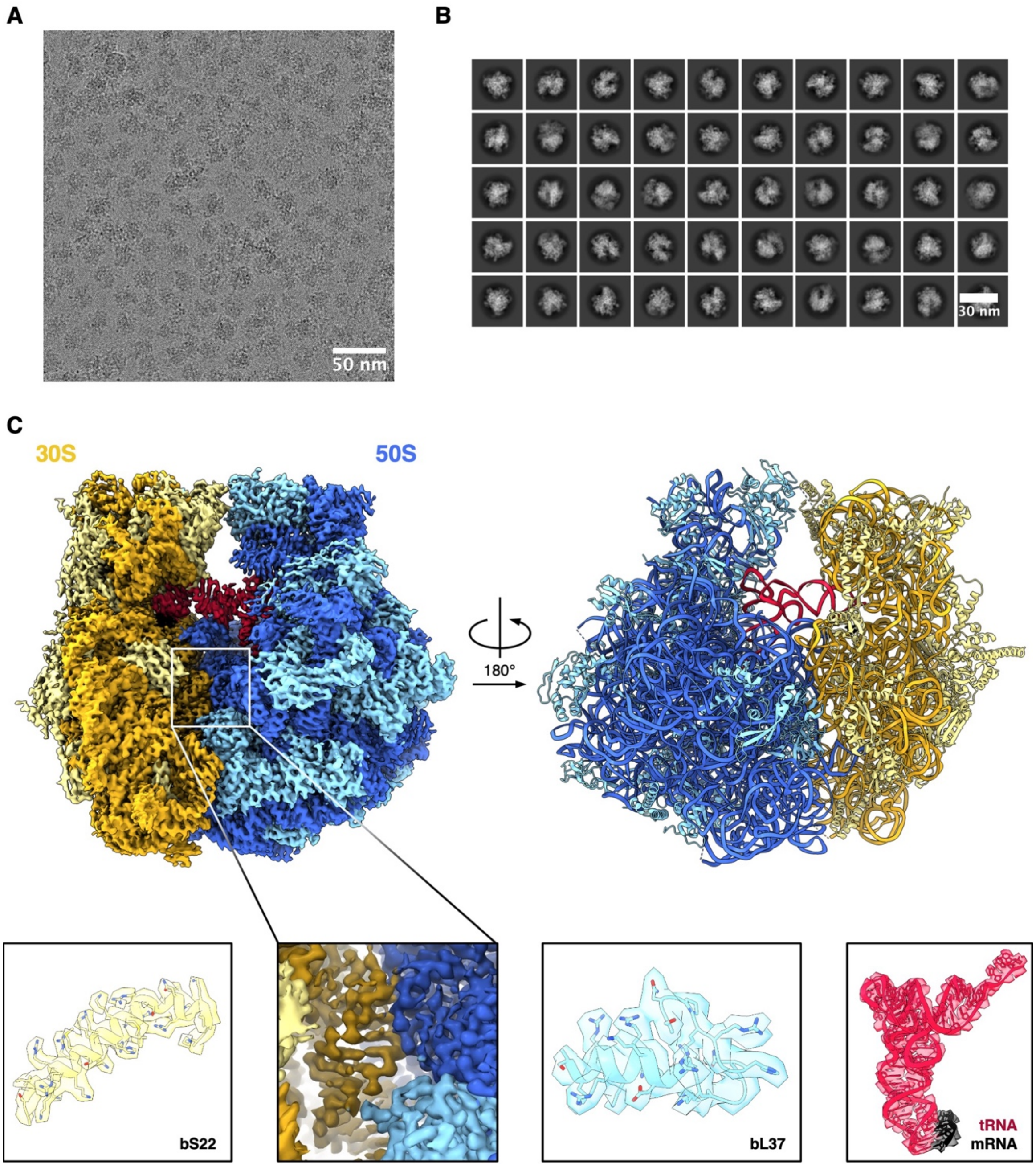

Figure 42: Single-particle analysis of *C. glutamicum* 70S ribosome
A: Representative micrograph of single-particle analysis data acquisition. **B:** Selected 2D classes for ab-initio model reconstruction containing 562,059 particles in total. **C:** EM-density map after homogenous refinement and corresponding molecular model. The 50S subunit is colored in blue and the 30S in yellow with RNA in dark shade and protein components in light shade. Highlighted are the Actinomycetota-specific proteins bS22 and bL37, the RNA interface between 50S and 30S subunit, mRNA (black), and P-/P-tRNA (red).

To investigate the function of the ribosomal protein bS22 and the influence of the methyltransferase KsgA on Cg70S, two knock-out strains with deletions in the respective genes were generated, namely ΔbS22 and ΔKsgA. Using the single-particle analysis approach described above for the Cg70S, the structures of the

ΔbS22 70S ribosome (hereafter ΔbS22) and ΔKsgA 70S ribosome (hereafter ΔKsgA) were solved in addition to the wildtype. Subsequently, all the three ribosome purifications were mixed with the antibiotic Kasugamycin, resulting in a total of six final cryo-EM datasets with three in the absence and three in the presence of Kasugamycin. All datasets, except for Cg70S, were collected on a Talos Arctica 200 kV instrument at 100,000x magnification. The defocus was varied between -0.5 to -3.0 µm. Data processing was performed similar as for the Cg70S. The resolution of the six final reconstructions was estimated by the FSC = 0.143 cutoff and is ranging between 2.5 and 3.2 Å (Figure 43). Table 6 summarizes further statistics on data collection and model building, samples containing Kasugamycin are indicated with *+Ksg*.

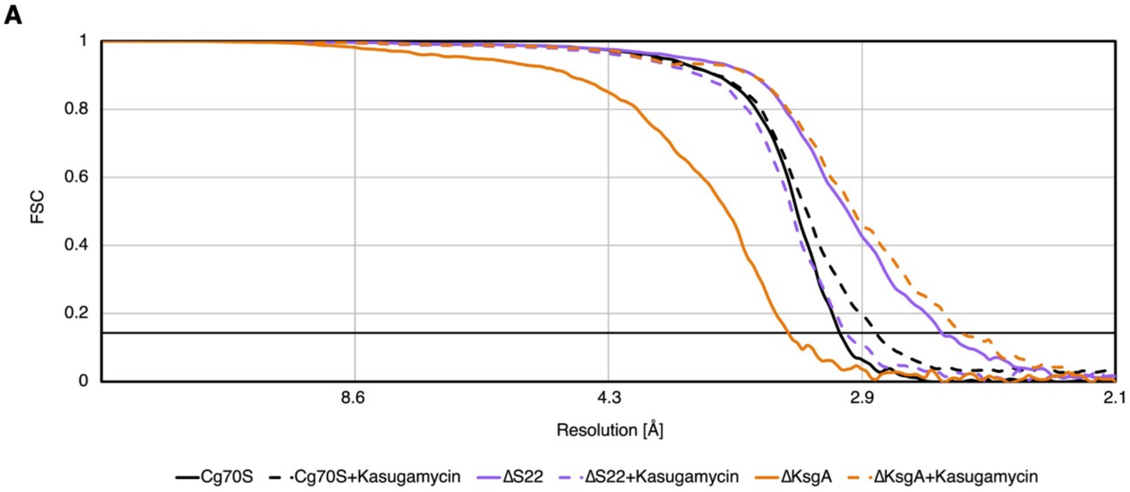

B

Sample	Kasugamycin	Resolution
Cg70S		2.9 Å
Cg70S	yes	2.8 Å
ΔS22		2.5 Å
ΔS22	yes	2.9 Å
ΔKsgA		3.1 Å
ΔKsgA	yes	2.5 Å

Figure 43: Fourier shell correlation of single-particle analysis and resolution at a glance
A: Global map resolution by Fourier shell correlation of two independent half-maps. Cg70S is colored in black, ΔbS22 in lilac, and ΔKsgA in orange. The samples containing Kasugamycin are represented by dotted lines. **B:** Resolution at which the FSC drops below the threshold of 0.143 in Å.

Table 6: SPA of *C. glutamicum* 70S ribosomes

	Cg70S	**Cg70S +Ksg**	**ΔbS22**	**ΔbS22 +Ksg**	**ΔKsgA**	**ΔKsgA +Ksg**
Movies	11,092	4,278	1,397	11,476	1,098	5,727
Magnification	96,000	100,000				
Voltage (kV)	300	200				
Total dose (e$^-$/Å^2)	40	35	25	34	35	35
Defocus range (*µ*M)	0.5 – 3.0					
Physical pixel size (Å)	0.808	0.8389				
Detector	Falcon 4i detector	K3 direct electron detector with BioQuantum energy filter				
Final no. of particles	562,059	510,770	395,010	864,516	146,262	330,241
Global map resolution (Å, FSC=0.143)	2.9	2.8	2.5	2.9	3.1	2.5
Local map resolution range (Å, FSC=0.500)	2.8-3.6	2.7-3.7	2.5-3.4	2.7-3.9	3.1-4.6	2.5-4.0
Initial model used (PDB-ID)	5O61					

	Cg70S	**Cg70S +Ksg**	**ΔbS22**	**ΔbS22 +Ksg**	**ΔKsgA**	**ΔKsgA +Ksg**
			Model refinement			
Model resolution	2.9	3.0	2.7	3.1	3.0	2.5
CC mask	0.86	0.92	0.77	0.81	0.87	0.82
CC box	0.77	0.84	0.69	0.78	0.82	0.79
CC peaks	0.72	0.83	0.62	0.70	0.80	0.76
CC volume	0.84	0.90	0.75	0.79	0.86	0.81
			Model composition			
Chains	55	55	52	54	49	51
Nonhydrogen atoms	141,469	141,469	138,704	141,189	133,461	135,777
Protein residues	5,894	5,894	5,549	5,862	5,296	5,581
Nucleotide residues	4,443	4,443	4,443	4,443	4,293	4,293
			Root-mean-square deviation (RMSD)			
Bond lengths (Å)	0.007	0.006	0.005	0.006	0.004	0.005
Bond angles (°)	0.670	0.682	0.794	0.705	0.579	0.681
			Validation			
MolProbity score	2.23	2.01	2.79	1.68	2.02	2.03
Clash score	7.16	5.42	14.42	7.50	5.52	5.99
Rotamer outliers (%)	4.51	3.46	8.14	0.21	3.36	3.23
			Ramachandran plot			
Favored (%)	95.09	95.59	93.25	96.09	95.35	95.46
Allowed (%)	4.91	4.39	6.75	3.89	4.65	4.52
Outliers (%)	0.00	0.00	0.00	0.02	0.00	0.02

3.3.2 The conformational landscape of *C. glutamicum* 70S ribosome

To shed light on the structural modes of the actively translating Cg70S, dedicated three-dimensional classification was performed with the *3D classification* job in CryoSPARC (CryoSPARC Guide 2023b). After refinement of all EM-density maps, each particle set was classified into ten classes initiated by principal component analysis (PCA). During this *in silico* purification, five unique conformational stats of the 70S ribosome distinguished by their tRNA occupation and small subunit rotation were identified in the datasets. In a second round of three-dimensional classification, the identified unique classes were used as templates for the classification. The three-dimensional classification workflow is highlighted in Figure 44. For each of the six different datasets, the occupancy of the five unique states differed. The relative occupancy for each dataset is listed in Table 7. (The difference in occupancy will be looked at again in detail in the Results sections 3.3.3, 3.3.4, and 3.3.5.)

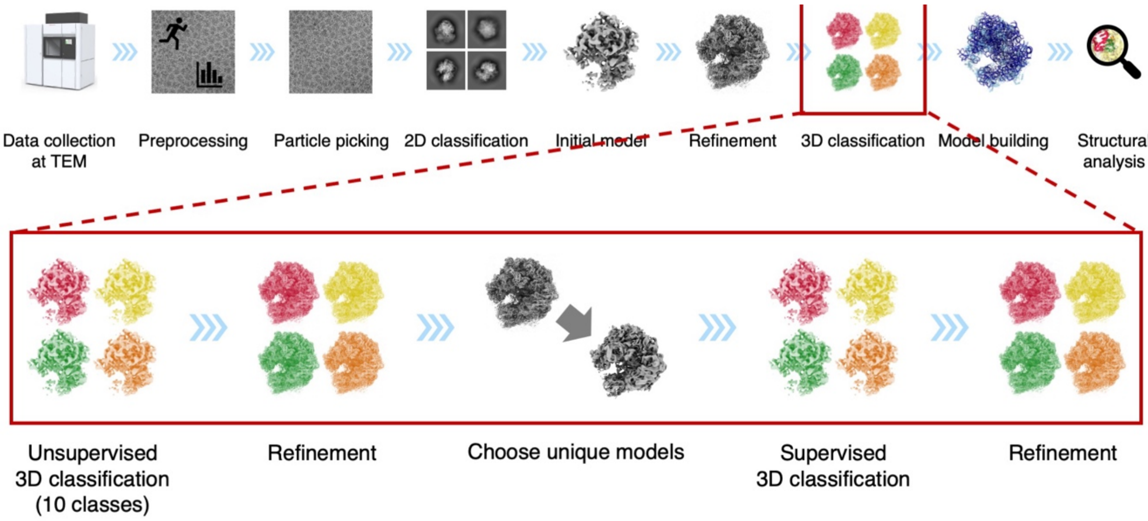

Figure 44: Three-dimensional classification processing pipeline
Schematic of the followed single-particle analysis workflow highlighting the three-dimensional classification steps performed on the here presented datasets. First, a three-dimensional classification was performed sorting the particles into 10 classes with the *3D classification* job in cryoSPARC initialized by principal component analysis. After refinement, unique models were identified in the classes and used as templates in a second supervised three-dimensional classification. A final refinement was performed to obtain the high-resolution EM-density maps of the different conformational states.

Table 7: Assignment of translational states based on three-dimensional classification

	A-state	P-state	Transition state	E-state	No tRNA
Cg70S	26%	45%	16%	13%	-
Cg70S + Kasugamycin	-	20%	23%	15%	42%
ΔS22	25%	46%	20%	9%	-
ΔS22 + Kasugamycin	-	18%	16%	20%	46%
ΔKsgA	-	51%	22%	12%	15%
ΔKsgA + Kasugamycin	-	51%	30%	8%	10%

In the following paragraph, only the wildtype sample is described in more detail because the molecular structures of the defined states did not differ between Cg70S and ΔbS22 or ΔKsgA. For Cg70S, the most populated class (45 %) is represented by particles containing a P/P-site tRNA (P-state), whereas the second most populated class (26 %) contains an additional A/A-site tRNA (AP-state). The class with a P/E-site and an A/P-site tRNA (transition state) contains 16 % of the particles and the class with a single E-site tRNA (E-state) contains 13 %. Although detected in other datasets, the wildtype sample does not show a class of an empty 70S ribosome (no tRNA). The different states are presented in Figure 45A. The quality and resolution of the P-state, AP-state, and transition state EM-density maps allowed to build atomic models for rRNAs, rproteins, mRNA, and tRNA components based on the molecular model built before three-dimensional classification (described in the Results and Discussion section 3.3.1). When the EM-density maps of the P-state and AP-state were aligned on the large subunit, their small subunit was well overlapping with only a small displacement in the shoulder region of the small subunit of the AP-state due to A-site tRNA binding (Figure 45B). The transition state shows a fully rotated small subunit and shifted tRNAs with the peptidyl chain already transferred to the A/P-site tRNA. The P/E-site tRNA's anticodon loop is still in the decoding center of the small subunit and the A/P-site tRNA' anticodon loop in the A-site while both tRNA's acceptor stems are shifted to E-site and P-site in the large ribosomal subunit. The small subunit of the E-state mainly overlaps with the small subunit of the P-state in the body and shoulder region but shows a rotated head due to E-site tRNA binding (Figure 45B).

As the conformational state without a tRNA present could not be observed in the wildtype sample, no EM-density map for it is shown in Figure 45. (It is to note that for Cg70S with Kasugamycin present, the EM-density map without a tRNA present aligned perfectly to the here presented P-state EM-density map, excluding the differenced in density for P-site tRNA, mRNA, and Kasugamycin).

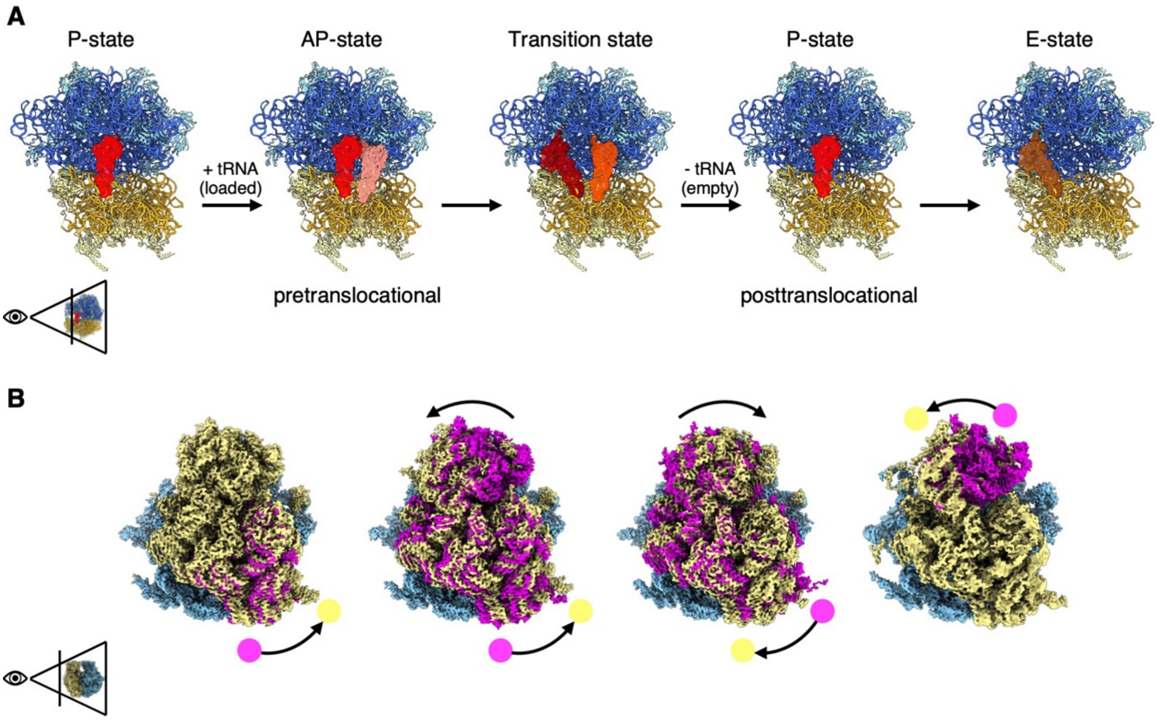

Figure 45: Conformational landscape of the *C. glutamicum* 70S ribosome
A: Molecular models of four of the five unique classes found in three-dimensional classification. Particles were sorted according to tRNA occupation and small subunit rotation. **B:** Difference in small subunit rotation between the states shown in A. The EM density of the starting state is shown in pink and the EM density of the final state in yellow. Arrows are indicating the direction of rotation.

3.3.3 Structural characterization of Kasugamycin binding and its influence on the translational landscape of the *C. glutamicum* 70S ribosome

As the molecular mechanism of protein biosynthesis inhibition by Kasugamycin is not fully understood yet, the Cg70S sample was mixed with Kasugamycin and SPA performed. After three-dimensional classification of the Cg70S + Kasugamycin sample, the in the literature described binding pocket of Kasugamycin (Schuwirth et al. 2006; Paternoga et al. 2023) was observed to bind Kasugamycin in the Cg70S dependent on the conformational state of the ribosome. In the P-state no density for Kasugamycin could be observed, instead the density of an mRNA fragment is visible in the mRNA path (Figure 46A). The density for Kasugamycin could only be observed clearly in the conformational state with no tRNA present (Figure 46B). The EM-density map for the transition state showed densities for both mRNA and Kasugamycin, but compared to the conformational states described above these densities are less prominent and appear relatively smeared (Figure 46C). To note, the model for the transition state displayed here shows a steric clash between Kasugamycin and the mRNA, which is sterically impossible. Last, in the E-state a clear density for Kasugamycin as well as part of the mRNA fragment is visible. The mRNA is shifted toward the E-site so that no steric clash is hindering simultaneous mRNA and Kasugamycin binding (Figure 46D). For the Cg70S + Kasugamycin dataset no A-state could be observed. In general, Kasugamycin is bound in the same binding pocket as has had been described for *E. coli* (Schuwirth et al. 2006; Paternoga et al. 2023) by the *C. glutamicum* bases A772, A774, G907, A1480, G1487, and U1488 of the 16S rRNA.

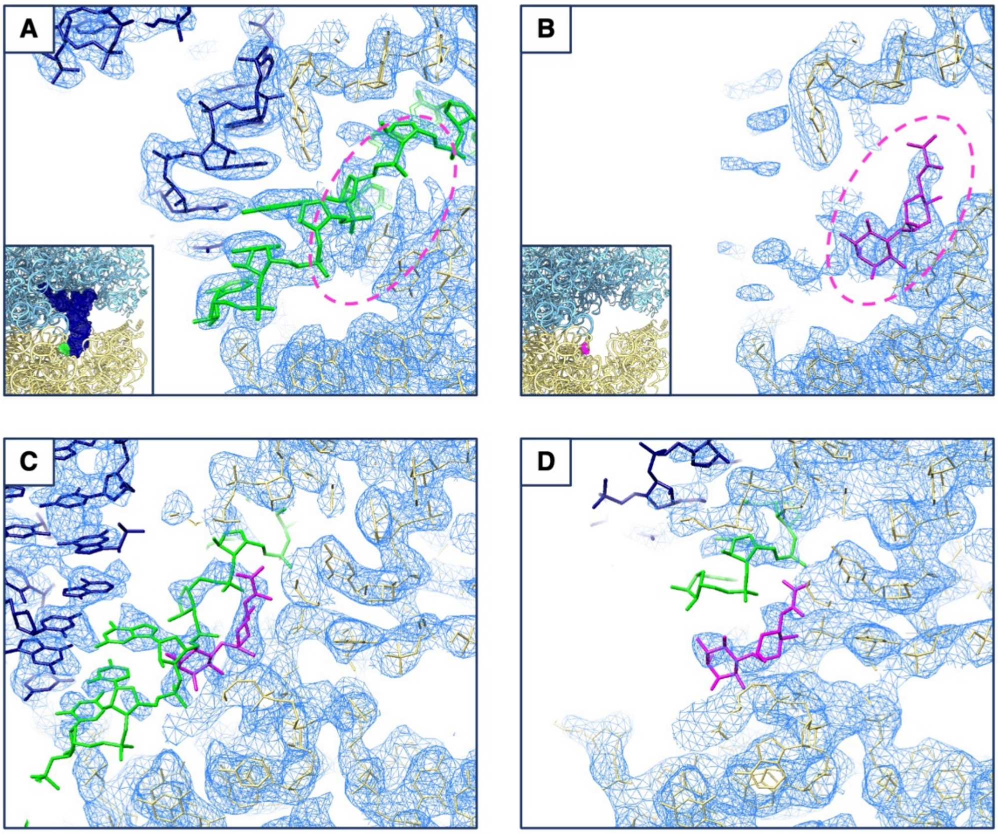

Figure 46: Kasugamycin binding pocket in the Cg70S
Zoom into the decoding center of the Cg70S for **A:** P-state, **B:** no tRNA present, **C:** transition state, **D:** E-state. In dark blue is the respective tRNA, in green the mRNA fragment, in magenta Kasugamycin, in yellow the small subunit and in light blue the large subunit shown. The small inlets in A and B are to locate the components in the Cg70S.

The difference in class occupancy between the Cg70S and Cg70S + Kasugamycin sample is highlighted in Figure 47. From the large difference of area occupied in the radar chart between the two datasets, it becomes clear that Kasugamycin has a severe effect on the conformational landscape of the 70S ribosome with a shift towards non-functional classes, the E-state and without a tRNA respectively.

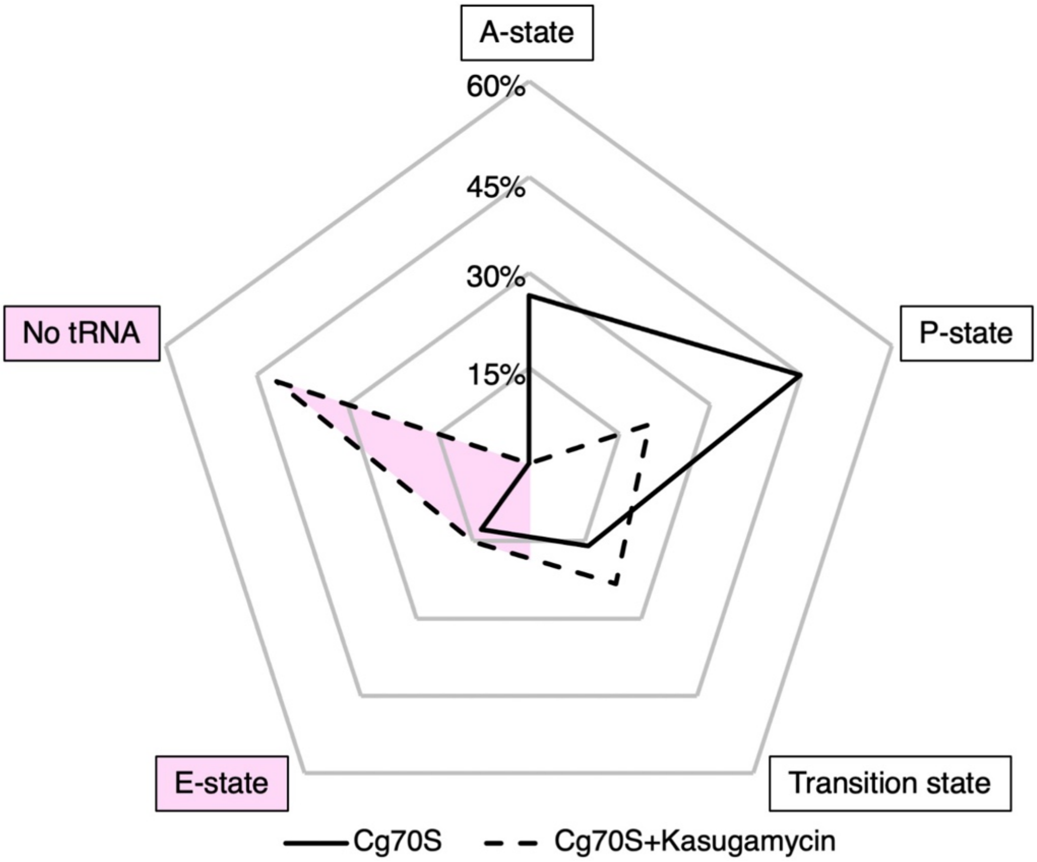

Figure 47: Conformational landscape of the Cg70S and Cg70S + Kasugamycin
Relative occupancy of each state as listed in Table 7 are shown in a radar chart for Cg70S and Cg70S + Kasugamycin. Conformational states which sterically allow Kasugamycin binding are highlighted in magenta.

3.3.4 Influence of ∆bS22 on the structure, conformational landscape, and Kasugamycin resistance of *C. glutamicum* 70S ribosome

In an adaptive laboratory evolution assay, Susana Matamouros identified the ∆bS22 knock-out strain to have a higher resistance to the antibiotic Kasugamycin (unpublished). The bS22 protein is a 33 amino acid protein that is rich in basic residues (27% lysine, 27% arginine, 3% histidine). The primary and three-dimensional structure of bS22 is shown in Figure 48A and the electrostatic surface of bS22 in Figure 48B. The positively charged surface of bS22 matches the negatively charged binding pocket formed by the 16S rRNA H44 and H45, located at the tip of the H44 (Figure 48C). In this position, bS22 is mediating contact between the body and head of the small subunit. The C-terminus of bS22 protrudes towards the helix 70 of the 23S rRNA. The wildtype and ∆bS22 structures of the 70S ribosome have an almost complete structural overlap except for the missing density of bS22 (Figure 48C). To investigate how the bS22 protein affects the translational activity of the 70S ribosome, the rotation axis of the small subunit proteins was analyzed. As the bS22 protein sits close to the average rotational axis of the 30S small subunit proteins, during ratcheting, bS22 rotates rather than being shifted in its spatial position. During ratcheting the contacts of bS22 to the 16S rRNA of the small subunit does not change. In both states bS22 connects the H44 of the body (sometimes called spine) with the H45 of the shoulder in the 16S rRNA. The C-terminus of bS22 reaches into the large subunit. Comparing the ratcheting movement of *C. glutamicum* 70S ribosomes to the ∆bS22 mutant, the average rotational axis is slightly shifted and the average rotational angle is slightly higher, from 10.4° for the wildtype to 12° for ∆bS22, respectively (Figure 48D). In Figure 48E the difference in rotation angle for each small subunit protein is displayed in a color-coded way from lowest in green to highest in red.

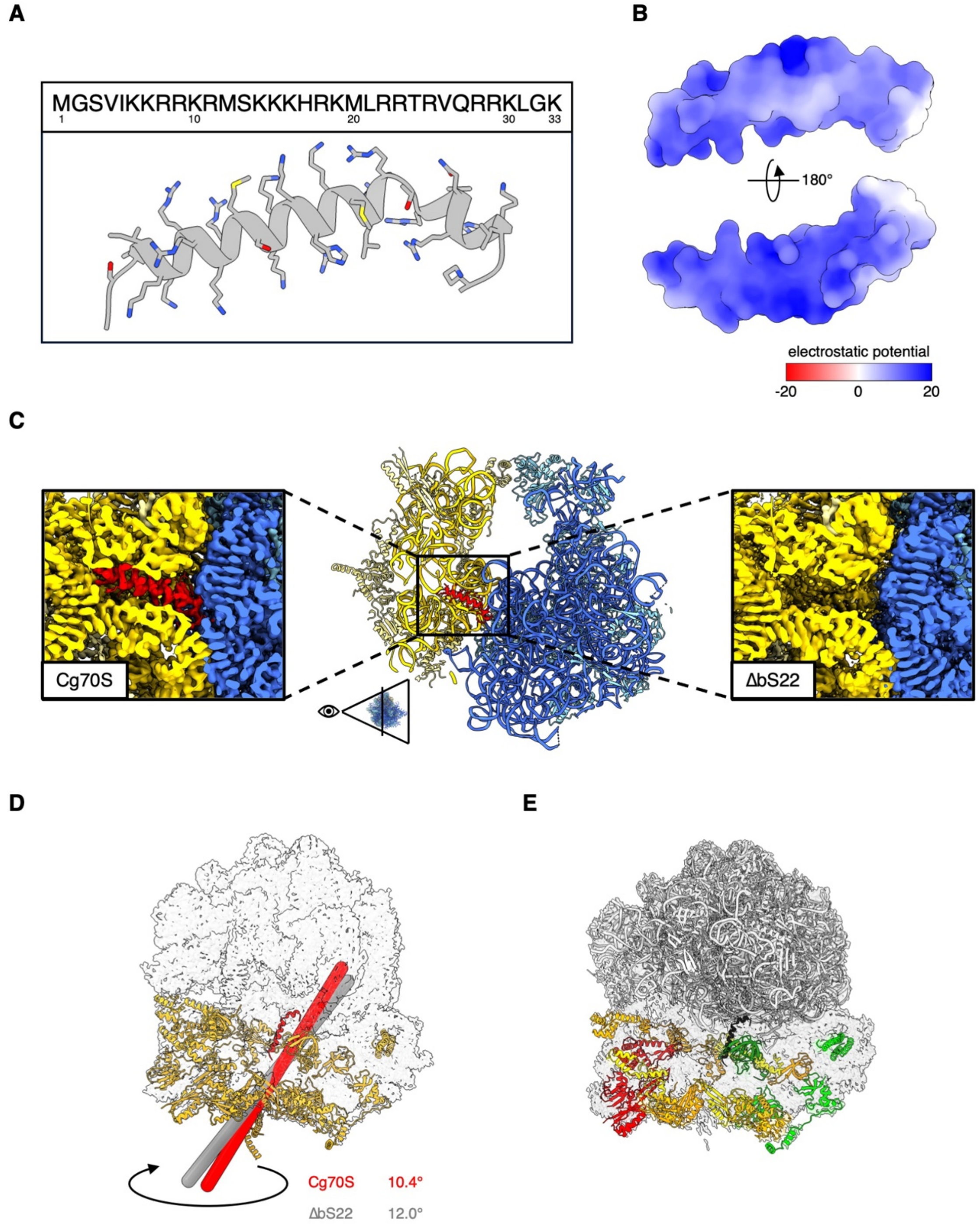

Figure 48: bS22 in the Cg70S ribosome
A: Primary and three-dimensional structure of bS22. **B:** Electrostatic potential of bS22. **C:** bS22 in the Cg70S molecular model. Zoom into the density maps of Cg70S and ΔbS22. bS22 is colored in red, the large subunit in blue, and the small subunit in yellow. **D:** Rotation axis of the small subunit proteins of the Cg70S (red) and ΔbS22 (grey). bS22 is colored in red, small subunit proteins in yellow. **E:** Small subunit proteins colored according to the difference between their rotation angle in Cg70S and ΔbS22, from largest difference in red, to smallest difference in dark green. bS22 is colored in black.

Strikingly not all proteins of the small subunit are affected in the same way by deletion of bS22. As illustrated in Figure 48E, proteins in the head region of the small subunit tend to have a larger shift in rotational angle compared to proteins of the body and shoulder. By comparing the average difference in rotation for the body parts of the small ribosomal subunit, the average of the head is with 0.97 significantly higher than the average of 0.58 over all proteins. Both body (0.42) and shoulder (0.39) have a slightly lower average than the whole small subunit. The rotation difference for each small subunit protein is displayed in Figure 49B clustered according to their location in the small subunit.

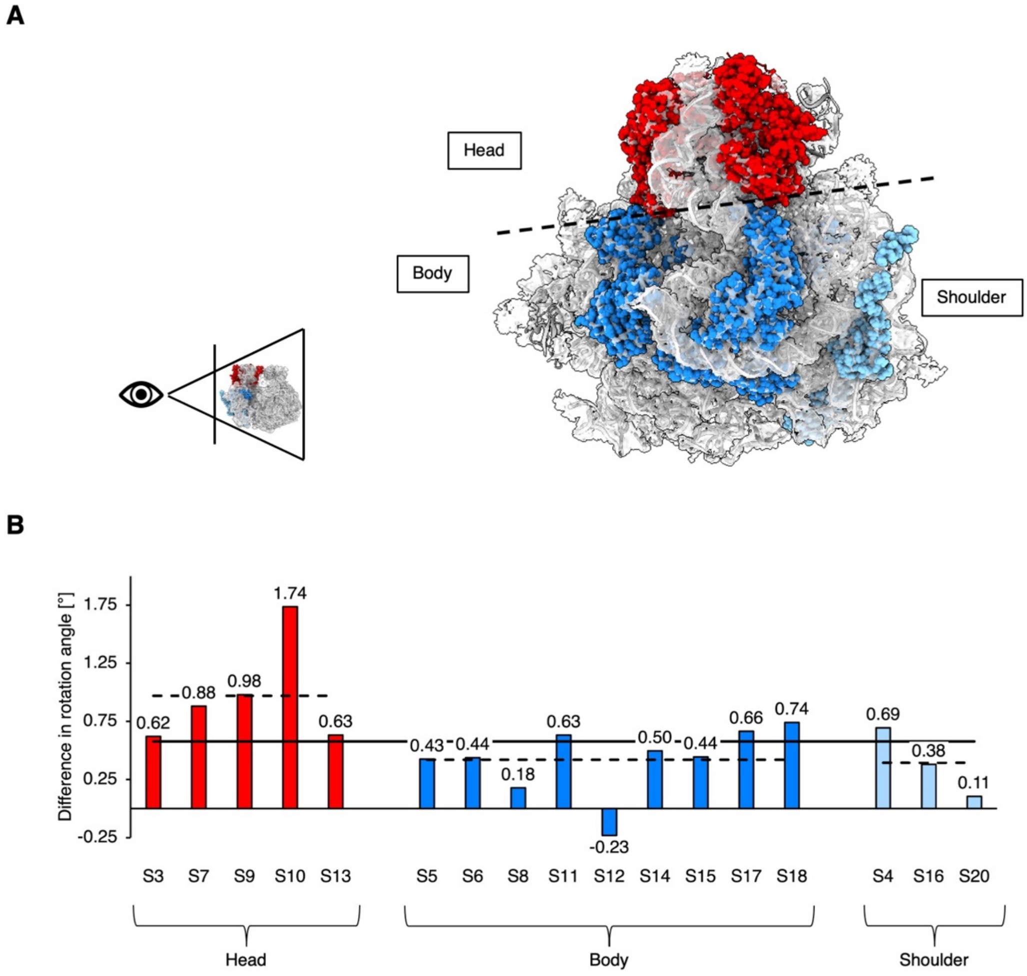

Figure 49: Rotation of small subunit proteins in Cg70S and ΔbS22
A: View of the small subunit with indications to the body parts. Small subunit proteins of the head are colored in read, of the body in dark blue and of the shoulder in light blue. **B:** Rotation difference for each small subunit protein between Cg70S and ΔbS22. The average over all proteins is displayed as a black line, the average of the specific body parts is displayed in a dashed line.

Since the structure of the 70S ribosome is almost unaffected by the deletion of bS22, the higher resistance of the ΔbS22 mutant strain is not straightforward to explain. Taking a look at the conformational landscape of Cg70S compared to the ΔbS22 mutant, the mutation does not affect the distribution significantly in absence and presence of the antibiotic Kasugamycin. Figure 50A and Figure 50B represent the conformational landscape in absence and presence of Kasugamycin. In both cases the areas occupied in the radar chart between wildtype and ΔbS22 mutant show no significant differences.

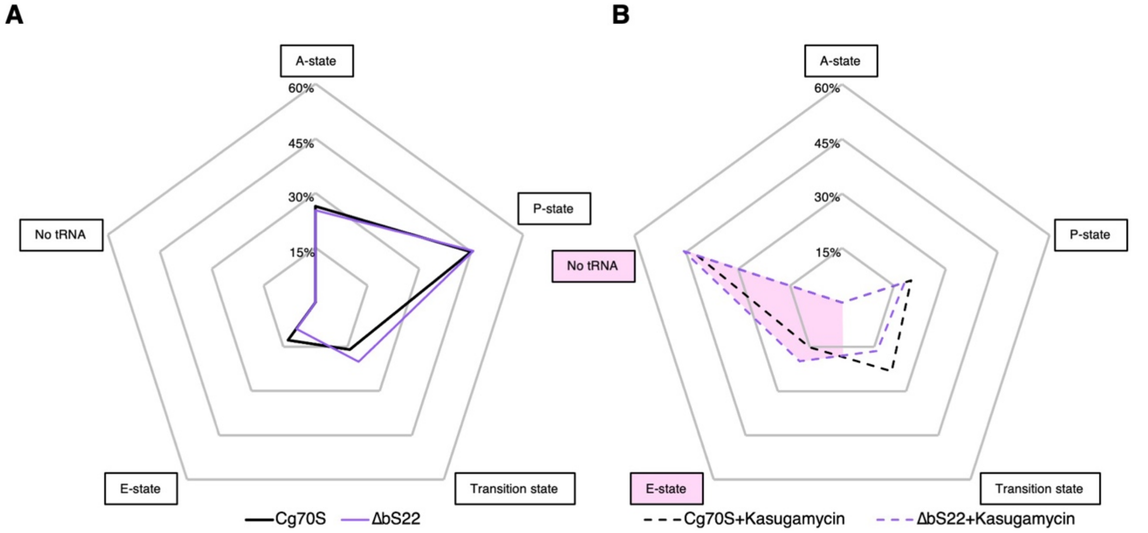

Figure 50: Conformational landscape of the Cg70S compared to ΔbS22 70S
The relative occupancy of each translational state as listed in Table 7 is shown in a radar chart for Cg70S and ΔbS22 in **A** and Cg70S + Kasugamycin and ΔbS22 + Kasugamycin in **B**. Conformational states which sterically allow Kasugamycin binding are highlighted in magenta.

3.3.5 Influence of ΔKsgA on the structure, conformational landscape, and Kasugamycin resistance of *C. glutamicum* 70S ribosome

Similar as described in the literature for *E. coli*, ΔKsgA knock-out strains of *C. glutamicum* show an increased resistance towards the antibiotic Kasugamycin (Susana Matamouros, unpublished). Similar to the observation for ΔbS22, the overall structure of ΔKsgA matches that of the wildtype. At the obtained resolution within the core of the ribosome, the observed densities of the RNA bases A1500 and A1501 in the 16S rRNA revealed the lack of dimethylation in ΔKsgA in comparison to Cg70S (Figure 51A and Figure 51B). To investigate the difference in methylation state, EM-density maps were displayed at the same contour level of the RNA backbone and in Figure 51B the difference in density for the base is clearly visible. In three-dimensional classification, the differences between the occupancy of the defined conformational states for ΔKsgA compared to the wildtype are significantly shifted, different than for ΔbS22 and the wildtype. In both ΔKsgA datasets, no A-state could be observed. The absence of the A-state induces a fundamental change in the area occupied in the radar chart between ΔKsgA and Cg70S (Figure 51C). While Kasugamycin induced for both, Cg70S and ΔbS22, a significant change in occupied area in absence and presence of it, the area occupied by ΔKsgA in the radar chart is unaffected by Kasugamycin (Figure 51D). Compared to the wildtype, the population of conformational states in which Kasugamycin binding is sterically possible is significantly lower for ΔKsgA resulting in a higher occupancy of biological active conformational states.

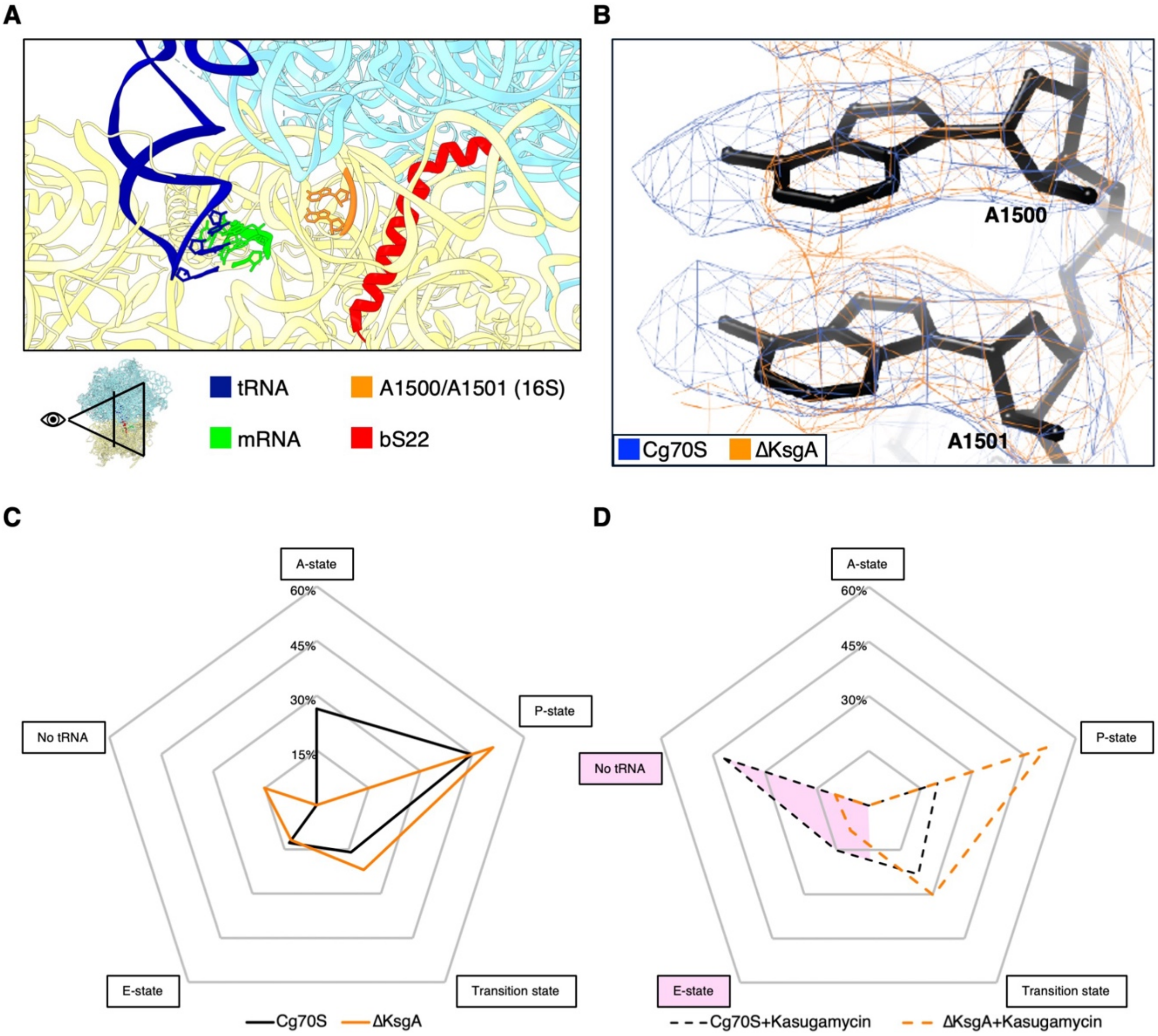

Figure 51: Conformational landscape of the Cg70S compared to ΔKsgA 70S
A: Surrounding of the bases A1500 and A1501 of the 16S rRNA with the 30S subunit colored in yellow, the 50S subunit in light blue, a P/P-tRNA in dark blue, an mRNA fragment in green, the bases A1500 and A1501 of the 16S rRNA in orange, and bS22 in red. **B:** Close-up on the bases A1500 and A1501 of the 16S rRNA. The EM-density map of Cg70S is colored in blue and of ΔKsgA in orange. **C:** The relative occupancy of each translational state as listed in Table 7 are shown in a radar chart for Cg70S and ΔKsgA. **D**. The relative occupancy of each translational state as listed in Table 7 are shown in a radar chart for Cg70S and ΔKsgA in presence of Kasugamycin. Conformational states which sterically allow Kasugamycin binding are highlighted in magenta.

3.3.6 Discussion

The structure of the Cg70S ribosome presented here matches closely the related structure of the Actinomycetota 70S ribosomes of *M. smegmatis* (Hentschel et al. 2017). For the first time, the conformational AP-state and transitions state could be observed for Actinomycetota ribosomes, improving the structural data available for functional analysis of this specific kind of ribosome. Due to successful three-dimensional classification several states of the actively translating ribosome described could be mapped to the in the Results and Discussion section 3.3.2 presented experimental structures. The here identified AP-state was associated with a pretranslocational state that is characterized by a not yet transferred peptidyl-chain (Frank et al. 2007). The transition state with rotated small subunit is considered an intermediate state. During the ratcheting motion, the translocation of the peptidyl-chain from P-site to A-site tRNA takes place. In the here presented transition state the transfer of the peptidyl-chain from the P-site tRNA to the A-site tRNA already took place, while both tRNAs are still in the process of translocation. During the back rotation of the small subunit the P/E-site tRNA is released while the A/P-site tRNA is completely translocated to the P-site. This state is represented by the P-state with a single P/P-site tRNA and termed posttranslocational in accordance with the nomination of the literature (Frank et al. 2007).

In the literature, the Kasugamycin binding pocket in *E. coli* 70S ribosomes is described to be located in the mRNA path in close proximity to the decoding center (Schuwirth et al. 2006; Paternoga et al. 2023). In *C. glutamicum* 70S ribosomes, Kasugamycin binds the exact same base network as described for *E. coli* (Schuwirth et al. 2006; Paternoga et al. 2023), corresponding to *C. glutamicum* bases: A772, A774, G907, A1480, G1487, and U1488 of the 16S rRNA. Interestingly, the density for Kasugamycin is only clearly visible after three-dimensional classification. After inspection of the EM-density maps after three-dimensional classification it becomes clear, that in the P-state, the mRNA is sterically hindering Kasugamycin binding making it impossible for both components to be present at the same time, suggesting a competitive inhibition mechanism of Kasugamycin binding. The dataset of Cg70S + Kasugamycin has about 42 % of particles sorted into the class with no tRNA present. In the corresponding reconstructed EM-density map, Kasugamycin is clearly visible. The data thereby suggest that Kasugamycin is replacing the mRNA and stabilizing fully assembled 70S ribosomes without any tRNA bound that are usually rapidly recycled (Nakamura et al. 1996). In the transition state, Kasugamycin and mRNA density are present but the model clearly shows that this combination is impossible due to steric clashes of the molecules. This class is most likely the result of two poorly separated states. The last class to be discussed, the E-state, again shows density for Kasugamycin as well as for mRNA and E-site tRNA. Compared to the P-state, in the E-state the tRNA has left the decoding center and moved on giving room for the mRNA to dissociate form the decoding center and opening up a spot for Kasugamycin to bind. In the E-state, mRNA and Kasugamycin can therefore stably coexist. The A-state cannot be observed for a sample including Kasugamycin and is, thus, not relevant to discuss in the context of Kasugamycin binding, but the absence of A-state ribosomes is a strong indication towards the bacteriostatic action of Kasugamycin by inhibiting active translation (Schluenzen et al. 2006). The bacteriostatic action of Kasugamycin has been described early on with experiments pointing to initiation inhibition (Okuyama et al. 1971; Moll and Bläsi 2002; Schuwirth et al. 2006). Here, only fully assembled ribosomes were investigated and the presented data suggests that the binding of Kasugamycin modifies the conformational landscape of the 70S ribosome severely by stabilizing empty 70S ribosomes. Thus, the biostatic action of Kasugamycin may be explained by the binding of resources of the protein biosynthesis machinery, slowing down protein biosynthesis dramatically and keeping valuable nutrients from being recycled.

Preliminary experiments performed by Susana Matamourus (IBG-1), suggested that the deletion of ∆bS22 increases Kasugamycin resistance for *C. glutamicum*. In *in vitro* experiments of extracted 70S ribosomes, no difference in translation accuracy between Cg70S and ∆bS22, and only a slight increase in translation efficiency for ∆bS22 ribosomes could be observed. These results match with the here presented structural results as the structure and the conformational landscape of Cg70s and ∆bS22 are alike. Although a small difference for the rotational axis of the ∆bS22 small subunit and a higher flexibility in the head region could be observed, this does not seem to affect the function of the ribosome significantly. In contrast, *in vivo* experiments showed a cold sensitive phenotype for the ΔbS22 knock-out strain, as well as a reduced fitness in growth experiments against the wildtype in which the mutant was overgrown (Susana Matamouros, unpublished). A cold sensitive phenotype is often associated with small subunit maturation (Guthrie et al. 1969; Nashimoto et al. 1971; Dammel and Noller 1993). Sun et al. recently showed, that ΔKsgA is important for the rescue of the small subunits which adopted a misfolded structure during maturation (Sun et al. 2023). Since bS22 is located in close proximity to the KsgA binding site for methylation of A1500 and A1501, the presented data suggests that bS22 is not actively involved in translation but more important in small subunit maturation. This hypothesis is in line with the cold-sensitive phenotype observed for the ΔbS22 knock-out strain. A possible explanation for an increased resistance to Kasugamycin of the ΔbS22 knock-out strain is that upon knock-out an increase in misfolded small subunits accumulate within the cell, increasing the quantity of possible targets for Kasugamycin to bind to, leaving more 70S ribosomes active. Another possible explanation, is that the accumulation of misfolded small subunits triggers a ribosomal rescue system within *C. glutamicum*, being helpful also in the stress response towards Kasugamycin.

A similar picture as for the ΔbS22 knock-out strain can be drawn for the ΔKsgA knock-out strain *in vivo*. Strikingly, the mutation itself seems to have a strong influence on the conformational landscape of the ribosome increasing the difficulty for interpretation. Additionally, when Kasugamycin was present in the sample, the occupancy for the defined conformational states of ΔKsgA hardly changed, which may be due to a lower affinity of Kasugamycin towards ΔKsgA. As a result, compared to wildtype and ΔbS22, the amount of particles in the Kasugamycin induced inactive states is much lower. The base residues A1500 and A1501 are not involved in Kasugamycin binding but are in close proximity to the binding pocket. Their different electrostatic potential could lead to a decrease in Kasugamycin affinity. Further, the *in vivo* effects for a higher Kasugamycin affinity may be very similar as the ones discussed for the ΔbS22 knock-out strain.

As the results suggest that the two resistant mutants have an altered small subunit maturation, further studies need to be performed with a focus on the 30S subunit. Single-particle analysis of purified 30S subunits from *C. glutamicum* can give information about when and how bS22 is incorporated into the 16S rRNA and how the absence of bS22 can alter the maturation process. Further, affinity assays for different 70S ribosomes as well as 30S variants can give a deeper insight in why the translational landscape of the different knock-out strains is modulated differently.

4 Outlook

Cryo-EM has undergone transformative advancements in recent years, revolutionizing the ability to visualize biological structures at near-atomic resolution. This technique, leveraging both transmission electron microscopy and the newly developing scanning transmission electron microscopy, holds immense promise for elucidating intricate details of macromolecular assemblies and cellular landscapes.

Single-particle analysis, a cornerstone of cryo-EM, has seen rapid improvements in resolution and throughput within the last decade. Current trends suggest a continued shift towards high-resolution imaging of smaller complexes and dynamic biological systems. Innovations in detector technology, image processing algorithms, and data collection strategies are enhancing the attainable resolution and reliability of single-particle analysis. The future holds the promise of near-atomic resolution structures for an increasing range of biomolecules, including membrane proteins and dynamic complexes previously considered challenging. For the here presented *C. glutamicum* 70S ribosomes as well as the human 80S ribosome, improvements of three-dimensional classification to disentangle three-dimensional flexibility can assist in solving the dynamic range of the molecular motion during protein biosynthesis. As ribosomes are highly versatile complexes undergoing constant assembly and disassembly together with tRNAs and different translational factors, improvement of classification routines and flexibility analysis are critical in solving the mechanistic of protein biosynthesis and identifying conserved and differential evolved aspects of it. These methods will benefit from a higher number of particles imaged to also capture states with a low population number. Therefore, improved results can be expected from more rapid data collection to maximize particle output, less intensive storage formats, and faster and more efficient computing algorithms. In addition to three-dimensional classification, tools for interpolating between distinct states by molecular modeling, eventually supported with artificial intelligence, are needed to complete the final mechanistic model of molecular movement and identify the hierarchy of interactions between the distinct states.

Cryo-ET enables the visualization of biological structures in their native context, providing three-dimensional reconstructions of cells and organelles at nanometer-scale resolution. As cryo-ET becomes more accessible and sample efficient, it will play an essential role in understanding cellular architecture and dynamics. Future directions will likely involve improvements in sample preparation methods, enhanced computational tools for tomographic reconstruction, and integration with other imaging modalities for correlative approaches. A robust workflow, with high reliable throughput in a correlative light and electron microscopy pipeline, is the basis to study p62 *in situ*. Studies on p62 would benefit of improved milling conditions and tomography data acquisitions, as well as robust and fast reconstructions algorithms. The improvement of segmentation supported by artificial intelligence will lead to more efficient and reliable identification of feature structures in larger datasets. With increased speed in data acquisition and processing, the analyzation of statistically relevant data becomes more feasible helping especially in cases of comparison between different conditions in *in situ* studies.

To bridge gaps in resolution and enabling comprehensive structural and functional studies, a key trend in cryo-EM is the integration with complementary techniques such as X-ray crystallography, nuclear magnetic resonance (NMR) spectroscopy, and mass spectrometry. These multimodal approaches can provide a holistic view of biological systems. Furthermore, emerging hybrid methods combining cryo-EM with spectroscopy, super-resolution microscopy, and energy-dispersive X-ray microscopy (EDX) will help the comprehensive characterization of biomolecular structures and interactions. The results of the hybrid method used by Sabrina Berkamp in *in situ* elemental characterization of p62 bodies with EDX led to the discovery of a co-localization with unusually high calcium concentrations, which could be shown to induce phase separation of p62 filaments *in vitro* in this thesis. A vivid knowledge-transfer between life science and material science can result in new hybrid methods to better characterize biological samples.

In conclusion, the future of cryo-EM for biological research is incredibly promising. With ongoing innovations in instrumentation, computational tools, and sample preparation techniques, cryo-EM will continue to push the boundaries of our understanding of complex biological structures and processes. The convergence of cryo-EM with other imaging and spectroscopic methods will pave the way for transformative discoveries in structural biology, with profound implications for drug discovery, bioengineering, and understanding fundamental life processes.

5 Material and Methods

5.1 Material

5.1.1 Plasmids

Table 8 and Table 9 summarize all plasmids used for recombinant protein expression of NUFIP1 or p62, including their genotype and reference.

Table 8: Plasmids NUFIP1

Name	Plasmid	Specifications	Purpose	Reference
NUFIP1-mCherry-YFP	pcDNA3.1	NUFIP1 with C-terminal mCherry, V5-tag, eYFP after HRV 3C site	Live cell imaging	This thesis
NUFIP1-mCherry-pIRES-CFP-LC3B	pIRES	NUFIP1 with C-terminal mCherry, V5-tag, 8x His-tag after HRV 3C site; LC3B after IRES site with C-terminal CFP	Live cell imaging	This thesis
MBP-NUFIP1	pIRES	NUFIP1 with N-terminal MBP before HRV 3C site, C-terminal V5-tag, 8x His-tag after HRV 3C site; eGFP after IRES site	Protein expression	This thesis

Table 9: Plasmids p62

Name	Plasmid	Specifications	Purpose	Reference
MBP-p62	pETM43	p62 with N-terminal MBP before HRV 3C site, C-terminal 6x His-tag after HRV 3C site	Protein expression	(Mostafavi 2022)

Name	Plasmid	Specifications	Purpose	Reference
MBP-mCherry-p62	pETM43	p62 with N-terminal MBP before HRV 3C site, N-terminal mCherry, C-terminal 6x His-tag after HRV 3C site	Protein expression	This thesis
GST-LC3B	pGEX	LC3B with N-terminal GST after HRV 3C site	Protein expression	This thesis
GST-LC3Be	pGEX	LC3B-I with N-terminal GST after HRV 3C site, A45T etc.	Protein expression	This thesis
GST-LC3B-Cys	pGEX	LC3B-I with N-terminal GST after HRV 3C site, C-terminal cysteine	Protein expression	This thesis
GST-4xUbiquitin	pGEX	4x linear Ubiquitin (human) with N-terminal GST after thrombin site	Protein expression	(Wurzer et al. 2015)
GST-HRV3C	pGEX	HRV 3C protease with N-terminal GST	Protein expression	This thesis

5.1.2 Cell lines, bacterial strains, media, and supplements

Cell lines were stored in cryopreservation below -130°C and bacterial strains were stored at -80°C. Table 10 list all cell lines and bacterial strains used in this thesis with their reference and usage.

Table 10: Cell lines and bacterial strains

Name	Reference	Purpose
HeLa	Markus Tusche; Institute of Biological Information Processing: Structural Biochemistry (IBI-7), Forschungszentrum Jülich, Jülich, Germany	Immunofluorescence assay; transient protein expression for fluorescence microscopy
FreeStyle™ 293-F	R79007; Thermo Fisher Scientific; Waltham, Massachusetts, United States	Transient protein expression for purification
E. coli DH5α	C2987; New England Biolabs; Ipswich, Massachusetts, United States	Amplification of plasmid DNA for mini-prep
E. coli One Shot™ TOP10	C4040; Thermo Fisher Scientific; Waltham, Massachusetts, United States	Amplification of plasmid DNA for maxi-prep
E. coli BL21(DE3)	C2527; New England Biolabs; Ipswich, Massachusetts, United States	Recombinant protein expression for purification

Supplier/recipes of the media used in human cell culture or bacterial growth and expression are listed in Table 11. All self-prepared media were prepared with ddH$_2$O, sterilized by autoclavation, and stored at 4°C.

Table 11: Media

Medium	Composition (and Supplier)
Gibco™ DMEM, high glucose, GlutaMAX™ Supplement (DMEM-medium)	With: high glucose, GlutaMAX™, phenol red Without: sodium pyruvate (Thermo Fisher Scientific; Waltham, Massachusetts, United States)
Gibco™ DMEM, no glucose (DMEM-medium without glucose)	With: L-glutamine, phenol red Without: glucose, sodium pyruvate, Hepes (Thermo Fisher Scientific; Waltham, Massachusetts, United States)
Gibco™ Earle's balanced salt solution (EBSS)	(Thermo Fisher Scientific; Waltham, Massachusetts, United States)
Gibco™ Fetal Bovine Serum (FBS)	(Thermo Fisher Scientific; Waltham, Massachusetts, United States)
Gibco™ FreeStyle™ 293 Expression Medium	(Thermo Fisher Scientific; Waltham, Massachusetts, United States)
LB-medium	10 g/L tryptone 5 g/L yeast extract 5 g/L sodium chloride
TB-medium	12 g/L tryptone 24 g/L yeast extract 12,54 g/L dipotassium phosphate 2,31 g/L monopotassium phosphate
LB-agar	10 g agar in 500 mL LB-medium

5.1.3 Protein purification and characterization buffers

All buffers were prepared from sterile filtered stock solutions with ddH$_2$O. Buffers used in chromatography at ÄKTA pure™ 25 or ÄKTA pure™ micro (Cytiva; Marlborough, Massachusetts, United States) were sterile filtered and degassed. Table 12 listed all general buffers, Table 13 lists all buffers used in purification experiments regarding of NUFIP,

Table 14 lists all buffers used in purification experiments of p62, and Table 15 lists all buffers used in purification of GST-fusion proteins.

Table 12: Buffers

Name	Buffer	Salt	Additive
5x SDS loading dye	1.5 M TRIS pH 6.8	5 g/L Bromophenol blue sodium salt	40% (v/v) Glycerol 8% (v/v) β-Mercaptoethanol 8% (w/v) SDS
TAE	40 mM TRIS	20 mM Glacial acetic acid	10 mM EDTA
TBS(-T)	25 mM TRIS pH 7.4	140 mM NaCl 2.7 mM KCl	(0.1% Tween® 20)

Table 13: NUFIP1 purification buffers

Name	Buffer	Salt	Additive
Hypotonic buffer	40 mM Hepes pH 7.4	10 mM KCl 1.5 mM $MgCl_2$	0.2 mM PMSF 0.5 mM DTT
Nuclear lysis buffer	40 mM Hepes pH 7.4	300 mM NaCl 2.5 mM $MgCl_2$	0.2 mM PMSF 0.5 mM DTT
Cryo lysis buffer	40 mM Hepes pH7.4	300 mM NaCl 10 mM $MgCl_2$ 10 μM $ZnCl_2$	0.2 mM PMSF 1 mM DTT
Sucrose cushion	40 mM Hepes pH 7.4	150 mM KCl 2.5 mM $MgCl_2$	40% Sucrose 0.5 mM DTT
NUFIP1 equilibration buffer	40 mM Hepes pH 7.4	300 mM NaCl 2.5 mM $MgCl_2$	
NUFIP1 elution buffer	40 mM Hepes pH 7.4	300 mM NaCl 2.5 mM $MgCl_2$	25 mM Maltose
Resuspension buffer	40 mM Hepes pH 7.4	150 mM KCl 2.5 mM $MgCl_2$	

Name	Buffer	Salt	Additive
Ribosomal Elution buffer	40 mM Hepes pH 7.4	150 mM KCl 2.5 mM $MgCl_2$	25 mM Maltose
Cryo sucrose cushion	40 mM Hepes pH 7.4	150 mM KCl 10 mM $MgCl_2$ 10 µM $ZnCl_2$	40% Sucrose 0.5 mM DTT
Cryo resuspension buffer	40 mM Hepes pH 7.4	150 mM KCl 10 mM $MgCl_2$ 10 µM $ZnCl_2$	
Cryo elution buffer	40 mM Hepes pH 7.4	150 mM KCl 10 mM $MgCl_2$ 10 µM $ZnCl_2$	25 mM Maltose

Table 14: p62 purification buffers

Name	Buffer	Salt	Additive
Lysis buffer	25 mM Hepes pH 8.0	1 M NaCl 2.5 mM $MgSO_4$ 10 µM $ZnCl_2$	4 mM DTT
Equilibration buffer	25 mM Hepes pH 8.0	500 mM NaCl 2.5 mM $MgSO_4$	4 mM DTT
IMAC wash buffer	25 mM Hepes pH 8.0	500 mM NaCl 2.5 mM $MgSO_4$	4 mM DTT 30 mM Imidazole
IMAC elution buffer	25 mM Hepes pH 8.0	500 mM NaCl 2.5 mM $MgSO_4$	4 mM DTT 300 mM Imidazole
MBP elution buffer	25 mM Hepes pH 8.0	500 mM NaCl 2.5 mM $MgSO_4$	4 mM DTT 25 mM Maltose
Storage buffer	25 mM Hepes pH 7.4	500 mM NaCl 2.5 mM $MgSO_4$	0.5 mM TCEP
Interaction buffer	25 mM Hepes pH 7.4	150 mM NaCl 2.5 mM $MgSO_4$	0.5 mM TCEP

Table 15: GST-fusion protein buffers

Name	Buffer	Salt	Additive
Lysis buffer	25 mM Hepes pH 7.4	300 mM NaCl	4 mM DTT
GST equilibration buffer	25 mM Hepes pH 7.4	300 mM NaCl	1 mM DTT
GST elution buffer	25 mM Hepes pH 7.4	300 mM NaCl	10 mM glutathione (reduced) 1 mM DTT
GST storage buffer	25 mM Hepes pH 7.4	300 mM NaCl	1 mM DTT

5.1.4 Chromatography resins and columns

Chromatography resins used in table-top chromatography and chromatography columns use at ÄKTA pure™ 25 chromatography system or ÄKTA pure™ micro are listed in Table 16.

Table 16: Chromatography resins and columns

Name	System	Manufacturer
Amylose resin	Gravity flow	New England Biolabs; Ipswich, Massachusetts, United States
Glutathione Sepharose™ 4 Fast Flow	Gravity flow	Cytiva; Marlborough, Massachusetts, United States
HiLoad™ 16/600 Superdex™ 200 pg	ÄKTA pure™ 25	Cytiva; Marlborough, Massachusetts, United States
HiLoad™ 16/600 Superose™ 6 pg	ÄKTA pure™ 25	Cytiva; Marlborough, Massachusetts, United States

Name	System	Manufacturer
HiPrep™ 16/60 Sephacryl™ S-500 HR	ÄKTA pure™ micro	Cytiva; Marlborough, Massachusetts, United States
HiPrep™ 26/10 Desalting	ÄKTA pure™ 25	Cytiva; Marlborough, Massachusetts, United States
Protino® Ni-NTA agarose	Gravity flow	Macherey-Nagel; Düren, Germany

5.1.5 Software and online tools

All software and online tools used in this thesis are listed in Table 17 with a short application description and the respective reference.

Table 17: Software

Name	Application	Reference
Amira Software for cell biology	Filtering and display of tomograms	Thermo Fisher Scientific; Eindhoven, the Netherlands
AreTOMO	Tomogram reconstruction	(Zheng et al. 2022b)
Coot	Model building	(Emsley et al. 2010)
CryoSPARC	Processing of EM data	Structura Biotechnology Inc.; Toronto, Canada
CryoSPARC LIVE	Preprocessing of EM data	Structura Biotechnology Inc.; Toronto, Canada
Dragonfly	Tomogram segmentation	(Heebner et al. 2022)
EPU	SPA data acquisition, screening of grids	Thermo Fisher Scientific; Eindhoven, the Netherlands
Expasy - ProtParam	Protein parameters from protein sequence	Swiss Institute of Bioinformatics; Lausanne, Switzerland

Name	Application	Reference
Expasy - Translate	Translate DNA sequence to protein sequence	Swiss Institute of Bioinformatics; Lausanne, Switzerland
Fiji	Visualization fluorescence data, Insertion of scalebars	(Schindelin et al. 2012)
GATAN	Handling of K3	Gatan, Inc.; Pleasanton, California, United States
IMOD	Visualization of tomogram data	Regents of the University of Colorado; Boulder, Colorado, United States
IsoNet	Tomogram denoising and missing wedge correction	(Liu et al. 2022)
LocScale	EM-density map refinement	(Jakobi et al. 2017)
MemBrain	Tomogram segmentation	(Lamm et al. 2022)
MoleculeSketch	Molecular drawings	© 2014 Stefan Dolder
ParaView	Visualization of membrane segmentation	Kitware, Inc; Clifton Park, New York, United States
Phenix	Model refinement	(Liebschner et al. 2019)
SnapGene Viewer	DNA visualization, cloning experiments	SnapGene; Boston, Massachusetts, United States)
Surface Morphometrics	Statistical analysis of membrane segments	(Barad et al. 2022)
TIA	Handling of EM	Thermo Fisher Scientific; Eindhoven, the Netherlands

Name	Application	Reference
Tm Calculator tool	Calculation of melting temperature for DNA primer	New England Biolabs; Ipswich, Massachusetts, United States).
TOMO	Cryo-ET data acquisition	Thermo Fisher Scientific; Eindhoven, the Netherlands
UCSF Chimera	Visualization of EM-density maps	Resource for Biocomputing, Visualization, and Informatics at the University of California; San Francisco, California, United States
UCSF ChimeraX	Visualization of EM-density maps	Resource for Biocomputing, Visualization, and Informatics at the University of California; San Francisco, California, United States
WARP	Preprocessing of EM data	(Tegunov and Cramer 2019)
Zen	Data acquisition light microscopy	Carl Zeiss Microscopy Deutschland GmbH; Oberkochen, Germany

5.2 Molecular biological methods

5.2.1 Plasmid isolation

For amplification, plasmid DNA was transformed into *E. coli* DH5α (C2987; New England Biolabs; Ipswich, Massachusetts, United States) by heat shock as described in the corresponding manual. After transformation, cells were cultivated in an overnight enrichment culture of 7 mL LB-medium at 37°C with the respective antibiotic for selection. Plasmid isolation was performed with the Monarch Plasmid Miniprep Kit (New England Biolabs; Ipswich, Massachusetts, United States) following the standard procedure. The DNA concentration was determined with UV spectrophotometry as described in 5.6.1. The plasmid DNA was frozen at -20°C for storage.

5.2.2 Plasmid isolation for human cell culture

For transfection of mammalian cells, plasmid DNA was transformed into *E. coli* One Shot™ TOP10 (C4040; Thermo Fisher Scientific; Waltham, Massachusetts, United States) by heat shock as described in the corresponding manual. After transformation, cells were cultivated in an overnight enrichment culture of 7 mL LB-medium at 37°C with the respective antibiotic for selection. The main culture was inoculated in 650 mL TB-medium supplemented with the respective antibiotic for selection and cultivated for another 24 h at 30°C. The cells were harvested at 5,000 xg and 10°C (15 min). The supernatant was discarded and the pellet used in plasmid isolation with the QIAGEN Plasmid Plus Maxi Kit (QIAGEN, Venlo, the Netherlands) according to the enclosed manual. The DNA concentration was determined with UV spectrophotometry as described in 5.6.1. The plasmid DNA was frozen at -20°C for storage.

5.2.3 Polymerase chain reaction and Dpn1 digestion

Polymerase chain reaction (PCR) was performed to amplify DNA fragments used in molecular cloning. Primer were designed with SnapGene Viewer (SnapGene, Boston, Massachusetts, United States) and synthesized at Integrated DNA Technologies, BVBA, Leuven, Belgium. The PCR reaction was set up with the Q5® High-Fidelity PCR Kit (New England Biolabs; Ipswich, Massachusetts, United States) as indicated in Table 18.

Table 18: PCR reaction set-up

Component	Volume	Final concentration
5x Q5-buffer	10 µL	1x
dNTPs (10 mM)	1 µL	200 µM
Forward primer	1 µL	0.5 µM
Reverse primer	1 µL	0.5 µM
Template DNA (200 ng/µL)	1 µL	14 ng
Q5 polymerase	0.5 µL	1.0 units
ddH_2O	35.5 µL	-

The annealing temperature of each individual primer was calculated with the Tm Calculator tool (New England Biolabs; Ipswich, Massachusetts, United States). The PCR was performed in a FlexCycler^2 (Analytik Jena AG, Jena, Germany) according to the scheme shown in Table 19.

Table 19: PCR reaction scheme

Step		**Temperature**	**Time**
Initial denaturation		98°C	30 s
30 cycles	Denaturation	98°C	10 s
	Annealing	Tm of respective primer	15 s
	Elongation	72°C	20 s per kb of PCR product
Final extension		72°C	5 min
Hold		4°C	

After PCR, 20 U of DpnI (New England Biolabs; Ipswich, Massachusetts, United States) were added to the reaction to degrade template DNA for 1 h at 37°C. The reaction was stopped by adding 10 µL of DNA loading dye (0.05% (w/v) Bromphenol blue, 34% (v/v) Glycerol, 0.1 M EDTA). Samples were stored at -20°C.

5.2.4 Agarose gel electrophoresis and DNA clean-up

Agarose gel electrophoresis was performed as described before to monitor the success of PCR and Dpn1 digestion (Sambrook and Russell 2001). Agarose gels were prepared shortly before usage with 1% agarose solubilized in TAE buffer containing 5 µL GelRed® Nucleic Acid Stain (Merck KGaA; Darmstadt, Germany) per 50 mL. 10 µL of the GeneRuler 1 kb DNA Ladder (Thermo Fisher Scientific; Waltham, Massachusetts, United States) for size prediction of the DNA fragments and all of the DpnI digestion (5.2.3) were loaded onto the gel. The electrophoreses was performed in TAE buffer for 1 h at a constant voltage of 100 V. Agarose gels were imaged with ChemiDoc™ MP Imaging System (Biorad Laboratories Inc.; Hercules, California, United States). If required, the separated DNA fragments were extracted from the gel and purified with NucleoSpin™ Gel and PCR Clean-up Kit (Macherey-Nagel, Düren, Germany) following the standard procedure. DNA was eluted in the included elution buffer and stored at -20°C.

5.2.5 DNA assembly and transformation for selection

DNA assembly was performed with the NEBuilder® HiFi DNA Assembly Master Mix (New England Biolabs; Ipswich, Massachusetts, United States). The respective backbone DNA was mixed with the insert DNA in the in the manual of the kit recommended ratio and concentration. If necessary, the backbone/insert mix topped up to 10 µL with ddH_2O. 10 µL of the master mix were added to the DNA (final volume 20 µL) and the reaction incubated at 50°C for 15 min sharp. 5 µL of the reaction were transformed into *E. coli* DH5α (New England Biolabs; Ipswich, Massachusetts, United States) by heat shock as described in the corresponding manual. The transformed cells were plated on LB-agar containing the respective antibiotic for selection and incubated overnight at 37°C. To prepare DNA for sequencing, multiple colonies were picked and cultivated in 7 mL LB-medium containing the respective antibiotic at 37°C overnight. The DNA was isolated as described in 5.2.1 and send to sequencing according to 5.2.6.

5.2.6 Sanger Sequencing

To validate all pre-existing and newly cloned constructs, the plasmid DNA was sequenced by the Sanger method (Sanger et al. 1977) at Microsynth AG (Balgach, Switzerland). The samples were prepared according to the requirements of the company. The results were obtained as DNA sequence and sequencing results were analyzed with SnapGene Viewer (SnapGene; Boston, Massachusetts, United States).

5.3 Human cell culture

5.3.1 Quantifying cell density in liquid cultures with cell counting

Quantification of cells in liquid medium was performed by cell counting. The viability of the culture was examined with the trypan blue exclusion test of cell viability (Strober 1997). To do so, samples were mixed 1:1 with trypan blue (Thermo Fisher Scientific; Waltham, Massachusetts, United States) and 10 µL loaded into a Countess™ Cell Counting Chamber Slide (Thermo Fisher Scientific; Waltham, Massachusetts, United States). Cell density and viability was determined at the Countess II automated cell counter (Thermo Fisher Scientific; Waltham, Massachusetts, United States). Afterwards, the sample was discarded.

5.3.2 Maintenance of FreeStyle™ 293-F cell line

In this thesis the FreeStyle™ 293-F cell line (Thermo Fisher Scientific; Waltham, Massachusetts, United States) was used for transient protein expression in suspension. In all steps cells were cultivated in Gibco™ FreeStyle™ 293 Expression Medium (Thermo Fisher Scientific; Waltham, Massachusetts, United States) (expression medium), unless stated otherwise. All cell culture media, additives, and disposables were sterilized before usage and cell passaging performed in a sterile hood. Cells were stored in 1 mL aliquots in cryopreservation below -130°C. For cell culture experiments, cells were thawed at 37°C and immediately after thawing were added into 9 ml of pre-warmed expression medium. The resuspension was centrifuged at 100 xg, 37°C for 5 min. The supernatant was discarded and the pellet resuspended in 30 ml pre-warmed expression medium supplemented with 1:100 Penicillin-Streptomycin (10.000 U/ml) (Thermo Fisher Scientific; Waltham, Massachusetts, United States). Cells were incubated in sterile single-use Erlenmeyer flasks with plain bottom (Thermo Fisher Scientific; Waltham, Massachusetts, United States) at 37°C and 8% CO_2 in a Minitron incubation shaker (Infors HT; Bottmingen, Switzerland) with a shaking diameter of 5 cm. Dependent on the culture size, the size of the flask and shaking rate was adjusted to ensure sufficient oxygen supply and a low shear force, see Table 20 for details. The cell count was kept between 0.5 to $3x10^6$ cells/mL and before starting transfection experiments cells were passaged at least three times.

Table 20: HEK293F cell culture

Culture volume	Flask size	Shaking rate
30 mL	125 mL	125 rpm
100-200 mL	500 mL	125 rpm
200-400 mL	1000 L	100 rpm
400-800 mL	2000 L	100 rpm

5.3.3 Transient protein expression in FreeStyle™ 293-F cells

To transiently express target proteins in FreeStyle™ 293-F cell line (Thermo Fisher Scientific; Waltham, Massachusetts, United States), plasmid DNA was transfected into the cells by polyethylenimine (PEI). Cells were cultivated as described in 5.3.2 and the last passage was performed 48 h before transfection. The cell count and viability of the culture was determined as described in 5.3.1. A 1 mL sample of the culture was harvested at 2,000 xg, 4°C for 4 min The supernatant was discarded and the pellet frozen at -20°C for SDS-PAGE. The culture was harvest in a sterile centrifugation cone at 100 xg and 37°C for 5 min. The supernatant was discarded and the cell pellet resuspended in 90% of the volume needed to obtain a cell density of $3x10^6$ cells/mL. The cells were incubated for 1 h at 37°C, and 8% CO_2 before transfection. Plasmid DNA was prepared at high concentration as described in 5.2.2. To transfect the cells with 1.0 µg/mL plasmid DNA, the respective amount of plasmid DNA was added into 5% of the volume needed to obtain a cell density of $3x10^6$ cells/mL in expression medium. 3 µg linear polyethyleneimine (PEI) (Merck KGaA; Darmstadt, Germany) per $1x10^6$ cells were prepared from a 1 mg/mL PEI stock solution in the remaining 5% of the volume needed to obtain a cell density of $3x10^6$ cells/ml in expression medium. The DNA and PEI solutions were sterile filtered and mixed by adding PEI to DNA drop by drop. The DNA/PEI mix was incubated at RT for 5 min before adding it into the culture drop by drop. The cells were cultivated at 37°C and 8% CO_2 for 24 h. After 24 h the cell count and viability of the culture was determined as described in 5.3.1. 10 µL of the culture were used in bright field microscopy at ZEISS Axio Observer (Carl Zeiss Microscopy Deutschland GmbH; Oberkochen, Germany) in phase contrast and with a filter set for green fluorescence. A 1 mL sample was taken as described above for SDS-PAGE. The culture was diluted 1:3 with expression medium and valproic acid (VPA) (Merck KGaA; Darmstadt, Germany) was added to a final concentration of 3.75 mM. The culture was supplemented with 1:100 Penicillin-Streptomycin (10.000 U/ml) (Thermo Fisher Scientific; Waltham, Massachusetts, United States). After 48 and 72 h, the cell count and viability was checked as described in 5.3.1, light microscopy performed and a sample for SDS-PAGE was taken as described above. After 72 h the culture was harvested at 2,000 xg for 5 min, the supernatant was discarded, and the pellet weighed and frozen at -80°C. SDS-samples were resuspended in RIPA Lysis and Extraction Buffer (Thermo Fisher Scientific; Waltham, Massachusetts, United States) to a final concentration of 5x10^6 cells/mL. The lysis was performed at 4°C for 15 min with constant mild mixing. The cell debris was pelleted by centrifugation at 20,000 xg for 20 min, the supernatant decanted and used in SDS-PAGE as described in 5.6.3.

5.3.4 Maintenance of HeLa

HeLa cells were obtained from Markus Tusche (IBG-7) and the 1 mL aliquots in cryopreservation maintained by Sabrina Berkamp (ER-C-3). A 1 mL aliquot was quickly thawed at 37°C and mixed with 9 mL DMEM-medium (pre-warmed). The cells were pelleted by centrifugation at 100 xg and 37°C for 5 min. The supernatant was discarded and the pellet resuspended in 12 mL pre-warmed DMEM-medium and transferred into Falcon® 75cm² rectangular straight neck cell culture flask with vented cap (Corning Inc; Corning, New York, United States). Cells were incubated at 37°C and 5% CO_2. The cells were maintained for at least five passages after thawing before immunofluorescence and transient protein expression experiments. Cells were passaged at a confluency of 70-80% and split 1:13.

5.3.5 Immunofluorescence staining and imaging

Immunofluorescence staining and imaging was performed with HeLa cells and target specific antibodies. The cells were seeded with a density of 50,000 cells/dish in 2 mL DMEM-medium 24 h before transfection in a CELLview cell culture dish, one compartment, TC treated, sterile (Greiner Bio-One; Kremsmünster, Austria) and incubated at 37°C and 5% CO_2. To test different conditions of autophagy induction, the DMEM-medium was removed and replaced by EBSS, DMEM-medium without glucose (both 4 h incubation time) or DMEM-medium containing 250 nM mTOR-Inhibitor XI, Torin 1 (Merck KGaA; Darmstadt, Germany) (2 h incubation time). As a control DMEM-medium was replaced by fresh DMEM-medium. The medium was removed and cells washed with 2 mL cold Gibco™ PBS pH 7.4 (Thermo Fisher Scientific; Waltham, Massachusetts, United States) before adding 2 mL of cold methanol. Methanol fixation and permeabilization was performed for 10 min at -20°C. The methanol was removed and the fixed cells washed thrice with 1 mL of 5% bovine serum albumin (Merck KGaA; Darmstadt, Germany) in Gibco™ PBS pH 7.4 (Thermo Fisher Scientific; Waltham, Massachusetts, United States) (5% BSA). The last washing step was incubated for 10 min at room temperature to block all possible protein binding sites. Each dish was incubated with 500 µL of the respective antibody solution in 5% BSA. The NUFIP1 antibody (PA5-56308) produced in rabbit (Thermo Fisher Scientific; Waltham, Massachusetts, United States) was used in a working dilution of 1:500 and the Anti-p62 (SQSTM1) pAb (PM045) produced in rabbit (MEDICAL & BIOLOGICAL LABORATORIES CO., LTD; Tokyo, Japan) in a dilution of 1:500. Fixed cells were incubated with the first antibody for 1 h at room temperature. The antibody solution was removed and the fixed cells were washed thrice with 1 mL 5% BSA. Each dish was incubated with 500 µL of the secondary antibody (anti-rabbit IgG (H+L), CF™ 488A antibody produced in goat (SAB4600044) (Merck KGaA; Darmstadt, Germany)) in a 1:500 working dilution in 5% BSA for 45 min at room temperature in the dark. Afterwards, the fixed cells were washed four times with Gibco™ PBS pH 7.4 (Thermo Fisher Scientific; Waltham, Massachusetts, United States) and finally incubated in 500 µL Gibco™ PBS pH 7.4 (Thermo Fisher Scientific; Waltham, Massachusetts, United States) with one drop of NucBlue™ Live ReadyProbes™ Reagent (Hoechst 33342) (Thermo Fisher Scientific; Waltham, Massachusetts, United States) for 20 min in the dark. The cells were sealed with a coverslip and imaged at a ZEISS Axio Observer (Carl Zeiss Microscopy Deutschland GmbH; Oberkochen, Germany) in phase contrast and with a filter set for green fluorescence.

5.3.6 Transient protein expression in HeLa and live cell imaging

To transiently expression target proteins in HeLa cells and observe their cellular location, plasmid DNA was transfected into the cells by non-liposomal transfection with FuGENE® HD Transfection Reagent (Promega Corporation, Madison, Wisconsin, United States). Plasmid DNA was prepared at high concentrations as described in 5.2.2. Cells were seeded with a density of 50,000 cells/dish in 2 mL DMEM-medium 24 h before transfection in a CELLview cell culture dish, one compartment, TC treated, sterile (Greiner Bio-One; Kremsmünster, Austria) and incubated at 37°C and 5% CO_2. To transfect the cells with a ratio of 1 µg DNA to 3 µL transfection agent, 2 µg plasmid DNA and 6 µL FuGENE® HD Transfection Reagent (Promega Corporation, Madison, Wisconsin, United States) were mixed in 200 µL DMEM-medium. The transfection mixture was incubated at room temperature for 5 min. The medium in the dish was replaced by 1.8 mL fresh DMEM-medium and each dish was transfected with 200 µL of transfection mixture. Cells were incubated at 37°C and 5% CO_2.

To test different conditions of autophagy induction, the DMEM-medium was removed after 24 h and replaced by EBSS, DMEM-medium without glucose (both 4 h incubation time) or DMEM-medium containing 250 nM mTOR-Inhibitor XI, Torin 1 (Merck KGaA; Darmstadt, Germany) (2 h incubation time). As a control DMEM-medium was replaced by fresh DMEM-medium. 20 min before imaging, two drops of NucBlue™ Live ReadyProbes™ Reagent (Hoechst 33342) (Thermo Fisher Scientific; Waltham, Massachusetts, United States) was added to the cells. Confocal fluorescence microscopy was performed at a LSM 700 (Carl Zeiss Microscopy Deutschland GmbH; Oberkochen, Germany) with an Objective Plan-Apochromat 63x/1.4 Oil DIC M27 (Carl Zeiss Microscopy Deutschland GmbH; Oberkochen, Germany).

5.4 Microbiological Methods

5.4.1 Quantifying cell density in liquid cultures with OD_{600}

The intensity loss of an incident beam of light at λ = 600 passing through a bacterial culture is mostly due to scattering of the light by the cells. The loss in initial intensity follows the Lambert-Beer Law which is described in 5.6.1 in detail resulting in a direct relation between intensity loss and cell density in the culture. Thereby the relation between intensity loss and cell number is only linear in a range until approximately $OD_{600} = 0.8$, so samples with a higher absorbance need to be diluted with fresh medium until the $OD_{600} < 0.8$ (Mandelstam and McQuillen 1973). To quantify the cell density in a culture, the optical density at $\lambda = 600$ nm (OD_{600}) was determined with a DiluPhotometer™ (Implen; Munich, Germany). Pure medium was used as a blank to correctly determined the intensity loss of the culture. If the absorbance was above $OD_{600} = 0.8$, the culture was diluted with fresh medium and the obtained OD_{600} multiplied by the dilution factor.

5.4.2 Transformation and Pre-culture

Transformation of plasmid DNA into *E. coli* BL21(DE3) (C2527; New England Biolabs; Ipswich, Massachusetts, United States) was performed applying the heat shock method (Van Die et al. 1983). For transformation, the cells were gently thawed on ice, plasmid DNA in a ratio of 200 ng DNA per 50 µL cells added, and the cells left on ice for 30 min. The heat shock was performed at 42°C for 30 s in a ThermoMixer® C equipped with SmartBlock 1.5 mL (Eppendorf SE; Hamburg, Germany). Directly after the heat shock, 700 µL of LB-medium were added to the cells, and the cells incubated for 1 h at 37°C and 600 rpm in a ThermoMixer® C equipped with SmartBlock 1.5 mL (Eppendorf SE; Hamburg, Germany) to regenerate. Afterwards, the culture was spun down at 2,000 xg for 4 min and 700 µL of the supernatant were removed. The pellet was resuspended in the remaining supernatant. The resuspension was used to inoculate a pre-culture in 40 mL LB-medium with the respective antibiotic for selection. Liquid pre-cultures were incubated at 37°C and 130 rpm in a Multitron Pro incubation shaker (Infors HT; Bottmingen, Switzerland).

5.4.3 Recombinant protein expression in *E. coli* BL21(DE3)

The expression of target proteins in *E. coli* was regulated by the T7 promoter which is recognized only by the T7 polymerase. In *E. coli* BL21(DE3) (C2527; New England Biolabs; Ipswich, Massachusetts, United States) the expression of the T7 polymerase is under the regulation of the lac operon and requires induction. The expression medium was manually supplemented with IPTG to induce T7 polymerase protein expression and consequently target protein expression at a particular cell density. IPTG is a molecular mimic of lactose, which activates expression similarly but cannot be metabolized (Marbach and Bettenbrock 2012). The overall procedure of protein expression and cell harvest was similar for the different target proteins. First, the OD_{600} of the pre-culture was determined (5.4.1). To calculate the volume of pre-culture needed to achieve the starting OD_{600} in the expression culture, the following equation was used:

$$V_{pre} = V_{expr} \cdot \frac{OD_{600,expr}}{OD_{600,pre}} \tag{2}$$

where $\mathbf{V_{pre}}$ is the needed inoculation volume of the pre-culture [mL], $\mathbf{OD_{600,pre}}$ the OD_{600} of the pre-culture [-], $\mathbf{V_{expr}}$ the total volume of the expression culture [mL], and $\mathbf{OD_{600,expr}}$ the starting OD_{600} of the expression culture [-]. The calculated volume of pre-culture was added to freshly prepared medium of the expression culture containing the respective antibiotic for selection in a sterile hood. Expression cultures were cultivated in TB-medium with 250 mL medium in a 2 L Erlenmeyer flask with three baffles at 120 rpm in a Multitron Pro incubation shaker (Infors HT; Bottmingen, Switzerland). The starting temperature was 37°C and the desired starting $OD_{600} \approx 0.05$. The OD_{600} of the expression culture was monitored at different time points to track cell growth and determine the right time for induction ($OD_{600} \approx 2$-3). For all p62-constructs, the temperature was set to 22°C after induction and the culture was cultivated overnight (at least 20 h). All LC3B variants, GST-4xUb, and GST-HRV3C were cultivated for 4 h at 37°C after induction. Before cell harvest, the OD_{600} was checked. To harvest the cells, the entire expression culture was centrifuged at 5,000 xg and 10°C for 15 min. The supernatant was discarded. The pellets were resuspended in 0.9% sodium chloride, the resuspension transferred into a 50 mL conical centrifugation tube and centrifuged at 5,000 xg and 10°C for 10 min. The supernatant was discarded, the pellets were weighed and frozen at -20°C.

5.5 Purification and sample preparation

5.5.1 Fractionation of FreeStyle^{TM} 293-F

Since eucaryotic cells contain several different organelles surrounded by a membrane barrier, the cytoplasmic fraction can be separated from those already during lysis (Holden and Horton 2009). All following steps were conducted at 4°C, either on ice or in the cold room. All devices were cleaned with disinfection and afterwards rinsed with ddH_2O. To avoid RNase contamination, the workspace was repeatedly cleaned with RNase*Zap*™ (Thermo Fisher Scientific; Waltham, United States). To split FreeStyle™ 293-F (Thermo Fisher Scientific; Waltham, United States) into nuclear, cytoplasmic and ribosomal fraction, first, a mild cell lysis was performed by resuspending the cell pellet (m = 6.71 g) in 20 mL hypotonic buffer with one cOmplete™ (EDTA-free Protease Inhibitor Cocktail) (Merck KGaA; Darmstadt, Germany) and 0.2 U/mL RNasin® Ribonuclease Inhibitor (Promega Corporation, Madison, Wisconsin, United States). After swelling of the cells due to the hypotonic conditions of the buffer, the plasma membrane was disrupted with ten strokes in a glass Dounce homogenizer with the loose (Type A) pestle. The efficiency of the lysis was confirmed under the light microscope with trypan blue staining. Cells with a disrupted cell wall accumulate the dye and appear as blue in the light microscope, while healthy cells remain unstained (Strober 1997). Intact nuclei were collected at 3,300 xg for 15 min (4°C). The supernatant (cytoplasmic + ribosomal fraction) was decanted and the pellet resuspended in 20 mL nuclear lysis buffer (nuclear fraction). Disruption of the nuclei in the nuclear fraction was performed in a glass Dounce homogenizer with the tight (Type B) pestle and ten strokes. To clear the nuclear proteins from cellular debris, the nuclear fraction was centrifuged at 30,000 xg and 4°C for 30 min. The supernatant was decanted and the pellet discarded. To separate the ribosomal from the cytoplasmic fraction, a density gradient centrifugation was performed (Khatter et al. 2014). Four 10 mL 40% sucrose cushions were prepared in 26.3 mL polycarbonate bottles (Beckman Coulter; Brea, California, United States). The salt content of the cytoplasmic + ribosomal fraction was adjusted to 300 mM with 5 M sodium chloride stock solution, and 5 mL loaded onto each of the sucrose cushions. Ultracentrifugation was performed at 100,000 xg and 4°C for 16 h in a Type 70 Ti rotor (Beckman Coulter; Brea, California, United States) and an Optima™ XPN-80 centrifuge (Beckman Coulter; Brea, California, United States) at 4°C. The supernatant (cytoplasmic fraction) was decanted, the pellets washed each with 6 mL resuspension buffer, and pooled into 25 mL resuspension buffer (ribosomal fraction). For all three fractions, 3 mL of amylose resin (New England Biolabs; Ipswich, Massachusetts, United States) were equilibrated in either NUFIP1 equilibration buffer (nuclear and cytoplasmic fraction) or resuspension buffer (ribosomal fraction). The respective fraction was loaded and the flow through collected. The resin was washed with 10 CV of the respective equilibration buffer, and proteins eluted in NUFIP1 elution buffer (nuclear and cytoplasmic fraction) or ribosomal elution buffer (ribosomal fraction). Elution fractions were collected à 1 CV (E_1-E_{10}). The protein or RNA concentration in the elution fractions was determined as described in 5.6.1. Of all fractions, SDS-samples for SDS-PAGE were prepared by mixing 40 µL of sample with 10 µL 5x SDS-dye.

5.5.2 Ribosome extraction from FreeStyle™ 293-F for SPA

Ribosomes of three different conditions were extracted for comparison. To induce autophagy, FreeStyle™ 293-F cells (Thermo Fisher Scientific; Waltham, Massachusetts, United States) were incubated with 250 nM mTOR-Inhibitor XI, Torin 1 (Merck KGaA; Darmstadt, Germany) for 2 h before harvest. To increase bound NUFIP1 to the ribosomes, FreeStyle™ 293-F cells (Thermo Fisher Scientific; Waltham, Massachusetts, United States) were transfected with MBP-NUFIP1 as described in 5.3.3. As control cells were incubated in expression medium and directly harvested.

The cell pellets were resuspended in 1.25 mL cryo lysis buffer per 1 g supplemented with one cOmplete™ (EDTA-free Protease Inhibitor Cocktail) (Merck KGaA; Darmstadt, Germany) per 50 mL and 0.2 U/mL RNasin® Ribonuclease Inhibitor (Promega Corporation, Madison, Wisconsin, United States). The plasma membrane was disrupted in a glass Dounce homogenizer with the tight (Type B) pestle with 20 strokes. The cell debris was removed by centrifugation at 30,000 xg, 4°C for 30 min. The supernatant was decanted and used in density gradient ultracentrifugation. 10 mL of the 40% sucrose cushion were prepared in 26.3 mL polycarbonate bottles (Beckman Coulter; Brea, California, United States) and 12 mL cell lysis layered on top. Ultracentrifugation was performed at 100,000 xg and 4°C for 16 h in a Type 70 Ti rotor (Beckman Coulter; Brea, California, United States) and an Optima™ XPN-80 centrifuge (Beckman Coulter; Brea, California, United States) at 4°C. The supernatant was discarded, and the pellets washed with each 6 mL cryo resuspension buffer. All pellets were pooled into 4 ml of cryo resuspension buffer. For ribosomes extracted from the MBP-NUFIP1 transfected cells, 3 mL of regenerated amylose resin were equilibrated in cryo resuspension buffer. The resuspended ribosomes were loaded, the flow through was collected, and the resin washed with 10 CV cryo resuspension buffer. Bound proteins were eluted with cryo elution buffer and fractions E_1-E_8 collected (1 mL). The RNA content in the elution fractions was determined by UV absorbance spectrophotometry (5.6.1). E_2 and E_3 as well as the resuspension of the control and Torin 1 sample were concentrated by ultracentrifugation at 150,000 xg, 4°C for 17 h in a TLA-55 Fixed-Angle Rotor (Beckman Coulter; Brea, California, United States) and an Optima^{TM} MAX-XP (Beckman Coulter; Brea, California, United States). The supernatant was removed, the pellets resuspended in 20 µL resuspension buffer. The RNA content in the elution fractions was determined by UV absorbance spectrophotometry (5.6.1), and SDS-samples prepared of all fractions. The resuspended ribosomes were subsequently plunge frozen as described in 5.7.2.

5.5.3 Cell lysis of *E. coli* BL21(DE3)

Mechanical cell lysis prior to purification was performed utilizing high-pressure homogenization. The respective pellet was thawed on ice and all following steps were conducted on ice unless stated otherwise. The pellet was resuspended in 50 mL lysis buffer containing one cOmplete™ (EDTA-free Protease Inhibitor Cocktail) (Merck KGaA; Darmstadt, Germany) per 5 g of cell pellet. The lysis buffer was protein dependent, see Table 14 and Table 15 for details. The resuspension was homogenized in a glass homogenizer (DWK Life Sciences Kimble™ Kontes™ Dounce Tissue Grinders (Thermo Fisher Scientific; Waltham, Massachusetts, United States) with a clearance of 0.07 mm. The volume of the resuspension was adjusted with lysis buffer to a total of 10 mL per 1 g of cell pellet. Afterwards, the resuspension was pumped through a CF1 Cell Disrupter (high-pressure homogenizer) (I&L Biosystems GmbH; Königswinter, Germany) cooled to 20°C at 1.7 bar. The procedure was repeated three times; the resuspension was kept on ice in between. To clear the soluble fraction from the insoluble cell debris, the homogenate was centrifuged at 50,000 xg and 10°C for 30 min. The supernatant was immediately decanted from the pellet and used as load (L) in either immobilize metal ion affinity chromatography (5.5.4) or Glutathione S-transferase affinity chromatography (5.5.6) for protein purification.

5.5.4 Immobilized metal ion affinity chromatography

For purification of MBP-p62 and MBP-mCherry-p62, immobilized metal ion affinity chromatography (IMAC) was used as a first chromatographic purification step since both proteins contained an artificial 6x histidine tag (His-tag). In IMAC, it is taken advantage of the fact that polyhistidine binds to immobilized metal ions, whereas most other host proteins do not and flow through the column. Elution of the His-tagged proteins can either be achieved by adding a competing substance, e.g. imidazole, or shifting the pH to an acidic milieu (Hengen 1995). The IMAC was performed as gravity flow chromatography in an Econo-Column® (Bio-Rad Laboratories Inc.; Hercules, United States) with a diameter of 2.5 cm packed with Ni-NTA resin (Table 16). The column volume (CV) of the resin was dependent on the weighed of the pellet, approximately 0.5 mL of resin were used per 1 g of cells. All following steps were performed at 4°C, samples were kept at 4°C or on ice. Before loading, the resin was washed with 4 CV ddH$_2$O and equilibrated in 4 CV equilibration buffer. The cleared cell lysate was loaded onto the column completely (L), and the flow-through (FT) collected. The first washing step was performed with 4 CV lysis buffer (W1) and the second washing step with 3 CV IMAC wash buffer (W2). W1 and W2 were collected. The elution was carried out with IMAC elution buffer and collected in fractions of 5 mL (E$_1$-E$_{10}$). A sample of each step was taken for SDS-PAGE analysis. The respective elution fraction(s) containing the target protein were used in Maltose-binding protein affinity chromatography (5.5.5) (MBP-p62) or preparative size exclusion chromatography (5.5.7) (MBP-mCherry-p62).

5.5.5 Maltose-binding protein affinity chromatography

Maltose-binding protein (MBP) affinity chromatography is based on the specific interaction of MBP with amylose. Elution of bound MBP can be achieved by adding maltose in the elution buffer (Ferenci and Klotz 1978). 5 mL of amylose resin (Table 16) were equilibrated in equilibration buffer in a gravity flow Econo-Column® (Bio-Rad Laboratories Inc.; Hercules, United States) with a diameter of 2.5 cm. All following steps were performed at 4°C, samples were kept at 4°C or on ice. The elution of the IMAC was loaded onto the column and incubated for 30 min. The flow-through (FT) was collected and the resin washed with 10 CV of equilibration buffer. MBP elution buffer was used to elute bound proteins and elution fractions collected á 5 mL (E_1-E_8). A sample of each step was taken for SDS-PAGE analysis. The respective elution fraction(s) containing the target protein were used in desalting chromatography (5.5.8).

5.5.6 Glutathione S-transferase affinity chromatography

For purification of GST-LC3B(e)/(-Cys) and GST-4xUbiquitin, Glutathione S-transferase (GST) affinity chromatography was performed (Smith and Johnson 1988). Per 1 g of pellet, approximately 0.75 mL of GST affinity resin (Table 16) were equilibrated in GST equilibration buffer. The complete lysate was loaded onto the column (L) and the flow through (FT) collected. The affinity resin was washed with 10 CV GST equilibration buffer and the wash (W) collected. Proteins were eluted in GST elution buffer and elution fractions (E_1-E_8) á 1 CV collected. Of all fractions SDS-samples for SDS-PAGE were prepared. The respective elution fraction(s) containing the target protein were used in desalting chromatography (5.5.8) (GST-LC3B(e)/(-Cys)) or preparative size exclusion chromatography (GST-4xUbiquitin).

For purification of LC3B(e)/(-Cys) after GST-HRV3C digestion, 1 mL of GST affinity resin was loaded into a 1 mL column operated with a syringe. The column was equilibrated in GST equilibration buffer and the digestion reaction loaded. The flow through (FT) was collected as it contained the protein of interest. The column was washed with 2 CV of GST equilibration buffer and the wash collect in two equal fractions (W_1,W_2). Bound proteins were eluted in 4 CV GST elution buffer and two elution fractions of equal size collected (E_1,E_2). Of each fraction a sample for SDS-PAGE was prepared and the fractions containing the target protein were pooled for further experiments.

5.5.7 Preparative size exclusion chromatography

To polish the elution fractions of IMAC or GST affinity chromatography, a preparative size exclusion chromatography (pSEC) was implemented utilizing an

ÄKTA pure™ 25 (Cytiva; Marlborough, Massachusetts, United States). The porous material used in size exclusion chromatography separates analytes due to their hydrodynamic radius and is therefore suitable for separating proteins with different sizes and conduct buffer change (Barth et al. 1994). The chromatography column used was dependent on the target protein size and sample volume. MBP-mCherry-p62 forms larger oligomers and was loaded onto a HiLoad™ 16/600 Superose™ 6 pg (Cytiva; Marlborough, Massachusetts, United States) while GST-4xUbiquitin was further purified with HiLoad™ 16/600 Superdex™ 200 pg (Cytiva; Marlborough, Massachusetts, United States). The selected column was equilibrated in the respective storage buffer prior to the run. The elution was loaded onto the column by manual load exploiting the maximal sample volume of the columns according to the manufacturer. If the volume of the elution fractions exceeded the maximal recommend load, membrane filtration was applied to concentrate the sample to a suitable volume (5.5.9). Isocratic elution was performed in 1.2 CV of the respective storage buffer and collected in 1 or 2 mL fractions with a Fraction Collector F9-R (Cytiva; Marlborough, Massachusetts, United States). The absorbance at wavelengths λ = 280 nm in the elution was monitored and plotted against the elution volume. The resulting chromatogram was analyzed regarding the elution volume of absorbance peaks and their peak height. Additionally, a sample of the elution fraction of each peak maximum was taken for SDS-PAGE. The elution fractions containing the target protein were identified and pooled. The protein concentration in the pool was determined with UV absorbance spectrophotometry (5.6.1) and the pool aliquoted, flash frozen in liquid nitrogen and aliquots stored at -80°C.

5.5.8 Desalting chromatography

For desalting/buffer change, the HiPrep™ desalting column (Cytiva; Marlborough, Massachusetts, United States) connected to an ÄKTA pure™ 25 (Cytiva; Marlborough, Massachusetts, United States) was utilized. The column was equilibrated in the respective storage buffer, and 5 – 10 mL of sample loaded with a capillary loop. If the volume of the elution fractions exceeded the maximal recommend load, membrane filtration was applied to concentrate the sample to a suitable volume (5.5.9). The elution was collected with Fraction Collector F9-R

(Cytiva; Marlborough, Massachusetts, United States) in 3 mL fractions. The UV absorbance in the elution was monitored at λ = 280 nm and the respective fractions containing protein picked and pooled. The protein concentration in the pool was determined with UV absorbance spectrophotometry (5.6.1) and the pool aliquoted, flash frozen in liquid nitrogen and aliquots stored at -80°C.

5.5.9 Membrane filtration

The molecular weight cut-off (MWCO) of the concentrator (Amicon® Ultra Centrifugal Filters 0.5-15 mL (Merck KGaA; Darmstadt, Germany)) was selected according to the size of the target protein. The MWCO was choosen to be at least two times smaller than the estimated protein weight to retain the target protein while buffer and small molecules are able to pass the membrane. Before usage, the concentrator was rinsed with ddH_2O to wash off fabrication residues and afterwards equilibrated in sample buffer. Membrane filtration was performed at 3,000 xg and 10°C to either increase protein concentration in the sample or reduce the sample volume. The protein concentration was monitored by UV absorbance spectrophotometry (5.6.1).

5.6 Biochemical, biophysical, and immunological Methods

5.6.1 Quantitation of nucleotide/protein concentration in solution with UV absorbance spectrophotometry

Biomolecules show absorbance maxima of UV light at characteristic wavelengths (DNA: λ = 260 nm; proteins: λ = 280 nm) with a linear relationship between absorbance and concentration of the analyte described by the Lambert-Beer-Law:

$$A_\lambda = log_{10}\left(\frac{I_0}{I_T}\right) = \varepsilon_\lambda \cdot c \cdot d \tag{3}$$

where $\mathbf{A_\lambda}$ is the absorbance at wavelength λ [-], $\mathbf{I_0}$ the incident intensity [-], $\mathbf{I_T}$ the transmitted intensity [-], $\boldsymbol{\varepsilon_\lambda}$ the molar extinction coefficient [$M^{-1} \cdot cm^{-1}$], **c** the concentration of analyte in solution [M], and **d** the path length of the sample [cm]. Therefore, the DNA or protein concentration of samples was determined with UV spectrophotometry applying the Lambert-Beer-Law (Lambert 1760; Grimsley and Pace 2003). The molecular extinction coefficient of double-stranded DNA is sequence independent and given as an average mass extinction coefficient of

$0.02\ M^{-1}\cdot cm^{-1}$ (Sambrook and Russell 2001). The molecular extinction coefficient of proteins is sequence-dependent and was calculated for each target protein with the Expasy - ProtParam tool (Swiss Institute of Bioinformatics; Lausanne, Switzerland). The absorbance at $\lambda = 260$ or $\lambda = 280$ nm was measured with a NanoDrop Microvolume Spectrophotometer (Thermo Fisher Scientific; Waltham, Massachusetts, United States) at room temperature. The total sample volume was 2 µL. The respective buffer was used as blank for absorbance correction.

5.6.2 Quantification of lipids by fluorescence spectrophotometry

Quantification of lipids by fluorescence spectrophotometry was performed in the Infinite® M Nano (Tecan Group AG; Männedorf, Switzerland) plate reader. The basis for concentration determination is similar as described in 5.6.1 with a linear relationship between concentration of the ATTO 390 dye and the fluorescent signal. Measurements were performed in a Greiner 96-well microtiter plate with flat bottom and black polypropylene wells (Greiner Bio-One; Kremsmünster, Austria) with a volume of 75 µL per sample. The excitation wavelength was set to 390 nm and an emission scan performed from 420 to 550 nm with a step of 5 nm. Gain and Z-positioning were calculated from the well containing the highest dilution of the calibration curve. For the calibration curve, the following dilutions of the extruded lipids were measured: 0.06 mg/mL, 0.3 mg/mL, 2 mg/mL. The fluorescence signal of the first peak of the SEC of LC3B-Cys coated liposomes (described in 5.6.6) was simultaneously measured. The fluorescence signal of the calibration was plotted over the lipid concentration and linear regression applied. The obtained signal of sample was inserted into the linear regression to determine the lipid concentration in the fraction.

5.6.3 SDS-Polyacrylamide gel electrophoresis

SDS-Polyacrylamide gel electrophoresis (SDS-PAGE) was carried out as previously described (Laemmli 1970). SDS-samples were cooked for 5 min at 95°C in a ThermoMixer® C equipped with SmartBlock 1.5 mL (Eppendorf SE; Hamburg, Germany). Electrophoresis was performed in Western-Ready MES SDS-PAGE Running Buffer (10X) (Biozym Scientific GmbH; Oldendorf, Germany) at 180 V for roughly 35 min depending on the size of the target protein with 4-12% Bis-Tris gels

(Merck KGaA; Darmstadt, Germany). For molecular weight estimation, a molecular weight marker was loaded onto the SDS-gel in addition to the samples. To visualize the protein bands within the gel, the gel was stained with InstantBlue® Coomassie Protein Stain (ISB1L) (Abcam; Cambridge, United Kingdom) (Zehr et al. 1989). The SDS-gel was incubated in Coomassie staining solution (preheated to 60°C) for 15 min before destaining in ddH_2O until the protein bands were clearly visible. The Coomassie-stained SDS-gels were documented with the Azure Sapphire RGB Biomolecular Imager (azure biosystems; Dublin, California, United States).

5.6.4 Immunospecific staining of SDS-gels (Western Blot)

To detected and identify target proteins with specific antibodies, Western Blots of SDS-gels were made. After SDS-Page (5.6.3), the SDS-gel was blotted onto a PVDF membrane instead of Coomassie staining. To transfer the proteins the Trans-Blot Turbo Transfer System (Biorad Laboratories Inc.; Hercules, California, United States) with the Trans-Blot Turbo Mini 0.2 µm PVDF Transfer Packs (Biorad Laboratories Inc.; Hercules, California, United States) was used. The blot was assembled as follow in the cassette: four filter paper, membrane, SDS-gel, four filter paper. The electrophoresis was carried out for 7 min at 25 V and 1.3 A. After blotting, the membrane was transferred into a 50 mL conical centrifugation tube and washed with TBS-T (2x 5 min, 1x 15 min) on a roll mixer. All following steps were conducted on a roll mixer to ensure an equal distribution of buffer over the membrane. Non-fat dried milk powder was suspended in TBS-T (5% (w/v)) to block all remaining free binding sites of the membrane. The membrane was incubated with the blocking buffer for 1 h. To wash off all unbound milk powder, a washing step was performed by incubation of the membrane in 15 mL TBS-T (2x 5 min, 1x 15 min). The primary antibody was diluted to a final concentration of 1 µg/mL in 10 mL TBS-T and the membrane was incubated with the solution for at 4°C overnight. To wash off all unbound primary antibody, a washing step was performed with 15 mL TBS-T (2x 5 min, 1x 15 min). The secondary antibody was diluted to a final concentration of 1 µg/mL in 10 mL TBS-T and the membrane was incubated with the solution for 2 h at 4°C. To wash off all unbound secondary antibody, a washing step was performed with 15 mL TBS-T (2x 5 min, 1x 15 min). For detection, the Amersham™ ECL™ Prime Western Blotting Detection Reagent

(Cytiva; Marlborough, Massachusetts, United States) was used. The signal of the peroxidase (HRP) coupled to the secondary antibody was detected with the Azure Sapphire RGB Biomolecular Imager (azure biosystems; Dublin, California, United States) over the time course of 1 min each 10 s.

5.6.5 Pull-down assay

To pull-down MBP-p62 or MBP-mCherry-p62 with LC3B, GST-LC3B and GST-LC3Be were immobilized on GST affinity resin. Per sample 25 µL of GST affinity resin were equilibrated in interaction buffer. The purified proteins were mixed with each a final concentration of 4 µM in 25 µL of interaction buffer. The protein mix was added to the prepared GST affinity resin and the pull-down incubated at 4°C overnight with mild mixing from time to time. To wash off all unbound proteins, the GST affinity resin was spun down with a Fisherbrand™ Mini-Centrifuge (Fisher Scientific; Reinach, Switzerland) and the supernatant was removed. The resin was washed twice with interaction buffer by adding 25 µL interaction buffer, spin down, and supernatant removal. The bound proteins were eluted in 20 µL of interaction buffer with 5 µL of 5x SDS-loading dye at 95°C for 5 min. SDS-samples of the flow through and wash were prepared and SDS-PAGE with all samples performed as described in 5.6.3.

5.6.6 Liposome coating with LC3B-Cys

The final lipid mixture to prepare the liposomes to immobilize LC3B-Cys on the surface, should contain 5% DSPE-PEG(2000) Maleimide (Avanti Polar Lipids 880126C; Croda International Plc; East Yorkshire, United Kingdom) in DOPS (Avanti Polar Lipids 840035; Croda International Plc; East Yorkshire, United Kingdom) with 0.01% of fluorescent ATTO390-DOPE (ATTO-TEC GmbH; Siegen, Germany). The respective amount of each lipid solubilized in chloroform was transferred into a 2 mL test tube to achieve a final concentration of 20 mg/mL in 500 µL. Under nitrogen gas flow, the chloroform was evaporated, and a lipid film dried to the bottom of the test tube. To evaporate residual chloroform, the test tube was placed in a desiccator and dried overnight. The lipid film was resuspended in 350 µL interaction buffer and subjected to eight freeze/thaw cycles with freezing in liquid nitrogen and thawing at 37°C. Liposomes were extruded to a size of 50 nm with 15 strokes through an extruder polycarbonate (PC) membrane (Avanti Polar Lipids 610003; Croda International Plc; East Yorkshire, United Kingdom) with the Avanti Mini Extruder (Avanti Polar Lipids; Croda International Plc; East Yorkshire, United Kingdom). 350 µL of extruded liposomes were mixed with 150 µL of 260 µM LC3B-Cys and incubated at room temperature for 2 h and at 4°C overnight. To remove unbound protein, 500 µL were loaded for size exclusion chromatography on HiPrep 16/60 Sephacryl S-500 HR (Cytiva; Marlborough, Massachusetts, United States) connected to ÄKTA pure™ micro with a Fraction collector F9-T (Cytiva; Marlborough, Massachusetts, United States). pSEC was performed in interaction buffer with an isocratic elution, fractionation after 0.1 CV, and a fraction size of 250 µL. The absorbance in the elution was monitored at 280 nm (protein specific) and 390 nm (fluorescent dye). According to the chromatogram, two peaks were identified and the peak fractions saved for further experiments. Of each peak fraction a sample for SDS-PAGE was prepared by mixing 40 µL of sample with 10 µL of 5x SDS-loading dye. The lipid concentration in the P1 fraction was determined as described in 5.6.2.

5.6.7 Light microscopy of phase separation

GST-4xUbiquitin was labeled with Alexa Fluor™ 488 C_5 Maleimide (Thermo Fisher Scientific; Waltham, Massachusetts, United States) via a cysteine-maleimide bond. An aliquot of purified GST-4xUbiquitin was thawed and the protein concentration determined as described in 5.6.1. An aliquot of Alexa Fluor™ 488 C_5 Maleimide (Thermo Fisher Scientific; Waltham, Massachusetts, United States) with a concentration of 73.35 pmol was thawed and resuspended in 700 µL of 50 µM GST-4xUbiquitin (final concentration of dye: 104 nM). The reaction was incubated at room temperature for 2 h, and overnight at 4°C. Free dye was removed by a clean-up step via a 2 mL Zeba™ Dye and Biotin Removal Spin Column (Thermo Fisher Scientific; Waltham, Massachusetts, United States). The flow trough was collected and the labeling efficiency determined by absorbance spectrophotometry. The individual concentrations for protein (λ = 280 nm) and dye (λ = 488 nm) were determined as described in 5.6.1 and, under the approximation of one dye per protein, the labeled amount of GST-4xUbiquitin calculated by dividing the concentration of the dye by the concentration of the protein. To observe the phase separation in light microscopy, p62 filaments or mCherry-p62 were mixed with labeled GST-4xUbiquitin in different molar ratios: 0:15; 0.5:15, 1:15, 1:1. 10 µL of the mixture were immediately added into a Countess™ Cell Counting Chamber Slide (Thermo Fisher Scientific; Waltham, Massachusetts, United States) and bright field fluorescence images at ZEISS Axio Observer (Carl Zeiss Microscopy Deutschland GmbH; Oberkochen, Germany) with filter sets for green and red fluorescence acquired. As a control, if the observed structures are indeed phase separation, the procedure was repeated with buffer containing 1 or 5% 1,6-Hexanediol.

5.7 Electron microscopy

5.7.1 Negative stain electron microscopy

As specimen support TEM Grids (300 mesh, hexagonal, copper) (Gilder Grids Ltd; Lincolnshire, United Kingdom) were coated with a 3 nm (+/- 0.2 nm) thick carbon film (on top of a formvar film) by Pia Sundermeyer. To remove adsorbed hydrocarbons, clean, and turn the carbon film hydrophilic, grids were treated with glow discharge plasma in a PELCO easiGlow™ Glow Discharge Cleaning System (Ted Pella Inc, Redding, California, United States) at 15 mA and 0.39 mBar for 30 s. 3 µL of sample were applied to a grid and incubated for 1 min. Excess sample was drained with Whatman paper. Subsequently the grid was washed twice by adding 3 µL of sample buffer and draining with Whatman paper. To stain 3 µL of 2% uranyl acetate were applied to the grid and excess liquid drained either immediately or for the second time after 1 min. The grid was left to dry completely and afterwards stored in box until imaging. To image negative stain grids, the grids were loaded into the Talos™ L120C TEM for Life Sciences equipped with a 4k × 4k Ceta CMOS camera (Thermo Fisher Scientific; Eindhoven, the Netherlands) via a side-entry holder. Data collection was performed with EPU (Thermo Fisher Scientific; Eindhoven, the Netherlands).

5.7.2 Single-particle analysis of human 80S ribosomes

As sample carrier QUANTIFOIL® TEM grids R1.2/1.3, 200 mesh, copper (Quantifoil Micro Tools GmbH; Großlöbichau, Germany) were glow discharged in PELCO easiGlow™ Glow Discharge Cleaning System (Ted Pella Inc, Redding, California, United States) at 15 mA and 0.39 mBar for 30 s. The Vitrobot mark IV (Thermo Fisher Scientific; Eindhoven, the Netherlands) was used to vitrify single-particle analysis samples of ribosomes extracted from FreeStyle^{TM} 293-F cell line (Thermo Fisher Scientific; Waltham, Massachusetts, United States). The extraction is described in detail in 5.5.2. The chamber was precooled to 10°C and humidity set to 100%. 3.6 µL of the sample were applied to the grid, excess liquid blotted with Whatman paper and the sample plunge frozen in liquid ethane which was condensed into a cup cooled by liquid nitrogen shortly before plunging. Thereby the blot force was set to -5, the blot time was 7 s. Grids were stored in liquid nitrogen.

After autoloader clipping, the grids were loaded into a Talos Arctica 200 kV instrument (Thermo Fisher Scientific; Eindhoven, the Netherlands) equipped with a K3 direct electron detector with BioQuantum energy filter (Gatan, Inc., Pleasanton, California, United States). Micrographs were collected at 100,000x magnification with EPU (Thermo Fisher Scientific; Eindhoven, the Netherlands) with a defocus varied between -0.5 to -3 µm. Motion correction was performed on-the-fly by processing the raw micrographs in WARP (Tegunov and Cramer 2019). All further processing was performed in cryoSPARC (Structura Biotechnology Inc.; Toronto, Canada). CTF estimation was performed with the "*Patch CTF Estimation*" job type with default parameters. Particles were picked with the "*Blob picker*" job with a minimum particle diameter of 250 Å and a maximum particle diameter of 300 Å (otherwise default parameters). Particles were extracted with an extraction box size of 512 pixels with the "*Extract from Micrographs*" job. Particle extraction job. in an extraction box size of 512 pixels (pixel size = 0.84 Å). The extracted particles were sorted into 50 classes with the "*2D classification*" job and classes containing high resolution information particles manually selected with "*Select 2D classes*". Selected classes were used in "*Ab-initio Reconstruction*" and the obtained volume refined with "*Homogenous Refinement*" with the parameters "Optimize per-particle defocus" and "Optimize per-particle CTF params" turned on. As result, the sharpened EM map of the "*Homogenous Refinement*" job was retrieved. For structural analysis, the model with the PDB-ID: 6qzp Natchiar et al. 2017) was fitted into the EM maps, the fit inspected and results documented with

UCSF ChimeraX (Resource for Biocomputing, Visualization, and Informatics at the University of California; San Francisco, California, United States).

5.7.3 Cryo-ET of p62 filaments and GST-4xUbiquitin

As sample carrier QUANTIFOIL® TEM grids R2/1, 200 mesh, copper (Quantifoil Micro Tools GmbH; Großlöbichau, Germany) were glow discharged in PELCO easiGlow™ Glow Discharge Cleaning System (Ted Pella Inc, Redding, California, United States) at 15 mA and 0.39 mBar for 30 s. The Vitrobot mark IV (Thermo Fisher Scientific; Eindhoven, the Netherlands) was used to vitrify the samples for phase separation with CET. The chamber was precooled to 10°C and humidity set to 80%. 3.5 µL of the sample was applied to the grid, excess liquid blotted with Whatman paper and the sample plunge frozen in liquid ethane which was condensed into a cup cooled by liquid nitrogen shortly before plunging. Thereby the blot force was set to -10, the blot time was 5 s. Grids were stored in liquid nitrogen.

After autoloader clipping, the grids were loaded into a Titan Krios 300 kV instrument (Thermo Fisher Scientific; Eindhoven, the Netherlands) equipped with a K3 direct electron detector with BioContinuum energy filter (Gatan, Inc., Pleasanton, California, United States). Tomograms were collected at 64,000x with TOMO (Thermo Fisher Scientific; Eindhoven, the Netherlands) at a varying defocus between -2.0 to -4.0 µm. Motion correction was performed on-the-fly by processing the raw micrographs in WARP (Tegunov and Cramer 2019). Image stacks were created in WARP (Tegunov and Cramer 2019) and tomogram reconstruction performed with AreTOMO (Zheng et al. 2022b). To denoise the tomograms and perform missing wedge correction IsoNet (Liu et al. 2022) was used. The tomograms were filtered with "*recursive exponential filter*" in Amira Software for cell biology (Thermo Fisher Scientific; Eindhoven, the Netherlands) for display.

As a control experiments, tomograms recorded on p62 filaments by Julio Ortiz were processed. The tomograms were collected at a Talos Arctica 200 kV instrument (Thermo Fisher Scientific; Eindhoven, the Netherlands) equipped with a K3 direct electron detector with BioQuantum energy filter (Gatan, Inc., Pleasanton, California, United States) in SerialEM (Regents of the University of Colorado;

Boulder, Colorado, United States) with a phase plate. The tomograms were already reconstructed and gold fiducials removed. To denoise the tomograms and perform missing wedge correction IsoNet (Liu et al. 2022). The tomograms were filtered with "*recursive exponential filter*" in Amira Software for cell biology (Thermo Fisher Scientific; Eindhoven, the Netherlands) for display.

5.7.4 Cryo-ET of p62 filaments and LC3B-Cys coated liposomes

As sample carrier QUANTIFOIL® TEM grids R2/1, 200 mesh, copper (Quantifoil Micro Tools GmbH; Großlöbichau, Germany) were glow discharged in PELCO easiGlow™ Glow Discharge Cleaning System (Ted Pella Inc, Redding, California, United States) at 15 mA and 0.39 mBar for 30 s. All samples containing liposomes were vitrified utilizing the EM GP2 Automatic Plunge Freezer (Leica Microsystems; Wetzlar, Germany) with backside blotting option. The environment in the chamber was set to 10°C and 80% humidity with a 60% GN_2 flow. 4 µL of the sample were applied, excess liquid drained with Whatman paper and the grid plunged into liquid ethane. The temperature of the liquid ethane was set to -180°C and constantly monitored. The blot time was set to 3 s, with sensor blotting and 2 mm additional move. Grids were stored in liquid nitrogen.

After autoloader clipping, the grids were loaded into a Titan Krios 300 kV instrument (Thermo Fisher Scientific; Eindhoven, the Netherlands) equipped with a K3 direct electron detector with BioContinuum energy filter (Gatan, Inc., Pleasanton, California, United States). Tomograms were collected at 64,000x with TOMO (Thermo Fisher Scientific; Eindhoven, the Netherlands) at a varying defocus between -2.0 to -4.0 µm. Motion correction was performed on-the-fly by processing the raw micrographs in WARP (Tegunov and Cramer 2019). Image stacks were created in WARP (Tegunov and Cramer 2019) and tomogram reconstruction performed with AreTOMO (Zheng et al. 2022b). Segmentation of p62 filaments and membranes was performed in Dragonfly with a two-dimensional U-Net (Heebner et al. 2022). To denoise the tomograms and perform missing wedge correction IsoNet (Liu et al. 2022) was used. The membranes of the denoised tomograms were segmented with MemBrain (Lamm et al. 2022) and the Surface Morphometrics Toolkit (Barad et al. 2022) applied to extracted statistics from the membrane segmentation including curvature. The tomograms were filtered with “*recursive exponential filter*” in Amira Software for cell biology (Thermo Fisher Scientific; Eindhoven, the Netherlands) for display. The membrane segmentation was displayed colored according to the curvature with ParaView (Kitware, Inc; Clifton Park, New York, United States). The p62 and membrane segmentation together were displayed with UCSF ChimeraX (Resource for Biocomputing, Visualization, and Informatics at the University of California; San Francisco, California, United States).

5.7.5 Single-particle analysis of *C. glutamicum* 70S ribosomes

As sample carrier QUANTIFOIL® TEM grids R1.2/1.3, 200 mesh, copper (Quantifoil Micro Tools GmbH; Großlöbichau, Germany) were glow discharged in PELCO easiGlow™ Glow Discharge Cleaning System (Ted Pella Inc, Redding, California, United States) at 15 mA and 0.39 mBar for 30 s. The Vitrobot mark IV (Thermo Fisher Scientific; Eindhoven, the Netherlands) was used to vitrify single-particle analysis samples of ribosomes extracted from FreeStyle™ 293-F cell line (Thermo Fisher Scientific; Waltham, Massachusetts, United States). The extraction is described in detail in 5.5.2. The chamber was precooled to 10°C and humidity set to 100%. 3.6 µL of the sample were applied to the grid, excess liquid blotted with Whatman paper and the sample plunge frozen in liquid ethane which was condensed into a cup cooled by liquid nitrogen shortly before plunging. Thereby the blot force was set to -5, the blot time was 7 s. Grids were stored in liquid nitrogen.

After autoloader clipping, the grids were loaded into a Titan Krios 300 kV instrument equipped with a Falcon 4i detector (Thermo Fisher Scientific; Eindhoven, the Netherlands) (Cg70S) or Talos Arctica 200 kV instrument (Thermo Fisher Scientific; Eindhoven, the Netherlands) equipped with a K3 direct electron detector with BioQuantum energy filter (Gatan, Inc., Pleasanton, California, United States) (all other samples). Micrographs were collected at 96,000x or 100,000x magnification with EPU (Thermo Fisher Scientific; Eindhoven, the Netherlands) with a defocus varied between -0.5 to -3 µm. Motion correction was performed on-the-fly by processing the raw micrographs in cryoSPARC LIVE (Structura Biotechnology Inc.; Toronto, Canada) (Cg70S) or in WARP (Tegunov and Cramer 2019) (all other samples). All further processing was performed in cryoSPARC

(Structura Biotechnology Inc.; Toronto, Canada). CTF estimation was performed with the "*Patch CTF Estimation*" job type with default parameters. Particles were picked with the "*Blob picker*" job with a minimum particle diameter of 200 Å and a maximum particle diameter of 280 Å (otherwise default parameters). Particles were extracted with an extraction box size of 512 pixels with the "*Extract from Micrographs*" job. Particle extraction job. in an extraction box size of 512 pixels (pixel size = 0.84 Å). The extracted particles were sorted into 50 classes with the "*2D classification*" job and classes containing high resolution information particles manually selected with "*Select 2D classes*". Selected classes were used in "*Ab-initio Reconstruction*" and the obtained volume refined with "*Homogenous Refinement*" with the parameters "Optimize per-particle defocus" and "Optimize per-particle CTF params" turned on. As result, the sharpened EM map of the "*Homogenous Refinement*" job was retrieved. The refined particles and volume were used in "*3D classification*" into ten different classes with PCA mode initialization mode and 10 Å target resolution. Each volume after "*3D classification*" was refined with "*Homogenous Refinement*" with the parameters "Optimize per-particle defocus" and "Optimize per-particle CTF params" turned on. The unsharpened EM maps were retrieved and five unique models identified. These models were uploaded into each workspace with "*volume import*". The "*3D classification*" job was repeated with the imported volumes filtered to 20 Å resolution as initialization mode. Each volume after "*3D classification*" was refined with "*Homogenous Refinement*" with the parameters "Optimize per-particle defocus" and "Optimize per-particle CTF params" turned on. The sharpened EM maps were retrieved. Each EM map was assigned to one of the five unique classes and the particles per class counted.

The model with the PDB-ID: 5O61of the 70S ribosome of *M. smegmatis* (Hentschel et al. 2017) was fitted into the Cg70S structure by Daniel Mann and adjusted to the sequence of *C. glutamicum*. Missing proteins were built by me in Coot (Emsley et al. 2010). The Cg70S model was adjusted to fit the A-, transition, and E-state and the corresponding tRNA and mRNA fragments were built in Coot (Emsley et al. 2010) as well. All models were subsequently fitted into the densities of the Cg70S + Kasugamycin as well as ∆bS22 sample. The molecular model of Kasugamycin was extracted from the model with the PDB-ID: 4V4H of the *E. coli* 70S ribosome in complex with Kasugamycin (Schuwirth et al. 2006). After model building, the model was refined in Phenix with the “*Real-space refinement*” job (Liebschner et al. 2019) and the map was improved with LocScale (Jakobi et al. 2017)

6 References

Adrian M, Dubochet J, Lepault J, McDowall AW (1984) Cryo-electron microscopy of viruses. Nature 308:32–36. https://doi.org/10.1038/308032a0

Afonine PV, Poon BK, Read RJ, et al (2018) Real-space refinement in *PHENIX* for cryo-EM and crystallography. Acta Crystallogr Sect Struct Biol 74:531–544. https://doi.org/10.1107/S2059798318006551

Alers S, Löffler AS, Paasch F, et al (2011) Atg13 and FIP200 act independently of Ulk1 and Ulk2 in autophagy induction. Autophagy 7:1424–1433. https://doi.org/10.4161/auto.7.12.18027

Andersen A (1984) Simultaneous Algebraic Reconstruction Technique (SART): A superior implementation of the ART algorithm. Ultrason Imaging 6:81–94. https://doi.org/10.1016/0161-7346(84)90008-7

Andersen JS, Lam YW, Leung AKL, et al (2005) Nucleolar proteome dynamics. Nature 433:77–83. https://doi.org/10.1038/nature03207

Andrade-Tomaz M, De Souza I, Rocha CRR, Gomes LR (2020) The Role of Chaperone-Mediated Autophagy in Cell Cycle Control and Its Implications in Cancer. Cells 9:2140. https://doi.org/10.3390/cells9092140

Axe EL, Walker SA, Manifava M, et al (2008) Autophagosome formation from membrane compartments enriched in phosphatidylinositol 3-phosphate and dynamically connected to the endoplasmic reticulum. J Cell Biol 182:685–701. https://doi.org/10.1083/jcb.200803137

Backer JM (2016) The intricate regulation and complex functions of the Class III phosphoinositide 3-kinase Vps34. Biochem J 473:2251–2271. https://doi.org/10.1042/BCJ20160170

Bai X, Fernandez IS, McMullan G, Scheres SH (2013) Ribosome structures to near-atomic resolution from thirty thousand cryo-EM particles. eLife 2:e00461. https://doi.org/10.7554/eLife.00461

Bakker H, Bleeker A, Mul P (1996) Design and performance of an ultra-high-resolution 300 kV microscope. Ultramicroscopy 64:17–34. https://doi.org/10.1016/0304-3991(96)00026-5

Bakula D, Takacs Z, Proikas-Cezanne T (2013) WIPI β-propellers in autophagy-related diseases and longevity. Biochem Soc Trans 41:962–967. https://doi.org/10.1042/BST20130039

Baltanás FC, Casafont I, Weruaga E, et al (2011) Nucleolar disruption and cajal body disassembly are nuclear hallmarks of DNA damage-induced neurodegeneration in purkinje cells. Brain Pathol Zurich Switz 21:374–388. https://doi.org/10.1111/j.1750-3639.2010.00461.x

Banani SF, Lee HO, Hyman AA, Rosen MK (2017) Biomolecular condensates: organizers of cellular biochemistry. Nat Rev Mol Cell Biol 18:285–298. https://doi.org/10.1038/nrm.2017.7

Barad BA, Medina M, Fuentes D, et al (2022) A surface morphometrics toolkit to quantify organellar membrane ultrastructure using cryo-electron tomography. Cell Biology

Bardoni B, Schenck A, Louis Mandel J (1999) A Novel RNA-binding Nuclear Protein That Interacts With the Fragile X Mental Retardation (FMR1) Protein. Hum Mol Genet 8:2557–2566. https://doi.org/10.1093/hmg/8.13.2557

Bardoni B, Schenck A, Mandel J-L (2001) The Fragile X mental retardation protein. Brain Res Bull 56:375–382. https://doi.org/10.1016/S0361-9230(01)00647-5

Bartesaghi A, Merk A, Banerjee S, et al (2015) 2.2 Å resolution cryo-EM structure of β-galactosidase in complex with a cell-permeant inhibitor. Science 348:1147–1151. https://doi.org/10.1126/science.aab1576

Barth HG, Jackson Christian, Boyes BE (1994) Size Exclusion Chromatography. Anal Chem 66:595–620. https://doi.org/10.1021/ac00084a022

Beckers M, Mann D, Sachse C (2021) Structural interpretation of cryo-EM image reconstructions. Prog Biophys Mol Biol 160:26–36. https://doi.org/10.1016/j.pbiomolbio.2020.07.004

Berkamp S, Mostafavi S, Sachse C (2021) Structure and function of p62/SQSTM1 in the emerging framework of phase separation. FEBS J 288:6927–6941. https://doi.org/10.1111/febs.15672

Birgisdottir ÅB, Lamark T, Johansen T (2013) The LIR motif – crucial for selective autophagy. J Cell Sci 126:3237–3247. https://doi.org/10.1242/jcs.126128

Bjørkøy G, Lamark T, Brech A, et al (2005) p62/SQSTM1 forms protein aggregates degraded by autophagy and has a protective effect on huntingtin-induced cell death. J Cell Biol 171:603–614. https://doi.org/10.1083/jcb.200507002

Boeynaems S, Alberti S, Fawzi NL, et al (2018) Protein Phase Separation: A New Phase in Cell Biology. Trends Cell Biol 28:420–435. https://doi.org/10.1016/j.tcb.2018.02.004

Bohm I (2003) Apoptosis: The Complex Scenario for a Silent Cell Death. Mol Imaging Biol 5:2–14. https://doi.org/10.1016/S1536-1632(03)00024-6

Boke E, Ruer M, Wühr M, et al (2016) Amyloid-like Self-Assembly of a Cellular Compartment. Cell 166:637–650. https://doi.org/10.1016/j.cell.2016.06.051

Bozzola JJ, Russell LD (2006) Electron microscopy: principles and techniques for biologists, 2. ed., [Nachdr.]. Jones and Bartlett, Boston

Bracewell R (1956) Strip Integration in Radio Astronomy. Aust J Phys 9:198. https://doi.org/10.1071/PH560198

Bracewell RN (1990) Numerical Transforms. Science 248:697–704. https://doi.org/10.1126/science.248.4956.697

Brangwynne CP, Eckmann CR, Courson DS, et al (2009) Germline P Granules Are Liquid Droplets That Localize by Controlled Dissolution/Condensation. Science 324:1729–1732. https://doi.org/10.1126/science.1172046

Brenner S, Horne RW (1959) A negative staining method for high resolution electron microscopy of viruses. Biochim Biophys Acta 34:103–110. https://doi.org/10.1016/0006-3002(59)90237-9

Carter AP, Clemons WM, Brodersen DE, et al (2000) Functional insights from the structure of the 30S ribosomal subunit and its interactions with antibiotics. Nature 407:340–348. https://doi.org/10.1038/35030019

Carter CB, Williams DB (eds) (2016) Transmission Electron Microscopy: Diffraction, Imaging, and Spectrometry, 1st ed. 2016. Springer International Publishing : Imprint: Springer, Cham

Carter CB, Williams DB, Thomas JM (eds) (2016) Transmission electron microscopy: diffraction, imaging, and spectrometry. Springer, Cham, Switzerland

Center for celluar imaging: Electron Microscopy, University of Gothenburg (2021) Negative staining. https://www.gu.se/en/core-facilities/centre-for-cellular-imaging/electron-microscopy/negative-staining. Accessed 3 Mar 2024

Chagot M-E, Boutilliat A, Kriznik A, Quinternet M (2022) Structural Analysis of the Plasmodial Proteins ZNHIT3 and NUFIP1 Provides Insights into the Selectivity of a Conserved Interaction. Biochemistry acs.biochem.1c00792. https://doi.org/10.1021/acs.biochem.1c00792

Chao AW, Mess KH, Tigner M, Zimmermann F (2013) Handbook of Accelerator Physics and Engineering, 2nd edn. WORLD SCIENTIFIC

Cheng Y, Grigorieff N, Penczek PA, Walz T (2015) A Primer to Single-Particle Cryo-Electron Microscopy. Cell 161:438–449. https://doi.org/10.1016/j.cell.2015.03.050

Christenson KK, Eades JA (1988) Skew thoughts on parallelism. Ultramicroscopy 26:113–132. https://doi.org/10.1016/0304-3991(88)90384-1

Ciani B, Layfield R, Cavey JR, et al (2003) Structure of the Ubiquitin-associated Domain of p62 (SQSTM1) and Implications for Mutations That Cause Paget’s Disease of Bone. J Biol Chem 278:37409–37412. https://doi.org/10.1074/jbc.M307416200

Ciuffa R, Lamark T, Tarafder AK, et al (2015) The Selective Autophagy Receptor p62 Forms a Flexible Filamentous Helical Scaffold. Cell Rep 11:748–758. https://doi.org/10.1016/j.celrep.2015.03.062

Codogno P, Mehrpour M, Proikas-Cezanne T (2012) Canonical and non-canonical autophagy: variations on a common theme of self-eating? Nat Rev Mol Cell Biol 13:7–12. https://doi.org/10.1038/nrm3249

Cowley JM (1995) Diffraction physics, 3rd rev. ed. Elsevier Science B.V, Amsterdam ; New York

Crowther RA, DeRosier DJ, Klug A (1970) The reconstruction of a three-dimensional structure from projections and its application to electron microscopy. Proc R Soc Lond Math Phys Sci 317:319–340. https://doi.org/10.1098/rspa.1970.0119

CryoSPARC Guide (2023a) Job: 2D Classification. In: CryoSPARC Guide. https://guide.cryosparc.com/processing-data/all-job-types-in-cryosparc/particle-curation/job-2d-classification. Accessed 30 Apr 2024

CryoSPARC Guide (2023b) Job: 3D Classification (BETA). In: CryoSPARC Guide. https://guide.cryosparc.com/processing-data/all-job-types-in-cryosparc/variability/job-3d-classification-beta. Accessed 5 Mar 2024

Dabbs ER (1978) Kasugamycin-dependent mutants of Escherichia coli. J Bacteriol 136:994–1001. https://doi.org/10.1128/jb.136.3.994-1001.1978

Dammel CS, Noller HF (1993) A cold-sensitive mutation in 16S rRNA provides evidence for helical switching in ribosome assembly. Genes Dev 7:660–670. https://doi.org/10.1101/gad.7.4.660

Danev R, Buijsse B, Khoshouei M, et al (2014) Volta potential phase plate for in-focus phase contrast transmission electron microscopy. Proc Natl Acad Sci 111:15635–15640. https://doi.org/10.1073/pnas.1418377111

Danieli A, Martens S (2018) p62-mediated phase separation at the intersection of the ubiquitin-proteasome system and autophagy. J Cell Sci 131:jcs214304. https://doi.org/10.1242/jcs.214304

Date M, Itaya H, Matsui H, Kikuchi Y (2006) Secretion of human epidermal growth factor by Corynebacterium glutamicum. Lett Appl Microbiol 42:66–70. https://doi.org/10.1111/j.1472-765X.2005.01802.x

De Carlo S, Harris JR (2011) Negative staining and cryo-negative staining of macromolecules and viruses for TEM. Micron 42:117–131. https://doi.org/10.1016/j.micron.2010.06.003

De Oliveira TM, Van Beek L, Shilliday F, et al (2021) Cryo-EM: The Resolution Revolution and Drug Discovery. SLAS Discov 26:17–31. https://doi.org/10.1177/2472555220960401

Dinos G (2005) Deacylated tRNA is released from the E site upon A site occupation but before GTP is hydrolyzed by EF-Tu. Nucleic Acids Res 33:5291–5296. https://doi.org/10.1093/nar/gki833

Dobro MJ, Melanson LA, Jensen GJ, McDowall AW (2010) Plunge Freezing for Electron Cryomicroscopy. In: Methods in Enzymology. Elsevier, pp 63–82

Dobson CM (2003) Protein folding and misfolding. Nature 426:884–890. https://doi.org/10.1038/nature02261

Dooley HC, Razi M, Polson HEJ, et al (2014) WIPI2 Links LC3 Conjugation with PI3P, Autophagosome Formation, and Pathogen Clearance by Recruiting Atg12–5-16L1. Mol Cell 55:238–252. https://doi.org/10.1016/j.molcel.2014.05.021

Dries M, Hettler S, Gamm B, et al (2014) A nanocrystalline Hilbert phase-plate for phase-contrast transmission electron microscopy. Ultramicroscopy 139:29–37. https://doi.org/10.1016/j.ultramic.2014.01.002

Dubochet J, Adrian M, Chang J-J, et al (1988) Cryo-electron microscopy of vitrified specimens. Q Rev Biophys 21:129–228. https://doi.org/10.1017/S0033583500004297

Düster R, Kaltheuner IH, Schmitz M, Geyer M (2021) 1,6-Hexanediol, commonly used to dissolve liquid–liquid phase separated condensates, directly impairs kinase and phosphatase activities. J Biol Chem 296:100260. https://doi.org/10.1016/j.jbc.2021.100260

Egan DF, Chun MGH, Vamos M, et al (2015) Small Molecule Inhibition of the Autophagy Kinase ULK1 and Identification of ULK1 Substrates. Mol Cell 59:285–297. https://doi.org/10.1016/j.molcel.2015.05.031

Egerton RF (2005) Physical principles of electron microscopy: an introduction to TEM, SEM, and AEM. Springer, New York, NY

Emsley P, Lohkamp B, Scott WG, Cowtan K (2010) Features and development of *Coot*. Acta Crystallogr D Biol Crystallogr 66:486–501. https://doi.org/10.1107/S0907444910007493

Eyidi D, Hébert C, Schattschneider P (2006) Short note on parallel illumination in the TEM. Ultramicroscopy 106:1144–1149. https://doi.org/10.1016/j.ultramic.2006.04.029

Faruk MO, Ichimura Y, Kageyama S, et al (2021) Phase-separated protein droplets of amyotrophic lateral sclerosis-associated p62/SQSTM1 mutants show reduced inner fluidity. J Biol Chem 297:101405. https://doi.org/10.1016/j.jbc.2021.101405

Faruqi AR, McMullan G (2018) Direct imaging detectors for electron microscopy. Nucl Instrum Methods Phys Res Sect Accel Spectrometers Detect Assoc Equip 878:180–190. https://doi.org/10.1016/j.nima.2017.07.037

Fei J, Jadaliha M, Harmon TS, et al (2017) Quantitative analysis of multilayer organization of proteins and RNA in nuclear speckles at super resolution. J Cell Sci jcs.206854. https://doi.org/10.1242/jcs.206854

Feng Y, He D, Yao Z, Klionsky DJ (2014) The machinery of macroautophagy. Cell Res 24:24–41. https://doi.org/10.1038/cr.2013.168

Ferenci T, Klotz U (1978) Affinity chromatographic isolation of the periplasmic maltose binding protein of *Escherichia coli*. FEBS Lett 94:213–217. https://doi.org/10.1016/0014-5793(78)80940-5

Fernández ÁF, López-Otín C (2015) The functional and pathologic relevance of autophagy proteases. J Clin Invest 125:33–41. https://doi.org/10.1172/JCI73940

Filomeni G, De Zio D, Cecconi F (2015) Oxidative stress and autophagy: the clash between damage and metabolic needs. Cell Death Differ 22:377–388. https://doi.org/10.1038/cdd.2014.150

Fong K, Li Y, Wang W, et al (2013) Whole-genome screening identifies proteins localized to distinct nuclear bodies. J Cell Biol 203:149–164. https://doi.org/10.1083/jcb.201303145

Fossum ER, Hondongwa DB (2014) A Review of the Pinned Photodiode for CCD and CMOS Image Sensors. IEEE J Electron Devices Soc 2:33–43. https://doi.org/10.1109/JEDS.2014.2306412

Fouts KE, Barbour SD (1981) Transductional mapping of ksgB and a new Tn5-induced kasugamycin resistance gene, ksgD, in Escherichia coli K-12. J Bacteriol 145:914–919. https://doi.org/10.1128/jb.145.2.914-919.1981

Frank J (2006a) Three-Dimensional Electron Microscopy of Macromolecular Assemblies. Oxford University Press

Frank J (ed) (2006b) Electron Tomography. Springer New York, New York, NY

Frank J, Gao H, Sengupta J, et al (2007) The process of mRNA–tRNA translocation. Proc Natl Acad Sci 104:19671–19678. https://doi.org/10.1073/pnas.0708517104

Fromm SA, O'Connor KM, Purdy M, et al (2023) The translating bacterial ribosome at 1.55 Å resolution generated by cryo-EM imaging services. Nat Commun 14:1095. https://doi.org/10.1038/s41467-023-36742-3

Fujioka Y, Noda NN, Nakatogawa H, et al (2010) Dimeric Coiled-coil Structure of Saccharomyces cerevisiae Atg16 and Its Functional Significance in Autophagy. J Biol Chem 285:1508–1515. https://doi.org/10.1074/jbc.M109.053520

Fujita N, Hayashi-Nishino M, Fukumoto H, et al (2008) An Atg4B Mutant Hampers the Lipidation of LC3 Paralogues and Causes Defects in Autophagosome Closure. Mol Biol Cell 19:4651–4659. https://doi.org/10.1091/mbc.e08-03-0312

Fukagawa Y, Sawa T, Takeuchi T, Umezawa H (1968) STUDIES ON BIOSYNTHESIS OF KASUGAMYCIN. I. J Antibiot (Tokyo) 21:50–54. https://doi.org/10.7164/antibiotics.21.50

Galluzzi L, Pietrocola F, Bravo-San Pedro JM, et al (2015) Autophagy in malignant transformation and cancer progression. EMBO J 34:856–880. https://doi.org/10.15252/embj.201490784

Gan L, Jensen GJ (2012) Electron tomography of cells. Q Rev Biophys 45:27–56. https://doi.org/10.1017/S0033583511000102

Ganley IG, Lam DH, Wang J, et al (2009) ULK1·ATG13·FIP200 Complex Mediates mTOR Signaling and Is Essential for Autophagy. J Biol Chem 284:12297–12305. https://doi.org/10.1074/jbc.M900573200

Grant T, Grigorieff N (2015) Measuring the optimal exposure for single particle cryo-EM using a 2.6 Å reconstruction of rotavirus VP6. eLife 4:e06980. https://doi.org/10.7554/eLife.06980

Griffiths AJF (ed) (2008) Introduction to genetic analysis, 9. ed., 4. printing. Freeman, New York, NY [Basingstoke]

Grimsley GR, Pace CN (2003) Spectrophotometric Determination of Protein Concentration. Curr Protoc Protein Sci 33:. https://doi.org/10.1002/0471140864.ps0301s33

Guthrie C, Nashimoto H, Nomura M (1969) STRUCTURE AND FUNCTION OF *E. coli* RIBOSOMES, VIII. COLD-SENSITIVE MUTANTS DEFECTIVE IN RIBOSOME ASSEMBLY. Proc Natl Acad Sci 63:384–391. https://doi.org/10.1073/pnas.63.2.384

Gwinn DM, Shackelford DB, Egan DF, et al (2008) AMPK Phosphorylation of Raptor Mediates a Metabolic Checkpoint. Mol Cell 30:214–226. https://doi.org/10.1016/j.molcel.2008.03.003

Hagen WJH, Wan W, Briggs JAG (2017) Implementation of a cryo-electron tomography tilt-scheme optimized for high resolution subtomogram averaging. J Struct Biol 197:191–198. https://doi.org/10.1016/j.jsb.2016.06.007

Handwerger KE, Cordero JA, Gall JG (2005) Cajal Bodies, Nucleoli, and Speckles in the *Xenopus* Oocyte Nucleus Have a Low-Density, Sponge-like Structure. Mol Biol Cell 16:202–211. https://doi.org/10.1091/mbc.e04-08-0742

Hansen M, Rubinsztein DC, Walker DW (2018) Autophagy as a promoter of longevity: insights from model organisms. Nat Rev Mol Cell Biol 19:579–593. https://doi.org/10.1038/s41580-018-0033-y

Harauz G, Van Heel M (1986) Exact filters for general geometry three dimensional reconstruction. Optik 73:146–156

Hawkes PW (1980) Transfer functions and electron microscope image formation. In: Schlenker M, Fink M, Goedgebuer JP, et al. (eds) Imaging Processes and Coherence in Physics. Springer Berlin Heidelberg, Berlin, Heidelberg, pp 415–422

Heebner JE, Purnell C, Hylton RK, et al (2022) Deep Learning-Based Segmentation of Cryo-Electron Tomograms. J Vis Exp 64435. https://doi.org/10.3791/64435

Heide HG (1982) Design and operation of cold stages. Ultramicroscopy 10:125–154. https://doi.org/10.1016/0304-3991(82)90194-2

Helser TL, Davies JE, Dahlberg JE (1971) Change in Methylation of 16S Ribosomal RNA Associated with Mutation to Kasugamycin Resistance in Escherichia coli. Nature New Biol 233:12–14. https://doi.org/10.1038/newbio233012a0

Helser TL, Davies JE, Dahlberg JE (1972) Mechanism of Kasugamycin Resistance in Escherichia coli. Nature New Biol 235:6–9. https://doi.org/10.1038/newbio235006a0

Henderson R, Unwin PNT (1975) Three-dimensional model of purple membrane obtained by electron microscopy. Nature 257:28–32. https://doi.org/10.1038/257028a0

Hengen PN (1995) Purification of His-Tag fusion proteins from Escherichia coli. Trends Biochem Sci 20:285–286. https://doi.org/10.1016/S0968-0004(00)89045-3

Henne WM, Buchkovich NJ, Emr SD (2011) The ESCRT Pathway. Dev Cell 21:77–91. https://doi.org/10.1016/j.devcel.2011.05.015

Hentschel J, Burnside C, Mignot I, et al (2017) The Complete Structure of the Mycobacterium smegmatis 70S Ribosome. Cell Rep 20:149–160. https://doi.org/10.1016/j.celrep.2017.06.029

Herres D (2019) The difference between CCD and CMOS image sensing. https://www.testandmeasurementtips.com/the-difference-between-ccd-and-cmos-image-sensing-faq/. Accessed 1 Jan 2024

Hettler S, Kano E, Dries M, et al (2018) Charging of carbon thin films in scanning and phase-plate transmission electron microscopy. Ultramicroscopy 184:252–266. https://doi.org/10.1016/j.ultramic.2017.09.009

Hoang TV, Cavin X, Schultz P, Ritchie DW (2013) gEMpicker: a highly parallel GPU-accelerated particle picking tool for cryo-electron microscopy. BMC Struct Biol 13:25. https://doi.org/10.1186/1472-6807-13-25

Holden P, Horton WA (2009) Crude subcellular fractionation of cultured mammalian cell lines. BMC Res Notes 2:243. https://doi.org/10.1186/1756-0500-2-243

Hosokawa N, Hara T, Kaizuka T, et al (2009) Nutrient-dependent mTORC1 Association with the ULK1–Atg13–FIP200 Complex Required for Autophagy. Mol Biol Cell 20:1981–1991. https://doi.org/10.1091/mbc.e08-12-1248

Hurley JH, Young LN (2017) Mechanisms of Autophagy Initiation. Annu Rev Biochem 86:225–244. https://doi.org/10.1146/annurev-biochem-061516-044820

Hyman AA, Weber CA, Jülicher F (2014) Liquid-Liquid Phase Separation in Biology. Annu Rev Cell Dev Biol 30:39–58. https://doi.org/10.1146/annurev-cellbio-100913-013325

Ichimiya T, Yamakawa T, Hirano T, et al (2020) Autophagy and Autophagy-Related Diseases: A Review. Int J Mol Sci 21:8974. https://doi.org/10.3390/ijms21238974

Ikekawa T, Umezawa H, Iitaka Y (1966) The structure of kasugamycin hydrobromide by x-ray crystallographic analysis. J Antibiot (Tokyo) 19:49–50

Ilitchev A (2019) How Do You Make an Electron Beam? https://www.thermofisher.com/blog/materials/electron-source-fundamentals/. Accessed 1 Jan 2024

Itakura E, Kishi C, Inoue K, Mizushima N (2008) Beclin 1 forms two distinct phosphatidylinositol 3-kinase complexes with mammalian Atg14 and UVRAG. Mol Biol Cell 19:5360–5372. https://doi.org/10.1091/mbc.e08-01-0080

Itakura E, Mizushima N (2011) p62 targeting to the autophagosome formation site requires self-oligomerization but not LC3 binding. J Cell Biol 192:17–27. https://doi.org/10.1083/jcb.201009067

Jain S, Wheeler JR, Walters RW, et al (2016) ATPase-Modulated Stress Granules Contain a Diverse Proteome and Substructure. Cell 164:487–498. https://doi.org/10.1016/j.cell.2015.12.038

Jakobi AJ, Huber ST, Mortensen SA, et al (2020) Structural basis of p62/SQSTM1 helical filaments and their role in cellular cargo uptake. Nat Commun 11:440. https://doi.org/10.1038/s41467-020-14343-8

Jakobi AJ, Wilmanns M, Sachse C (2017) Model-based local density sharpening of cryo-EM maps. eLife 6:e27131. https://doi.org/10.7554/eLife.27131

Jha V, Roy B, Jahagirdar D, et al (2021) Structural basis of sequestration of the anti-Shine-Dalgarno sequence in the Bacteroidetes ribosome. Nucleic Acids Res 49:547–567. https://doi.org/10.1093/nar/gkaa1195

Johansen T, Lamark T (2020a) Selective Autophagy: ATG8 Family Proteins, LIR Motifs and Cargo Receptors. J Mol Biol 432:80–103. https://doi.org/10.1016/j.jmb.2019.07.016

Johansen T, Lamark T (2020b) Selective Autophagy: ATG8 Family Proteins, LIR Motifs and Cargo Receptors. J Mol Biol 432:80–103. https://doi.org/10.1016/j.jmb.2019.07.016

Johansen T, Sachse C (2015) The higher-order molecular organization of p62/SQSTM1. Oncotarget 6:16796–16797. https://doi.org/10.18632/oncotarget.4590

Joung I, Strominger JL, Shin J (1996) Molecular cloning of a phosphotyrosine-independent ligand of the p56lck SH2 domain. Proc Natl Acad Sci 93:5991–5995. https://doi.org/10.1073/pnas.93.12.5991

Jung CH, Jun CB, Ro S-H, et al (2009) ULK-Atg13-FIP200 Complexes Mediate mTOR Signaling to the Autophagy Machinery. Mol Biol Cell 20:1992–2003. https://doi.org/10.1091/mbc.e08-12-1249

Kaczanowska M, Rydén-Aulin M (2007) Ribosome Biogenesis and the Translation Process in *Escherichia coli*. Microbiol Mol Biol Rev 71:477–494. https://doi.org/10.1128/MMBR.00013-07

Kaiser SE, Mao K, Taherbhoy AM, et al (2012) Noncanonical E2 recruitment by the autophagy E1 revealed by Atg7–Atg3 and Atg7–Atg10 structures. Nat Struct Mol Biol 19:1242–1249. https://doi.org/10.1038/nsmb.2415

Kalinowski J, Bathe B, Bartels D, et al (2003) The complete Corynebacterium glutamicum ATCC 13032 genome sequence and its impact on the production of l-aspartate-derived amino acids and vitamins. J Biotechnol 104:5–25. https://doi.org/10.1016/S0168-1656(03)00154-8

Kamada Y, Funakoshi T, Shintani T, et al (2000) Tor-Mediated Induction of Autophagy via an Apg1 Protein Kinase Complex. J Cell Biol 150:1507–1513. https://doi.org/10.1083/jcb.150.6.1507

Kansanen E, Kuosmanen SM, Leinonen H, Levonen A-L (2013) The Keap1-Nrf2 pathway: Mechanisms of activation and dysregulation in cancer. Redox Biol 1:45–49. https://doi.org/10.1016/j.redox.2012.10.001

Katsuragi Y, Ichimura Y, Komatsu M (2016) Regulation of the Keap1–Nrf2 pathway by p62/SQSTM1. Curr Opin Toxicol 1:54–61. https://doi.org/10.1016/j.cotox.2016.09.005

Katsuragi Y, Ichimura Y, Komatsu M (2015) p62/SQSTM1 functions as a signaling hub and an autophagy adaptor. FEBS J 282:4672–4678. https://doi.org/10.1111/febs.13540

Kaushik S, Cuervo AM (2012) Chaperone-mediated autophagy: a unique way to enter the lysosome world. Trends Cell Biol 22:407–417. https://doi.org/10.1016/j.tcb.2012.05.006

Kawasaki M, Malac M, Li P, et al (2009) Convenient Electron Optics Set Up for Zernike Phase Microscopy in TEM. Microsc Microanal 15:1234–1235. https://doi.org/10.1017/S1431927609094598

Keiler KC (2015) Mechanisms of ribosome rescue in bacteria. Nat Rev Microbiol 13:285–297. https://doi.org/10.1038/nrmicro3438

Kettern N, Dreiseidler M, Tawo R, Höhfeld J (2010) Chaperone-assisted degradation: multiple paths to destruction. Biol Chem 391:481–489. https://doi.org/10.1515/bc.2010.058

Khatter H, Myasnikov AG, Mastio L, et al (2014) Purification, characterization and crystallization of the human 80S ribosome. Nucleic Acids Res 42:e49–e49. https://doi.org/10.1093/nar/gkt1404

Khavnekar S, Wan W, Majumder P, et al (2023) Multishot tomography for high-resolution in situ subtomogram averaging. J Struct Biol 215:107911. https://doi.org/10.1016/j.jsb.2022.107911

Kihara A, Noda T, Ishihara N, Ohsumi Y (2001) Two Distinct Vps34 Phosphatidylinositol 3–Kinase Complexes Function in Autophagy and Carboxypeptidase Y Sorting in *Saccharomyces cerevisiae*. J Cell Biol 152:519–530. https://doi.org/10.1083/jcb.152.3.519

Kim HG, Huot J, Pin F, et al (2020) Muscle Wasting in Cancer Involves Suppression of Ribosomal Production and Increased Expression of the Ribophagy Receptor NUFIP1. FASEB J 34:1–1. https://doi.org/10.1096/fasebj.2020.34.s1.03330

Kinoshita S, Udaka S, Shimono M (1957) Studies on the amino acid fermentation. J Gen Appl Microbiol 3:193–205. https://doi.org/10.2323/jgam.3.193

Kirisako T, Baba M, Ishihara N, et al (1999) Formation process of autophagosome is traced with Apg8/Aut7p in yeast. J Cell Biol 147:435–446. https://doi.org/10.1083/jcb.147.2.435

Kirisako T, Ichimura Y, Okada H, et al (2000) The Reversible Modification Regulates the Membrane-Binding State of Apg8/Aut7 Essential for Autophagy and the Cytoplasm to Vacuole Targeting Pathway. J Cell Biol 151:263–276. https://doi.org/10.1083/jcb.151.2.263

Kirkland EJ (1998) Advanced computing in electron microscopy. Plenum Press, New York

Knævelsrud H, Simonsen A (2010) Fighting disease by selective autophagy of aggregate-prone proteins. FEBS Lett 584:2635–2645. https://doi.org/10.1016/j.febslet.2010.04.041

Knoll M, Ruska E (1932) Das Elektronenmikroskop. Z F r Phys 78:318–339. https://doi.org/10.1007/BF01342199

Knot R (2023) What is the difference between cryo-EM and cryo-ET? https://blog.delmic.com/what-is-the-difference-between-cryo-em-and-cryo-et. Accessed 3 Mar 2024

Kocaturk NM, Akkoc Y, Kig C, et al (2019) Autophagy as a molecular target for cancer treatment. Eur J Pharm Sci 134:116–137. https://doi.org/10.1016/j.ejps.2019.04.011

Kohl H, Reimer L (2008) Transmission Electron Microscopy: Physics of Image Formation. Springer New York, New York, NY

Komatsu M, Ichimura Y (2010) Physiological significance of selective degradation of p62 by autophagy. FEBS Lett 584:1374–1378. https://doi.org/10.1016/j.febslet.2010.02.017

Komatsu M, Kurokawa H, Waguri S, et al (2010) The selective autophagy substrate p62 activates the stress responsive transcription factor Nrf2 through inactivation of Keap1. Nat Cell Biol 12:213–223. https://doi.org/10.1038/ncb2021

Kraft C, Deplazes A, Sohrmann M, Peter M (2008) Mature ribosomes are selectively degraded upon starvation by an autophagy pathway requiring the Ubp3p/Bre5p ubiquitin protease. Nat Cell Biol 10:602–610. https://doi.org/10.1038/ncb1723

Kraft C, Kijanska M, Kalie E, et al (2012) Binding of the Atg1/ULK1 kinase to the ubiquitin-like protein Atg8 regulates autophagy: Regulation of Atg1 kinase function. EMBO J 31:3691–3703. https://doi.org/10.1038/emboj.2012.225

Kristensen AR, Schandorff S, Høyer-Hansen M, et al (2008) Ordered Organelle Degradation during Starvation-induced Autophagy. Mol Cell Proteomics 7:2419–2428. https://doi.org/10.1074/mcp.M800184-MCP200

Kroemer G, Mariño G, Levine B (2010) Autophagy and the Integrated Stress Response. Mol Cell 40:280–293. https://doi.org/10.1016/j.molcel.2010.09.023

Ktistakis NT (2020) ER platforms mediating autophagosome generation. Biochim Biophys Acta BBA - Mol Cell Biol Lipids 1865:158433. https://doi.org/10.1016/j.bbalip.2019.03.005

Kumar N, Sharma S, Kaushal PS (2024) Cryo- EM structure of the mycobacterial 70S ribosome in complex with ribosome hibernation promotion factor RafH. Nat Commun 15:638. https://doi.org/10.1038/s41467-024-44879-y

Kwon DH, Park OH, Kim L, et al (2018) Insights into degradation mechanism of N-end rule substrates by p62/SQSTM1 autophagy adapter. Nat Commun 9:3291. https://doi.org/10.1038/s41467-018-05825-x

Laemmli UK (1970) Cleavage of Structural Proteins during the Assembly of the Head of Bacteriophage T4. Nature 227:680–685. https://doi.org/10.1038/227680a0

Lamark T, Johansen T (2012) Aggrephagy: Selective Disposal of Protein Aggregates by Macroautophagy. Int J Cell Biol 2012:1–21. https://doi.org/10.1155/2012/736905

Lamark T, Perander M, Outzen H, et al (2003) Interaction Codes within the Family of Mammalian Phox and Bem1p Domain-containing Proteins. J Biol Chem 278:34568–34581. https://doi.org/10.1074/jbc.M303221200

Lamark T, Svenning S, Johansen T (2017) Regulation of selective autophagy: the p62/SQSTM1 paradigm. Essays Biochem 61:609–624. https://doi.org/10.1042/EBC20170035

Lambert JH (1760) Photometria sive de mensura et gradibus luminis, colorum et umbrae. Eberhardt Klett, Augsburg, Germany

Lamm L, Righetto RD, Wietrzynski W, et al (2022) MemBrain: A deep learning-aided pipeline for detection of membrane proteins in Cryo-electron tomograms. Comput Methods Programs Biomed 224:106990. https://doi.org/10.1016/j.cmpb.2022.106990

Laplante M, Sabatini DM (2012) mTOR Signaling in Growth Control and Disease. Cell 149:274–293. https://doi.org/10.1016/j.cell.2012.03.017

LBEM A newer version of the Excel sheet to simulate the CTF of a TEM

Lee J-Y, Na Y-A, Kim E, et al (2016) The Actinobacterium Corynebacterium glutamicum, an Industrial Workhorse. J Microbiol Biotechnol 26:807–822. https://doi.org/10.4014/jmb.1601.01053

Lee Y-K, Lee J-A (2016) Role of the mammalian ATG8/LC3 family in autophagy: differential and compensatory roles in the spatiotemporal regulation of autophagy. BMB Rep 49:424–430. https://doi.org/10.5483/BMBRep.2016.49.8.081

Levin BDA (2021) Direct detectors and their applications in electron microscopy for materials science. J Phys Mater 4:042005. https://doi.org/10.1088/2515-7639/ac0ff9

Levine B, Kroemer G (2008) Autophagy in the Pathogenesis of Disease. Cell 132:27–42. https://doi.org/10.1016/j.cell.2007.12.018

Levine B, Mizushima N, Virgin HW (2011) Autophagy in immunity and inflammation. Nature 469:323–335. https://doi.org/10.1038/nature09782

Li S-A, Meng X-Y, Zhang Y-J, et al (2024) Progress in pH-Sensitive sensors: essential tools for organelle pH detection, spotlighting mitochondrion and diverse applications. Front Pharmacol 14:1339518. https://doi.org/10.3389/fphar.2023.1339518

Liebschner D, Afonine PV, Baker ML, et al (2019) Macromolecular structure determination using X-rays, neutrons and electrons: recent developments in *Phenix*. Acta Crystallogr Sect Struct Biol 75:861–877. https://doi.org/10.1107/S2059798319011471

Lim J, Lachenmayer ML, Wu S, et al (2015) Proteotoxic Stress Induces Phosphorylation of p62/SQSTM1 by ULK1 to Regulate Selective Autophagic Clearance of Protein Aggregates. PLOS Genet 11:e1004987. https://doi.org/10.1371/journal.pgen.1004987

Liu Q, Chang JW, Wang J, et al (2010) Discovery of 1-(4-(4-Propionylpiperazin-1-yl)-3-(trifluoromethyl)phenyl)-9-(quinolin-3-yl)benzo[h][1,6]naphthyridin-2(1 *H*)-one as a Highly Potent, Selective Mammalian Target of Rapamycin (mTOR) Inhibitor for the Treatment of Cancer. J Med Chem 53:7146–7155. https://doi.org/10.1021/jm101144f

Liu Y-T, Zhang H, Wang H, et al (2022) Isotropic reconstruction for electron tomography with deep learning. Nat Commun 13:6482. https://doi.org/10.1038/s41467-022-33957-8

Lomakin IB, Devarkar SC, Patel S, et al (2023) Sarecycline inhibits protein translation in *Cutibacterium acnes* 70S ribosome using a two-site mechanism. Nucleic Acids Res gkad103. https://doi.org/10.1093/nar/gkad103

López AR, Jørgensen MH, Havelund JF, et al (2023) Autophagy-mediated control of ribosome homeostasis in oncogene-induced senescence. Cell Rep 42:113381. https://doi.org/10.1016/j.celrep.2023.113381

Lőrincz P, Juhász G (2020) Autophagosome-Lysosome Fusion. J Mol Biol 432:2462–2482. https://doi.org/10.1016/j.jmb.2019.10.028

Mack HID, Zheng B, Asara JM, Thomas SM (2012) AMPK-dependent phosphorylation of ULK1 regulates ATG9 localization. Autophagy 8:1197–1214. https://doi.org/10.4161/auto.20586

Malac M, Beleggia M, Kawasaki M, et al (2012) Convenient contrast enhancement by a hole-free phase plate. Ultramicroscopy 118:77–89. https://doi.org/10.1016/j.ultramic.2012.02.004

Malac M, Hettler S, Hayashida M, et al (2021) Phase plates in the transmission electron microscope: operating principles and applications. Microscopy 70:75–115. https://doi.org/10.1093/jmicro/dfaa070

Mandelstam J, McQuillen K (1973) Biochemistry of bacterial growth, 2d ed. Wiley, New York

Manil-Ségalen M, Lefebvre C, Jenzer C, et al (2014) The C. elegans LC3 Acts Downstream of GABARAP to Degrade Autophagosomes by Interacting with the HOPS Subunit VPS39. Dev Cell 28:43–55. https://doi.org/10.1016/j.devcel.2013.11.022

Marbach A, Bettenbrock K (2012) lac operon induction in Escherichia coli: Systematic comparison of IPTG and TMG induction and influence of the transacetylase LacA. J Biotechnol 157:82–88. https://doi.org/10.1016/j.jbiotec.2011.10.009

Massover WH (1993) Positive staining of protein molecules for electron microscopy: polyiodination of the apoferritin shell in ferritin. Ultramicroscopy 52:383–387. https://doi.org/10.1016/0304-3991(93)90050-8

Matoba K, Kotani T, Tsutsumi A, et al (2020) Atg9 is a lipid scramblase that mediates autophagosomal membrane expansion. Nat Struct Mol Biol 27:1185–1193. https://doi.org/10.1038/s41594-020-00518-w

Matsuda Y, Itaya H, Kitahara Y, et al (2014) Double mutation of cell wall proteins CspB and PBP1a increases secretion of the antibody Fab fragment from Corynebacterium glutamicum. Microb Cell Factories 13:56. https://doi.org/10.1186/1475-2859-13-56

Matsumoto G, Wada K, Okuno M, et al (2011) Serine 403 Phosphorylation of p62/SQSTM1 Regulates Selective Autophagic Clearance of Ubiquitinated Proteins. Mol Cell 44:279–289. https://doi.org/10.1016/j.molcel.2011.07.039

McEwan DG, Dikic I (2011) The Three Musketeers of Autophagy: phosphorylation, ubiquitylation and acetylation. Trends Cell Biol 21:195–201. https://doi.org/10.1016/j.tcb.2010.12.006

McMullan G, Chen S, Henderson R, Faruqi AR (2009) Detective quantum efficiency of electron area detectors in electron microscopy. Ultramicroscopy 109:1126–1143. https://doi.org/10.1016/j.ultramic.2009.04.002

Meacham GC, Patterson C, Zhang W, et al (2001) The Hsc70 co-chaperone CHIP targets immature CFTR for proteasomal degradation. Nat Cell Biol 3:100–105. https://doi.org/10.1038/35050509

Merk A, Bartesaghi A, Banerjee S, et al (2016) Breaking Cryo-EM Resolution Barriers to Facilitate Drug Discovery. Cell 165:1698–1707. https://doi.org/10.1016/j.cell.2016.05.040

Metlagel Z, Otomo C, Takaesu G, Otomo T (2013) Structural basis of ATG3 recognition by the autophagic ubiquitin-like protein ATG12. Proc Natl Acad Sci 110:18844–18849. https://doi.org/10.1073/pnas.1314755110

Mishra S, Ahmed T, Tyagi A, et al (2018) Structures of Mycobacterium smegmatis 70S ribosomes in complex with HPF, tmRNA, and P-tRNA. Sci Rep 8:13587. https://doi.org/10.1038/s41598-018-31850-3

Mizushima N, Kuma A, Kobayashi Y, et al (2003) Mouse Apg16L, a novel WD-repeat protein, targets to the autophagic isolation membrane with the Apg12-Apg5 conjugate. J Cell Sci 116:1679–1688. https://doi.org/10.1242/jcs.00381

Mizushima N, Noda T, Yoshimori T, et al (1998a) A protein conjugation system essential for autophagy. Nature 395:395–398. https://doi.org/10.1038/26506

Mizushima N, Sugita H, Yoshimori T, Ohsumi Y (1998b) A New Protein Conjugation System in Human. J Biol Chem 273:33889–33892. https://doi.org/10.1074/jbc.273.51.33889

Moll I, Bläsi U (2002) Differential inhibition of 30S and 70S translation initiation complexes on leaderless mRNA by kasugamycin. Biochem Biophys Res Commun 297:1021–1026. https://doi.org/10.1016/S0006-291X(02)02333-1

Molliex A, Temirov J, Lee J, et al (2015) Phase Separation by Low Complexity Domains Promotes Stress Granule Assembly and Drives Pathological Fibrillization. Cell 163:123–133. https://doi.org/10.1016/j.cell.2015.09.015

Moscat J, Diaz-Meco MT (2011) Feedback on Fat: p62-mTORC1-Autophagy Connections. Cell 147:724–727. https://doi.org/10.1016/j.cell.2011.10.021

Mostafavi S (2022) Structural insights into selective autophagy and cellular membrane remodeling. Heinrich-Heine Universität

Müller F, Ackermann P, Margot P (2011) Fungicides, Agricultural, 2. Individual Fungicides. In: Wiley-VCH (ed) Ullmann’s Encyclopedia of Industrial Chemistry, 1st edn. Wiley

Munita JM, Arias CA (2016) Mechanisms of Antibiotic Resistance. Microbiol Spectr 4:4.2.15. https://doi.org/10.1128/microbiolspec.VMBF-0016-2015

Nähse V, Raiborg C, Tan KW, et al (2023) ATPase activity of DFCP1 controls selective autophagy. Nat Commun 14:4051. https://doi.org/10.1038/s41467-023-39641-9

Nakamura Y, Ito K, Isaksson LA (1996) Emerging Understanding of Translation Termination. Cell 87:147–150. https://doi.org/10.1016/S0092-8674(00)81331-8

Nakane T, Kotecha A, Sente A, et al (2020) Single-particle cryo-EM at atomic resolution. Nature 587:152–156. https://doi.org/10.1038/s41586-020-2829-0

Nakatogawa H, Ichimura Y, Ohsumi Y (2007) Atg8, a Ubiquitin-like Protein Required for Autophagosome Formation, Mediates Membrane Tethering and Hemifusion. Cell 130:165–178. https://doi.org/10.1016/j.cell.2007.05.021

Nakatogawa H, Suzuki K, Kamada Y, Ohsumi Y (2009) Dynamics and diversity in autophagy mechanisms: lessons from yeast. Nat Rev Mol Cell Biol 10:458–467. https://doi.org/10.1038/nrm2708

Nashimoto H, Held W, Kaltschmidt E, Nomura M (1971) Structure and function of bacterial ribosomes. J Mol Biol 62:121–138. https://doi.org/10.1016/0022-2836(71)90135-5

Natchiar SK, Myasnikov AG, Kratzat H, et al (2017) Visualization of chemical modifications in the human 80S ribosome structure. Nature 551:472–477. https://doi.org/10.1038/nature24482

Nguyen A, Lugarini F, David C, et al (2023) Metamorphic proteins at the basis of human autophagy initiation and lipid transfer. Mol Cell 83:2077-2090.e12. https://doi.org/10.1016/j.molcel.2023.04.026

Ochi K, Kim J-Y, Tanaka Y, et al (2009) Inactivation of KsgA, a 16S rRNA Methyltransferase, Causes Vigorous Emergence of Mutants with High-Level Kasugamycin Resistance. Antimicrob Agents Chemother 53:193–201. https://doi.org/10.1128/AAC.00873-08

Ohi M, Li Y, Cheng Y, Walz T (2004) Negative staining and image classification — powerful tools in modern electron microscopy. Biol Proced Online 6:23–34. https://doi.org/10.1251/bpo70

Oikonomou CM, Chang Y-W, Jensen GJ (2016) A new view into prokaryotic cell biology from electron cryotomography. Nat Rev Microbiol 14:205–220. https://doi.org/10.1038/nrmicro.2016.7

Okuyama A, Machiyama N, Kinoshita T, Tanaka N (1971) Inhibition by kasugamycin of initiation complex formation on 30S ribosomes. Biochem Biophys Res Commun 43:196–199. https://doi.org/10.1016/s0006-291x(71)80106-7

Okuyama A, Tanaka N (1972) Differential effects of aminoglycosides on cistron-specific initiation of protein synthesis. Biochem Biophys Res Commun 49:951–957. https://doi.org/10.1016/0006-291x(72)90304-x

Okuyama A, Yoshikawa M, Tanaka N (1974) Alteration of ribosomal protein S2 in kasugamycin-resistant mutant derived from AB312. Biochem Biophys Res Commun 60:1163–1169. https://doi.org/10.1016/0006-291X(74)90434-3

Orloff J (ed) (2009) Handbook of charged particle optics, 2. ed. CRC Press/ Taylor & Francis, Boca Raton, Fla.

Orlova EV, Saibil HR (2011) Structural Analysis of Macromolecular Assemblies by Electron Microscopy. Chem Rev 111:7710–7748. https://doi.org/10.1021/cr100353t

Ortmann De Percin Northumberland C, Sachse C (2023) Eiskalte Schnappschüsse von Biomolekülen: Kryo-Elektronenmikroskopie. Phys Unserer Zeit 54:116–123. https://doi.org/10.1002/piuz.202301669

Ossareh-Nazari B, Niño CA, Bengtson MH, et al (2014) Ubiquitylation by the Ltn1 E3 ligase protects 60S ribosomes from starvation-induced selective autophagy. J Cell Biol 204:909–917. https://doi.org/10.1083/jcb.201308139

Otomo C, Metlagel Z, Takaesu G, Otomo T (2013) Structure of the human ATG12~ATG5 conjugate required for LC3 lipidation in autophagy. Nat Struct Mol Biol 20:59–66. https://doi.org/10.1038/nsmb.2431

Øverbye A, Brinchmann MF, Seglen PO (2007) Proteomic Analysis of Membrane-Associated Proteins from Rat Liver Autophagosomes. Autophagy 3:300–322. https://doi.org/10.4161/auto.3910

Pan J-A, Sun Y, Jiang Y-P, et al (2016) TRIM21 Ubiquitylates SQSTM1/p62 and Suppresses Protein Sequestration to Regulate Redox Homeostasis. Mol Cell 61:720–733. https://doi.org/10.1016/j.molcel.2016.02.007

Papinski D, Kraft C (2016) Regulation of Autophagy By Signaling Through the Atg1/ULK1 Complex. J Mol Biol 428:1725–1741. https://doi.org/10.1016/j.jmb.2016.03.030

Patel A, Lee HO, Jawerth L, et al (2015) A Liquid-to-Solid Phase Transition of the ALS Protein FUS Accelerated by Disease Mutation. Cell 162:1066–1077. https://doi.org/10.1016/j.cell.2015.07.047

Paternoga H, Crowe-McAuliffe C, Bock LV, et al (2023) Structural conservation of antibiotic interaction with ribosomes. Nat Struct Mol Biol. https://doi.org/10.1038/s41594-023-01047-y

Poldermans B, Goosen N, Van Knippenberg PH (1979) Studies on the function of two adjacent N6,N6-dimethyladenosines near the 3’ end of 16 S ribosomal RNA of Escherichia coli. I. The effect of kasugamycin on initiation of protein synthesis. J Biol Chem 254:9085–9089

Polson HEJ, De Lartigue J, Rigden DJ, et al (2010) Mammalian Atg18 (WIPI2) localizes to omegasome-anchored phagophores and positively regulates LC3 lipidation. Autophagy 6:506–522. https://doi.org/10.4161/auto.6.4.11863

Proikas-Cezanne T, Takacs Z, Dönnes P, Kohlbacher O (2015) WIPI proteins: essential PtdIns3 *P* effectors at the nascent autophagosome. J Cell Sci jcs.146258. https://doi.org/10.1242/jcs.146258

Proikas-Cezanne T, Waddell S, Gaugel A, et al (2004) WIPI-1α (WIPI49), a member of the novel 7-bladed WIPI protein family, is aberrantly expressed in human cancer and is linked to starvation-induced autophagy. Oncogene 23:9314–9325. https://doi.org/10.1038/sj.onc.1208331

Puissant A, Fenouille N, Auberger P (2012) When autophagy meets cancer through p62/SQSTM1. Am J Cancer Res 2:397–413

Punjani A, Fleet DJ (2021) 3D variability analysis: Resolving continuous flexibility and discrete heterogeneity from single particle cryo-EM. J Struct Biol 213:107702. https://doi.org/10.1016/j.jsb.2021.107702

Punjani A, Fleet DJ (2023) 3DFlex: determining structure and motion of flexible proteins from cryo-EM. Nat Methods. https://doi.org/10.1038/s41592-023-01853-8

Punjani A, Rubinstein JL, Fleet DJ, Brubaker MA (2017) cryoSPARC: algorithms for rapid unsupervised cryo-EM structure determination. Nat Methods 14:290–296. https://doi.org/10.1038/nmeth.4169

Putyrski M, Vakhrusheva O, Bonn F, et al (2020) Disrupting the LC3 Interaction Region (LIR) Binding of Selective Autophagy Receptors Sensitizes AML Cell Lines to Cytarabine. Front Cell Dev Biol 8:208. https://doi.org/10.3389/fcell.2020.00208

Quinternet M, Chagot M-E, Rothé B, et al (2016) Structural Features of the Box C/D snoRNP Pre-assembly Process Are Conserved through Species. Structure 24:1693–1706. https://doi.org/10.1016/j.str.2016.07.016

Rabinowitz JD, White E (2010) Autophagy and Metabolism. Science 330:1344–1348. https://doi.org/10.1126/science.1193497

Radermacher M (1992) Weighted Back-Projection Methods. In: Frank J (ed) Electron Tomography. Springer US, Boston, MA, pp 91–115

Ramakrishnan V (2002) Ribosome Structure and the Mechanism of Translation. Cell 108:557–572. https://doi.org/10.1016/S0092-8674(02)00619-0

Ravenhill BJ, Boyle KB, von Muhlinen N, et al (2019) The Cargo Receptor NDP52 Initiates Selective Autophagy by Recruiting the ULK Complex to Cytosol-Invading Bacteria. Mol Cell 74:320-329.e6. https://doi.org/10.1016/j.molcel.2019.01.041

Ravikumar B, Vacher C, Berger Z, et al (2004) Inhibition of mTOR induces autophagy and reduces toxicity of polyglutamine expansions in fly and mouse models of Huntington disease. Nat Genet 36:585–595. https://doi.org/10.1038/ng1362

RCSB PDB PDB PDB Statistics: Growth of Structures from 3DEM Experiments Released per Year. https://www.rcsb.org/stats/growth/growth-em. Accessed 19 Apr 2024

Rennick JJ, Nowell CJ, Pouton CW, Johnston APR (2022) Resolving subcellular pH with a quantitative fluorescent lifetime biosensor. Nat Commun 13:6023. https://doi.org/10.1038/s41467-022-33348-z

Rogov V, Dötsch V, Johansen T, Kirkin V (2014) Interactions between Autophagy Receptors and Ubiquitin-like Proteins Form the Molecular Basis for Selective Autophagy. Mol Cell 53:167–178. https://doi.org/10.1016/j.molcel.2013.12.014

Rohou A, Grigorieff N (2015) CTFFIND4: Fast and accurate defocus estimation from electron micrographs. J Struct Biol 192:216–221. https://doi.org/10.1016/j.jsb.2015.08.008

Rose HH (2008) Optics of high-performance electron microscopes. Sci Technol Adv Mater 9:014107. https://doi.org/10.1088/0031-8949/9/1/014107

Rosenthal PB, Crowther RA, Henderson R (2003) An objective criterion for resolution assessment in single-particle electron Microscopy. (Appendix to: Rosenthal, P.B., Henderson, R., 2003. Optimal determination of particle orientation, absolute hand, and contrast loss in single-particle electron cryomicroscopy. J. Mol. Biol. 333, 721–745). J Mol Biol 333:743–745

Rosenthal PB, Henderson R (2003) Optimal Determination of Particle Orientation, Absolute Hand, and Contrast Loss in Single-particle Electron Cryomicroscopy. J Mol Biol 333:721–745. https://doi.org/10.1016/j.jmb.2003.07.013

Rostislavleva K, Soler N, Ohashi Y, et al (2015) Structure and flexibility of the endosomal Vps34 complex reveals the basis of its function on membranes. Science 350:aac7365. https://doi.org/10.1126/science.aac7365

Rubinstein JL, Brubaker MA (2015) Alignment of cryo-EM movies of individual particles by optimization of image translations. J Struct Biol 192:188–195. https://doi.org/10.1016/j.jsb.2015.08.007

Ruska H, Borries BV, Ruska E (1939) Die Bedeutung der Übermikroskopie für die Virusforschung. Arch Für Gesamte Virusforsch 1:155–169. https://doi.org/10.1007/BF01243399

Russell RC, Tian Y, Yuan H, et al (2013) ULK1 induces autophagy by phosphorylating Beclin-1 and activating VPS34 lipid kinase. Nat Cell Biol 15:741–750. https://doi.org/10.1038/ncb2757

Saio T, Yokochi M, Inagaki F (2009) The NMR structure of the p62 PB1 domain, a key protein in autophagy and NF-κB signaling pathway. J Biomol NMR 45:335–341. https://doi.org/10.1007/s10858-009-9370-7

Sambrook J, Russell DW (2001) Molecular cloning: a laboratory manual, 3rd ed. Cold Spring Harbor Laboratory Press, Cold Spring Harbor, N.Y

Sanger F, Nicklen S, Coulson AR (1977) DNA sequencing with chain-terminating inhibitors. Proc Natl Acad Sci 74:5463–5467. https://doi.org/10.1073/pnas.74.12.5463

Sanz L (1999) The interaction of p62 with RIP links the atypical PKCs to NF-kappa B activation. EMBO J 18:3044–3053. https://doi.org/10.1093/emboj/18.11.3044

Savir Y, Tlusty T (2013) The Ribosome as an Optimal Decoder: A Lesson in Molecular Recognition. Cell 153:471–479. https://doi.org/10.1016/j.cell.2013.03.032

Saxton RA, Sabatini DM (2017) mTOR Signaling in Growth, Metabolism, and Disease. Cell 168:960–976. https://doi.org/10.1016/j.cell.2017.02.004

Scarff CA, Fuller MJG, Thompson RF, Iadanza MG (2018) Variations on Negative Stain Electron Microscopy Methods: Tools for Tackling Challenging Systems. J Vis Exp 57199. https://doi.org/10.3791/57199

Scheres SHW (2016) Processing of Structurally Heterogeneous Cryo-EM Data in RELION. In: Methods in Enzymology. Elsevier, pp 125–157

Scherzer O (1949) The Theoretical Resolution Limit of the Electron Microscope. J Appl Phys 20:20–29. https://doi.org/10.1063/1.1698233

Schindelin J, Arganda-Carreras I, Frise E, et al (2012) Fiji: an open-source platform for biological-image analysis. Nat Methods 9:676–682. https://doi.org/10.1038/nmeth.2019

Schluenzen F, Takemoto C, Wilson DN, et al (2006) The antibiotic kasugamycin mimics mRNA nucleotides to destabilize tRNA binding and inhibit canonical translation initiation. Nat Struct Mol Biol 13:871–878. https://doi.org/10.1038/nsmb1145

Schuwirth BS, Day JM, Hau CW, et al (2006) Structural analysis of kasugamycin inhibition of translation. Nat Struct Mol Biol 13:879–886. https://doi.org/10.1038/nsmb1150

Shasmal M, Sengupta J (2012) Structural Diversity in Bacterial Ribosomes: Mycobacterial 70S Ribosome Structure Reveals Novel Features. PLoS ONE 7:e31742. https://doi.org/10.1371/journal.pone.0031742

Shim MS, Nettesheim A, Hirt J, Liton PB (2019) The autophagic protein LC3 translocates to the nucleus and localizes in the nucleolus associated to NUFIP1 in response to cyclic mechanical stress. Autophagy 1–14. https://doi.org/10.1080/15548627.2019.1662584

Shpilka T, Weidberg H, Pietrokovski S, Elazar Z (2011) Atg8: an autophagy-related ubiquitin-like protein family. Genome Biol 12:226. https://doi.org/10.1186/gb-2011-12-7-226

Sigworth FJ (2016) Principles of cryo-EM single-particle image processing. Microscopy 65:57–67. https://doi.org/10.1093/jmicro/dfv370

Smith DB, Johnson KS (1988) Single-step purification of polypeptides expressed in Escherichia coli as fusions with glutathione S-transferase. Gene 67:31–40. https://doi.org/10.1016/0378-1119(88)90005-4

Sparling PF, Ikeya Y, Elliot D (1973) Two Genetic Loci for Resistance to Kasugamycin in *Escherichia coli*. J Bacteriol 113:704–710. https://doi.org/10.1128/jb.113.2.704-710.1973

Stalling D, Westerhoff M, Hege H-C (2005) Amira: A highly interactive system for visual data analysis." The visualization handbook, 38th edn.

Stanley RE, Blaha G, Grodzicki RL, et al (2010) The structures of the anti-tuberculosis antibiotics viomycin and capreomycin bound to the 70S ribosome. Nat Struct Mol Biol 17:289–293. https://doi.org/10.1038/nsmb.1755

Strober W (1997) Trypan Blue Exclusion Test of Cell Viability. Curr Protoc Immunol 21:. https://doi.org/10.1002/0471142735.ima03bs21

Strome S, Wood WB (1982) Immunofluorescence visualization of germ-line-specific cytoplasmic granules in embryos, larvae, and adults of Caenorhabditis elegans. Proc Natl Acad Sci 79:1558–1562. https://doi.org/10.1073/pnas.79.5.1558

Sun J, Kinman LF, Jahagirdar D, et al (2023) KsgA facilitates ribosomal small subunit maturation by proofreading a key structural lesion. Nat Struct Mol Biol 30:1468–1480. https://doi.org/10.1038/s41594-023-01078-5

Sun Q, Fan W, Chen K, et al (2008) Identification of Barkor as a mammalian autophagy-specific factor for Beclin 1 and class III phosphatidylinositol 3-kinase. Proc Natl Acad Sci U S A 105:19211–19216. https://doi.org/10.1073/pnas.0810452105

Taherbhoy AM, Tait SW, Kaiser SE, et al (2011) Atg8 Transfer from Atg7 to Atg3: A Distinctive E1-E2 Architecture and Mechanism in the Autophagy Pathway. Mol Cell 44:451–461. https://doi.org/10.1016/j.molcel.2011.08.034

Takahashi Y, He H, Tang Z, et al (2018) An autophagy assay reveals the ESCRT-III component CHMP2A as a regulator of phagophore closure. Nat Commun 9:2855. https://doi.org/10.1038/s41467-018-05254-w

Takahashi Y, Liang X, Hattori T, et al (2019) VPS37A directs ESCRT recruitment for phagophore closure. J Cell Biol 218:3336–3354. https://doi.org/10.1083/jcb.201902170

Tegunov D, Cramer P (2019) Real-time cryo-electron microscopy data preprocessing with Warp. Nat Methods 16:1146–1152. https://doi.org/10.1038/s41592-019-0580-y

Thermo Fisher Scientific (2024) Krios G4 Cryo-TEM

Tietz H (2008) Design and Characterization of 64 MegaPixel Fiber Optic Coupled CMOS Detector for Transmission Electron Microscopy. Microsc Microanal 14:804–805. https://doi.org/10.1017/S1431927608084675

Tirumalai MR, Rivas M, Tran Q, Fox GE (2021) The Peptidyl Transferase Center: a Window to the Past. Microbiol Mol Biol Rev 85:e00104-21. https://doi.org/10.1128/MMBR.00104-21

Turco E, Witt M, Abert C, et al (2019a) FIP200 Claw Domain Binding to p62 Promotes Autophagosome Formation at Ubiquitin Condensates. Mol Cell 74:330-346.e11. https://doi.org/10.1016/j.molcel.2019.01.035

Turco E, Witt M, Abert C, et al (2019b) FIP200 Claw Domain Binding to p62 Promotes Autophagosome Formation at Ubiquitin Condensates. Mol Cell 74:330-346.e11. https://doi.org/10.1016/j.molcel.2019.01.035

Uemura T, Yamamoto M, Kametaka A, et al (2014) A Cluster of Thin Tubular Structures Mediates Transformation of the Endoplasmic Reticulum to Autophagic Isolation Membrane. Mol Cell Biol 34:1695–1706. https://doi.org/10.1128/MCB.01327-13

Umezawa H, Hamada M, Suhara Y, et al (1965) Kasugamycin, a new antibiotic. Antimicrob Agents Chemother 5:753–757

Van Die IM, Bergmans HEN, Hoekstra WPM (1983) Transformation In Escherichia coli: Studies On The Role Of The Heat Shock In Induction Of Competence. Microbiology 129:663–670. https://doi.org/10.1099/00221287-129-3-663

Van Heel M, Schatz M (2005) Fourier shell correlation threshold criteria. J Struct Biol 151:250–262. https://doi.org/10.1016/j.jsb.2005.05.009

Vietri M, Radulovic M, Stenmark H (2020) The many functions of ESCRTs. Nat Rev Mol Cell Biol 21:25–42. https://doi.org/10.1038/s41580-019-0177-4

Vila-Sanjurjo A, Squires CL, Dahlberg AE (1999) Isolation of kasugamycin resistant mutants in the 16 S ribosomal RNA of Escherichia coli. J Mol Biol 293:1–8. https://doi.org/10.1006/jmbi.1999.3160

Wade RH (1992) A brief look at imaging and contrast transfer. Ultramicroscopy 46:145–156. https://doi.org/10.1016/0304-3991(92)90011-8

Wade RH, Frank J (1977) Electron microscope transfer functions for partially coherent axial illumination and chromatic defocus spread. Opt Jena 49:81–92

Wan W, Briggs J a. G (2016) Cryo-Electron Tomography and Subtomogram Averaging. Methods Enzymol 579:329–367. https://doi.org/10.1016/bs.mie.2016.04.014

Wang JT, Smith J, Chen B-C, et al (2014) Regulation of RNA granule dynamics by phosphorylation of serine-rich, intrinsically disordered proteins in C. elegans. eLife 3:e04591. https://doi.org/10.7554/eLife.04591

Wang L, Klionsky DJ, Shen H-M (2023) The emerging mechanisms and functions of microautophagy. Nat Rev Mol Cell Biol 24:186–203. https://doi.org/10.1038/s41580-022-00529-z

Wang L, Shkolnisky Y, Singer A (2013) A Fourier-based Approach for Iterative 3D Reconstruction from Cryo-EM Images. arXiv:13075824

Watanabe Y, Tatebe H, Taguchi K, et al (2012) p62/SQSTM1-Dependent Autophagy of Lewy Body-Like α-Synuclein Inclusions. PLoS ONE 7:e52868. https://doi.org/10.1371/journal.pone.0052868

Weidberg H, Elazar Z (2011) TBK1 Mediates Crosstalk Between the Innate Immune Response and Autophagy. Sci Signal 4:. https://doi.org/10.1126/scisignal.2002355

Weidberg H, Shpilka T, Shvets E, et al (2011) LC3 and GATE-16 N Termini Mediate Membrane Fusion Processes Required for Autophagosome Biogenesis. Dev Cell 20:444–454. https://doi.org/10.1016/j.devcel.2011.02.006

Wesselborg S, Stork B (2015) Autophagy signal transduction by ATG proteins: from hierarchies to networks. Cell Mol Life Sci 72:4721–4757. https://doi.org/10.1007/s00018-015-2034-8

White E, DiPaola RS (2009) The Double-Edged Sword of Autophagy Modulation in Cancer. Clin Cancer Res 15:5308–5316. https://doi.org/10.1158/1078-0432.CCR-07-5023

Williams DB, Carter CB (2009) Transmission Electron Microscopy. Springer US, Boston, MA

Wurzer B, Zaffagnini G, Fracchiolla D, et al (2015) Oligomerization of p62 allows for selection of ubiquitinated cargo and isolation membrane during selective autophagy. eLife 4:e08941. https://doi.org/10.7554/eLife.08941

Wyant GA, Abu-Remaileh M, Frenkel EM, et al (2018) NUFIP1 is a ribosome receptor for starvation-induced ribophagy. Science 360:751–758. https://doi.org/10.1126/science.aar2663

Xie Z, Klionsky DJ (2007) Autophagosome formation: core machinery and adaptations. Nat Cell Biol 9:1102–1109. https://doi.org/10.1038/ncb1007-1102

Xie Z, Nair U, Klionsky DJ (2008) Atg8 Controls Phagophore Expansion during Autophagosome Formation. Mol Biol Cell 19:3290–3298. https://doi.org/10.1091/mbc.e07-12-1292

Yang K, Chang J-Y, Cui Z, et al (2017) Structural insights into species-specific features of the ribosome from the human pathogen Mycobacterium tuberculosis. Nucleic Acids Res 45:10884–10894. https://doi.org/10.1093/nar/gkx785

Yim SS, An SJ, Choi JW, et al (2014) High-level secretory production of recombinant single-chain variable fragment (scFv) in Corynebacterium glutamicum. Appl Microbiol Biotechnol 98:273–284. https://doi.org/10.1007/s00253-013-5315-x

Yim SS, Choi JW, Lee RJ, et al (2016) Development of a new platform for secretory production of recombinant proteins in *Corynebacterium glutamicum*. Biotechnol Bioeng 113:163–172. https://doi.org/10.1002/bit.25692

Yin Z, Pascual C, Klionsky D (2016) Autophagy: machinery and regulation. Microb Cell 3:588–596. https://doi.org/10.15698/mic2016.12.546

Yoshii A, Moriyama H, Fukuhara T (2012) The Novel Kasugamycin 2′- *N* - Acetyltransferase Gene *aac(2′)-IIa* , Carried by the IncP Island, Confers Kasugamycin Resistance to Rice-Pathogenic Bacteria. Appl Environ Microbiol 78:5555–5564. https://doi.org/10.1128/AEM.01155-12

Yoshikawa M, Okuyama A, Tanaka N (1975) A Third Kasugamycin Resistance Locus, *ksgC* , Affecting Ribosomal Protein S2 in *Escherichia coli* K-12. J Bacteriol 122:796–797. https://doi.org/10.1128/jb.122.2.796-797.1975

You Z, Jiang W-X, Qin L-Y, et al (2019) Requirement for p62 acetylation in the aggregation of ubiquitylated proteins under nutrient stress. Nat Commun 10:5792. https://doi.org/10.1038/s41467-019-13718-w

Yu Z-Q, Ni T, Hong B, et al (2012) Dual roles of Atg8−PE deconjugation by Atg4 in autophagy. Autophagy 8:883–892. https://doi.org/10.4161/auto.19652

Zachari M, Ganley IG (2017) The mammalian ULK1 complex and autophagy initiation. Essays Biochem 61:585–596. https://doi.org/10.1042/EBC20170021

Zaffagnini G, Savova A, Danieli A, et al (2018) p62 filaments capture and present ubiquitinated cargos for autophagy. EMBO J 37:e98308. https://doi.org/10.15252/embj.201798308

Zehr BD, Savin TJ, Hall RE (1989) A one-step, low background Coomassie staining procedure for polyacrylamide gels. Anal Biochem 182:157–159. https://doi.org/10.1016/0003-2697(89)90734-3

Zhang G, Wang Z, Du Z, Zhang H (2018) mTOR Regulates Phase Separation of PGL Granules to Modulate Their Autophagic Degradation. Cell 174:1492-1506.e22. https://doi.org/10.1016/j.cell.2018.08.006

Zheng Q, Chen Y, Chen D, et al (2022a) Calcium transients on the ER surface trigger liquid-liquid phase separation of FIP200 to specify autophagosome initiation sites. Cell 185:4082-4098.e22. https://doi.org/10.1016/j.cell.2022.09.001

Zheng S, Wolff G, Greenan G, et al (2022b) AreTomo: An integrated software package for automated marker-free, motion-corrected cryo-electron tomographic alignment and reconstruction. J Struct Biol X 6:100068. https://doi.org/10.1016/j.yjsbx.2022.100068

Zhou ZH (2008) Towards atomic resolution structural determination by single-particle cryo-electron microscopy. Curr Opin Struct Biol 18:218–228. https://doi.org/10.1016/j.sbi.2008.03.004

Zivanov J, Nakane T, Scheres SHW (2020) Estimation of high-order aberrations and anisotropic magnification from cryo-EM data sets in RELION-3.1. IUCrJ 7:253–267. https://doi.org/10.1107/S2052252520000081

Zuo JM (2017) Advanced transmission electron microscopy: imaging and diffraction in nanoscience. Springer, New York, NY

7 Supplement

7.1 List of Figures

Figure 1: Basic set-up of a transmission electron microscope 2
Figure 2: Electron sources in transmission electron microscopy........................... 4
Figure 3: Electron detectors 8
Figure 4: The contrast transfer function... 12
Figure 5: Negative stain electron microscopy.. 14
Figure 6: Single-particle analysis... 18
Figure 7: Atomic-model refinement and validation criteria 20
Figure 8: Cryogenic electron tomography 22
Figure 9: Autophagy pathways at a glance 25
Figure 10: Schematic illustration of macroautophagy degradation of cellular components 29
Figure 11: The NUFIP1 protein 36
Figure 12: The p62 protein 39
Figure 13: Three-dimensional structure of a helical filament formed by the PB1-domain of p62 and possible ways of interaction with binding partners................ 41
Figure 14: Material states of biological condensates in phase separation 43
Figure 15: Bacterial translation - a simplified elongation cycle............................ 46
Figure 16: The Actinomycetota ribosome.. 48
Figure 17: The bS22 protein in *F. johnsoniae* and *M. smegmatis*....................... 50
Figure 18: The antibiotic Kasugamycin and its binding to the 30S subunit of *E. coli* 51
Figure 19: Immunofluorescence assay of endogenous NUFIP1 56
Figure 20: Live-cell imaging of fluorescently labeled NUFIP1 57
Figure 21: Live-cell imaging of NUFIP1 traffic light reporter................................ 59
Figure 22: Live-cell imaging of NUFIP1 traffic light reporter with additional lysotracker dye 60
Figure 23: Transient protein expression of MBP-NUFIP1 in FreeStyle^{TM} 293-F cells 62

Figure 24: Purification of NUFIP1 63
Figure 25: Purification of MBP-NUFIP1 enriched ribosomes for SPA 66
Figure 26: SPA of 80S human ribosomes 68
Figure 27: Purification of MBP-p62 71
Figure 28: Purification of MBP-mCherry-p62 72
Figure 29: HRV3C digestion of MBP-p62 and MBP-mCherry-p62 73
Figure 30: Preparation of LC3B variants and labeled GST-4xUbiquitin 74
Figure 31: Preparation of LC3B-Cys covered liposomes 76
Figure 32: Calibration curve to determine the lipid concentration after size exclusion chromatography 77
Figure 33: Pull-down of MBP-p62 or MBP-mCherry-p62 by LC3B and LC3Be ... 79
Figure 34: Binding of LC3B and LC3Be to p62 filaments 80
Figure 35: Data processing workflow of tomograms collected on p62 filaments with LC3B covered liposomes 81
Figure 36: Cryogenic electron tomography of p62 filaments with LC3B covered liposomes 82
Figure 37: Phase separation of p62 and mCherry-p62 induced by GST-4xUbiquitin 84
Figure 38: Cryogenic electron tomography of p62 filaments 85
Figure 39: Cryogenic electron tomography of p62 filaments in phase separation 86
Figure 40: Cryogenic electron microscopy of p62 filaments in phase separation 87
Figure 41: *In vitro* phase separation of p62 filaments by divalent cations 89
Figure 42: Single-particle analysis of *C. glutamicum* 70S ribosome 96
Figure 43: Fourier shell correlation of single-particle analysis and resolution at a glance 97
Figure 44: Three-dimensional classification processing pipeline 100
Figure 45: Conformational landscape of the *C. glutamicum* 70S ribosome 102
Figure 46: Kasugamycin binding pocket in the Cg70S 103
Figure 47: Conformational landscape of the Cg70S and Cg70S + Kasugamycin 104
Figure 48: bS22 in the Cg70S ribosome 106

Figure 49: Rotation of small subunit proteins in Cg70S and ΔbS22 107
Figure 50: Conformational landscape of the Cg70S compared to ΔbS22 70S.. 108
Figure 51: Conformational landscape of the Cg70S compared to ΔKsgA 70S . 109

7.2 List of Tables

Table 1: Selective autophagy 32
Table 2: NUFIP1 protein concentration after purification.................................... 64
Table 3: SPA data collection of human 80S ribosomes 67
Table 4: Ratio of labeled GST-4xUbiquitin 75
Table 5: Concentration of lipids after size exclusion chromatography 77
Table 6: SPA of *C. glutamicum* 70S ribosomes 98
Table 7: Assignment of translational states based on three-dimensional classification 101
Table 8: Plasmids NUFIP1 119
Table 9: Plasmids p62 119
Table 10: Cell lines and bacterial strains 121
Table 11: Media 122
Table 12: Buffers 123
Table 13: NUFIP1 purification buffers 123
Table 14: p62 purification buffers 124
Table 15: GST-fusion protein buffers 125
Table 16: Chromatography resins and columns 125
Table 17: Software 126
Table 18: PCR reaction set-up 129
Table 19: PCR reaction scheme 130
Table 20: HEK293F cell culture 133

8 Acknowledgments

I would like to express my deepest gratitude to Professor Carsten Sachse for his unwavering support and exceptional scientific supervision throughout this journey. His insightful guidance and encouragement have been invaluable in shaping this thesis. I am truly grateful for his dedication and the opportunities he provided to enhance my research skills.

I am sincerely thankful to Professor Gunnar Schroeder for his mentorship and for serving as my second supervisor. His expert scientific advice and constructive feedback have significantly contributed to the development and refinement of this thesis.

I would like to express my gratitude to Dr. by Susana Matamouros for her exceptional work in preparing the *C. glutamicum* ribosome samples for vitrification. Her meticulous efforts have significantly contributed to the progress of this research. I also extend my thanks to her supervisor, Professor Michael Bott, for pursuing this collaboration.

I would like to extend my thanks to the members of the Sachse lab and ER-C-3 facility for their support throughout the years. Their friendliness, open-mindedness, and constant encouragement have created an inspiring and collaborative environment. I am deeply grateful for their camaraderie and the invaluable assistance they provided at every step of this journey. To highlight here, are Dr. Daniel Mann for ever lasting computational support, Dr. Sabrina Berkamp for always helpful advice on all matters of p62 and Claire Ortmann, Katerina Filopoulou and Dr. Olivera Korculanin for their support in all matters one can encounter.

I am profoundly grateful to my family, friends and guinea pigs for their support and encouragement throughout this journey. Their constant presence and belief in me have been a source of strength and motivation. I also appreciate the much-needed distractions and joyful moments they provided, which helped me maintain a balanced perspective during the more challenging times.